Solar Torque and Dissipation Dynamics for Tumbling Bodies: Theory and Observations

by

Conor J. Benson

B.S., North Carolina State University, 2015

M.S., University of Colorado, 2017

A thesis submitted to the

Faculty of the Graduate School of the

University of Colorado in partial fulfillment

of the requirements for the degree of

Doctor of Philosophy

Department of Aerospace Engineering Sciences

2021

Committee Members:

Daniel Scheeres, Chair

Hanspeter Schaub

Jay McMahon

Marcus Holzinger

Carolin Frueh

Benson, Conor J. (Ph.D., Department of Aerospace Engineering Sciences)

Solar Torque and Dissipation Dynamics for Tumbling Bodies: Theory and Observations

Thesis directed by Prof. Daniel Scheeres

Reflection and thermal re-emission of solar radiation can influence the rotational dynamics of small bodies via the Yarkovsky-O'Keefe-Radzievskii-Paddack (YORP) effect. The YORP effect plays a primary role in the dynamical evolution of small asteroids. Modeling and observations indicate that many defunct high-altitude earth-orbiting satellites are also driven by the YORP effect. However, no comprehensive YORP studies for defunct satellites in general rotation have been conducted. Better understanding of defunct satellite spin state evolution would improve solar radiation pressure modeling for orbit prediction and facilitate active debris removal and satellite servicing which require accurate target attitude information. This work explores the long-term general (uniform and tumbling) rotational dynamics of defunct satellites subject to the YORP effect, internal energy dissipation, and gravity gradient torques through dynamical modeling and observation analysis. Focus is placed on the well-documented and dynamically interesting GOES 8-12 geosynchronous satellites. Full dynamics models are developed which illustrate rich, previously undocumented behavior including tumbling cycles, sun-tracking precession, tumbling period resonances, and asymptotically stable tumbling states/limit cycles. Using osculating rotational elements, the relevant perturbations are then analytically and numerically averaged over the satellite's general rotation, defined by Jacobi elliptic functions. These new tumbling-averaged models capture and explain the full dynamics behavior and reduce computation times by several orders of magnitude. The tumbling-averaged models facilitate broad exploration and classification of small body spin state evolution. Techniques for extracting spin state information from tumbling satellite light curve and Doppler radar observations are then developed. Analysis of GOES 8-12 observations from 2014 - 2020 reveals diverse, evolving spin states and clear consistencies with dynamical theory. The averaged models are then applied to box-wing satellites and meter-sized asteroids.

Acknowledgements

Contents

Chapter

Tables

Table

Figures

Figure

Chapter 1

Introduction

1.1   Motivation

Geosynchronous (GEO) and medium earth orbit (MEO) grow increasingly important for communications, global positioning, earth observation, and weather forecasting. With continued launches and long or indefinite orbital lifetimes at higher altitudes due to negligible atmospheric drag or other natural de-orbit mechanisms [59, 91], many regions are becoming more crowded with active spacecraft and debris. For example, as of January 1, 2019, there were more than 1600 known objects near GEO, only 529 of which were actively controlled [65]. To protect these active assets and preserve valuable orbital regimes for future use, it is crucial to understand the long-term rotational dynamics of orbital debris. Many of these debris objects are retired, abandoned, or otherwise defunct satellites.

Optical light curve surveys have shown that defunct satellite spin rates are diverse and can change significantly over time. Karavaev et al. [57] and Papushev et al. [80] found spin periods of tens of seconds to several minutes for defunct three axis stabilized GEO satellites, some of which were quite variable. Cognion [27] and Ryan and Ryan [94] observed the family of five retired GOES 8-12 satellites. They found that one satellite was in fast uniform rotation with a variable spin rate [27], three appeared to be in non-principal axis rotation (i.e. tumbling) [27], and one decelerated in uniform rotation before appearing to transition to tumbling [27, 94]. Earl and Wade [34] collected long-term observations of several defunct GEO satellites in uniform rotation which exhibited cyclic spin period variation. Light curve studies by Silha et al. [105] also found high altitude satellites

and rocket bodies with spin periods ranging from seconds to tens of minutes. The spin periods of some objects varied over time [105]. This observed spin state diversity and variation is likely due in part to solar radiation torques via the Yarkovsky-O'Keefe-Radzievskii-Paddack (YORP) effect.

Advancing knowledge of long-term defunct satellite spin state evolution stands to provide a number of benefits. First of all, attitude information will improve projected area estimates for solar radiation (SRP) modeling. This will benefit long-term debris orbit prediction at higher altitudes where SRP is the primary non-gravitational perturbation. Also, a better understanding of debris spin cycles and maximum spin rates will aid modeling of material shedding. For example, most high area-to-mass (HAMR) objects at GEO are thought to be pieces of multi-layer insulation (MLI) that have shed off defunct satellites and upper stages [67].

With the growing debris population and the massive cost associated with designing, constructing, and launching satellites, a number of organizations are developing active debris removal (ADR) [6] and satellite servicing missions [28, 24]. Current and proposed methods generally require a chaser spacecraft to rendezvous with and physically grapple a target. Uncontrolled targets will generally be non-cooperative with arbitrary and potentially evolving spin states. Also, few if any satellites and rocket bodies currently in orbit have been designed for on-orbit docking. So knowledge of a target's spin state will be crucial, preferably well before rendezvous. Electromagnetic and electrostatic ADR approaches have been proposed that do not require physical contact to de-tumble a target [76, 9]. Electrostatic tractor approaches can also be used to re-orbit a spinning target without needing to de-tumble it first [97]. The efficiency of these various approaches depends significantly on the chaser-target relative geometry. For example, smaller relative separation distances generally provide higher efficiency. Knowledge of a target's spin pole direction will help minimize this separation distance while avoiding collision risk. De-tumble times also depend on the target's initial angular velocity. So target spin state predictions are still valuable for these touchless approaches. With variable spin state evolution, predicting future capture windows with slow rotation would also be advantageous. End of life orientations of solar arrays and other appendages may strongly affect solar torque magnitudes and subsequent long-term evolution. Further study of

this may help inform satellite decommission procedures to reduce spin rates and make them less variable. This would in turn facilitate active debris removal and satellite servicing.

1.2   The Yarkovsky and YORP Effects

Up until the late 20th century, the dynamical evolution of asteroids was widely thought to be dominated by gravitational interactions with large solar system bodies [60, 115, 117, 36, 89, 15, 103] and mutual collisions [50, 36, 118, 14, 30, 35, 17, 72]. Over the past several decades, a more subtle mechanism, solar radiation, has been found to play an important role in the orbital and rotational evolution of sub ~40 km asteroids [17, 111]. The Yarkovsky effect, named after Ivan Yarkovsky who first proposed it around the turn of the 20th century, is the process by which an asteroid's orbit slowly changes due to non-uniform re-emission of thermal radiation [75, 8]. As an asteroid rotates, its sunlit side heats up over the course of the day, reaching the highest temperature in the afternoon. Being hottest, this afternoon region emits more thermal radiation than other parts of the asteroid. The thermal radiation leaving the asteroid carries momentum and therefore exerts an equal and opposite push on the asteroid. So this uneven thermal emission results in a consistent net force which causes the asteroid's orbit to slowly change. For prograde rotation, the afternoon is on the trailing side of the asteroid, so the force is roughly along the orbital velocity direction which causes the asteroid's semi-major axis increases. For retrograde rotation, the afternoon is on the leading side and the semi-major axis instead decreases [92, 37]. This diurnal Yarkovsky component is accompanied by a seasonal component if an asteroid's spin pole has a projection in the orbit plane. For this seasonal component, the northern and southern hemispheres reach their highest temperatures in late summer and late winter respectively which results in a net force opposing the asteroid orbital velocity [92, 37]. So unlike the diurnal component, the seasonal component always reduces the asteroid's semi-major axis. The magnitudes of both Yarkovsky components depend on several factors including the asteroid's size, shape, spin rate, obliquity, and material properties [17, 111]. Most notably, the Yarkovsky drift rate is proportional to $1/D$ where D is the asteroid size [17, 111]. So all else equal, smaller asteroids are more susceptible to the Yarkovsky effect.

Through long-term observational campaigns and precise orbit determination, the Yarkovsky effect has been detected for an ever growing number of asteroids [111, 43], the first in 2003 for asteroid (6489) Golevka [25]. The Yarkovsky effect is now recognized as the most common mechanism for asteroid migration towards gravitational resonances in the main asteroid belt [37, 114, 17]. Perturbed by these resonances, asteroids are then pushed out of the main belt and towards the inner or outer solar system [36, 115, 117, 17, 111]. The Yarkovsky effect plays a key role in replenishing the near earth asteroid (NEA) population, which is depleted due to interactions with the large inner solar system bodies, namely impacts and ejections [17]. Studies of the observed Yarkovsky drift rates for more than 200 NEAs show a significant bias towards inward drift [38, 43]. Similarly, spin pole solutions of NEAs obtained from observations are skewed towards retrograde rotation [111]. These biases are consistent with Yarkovsky drift into the strong ν_6 resonance at the inner edge of the main asteroid belt, thought to be the most likely delivery route to the inner solar system [16].

Paralleling the Yarkovsky effect is its rotational analogue, the Yarkovsky-O'Keefe-Radzievskii-Paddack (YORP) effect. This phenomenon is the process by which reflected solar radiation and thermal re-emission torques change a body's spin state [93]. The term YORP was penned by Rubincam in 2000 [93] to recognize the earlier works of Yarkovsky [75, 8], Radzievskii [87], Paddack [78], and O'Keefe [74]. Assuming instant thermal re-emission of absorbed solar radiation, Rubincam [93] showed that the YORP effect should cause secular changes in the spin rate and obliquity of small uniformly rotating asteroids with some type of asymmetry. This includes shape asymmetry, variable surface albedo, and differences between the center of mass and center of figure (i.e. non-constant density). YORP-driven accelerations are proportional to $1/D^2$, so smaller bodies evolve much faster than larger ones [93]. This early investigation proposed the YORP cycle in which asteroids are driven towards obliquities of 90° where they spin down towards non-principal axis tumbling, eventually returning to uniform rotation due to internal energy dissipation to start the cycle again [93].

Using Rubincam's assumption of instant thermal emission, Vokrouhlicky and Capek [113] explored a wider variety of real and random asteroid shapes. They found that asteroids could be

tilted to arbitrary obliquities with significantly higher and roughly equal tendencies for asymptotic obliquities of $0°/180°$ or $90°$ (i.e. spin poles perpendicular or parallel to the orbit plane respectively) with a strong tendency for ultimate spin down. Capek and Vokrouhlicky [23] considered delayed re-emission of absorbed thermal radiation. They found thermal lag to significantly alter obliquity evolution, with the majority of asteroids exhibiting asymptotic values of $0°$ or $180°$. Furthermore, simulations showed roughly equal tendencies for asymptotic spin down and spin up [23]. Observational studies of small main belt asteroids show a strong bias for spin poles near the ecliptic normal directions [44, 45, 111], consistent with the asymptotic states of Capek and Vokrouhlicky [23].

In 2007, the first direct observational detection of the YORP effect was presented by Lowry et al. for the $\sim$120 m diameter asteroid (54509) YORP [68]. Analysis of light curve and radar observations taken between 2001 and 2005 indicate it is accelerating at a rate of $\sim 2 \times 10^{-4}$ deg/day^2. Since 2007, YORP detections have been made for a handful of additional NEAs including (25143) Itokawa and (101955) Bennu [111, 32, 49].

In 2007, Scheeres [100] developed the first explicit YORP model for uniform rotation, expressing the YORP torque as a Fourier series and averaging over both the asteroid's spin and orbit. Vokrouhlicky et al. [112] analyzed the YORP spin down of uniformly rotating asteroids with numerical simulations assuming instant thermal re-emission and found that they will not reach zero spin rate. Rather they begin tumbling and often spin up indefinitely. The tumbling regime was further explored by Cicalo and Scheeres [26] who developed a semi-analytical tumbling-averaged model, approximating the facet illumination function as a 2nd order Fourier series to facilitate analytical averaging. Breiter et al. [19] developed a new semi-analytically averaged model, relaxing the illumination function approximation of Cicalo and Scheeres and finding new stable and unstable spin state limit cycles. Breiter et al. [18] added internal energy dissipation to the prior tumbling model, finding asymptotic tumbling states with constant angular momentum and kinetic energy.

Overall, the YORP effect is now considered to be largely responsible for the ongoing rotational evolution and observed spin states of sub $\sim$10 km asteroids, particularly the high fraction of fast and slow rotators as well as the bias towards extreme obliquities [111]. In addition, YORP is thought

to play a vital role in the rotational fission of asteroids [99, 84, 102] as well as the formation and subsequent evolution of binary asteroid systems [29, 99, 69, 55]. Also, by modifying asteroid spin rates and obliquities, the YORP effect can effectively "steer" their Yarkovsky drift [111].

Given that defunct high altitude satellites and asteroids are subject to similar environmental perturbations (YORP, internal energy dissipation, and gravity gradients), study of defunct satellite dynamics may provide valuable insight about asteroid spin state evolution. Kilometer-sized asteroids generally evolve on timescales of hundreds of thousands to hundreds of millions of years [93, 113]. So the majority of knowledge about asteroid spin state evolution must be inferred from modeling and the current observational "snapshot" of the solar system. Slow rotation, limited observation windows, and daily observation gaps makes extracting asteroid spin states from observations challenging, especially for tumbling asteroids. Also, meter-sized asteroids, which should evolve rapidly due to YORP, are extremely difficult to observe given their small size. Intriguingly, all asteroids with current YORP detections are spinning up, suggesting a potential observational or dynamical bias favoring acceleration over deceleration [111, 32, 49]. Also, obliquity changes of specific asteroids have yet to be detected due to slow evolution and limited observation sensitivity [111]. Defunct satellites with much faster evolution, faster spin rates, and easily obtained observations may provide insight into asteroid YORP cycles and help test theories about their evolution.

1.3   The YORP Effect for Artificial Satellites

It has been known for many decades that solar radiation can significantly affect the rotational dynamics of artificial satellites and debris in earth orbit, particularly at high altitudes where atmospheric drag is absent and gravitational, magnetic, and eddy current torques from earth are small [54]. Most investigation to date have involved active satellites. Spin state analysis of the Ariel 1 satellite, launched in 1962, showed that the large, secular changes in its observed spin rate were due in part to solar radiation torques [3]. Fedor [39] showed that solar torques could explain the observed spin rate increase of the spin-stabilized Explorer VII satellite, whose spin rate increased from 28 - 34 rpm in 110 days. Smith and Kissell [106] found that the PAGEOS

balloon satellite had a variable spin rate and a spin axis that precessed about the moving sun line with a nearly constant coning angle of 65°. Patterson and Kissell [81] showed that solar torques due to PAGEOS' asymmetry were of similar magnitude to those required to obtain the observed spin rate change and precession rate. Pande [79] explored using solar torques and two steerable panels to re-orient the inertial spin pole of a spinning satellite. Harvie et al. [47] developed and successfully employed a spin-stabilized on-orbit storage mode for the family of five GOES 8-12 satellites that leveraged passive magnetic dipole coils to rotate the spin axis and maintain solar array sun-pointing. Simulations showed that using just solar torques to rotate the spin axis resulted in rapid spin down. Also, simulations and operational data demonstrated that solar torques were dependent on the solar array rotation angle which strongly affected evolution of the satellite's spin rate and inertial spin pole. Van der Ha and Lappas [110] developed a spin-averaged solar torque model for spin-stabilized spacecraft to study long-term spin pole drift. Tsuda et al. [108] developed a spin-averaged SRP model for solar sails and applied it to the IKAROS solar sail, showing that approximate sun-tracking could be maintained under certain conditions using just SRP torques.

The impact of solar torques on small orbital debris has also been investigated. Ojakangas and Hill conducted numerical simulations of solar torques on centimeter scale orbital debris showing large and chaotic changes in spin rate and attitude over short periods of time [73]. More recently, authors have studied the orbital evolution of HAMR objects with simulations that couple translational and rotational dynamics. Frueh et al. [41] investigated flat HAMR objects simulating MLI subject to SRP as well as gravitational and solar torques. They noted the importance of attitude considerations for long-term HAMR orbit propagation. Further research added electromagnetic forces and torques which were found to directly change the HAMR object's orbit and attitude, in turn affecting the SRP force and orbit evolution [40, 52, 53].

Significantly less research has been conducted on the long-term rotational dynamics of defunct satellites subject to solar radiation torques. To hopefully explain the spin period variation in light curve observations, Earl and Wade [34] developed a simple spin-averaged solar torque model for the HGS-1 satellite assuming its spin axis was inertially fixed in the ecliptic plane. By adjusting

phasing parameters in their model, they were able to match HGS-1's spin period amplitude as well as its ∼1 year oscillation period.

The most significant study of defunct satellite spin state evolution to date, and first to leverage asteroid literature, was conducted by Albuja et al. [1]. Using the uniform spin-averaged model of Scheeres [100], Albuja et al. [1] investigated representative models of Boeing 376 and Gorizont satellites. They showed that the theoretical Fourier YORP coefficients of the Gorizont model had the same magnitudes as those derived from observed spin rate evolution of Gorizont and Raduga satellites. This indicated that YORP was a plausible explanation for the observed spin rate evolution. Albuja et al. [2] further explored YORP with the defunct GOES 8 and 10 satellites. Observation analysis showed that GOES 8's spin period increased from 16.83 s to 75.66 s between December 2013 and July 2014 while GOES 10's spin period decreased from 31.1 s to 26.2 s between February and August 2014 [27, 94]. Albuja et al. [2] simulated GOES 8's YORP-driven evolution with a representative shape model. Starting with the December 2013 extracted spin periods as initial conditions, their simulations matched all subsequent spin periods to within 2 s. Furthermore, the simulations predicted that GOES 8 would continue spinning down and begin tumbling by late 2014. Light curve observations of GOES 8 collected in September 2015 and February 2016 lacked the clear periodicity of earlier observations, suggesting the satellite had in fact began to tumble [94, 2]. Nevertheless, the authors were only able to speculate about the satellite's spin rate. Given these findings, Albuja et al. hypothesized that some satellites may transition repeatedly between uniform and non-principal axis rotation due to the competing influences of YORP and internal energy dissipation from structural flexibility and residual fuel slosh [2]. As a satellite spins down from YORP it loses spin stability. At some point, YORP begins spinning the satellite up about the minimum inertia axis since it requires the least torque to accelerate. Albuja et al. propose that dissipation eventually overcomes the minimum axis YORP spin up, driving the satellite back to uniform rotation about the maximum inertia axis, the lowest energy state for a given angular momentum, where the cycle may start again [2].

Since the model of Albuja et al. [2] did not include internal energy dissipation, they were

unable to validate their hypothesis. In addition to dissipation, gravity gradient torques from earth may also play a role. Understanding the influence these perturbations have on tumbling rotation and being able to extract quantitative information from non-periodic light curves and other observations are necessary for forming a general picture of long-term defunct satellite spin state evolution.

The full dynamics (i.e. Euler's equations of motion and associated attitude coordinates) used by Albuja et al. [2] to briefly investigate tumbling YORP are not amenable to long-term numerical propagation as they require short integration time steps to maintain solution accuracy. More importantly, Euler's equations are expressed in terms of fast variables (i.e. attitude and angular velocity). Since we are interested in studying changes over long periods of time, slowly varying osculating elements (e.g. the rotational angular momentum vector and kinetic energy) are more appropriate. This is directly comparable to orbital dynamics, where equations of motion for the osculating orbital elements (i.e. semi-major axis, eccentricity, inclination, etc.) are often used. For example, the Lagrange planetary equations assume the disturbing forces driving the time derivatives of the osculating elements are conservative (i.e. can be expressed as gradients of potential functions) [58]. An alternative form are the Gauss equations, which generalize the perturbations to arbitrary accelerations (i.e. conservative or non-conservative) [7]. Assuming the disturbing forces are small perturbations, these equations can be averaged over short and long period variations to isolate secular contributions (e.g. [61, 21, 70]). Such averaged approaches have proven vital to understanding and exploring many aspects of long-term orbital dynamics [109]. This motivates development of analogous tumbling-averaged dynamics for defunct satellites in terms of osculating rotational elements, namely the rotational angular momentum vector and kinetic energy.

The uniform spin-averaged YORP work of Scheeres [100] and Albuja et al. [1, 2] are not applicable to tumbling satellites as the motion is driven by two generally incommensurate periods rather than one for the uniform case [95]. Also, the semi-analytical tumbling-averaged asteroidal models of Cicalo and Scheeres [26] and Breiter et al. [19, 18] average over the spin state and heliocentric orbit given the slow spin state evolution of asteroids. Orbit averaging is not appropriate for defunct satellites given their potential for significant short-term spin state changes. Also, these

asteroidal models only account for diffuse reflection which is insufficient for defunct satellites since many surfaces are dominated by specular reflections.

1.4   Contributions

The preceding discussion leads to the following thesis statement:

Thesis Statement

The general long-term rotational dynamics of defunct satellites subject to the YORP effect and internal energy dissipation have not been investigated. A more complete picture of these dynamics can be obtained by developing and exploring full and tumbling-averaged dynamical models. Spin state information extracted from satellite observations can provide insight and validate dynamical modeling. Enhanced knowledge will benefit space situational awareness, facilitate debris mitigation and satellite servicing efforts, and advance understanding of the dynamical evolution of small bodies in the solar system.

The dynamical and observational investigations in this work focus primarily on the five GOES 8-12 retired GEO weather satellites studied previously [2]. These satellites have well-documented mass properties and geometry. They have also been extensively observed [27, 94, 2] and are undergoing significant dynamical evoluiton [2]. While the GOES satellites constitute a small fraction of the diverse defunct satellite population, their above attributes make them nearly ideal targets for initial exploration and validation of dynamical modeling.

The contributions in this work can be separated into the following three areas:

Full Dynamical Modeling

- Explored the long-term spin state evolution of defunct satellites subject to the YORP effect, energy dissipation, and gravity gradient torques with Euler's equations of motion.

- Uncovered rich dynamical structure with YORP-driven tumbling cycles, angular momentum sun-tracking, capture into resonant tumbling states, and asymptotically stable tumbling states and limit cycles when dissipation and gravity gradients were considered.

Averaged Dynamical Modeling

- Developed semi-analytical and numerical tumbling-averaged dynamics models for solar radiation torques, internal energy dissipation, and gravity gradient torques that accurately capture the behavior of the full models while reducing computation time by up to three orders of magnitude.

- Utilized the computationally efficient averaged models to explain and explore the long-term behavior observed in the full dynamics.

Observation Analysis

- Conducted simulated optical light curve surveys with a high fidelity ray traced model to determine the dominant frequencies in tumbling satellite light curves.

- Leveraged Doppler radar observations to provide unambiguous precession period estimates and complement tumbling light curve analysis.

- Developed novel mono-static Doppler radar techniques for pole estimation.

- Applied these methodologies the extract rotation periods and pole directions from GOES 8-12 satellite observations, demonstrating consistency of satellite spin state time histories with dynamical modeling.

1.5   Publications

Journal Papers

- Benson C. J., Scheeres D. J., General Long-term Rotational Dynamics for Defunct Satellites, in preparation.

- Benson C. J., Scheeres D. J., Resonance-Averaged Solar Torque Dynamics for Tumbling Satellites, *Journal of Guidance, Control, and Dynamics*, in review.

- Benson C. J., Naudet C. J., Scheeres D. J., Jao J. S. et al., Radar and Optical Study of Defunct Geosynchronous Satellites, *Journal of the Astronautical Sciences*, published online May 20, 2021.

- Benson C. J., Scheeres D. J., Averaged Solar Torque Rotational Dynamics for Defunct Satellites, *Journal of Guidance, Control, and Dynamics*, Vol. 44(4), pp.749-766, 2021.

- Benson C. J., Scheeres D. J., Ryan W. H., Ryan E.V., Moskovitz N., GOES Spin State Diversity and the Implications for GEO Debris Mitigation, *Acta Astronautica*, Vol. 167, pp. 212-221, 2020.

- Benson C. J., Scheeres D. J., Moskovitz N., Spin State Evolution of Asteroid (367943) Duende During its 2013 Earth Flyby, *Icarus*, Vol. 340, April 2020.

- Moskovitz N. A., Benson C. J., Scheeres D.J., et al., Observational investigation of the 2013 near-Earth encounter by asteroid (367943) Duende, *Icarus*, Vol. 340, April 2020.

Conference Papers

- Benson C. J., Scheeres D. J., Averaged Rotational Dynamics of GEO Debris, 8th European Conference on Space Debris, Apr. 20-23, 2021.

- Benson C. J., Naudet C. J., Scheeres D. J., Jao J. S. et al., Radar and Optical Study of Defunct GEO Satellites, 21st Advanced Maui Optical and Space Surveillance Technologies Conference, Sept. 15-18, 2020.

- Benson C. J., Scheeres D. J., Averaged Solar Torque Rotational Dynamics for Defunct Satellites, AAS/AIAA Astrodynamics Specialist Conference, Aug. 9-12, 2020.

- Benson C. J., Scheeres D. J., Tumbling Averaged YORP Dynamics of defunct GEO Satellites, 1st International Orbital Debris Conference, Sugar Land, TX, Dec. 9-12, 2019.

- Benson C. J., Scheeres D. J., The YORP Effect for Tumbling Defunct GEO Satellites, AAS/AIAA Astrodynamics Specialist Conference, Portland, ME, Aug. 11-15, 2019.

- Benson C. J., Scheeres D. J., Ryan W. H., Ryan E. V., Moskovitz N., GOES Tumbling Spin State Evolution and the Implications for GEO Debris Mitigation (A6,10-C1.7,1,x46361), 69th International Astronautical Congress, Bremen, Germany, Oct. 1-5, 2018.

- Benson C. J., Scheeres D. J., Ryan W. H., Ryan E. V., Cyclic Complex Spin State Evolution of Defunct GEO Satellites, 19th Advanced Maui Optical and Space Surveillance Technologies Conference, Wailea, HI, Sept. 11-14, 2018.

- Benson C. J., Scheeres D. J., Ryan W. H., Ryan E. V., Moskovitz N., Rotation State Evolution of Retired Geosynchronous Satellites, 18th Advanced Maui Optical and Space Surveillance Technologies Conference, Wailea, HI, Sept. 19-22, 2017.

- Benson C. J., Scheeres D. J., Moskovitz N., Light-Curves of Retired Geosynchronous Satellites, 7th European Conference on Space Debris, Darmstadt, Germany, Apr. 18-21, 2017.

- Benson C. J., Scheeres D. J., Extraction and Assignment of Tumbling Asteroid and Defunct Satellite Rotation Periods from Simulated Light-Curve Observations (AAS 17-461), 27th AAS/AIAA Space Flight Mechanics Meeting, San Antonio, TX, Feb. 5-9, 2017.

Conference Abstracts

- Benson C. J., Scheeres D. J., Resonant Tumbling YORP for Defunct Artificial Satellites, 52nd Annual Meeting of the Division on Dynamical Astronomy, May 17-21, 2021.

- Scheeres D.J., Benson C.J., Brozovic M., Chesley S., Pravec P., Scheirich P., Abrupt Alteration of Apophis' Spin State and Its Implications, Apophis T-9, Nov. 4-6, 2020.

- Benson C. J., Scheeres D. J., YORP-Driven Spin State Evolution of Meter-Sized Asteroids, 51st Division on Dynamical Astronomy Annual Meeting, Aug. 3-7, 2020.

- Benson C. J., Scheeres D. J., Moskovitz N., Asteroid (367943) 2012 DA14 Flyby Spin State Analysis, AAS 49th Division for Planetary Sciences Meeting, Provo, UT, Oct. 15-20, 2017.

1.6   Organization

Chapter 2 outlines the modeling foundations including the full dynamics equations, attitude coordinates, relevant frames, and analytical solutions for torque-free rigid body rotation that figure prominently in our averaging approach. Chapter 2 also includes discussion of the attitude perturbations considered and their assumed formulations. The full dynamics are then explored in Chapter 3 for the defunct GOES 8 satellite. In this chapter, rich, previously undocumented dynamical behavior is presented.

Motivated by the full dynamical modeling results and the limited utility of the full dynamics for long-term studies, Chapter 4 focuses on development and validation of the semi-analytical and numerical tumbling-averaged dynamics models. Here, the resonant and non-resonant averaging approaches are outlined and the averaged solar torque, energy dissipation, and gravity gradient torque models are developed. These averaged models are then validated against the corresponding full dynamics. With the averaged models in place, Chapter 5 explores the averaged dynamics for the GOES 8-12 satellites, uncovering the mechanisms driving the behaviors observed in the full dynamics and exploring these behaviors in more detail.

With observations providing direct insight and playing crucial roles in theory validation and refinement, Chapter 6 focuses on methodologies for extracting satellite spin state information from non-resolved optical light curves and Doppler radar echoes. Here, significant emphasis is placed on tumbling spin state extraction. In Chapter 7, these methodologies are then applied to observations of the defunct GOES 8-12 satellites to better understand their spin state time histories. Resulting spin state estimates are then compared with dynamical modeling findings, showing clear consistencies. In Chapter 8, the averaged dynamics models are applied to a box-wing satellite and meter-sized asteroids.

Chapter 2

Dynamics and Perturbations

2.1   Euler's Equations

The rotational angular momentum vector of a single rigid body is given by [98],

$$\boldsymbol{H} = [I]\boldsymbol{\omega} \tag{2.1}$$

where $[I]$ is the satellite's inertia tensor and $\boldsymbol{\omega}$ is the angular velocity vector of the body-fixed $\mathcal{B}$ frame with respect to an inertially fixed frame $\mathcal{N}$.

Then, taking $\boldsymbol{M}$ as the sum of all external torques taken about the body center of mass, the inertial time derivative of $\boldsymbol{H}$ is given by,

$$\frac{^{\mathcal{N}}d}{dt}(\boldsymbol{H}) = \dot{\boldsymbol{H}} = \boldsymbol{M} \tag{2.2}$$

With $[I]$ constant in the $\mathcal{B}$ frame, it is most convenient to express $\boldsymbol{H}$ in this frame. Applying the transport theorem [98],

$$\frac{^{\mathcal{N}}d}{dt}(\boldsymbol{H}) = [I]\dot{\boldsymbol{\omega}} + [\tilde{\boldsymbol{\omega}}][I]\boldsymbol{\omega} = \boldsymbol{M} \tag{2.3}$$

where $[\tilde{\ }]$ is the skew-symmetric cross product operator. Rearranging yields Euler's equations of motion [98],

$$[I]\dot{\boldsymbol{\omega}} = -[\tilde{\boldsymbol{\omega}}][I]\boldsymbol{\omega} + \boldsymbol{M} \tag{2.4}$$

2.2   Attitude Coordinates

2.2.1   Euler Angles

The angular momentum frame is denoted by $\mathcal{H}$:$\{\hat{\boldsymbol{x}},\hat{\boldsymbol{y}},\hat{\boldsymbol{z}}\}$. Here $\hat{\boldsymbol{z}}$ is along the satellite's rotational angular momentum vector $\boldsymbol{H}$. The satellite body frame is given by $\mathcal{B}$:$\{\hat{\boldsymbol{b}}_1,\hat{\boldsymbol{b}}_2,\hat{\boldsymbol{b}}_3\}$. Rotation from $\mathcal{H}$ to $\mathcal{B}$, shown in Figure 2.1, is given by (3-1-3) (ϕ-θ-ψ) Euler angles [98]. These angles are commonly called the precession (ϕ), nutation (θ), and rotation (ψ) angles. The rotation matrix from the $\mathcal{H}$ frame to the $\mathcal{B}$ frame is given by $BH = R_3(\psi)R_1(\theta)R_3(\phi)$ where R_i denotes a principal rotation about the ith axis [98]. Expanded out, this is,

$$BH = \begin{bmatrix} \cos\phi\cos\psi - \cos\theta\sin\phi\sin\psi & \cos\psi\sin\phi + \cos\phi\cos\theta\sin\psi & \sin\psi\sin\theta \\ -\cos\phi\sin\psi - \cos\psi\cos\theta\sin\phi & \cos\phi\cos\psi\cos\theta - \sin\phi\sin\psi & \cos\psi\sin\theta \\ \sin\phi\sin\theta & -\cos\phi\sin\theta & \cos\theta \end{bmatrix} = \begin{bmatrix} a_{x1} & a_{y1} & a_{z1} \\ a_{x2} & a_{y2} & a_{z2} \\ a_{x3} & a_{y3} & a_{z3} \end{bmatrix}$$
$$(2.5)$$

So an arbitrary vector $\boldsymbol{f}$ in the $\mathcal{H}$ frame is given by,

$$\begin{bmatrix} f_x \\ f_y \\ f_z \end{bmatrix} = \begin{bmatrix} a_{x1} & a_{x2} & a_{x3} \\ a_{y1} & a_{y2} & a_{y3} \\ a_{z1} & a_{z2} & a_{z3} \end{bmatrix} \begin{bmatrix} f_1 \\ f_2 \\ f_3 \end{bmatrix}$$
$$(2.6)$$

where f_1, f_2, and f_3 are the $\mathcal{B}$ frame components.
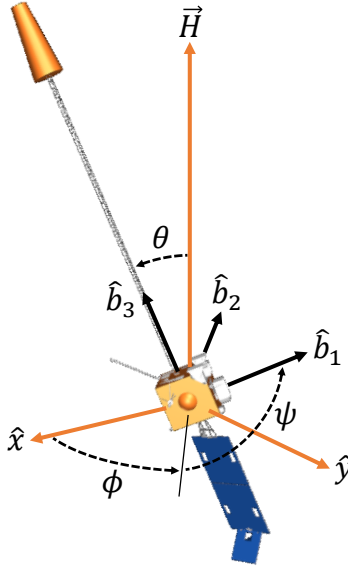
Figure 2.1: $\mathcal{H}$ and $\mathcal{B}$ frames

2.2.2 Orbit Frame

The rotating orbit frame is denoted by $\mathcal{O}$:$\{\hat{\boldsymbol{X}},\hat{\boldsymbol{Y}},\hat{\boldsymbol{Z}}\}$. This frame is centered at the satellite with $\hat{\boldsymbol{X}}$ along the heliocentric orbit angular momentum direction, $\hat{\boldsymbol{Z}}$ pointed towards the sun, and $\hat{\boldsymbol{Y}}$ in the orbital velocity direction (see Figure 2.2). The inertially fixed ecliptic frame is denoted by $\mathcal{N}$: $\{\hat{\boldsymbol{n}}_1, \hat{\boldsymbol{n}}_2, \hat{\boldsymbol{n}}_3\}$ where $\hat{\boldsymbol{n}}_1$ is along the equinox, $\hat{\boldsymbol{n}}_3$ is along earth's orbital angular momentum vector (coincident with $\hat{\boldsymbol{X}}$), and $\hat{\boldsymbol{n}}_2$ completes the right-handed system. The angular velocity of $\mathcal{O}$ with respect to $\mathcal{N}$ frame is $\boldsymbol{\omega}_{\mathcal{O}/\mathcal{N}} = n\hat{\boldsymbol{X}}$ where n is the heliocentric mean motion. Rotation from $\mathcal{O}$ to $\mathcal{H}$ is given by the rotation matrix $HO = R_2(\beta)R_3(\alpha)$. Written explicity,

$$HO = \begin{bmatrix} \cos\alpha\cos\beta & \cos\beta\sin\alpha & -\sin\beta \\ -\sin\alpha & \cos\alpha & 0 \\ \cos\alpha\sin\beta & \sin\alpha\sin\beta & \cos\beta \end{bmatrix} \qquad (2.7)$$

Consulting Figure 2.2, the "clocking" angle α and "coning" angle β are the spherical coordinates of $\hat{\boldsymbol{H}}$ in the $\mathcal{O}$ frame.
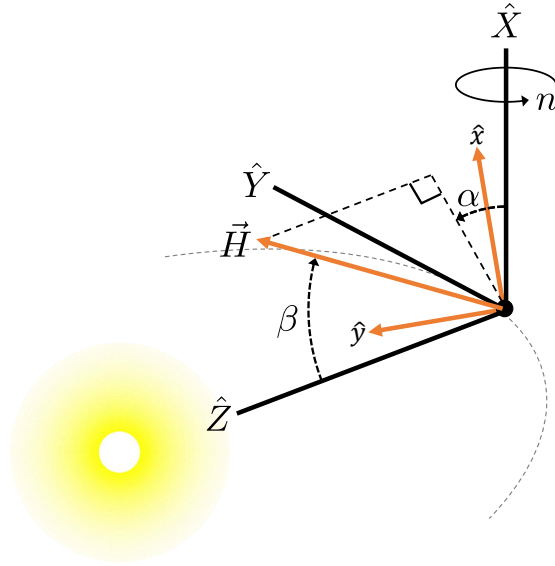
Figure 2.2: $\mathcal{O}$ and $\mathcal{H}$ frames

2.2.3 Quaternions

For the full dynamics, the body's attitude relative to the inertially fixed $\mathcal{N}$ frame is tracked using quaternions [98],

$$BN = \begin{bmatrix} \beta_0^2 + \beta_1^2 - \beta_2^2 - \beta_3^2 & 2(\beta_1\beta_2 + \beta_0\beta_3) & 2(\beta_1\beta_3 - \beta_0\beta_2) \\ 2(\beta_1\beta_2 - \beta_0\beta_3) & \beta_0^2 - \beta_1^2 + \beta_2^2 - \beta_3^2 & (\beta_2\beta_3 + \beta_0\beta_1) \\ 2(\beta_1\beta_3 + \beta_0\beta_2) & 2(\beta_2\beta_3 - \beta_0\beta_1) & \beta_0^2 - \beta_1^2 - \beta_2^2 + \beta_3^2 \end{bmatrix} \tag{2.8}$$

where β_0 is the scalar component. The kinematic differential equation for the quaternions is given by [98],

$$\begin{bmatrix} \dot{\beta}_0 \\ \dot{\beta}_1 \\ \dot{\beta}_2 \\ \dot{\beta}_3 \end{bmatrix} = \frac{1}{2} \begin{bmatrix} -\beta_1 & -\beta_2 & -\beta_3 \\ \beta_0 & -\beta_3 & \beta_2 \\ \beta_3 & \beta_0 & -\beta_1 \\ -\beta_2 & \beta_1 & \beta_0 \end{bmatrix} \begin{bmatrix} \omega_1 \\ \omega_2 \\ \omega_3 \end{bmatrix} \tag{2.9}$$

The full dynamics are propagated with MATLAB's ode113 numerical integrator.

2.3 Torque-Free Rigid Body Rotation

The rotational kinetic energy T of a single rigid body is given by,

$$T = \frac{1}{2}\boldsymbol{\omega}\cdot[I]\boldsymbol{\omega} \tag{2.10}$$

Using the angular momentum magnitude $H = |\boldsymbol{H}|$ and kinetic energy T, we define two parameters fundamental to torque-free rigid body dynamics. The first is the dynamic moment of inertia I_d which is given by,

$$I_d = H^2/2T \tag{2.11}$$

Assuming the $\mathcal{B}$ frame is a principal axis frame, we define the principal inertias $I_s \geq I_i \geq I_l$. We will assume the long axis convention where the $\hat{\boldsymbol{b}}_1$, $\hat{\boldsymbol{b}}_2$ and $\hat{\boldsymbol{b}}_3$ body axes are aligned with the intermediate (I_i), maximum (I_s), and minimum (I_l) principal moments of inertia respectively [95].

For torque-free rigid body rotation, I_d defines the closed path that $\boldsymbol{\omega}$ takes through the body frame, known as a polhode [64]. I_d is constrained to $[I_l, I_s]$ since T is bounded for a given H. When $I_l < I_d < I_i$, the satellite is said to be in a long axis mode (LAM) because $\boldsymbol{\omega}$ circulates about the satellite's "long" axis ($\hat{\boldsymbol{b}}_3$) which often closely aligns with the longest dimensional axis [64]. When $I_i < I_d < I_s$, the satellite is in a short axis mode (SAM) where $\boldsymbol{\omega}$ instead circulates about the "short" axis ($\hat{\boldsymbol{b}}_2$), which often closely aligns with the shortest dimensional axis. $I_d = I_l$ and $I_d = I_s$ correspond to principal axis rotation about $\hat{\boldsymbol{b}}_3$ and $\hat{\boldsymbol{b}}_2$ respectively. Finally $I_d = I_i$ denotes motion along the separatrix between LAMs and SAMs or uniform rotation about the intermediate axis, both of which are unstable. Various polhodes are illustrated in Figure 2.3 for the GOES 8 satellite assuming constant H. Here, the separatrices are shown in black.
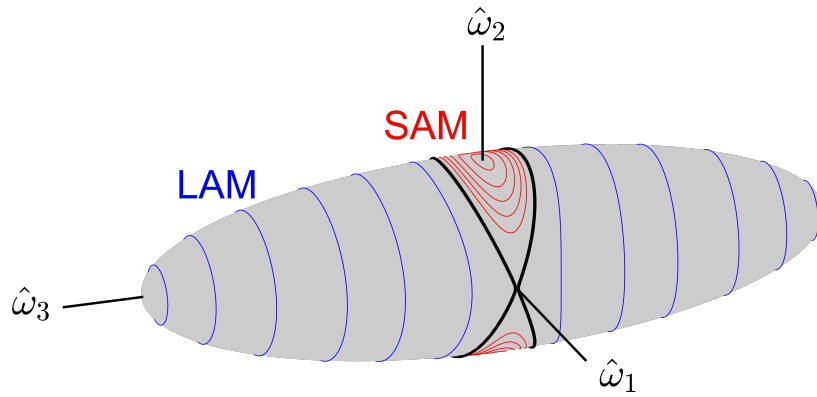
Figure 2.3: Angular velocity curves for long (LAM) and short (SAM) axis modes.

Complementing I_d is another fundamental quantity called the effective spin rate ω_e,

$$\omega_e = \frac{2T}{H} \tag{2.12}$$

which linearly scales the satellite's angular velocity components as shown in the following section. Together, I_d and ω_e yield the familiar looking expressions $H = I_d\omega_e$ and $T = \frac{1}{2}I_d\omega_e^2$.

Here we summarize the analytical solutions for torque-free rotation ($\boldsymbol{M} = 0$) which figure prominently throughout this work. Again the long axis convention is assumed with 3-1-3 (ϕ-θ-ψ) Euler angles used to rotate between the $\mathcal{H}$ and $\mathcal{B}$ frames. This is the same convention used in Ref. [95].

Equating $\boldsymbol{H}$ in the $\mathcal{H}$ and $\mathcal{B}$ frames with Eq. 2.5, we find,

$$a_{z1} = \sin\theta\sin\psi = \frac{I_i\omega_1}{I_d\omega_e} \tag{2.13}$$

$$a_{z2} = \sin\theta\cos\psi = \frac{I_s\omega_2}{I_d\omega_e} \tag{2.14}$$

$$a_{z3} = \cos\theta = \frac{I_l\omega_3}{I_d\omega_e} \tag{2.15}$$

The angles θ and ψ can be unambiguously calculated using Eqs. 2.13 - 2.15 with Eqs. 2.16 - 2.18 for LAMs or Eqs. 2.25 - 2.27 for SAMs. The equations for ϕ are much more complicated and are provided separately below.

2.3.1   Torque-Free Solutions for Long Axis Modes

For long axis modes (LAMs), the body frame angular velocity $\boldsymbol{\omega} = [\omega_1, \omega_2, \omega_3]^T$ is given by,

$$\omega_1 = \pm\omega_e\sqrt{\frac{I_d(I_d - I_l)}{I_i(I_i - I_l)}}\,\mathrm{sn}\,\tau \tag{2.16}$$

$$\omega_2 = \omega_e\sqrt{\frac{I_d(I_d - I_l)}{I_s(I_s - I_l)}}\,\mathrm{cn}\,\tau \tag{2.17}$$

$$\omega_3 = \pm\omega_e\sqrt{\frac{I_d(I_s - I_d)}{I_l(I_s - I_l)}}\,\mathrm{dn}\,\tau \tag{2.18}$$

where $\mathrm{cn}\,\tau$, $\mathrm{sn}\,\tau$, and $\mathrm{dn}\,\tau$ are Jacobi elliptic functions [95, 85, 22]. Examples of these functions are illustrated in Figure 2.4.

The $\pm$ distinguishes between the two possible LAM regions: $+$ for $\omega_3 > 0$ (LAM+) and $-$ for $\omega_3 < 0$ (LAM-) as shown in Figure 2.3. For LAMs, the linearly scaled time parameter τ is given by,

$$\tau = \tau_o + \omega_e\sqrt{\frac{I_d(I_i - I_l)(I_s - I_d)}{I_l I_i I_s}}(t - t_o) \tag{2.19}$$
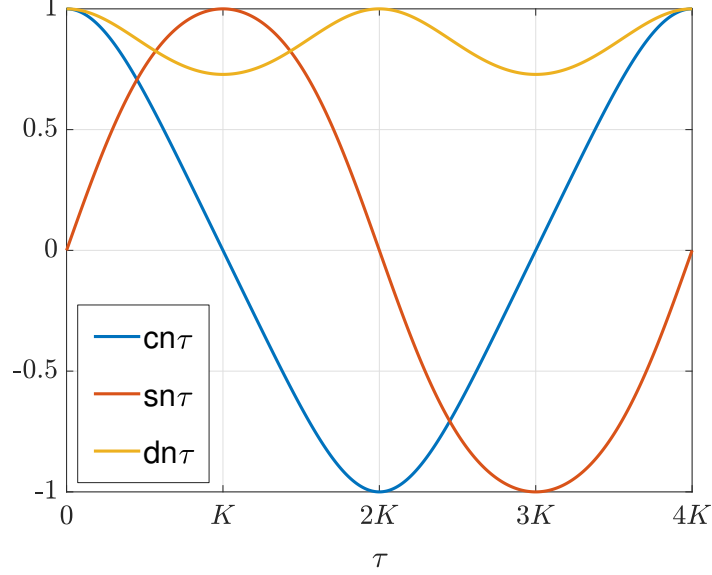
Figure 2.4: Examples of the Jacobi Elliptic Functions $\operatorname{cn}\tau$, $\operatorname{sn}\tau$, and $\operatorname{dn}\tau$

where t is the time and t_o, τ_o are the initial values. The period of $\operatorname{sn}\tau$ and $\operatorname{cn}\tau$ is $4K(k)$ while $\operatorname{dn}\tau$ is periodic on $2K(k)$ where $K(k)$ is the complete elliptic integral of the first kind [64, 85],

$$K(k) = \int_0^{\pi/2} \frac{du}{\sqrt{1 - k^2 \sin^2 u}} \tag{2.20}$$

and k is the modulus. The parameter n features in the torque-free solutions for ϕ and $P_{\bar{\phi}}$. For LAMs, k and n are given by,

$$k^2 = \frac{(I_s - I_i)(I_d - I_l)}{(I_i - I_l)(I_s - I_d)} \qquad n = \frac{I_l}{I_s}\frac{(I_s - I_i)}{(I_i - I_l)} \tag{2.21}$$

For LAMs, the Euler angle ϕ is given by [10],

$$\phi = \phi_o + \frac{H}{I_l}(t - t_o) - (I_s - I_l)\sqrt{\frac{I_i I_d}{I_l I_s(I_i - I_l)(I_s - I_d)}}\left[\bar{\Pi}(\tau, n) - \bar{\Pi}(\tau_o, n)\right] \tag{2.22}$$

where $\bar{\Pi}(\tau, n)$ is the modified incomplete elliptic integral of the third kind. Most routines for calculating the incomplete elliptic integral of the third kind $\Pi(\tau, n)$ (e.g. Ref. [85]) only accept $0 \leq \tau \leq K(k)$ even though τ increases unbounded with t. To calculate $\bar{\Pi}(\tau, n)$ correctly, we use the following algorithm [10]. Dropping the implied dependence of k on K for brevity, and defining the integer multiple $m = \operatorname{int}(\tau/K)$,

(1) If τ has most recently passed through an even multiple of K, i.e. if $\mathrm{mod}(m,2) = 0$,

$$\bar{\Pi}(\tau, n) = m\Pi(K, n) + \Pi(\tau - mK, n) \tag{2.23}$$

(2) Instead, if τ has most recently passed through an odd multiple of K, i.e. if $\mathrm{mod}(m,2) = 1$,

$$\bar{\Pi}(\tau, n) = (m + 1)\Pi(K, n) - \Pi\Big((m+1)K - \tau, n\Big) \tag{2.24}$$

where mod is the remainder after division modulo operator.

2.3.2 Torque-Free Solutions for Short Axis Modes

For short axis modes (SAMs), the body frame angular velocity $\boldsymbol{\omega} = [\omega_1, \omega_2, \omega_3]^T$ is given by,

$$\omega_1 = \omega_e \sqrt{\frac{I_d(I_s - I_d)}{I_i(I_s - I_i)}} \, \mathrm{sn}\, \tau \tag{2.25}$$

$$\omega_2 = \pm\omega_e \sqrt{\frac{I_d(I_d - I_l)}{I_s(I_s - I_l)}} \, \mathrm{dn}\, \tau \tag{2.26}$$

$$\omega_3 = \pm\omega_e \sqrt{\frac{I_d(I_s - I_d)}{I_l(I_s - I_l)}} \, \mathrm{cn}\, \tau \tag{2.27}$$

Again $+$ holds for $\omega_2 > 0$ and $-$ holds for $\omega_2 < 0$ (SAM+ and SAM−). For SAMs, τ, k, and n are,

$$\tau = \tau_o + \omega_e \sqrt{\frac{I_d(I_s - I_i)(I_d - I_l)}{I_l I_i I_s}}(t - t_o) \tag{2.28}$$

$$k^2 = \frac{(I_i - I_l)(I_s - I_d)}{(I_s - I_i)(I_d - I_l)} \qquad n = \frac{I_l}{I_s}\frac{(I_s - I_d)}{(I_d - I_l)} \tag{2.29}$$

For SAMs, ϕ is instead given by,

$$\phi = \phi_o + \frac{H}{I_l}(t - t_o) - (I_s - I_l)\sqrt{\frac{I_i I_d}{I_l I_s(I_s - I_i)(I_d - I_l)}}\Big[\bar{\Pi}(\tau, n) - \bar{\Pi}(\tau_o, n)\Big] \tag{2.30}$$

2.3.3 Fundamental Tumbling Periods

In general, torque-free rigid body rotation can be defined by two fundamental periods. Using the long axis convention, $P_{\bar{\phi}}$ is the average precession period of $\hat{\boldsymbol{b}}_3$ about $\boldsymbol{H}$ and P_ψ is the rotation period of $\hat{\boldsymbol{b}}_3$ about itself [95]. See Figure 2.5 for an illustration of these periods for the GOES satellite. For LAMs, P_ψ corresponds to continuous rotation, while for SAMs it corresponds to oscillation between two fixed values of ψ. We stress that $P_{\bar{\phi}}$ is the average precession period because for a triaxial body (i.e., with three distinct moments of inertia) the time for ϕ to increase by 2π is generally not constant. Here it useful to note that P_ψ is also the period of $\boldsymbol{\omega}$ in the $\mathcal{B}$ frame. P_θ is proportional to P_ψ and therefore not independent. For given moments of inertia, $P_{\bar{\phi}}$ and P_ψ are only functions of I_d and ω_e.

For LAMs and SAMs, $P_{\bar{\phi}}$ is given by,

$$P_{\bar{\phi}} = \frac{2\pi}{\omega_e} \frac{I_l}{I_d} \left[1 - \frac{(I_s - I_l)}{I_s} \frac{\Pi(K,n)}{K} \right]^{-1} \tag{2.31}$$

where n is given by the respective equations (Eq. 2.21 for LAMs and Eq. 2.29 for SAMs).

Then for LAMs, the expression for P_ψ is,

$$P_\psi = \frac{4}{\omega_e} \sqrt{\frac{I_l I_i I_s}{I_d(I_i - I_l)(I_s - I_d)}} K \tag{2.32}$$

whereas for SAMs,

$$P_\psi = \frac{4}{\omega_e} \sqrt{\frac{I_l I_i I_s}{I_d(I_s - I_i)(I_d - I_l)}} K \tag{2.33}$$
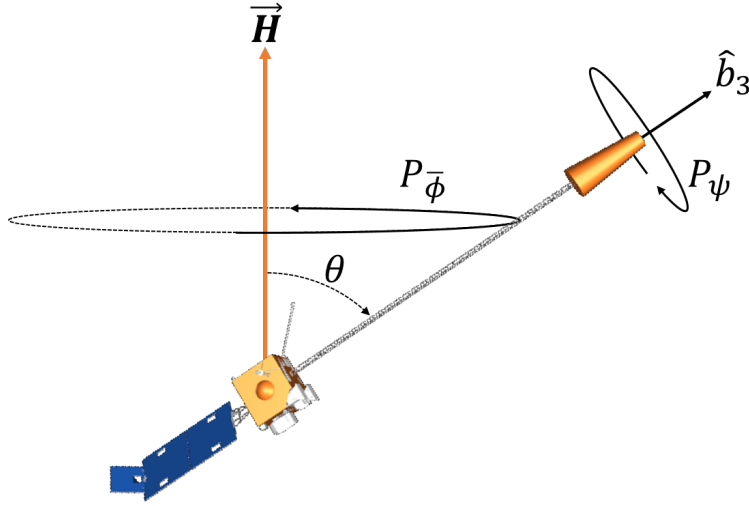
Figure 2.5: Fundamental tumbling periods illustrated for the GOES satellite (long axis convention)

One derived quantity that figures prominently throughout this work is the fundamental tumbling period ratio. For LAMs it is given by,

$$\frac{P_\psi}{P_{\bar{\phi}}} = \frac{2}{\pi}\sqrt{\frac{I_d I_i I_s}{I_l(I_i - I_l)(I_s - I_d)}}\left[K - \frac{(I_s - I_l)}{I_s}\Pi(K, n)\right] \tag{2.34}$$

and for SAMs,

$$\frac{P_\psi}{P_{\bar{\phi}}} = \frac{2}{\pi}\sqrt{\frac{I_d I_i I_s}{I_l(I_s - I_i)(I_d - I_l)}}\left[K - \frac{(I_s - I_l)}{I_s}\Pi(K, n)\right] \tag{2.35}$$

It is important to note that these period ratios are independent of the effective spin rate ω_e. They are only functions of the principal moments of inertia and I_d. For example, the I_d - period ratio relationship for the GOES 8 satellite is provided in Figure 2.6. Note that the period ratio has a lower bound, which differs for LAM and SAM states. Some period ratios ($\geq \sim 3.1$ for GOES 8) are possible for both LAM and SAM states. For all physical bodies, $P_\psi/P_{\bar{\phi}} \geq 1$ for SAMs and $P_\psi/P_{\bar{\phi}} \geq 0$ for LAMs [95]. Near the separatrix, denoted by the vertical dashed line in Figure 2.6, the time for $\boldsymbol{\omega}$ to circulate in the body frame (P_ψ) approaches infinity, so the period ratio goes to infinity as well.
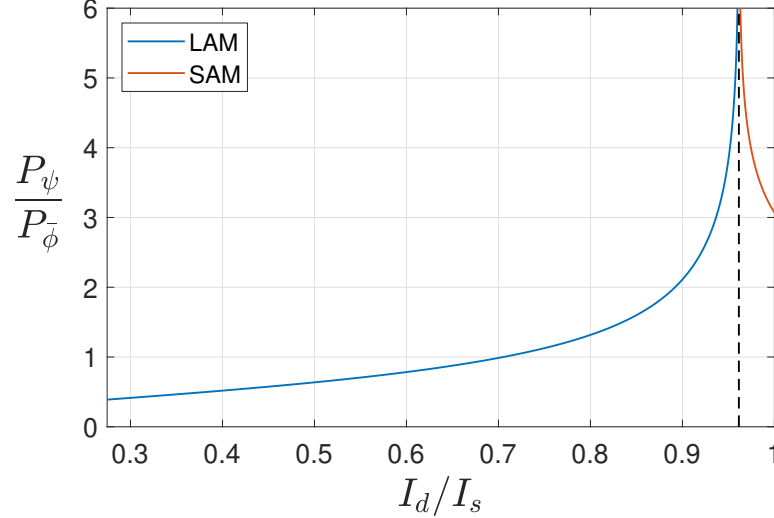
Figure 2.6: GOES 8 tumbling period ratio vs. normalized I_d

In general, provided the period ratio, the principal moments of inertia, and rotation mode (i.e. LAM or SAM), one can uniquely calculate I_d using Eq. 2.34 or 2.35 and the bisection method (since I_d has known bounds). Then either P_ψ or P_ϕ can be used to solve for ω_e.

2.4   Solar Radiation Torque

For this work, the faceted solar radiation force model provided by Scheeres [100] is used. This model accounts for absorption, specular reflection, and Lambertian diffuse reflection and re-emission. The satellite is assumed to remain in thermal equilibrium, so all absorbed radiation is immediately re-emitted. The solar radiation force acting on the ith satellite facet is given by,

$$\boldsymbol{f}_i = -P_{SRP}\Big[\{\rho_i s_i(2\hat{\boldsymbol{n}}_i\hat{\boldsymbol{n}}_i^{\mathrm{T}} - \mathbb{I}_{3\times3}) + \mathbb{I}_{3\times3}\}\hat{\boldsymbol{u}} + c_{di}\hat{\boldsymbol{n}}_i\Big]A_i\max(0, \hat{\boldsymbol{u}}\cdot\hat{\boldsymbol{n}}_i) \qquad (2.36)$$

Here, P_{SRP} is the solar radiation pressure (nominally $4.56{\times}10^{-6}$ N/m^2 at 1 AU), ρ_i is the total facet reflectivity, s_i is the fraction of total reflectivity that is specular, $\hat{\boldsymbol{n}}_i$ is the facet unit normal vector, $\mathbb{I}_{3\times3}$ is the 3×3 identity matrix, $\hat{\boldsymbol{u}}$ is the satellite to sun unit vector (equivalent to $\hat{\boldsymbol{Z}}$), A_i is the facet area, and $c_{di} = B(1 - \rho_i s_i)$ where B is the scattering coefficient (2/3 for Lambertian reflection). The illumination function $\max(0, \hat{\boldsymbol{u}}\cdot\hat{\boldsymbol{n}}_i)$ ensures that only illuminated facets contribute. Self-shadowing by other facets and multiple reflections are not considered.

The solar radiation torque acting on the faceted satellite model can then be calculated as,

$$\boldsymbol{M} = \sum_{i=1}^{n_f} \boldsymbol{r}_i \times \boldsymbol{f}_i \tag{2.37}$$

where $\boldsymbol{r}_i$ is the center of mass to the facet centroid position vector and n_f is the number of facets in the satellite shape model.

To simplify the dynamics, the satellite is assumed to be in circular heliocentric orbit with a semi-major axis of 1 AU. The satellite's earth orbit is neglected given its small size relative to its heliocentric orbit. This approximation was validated by Albuja et al. [2] for the GOES 8 and 10 satellites. Eclipses are also neglected because they are relatively short for high altitude satellites (e.g. a maximum of ~70 min at GEO) and only occur during specific times each year.

We will now discuss the GOES model used to validate and explore the YORP-driven dynamics in this work. The five NOAA GOES 8-12 geostationary weather satellites were built to nearly identical specifications by Space Systems/Loral and successively launched between 1994 and 2001. They were retired in sequential order from 2004 through 2013. The 26 facet GOES shape model used for this work is provided in Figure 2.7 with GOES 8's approximate end of life principal axes and solar array angle θ_{sa} of 17°. These satellites feature asymmetric geometry with a single solar array on the south side of the bus for thermal cooling requirements [31]. Opposite the array on the north side of the bus is a 3.3 m conical solar sail mounted on a 14.4 m deployable boom [107]. The sail's purpose is to balance solar radiation torques generated by the sun-tracking solar array [107]. A reflective, adjustable trim tab is mounted on the end of the solar array to finely balance the radiation torques which change over the course of the year due to the sun's varying $\mathcal{B}$ frame latitude [31]. During normal earth-observing operations, the satellite was oriented with the $+\hat{\boldsymbol{b}}_3$ axis along the GEO orbit angular momentum vector (north) and the bus face intersecting the $+\hat{\boldsymbol{b}}_2$ axis pointing at earth [107]. In this configuration, the solar array continuously tracked the sun, making one rotation relative to the bus once per day.

While the solar sail and trim tab combination effectively balances the solar array radiation

torques during normal sun-pointing operations, the asymmetries have the potential generate notable YORP torques outside of this regime (e.g. post-retirement). The geometry for these satellites are also well documented by Space Systems/Loral [107], greatly aiding dynamical modeling. Overall, these attributes make these satellites ideal targets for studying long-term dynamical evolution.
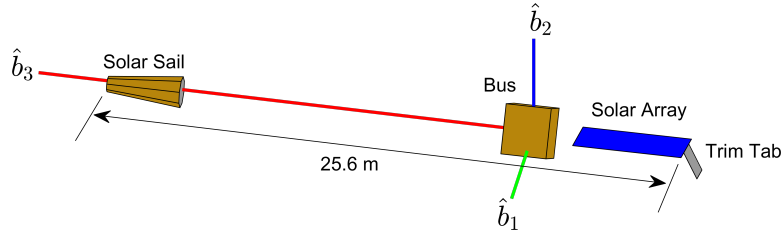
Figure 2.7: GOES 8 shape model with principal axes and major components labeled.

The predicted end of life mass, center of mass, and moments of inertia for each GOES satellite were provided by John Tsui of NOAA's Office of Satellite and Product Operations. For GOES 8 with a dry mass of 972 kg, its center of mass measured from the center of the bus in $\mathcal{B}$ frame components is $\boldsymbol{r}_c = $ [-8.7, -4.6, -16.1]$^\mathrm{T}$ cm. The reference inertia matrix for GOES 8 is given by,

$$[I]_\mathrm{ref} = \begin{bmatrix} 3475.2 & 54.6 & 29.4 \\ 54.6 & 3526.4 & -15.3 \\ 29.4 & -15.3 & 980.9 \end{bmatrix} \mathrm{kg \cdot m^2} \tag{2.38}$$

These reference inertias correspond to the 0° solar array position and are expressed in a frame with two axes normal to the bus faces intersected by $+\hat{\boldsymbol{b}}_1$ and $+\hat{\boldsymbol{b}}_2$ and the third axis along $\hat{\boldsymbol{b}}_3$. The solar array angle θ_{sa} is measured positive around $-\hat{\boldsymbol{b}}_3$, and $\theta_{sa} = 0°$ when the solar array sun-side and $+\hat{\boldsymbol{b}}_2$ face are parallel. To account for changes to the satellite's inertia matrix from rotation of the solar array, the array was modeled as a constant density rectangular prism with the corresponding inertias. For simplicity, the center of mass location was assumed to be constant irrespective of array rotation. An estimated array mass of 65 kg was obtained by scaling the mass-area ratio of the Landsat 7 satellite's solar array to the GOES array area [48]. Landsat

7 was developed at a similar time as GOES and both satellites have aluminum honeycomb solar array panels [107, 48]. The solar array inertia contribution was calculated by subtracting the $0°$ orientation array inertia matrix from the reference inertia matrix, rotating the array inertias to the correct orientation, and adding these back to the constant bus/solar sail inertia matrix. The principal inertias I_i, I_s and I_l and corresponding axes ($\hat{\boldsymbol{b}}_1$, $\hat{\boldsymbol{b}}_2$, and $\hat{\boldsymbol{b}}_3$) were then calculated by eigenvalue/eigenvector analysis. For GOES 8, the end of life principal inertias are $I_l = 980.5$, $I_i = 3432.1$, and $I_s = 3570.0$ kg·m^2.

The end of life solar array θ_{sa} and trim tab θ_{tt} angles for the five GOES satellites are given in Table 2.1. These were calculated from the shutdown epochs provided by John Tsui and information in Ref. [31]. The values differ considerably for the satellites due to different local times and seasons at shutdown with the array in sun-tracking mode. For the trim tab, $0°$ corresponds to the trim tab pointing directly out from the solar array. Positive angles are measured for rotation of the trim tab's front surface towards the array sun side. The trim tab's operational range was between $-70°$ and $-10°$ [31].

Table 2.1: GOES End of Life Solar Array and Trim Tab Angles

Satellite	θ_{sa}	θ_{tt}
GOES 8	17°	-60°
GOES 9	156°	-67°
GOES 10	311°	-14°
GOES 11	91°	-12°
GOES 12	139°	-55°

Table 2.2 provides the nominal optical properties assumed for the various GOES model components [12]. Note that most of the materials are MLI or aluminized tape which provide almost exclusively specular reflections.

Table 2.2: GOES Model Optical Properties

Component	Material	ρ_i	s_i
Bus	MLI	0.60	1
Solar Array front	Solar cell	0.27	1
Solar Array back	Graphite	0.07	0
Trim Tab front	Al tape	0.83	1
Trim Tab back	Graphite	0.07	0
Solar Sail sides/top	Al Kapton	0.66	1
Solar Sail base	Al tape	0.83	1

2.5   Internal Energy Dissipation

Realistic internal energy dissipation cannot simply be modeled with a control torque on a single rigid body as this will not conserve the angular momentum magnitude and direction. So a multi-body energy dissipation model was desired that conserved the inertial angular momentum vector while being simple and conducive to long-term simulations. The model provided by Rahn and Barba fits these criteria [88]. It consists of a rigid spacecraft with a spherical slug located at the satellite center of mass. Between the satellite and slug is a thin viscous fluid layer. This model was developed for low fidelity simulations of liquid fuel tanks. Although the GOES satellites were passivated of fuel at end of life, we assume this model can be used to simulate general spacecraft energy dissipation. Multi-body models with stiffness terms (e.g. springs) provide oscillation frequencies that are often much higher than the satellite rotation rate, requiring smaller integration time-steps and larger computational expense. For the chosen viscous slug model, the spacecraft and slug angular velocities are similar in magnitude, helping to improve computational efficiency. The equations of motion for the spacecraft and slug are,

$$[I]\dot{\boldsymbol{\omega}} = -[\tilde{\boldsymbol{\omega}}][I]\boldsymbol{\omega} + \mu\boldsymbol{\sigma} + \boldsymbol{M} \tag{2.39}$$

$$\dot{\boldsymbol{\sigma}} = -\dot{\boldsymbol{\omega}} - [\tilde{\boldsymbol{\omega}}]\boldsymbol{\sigma} - \frac{\mu}{J}\boldsymbol{\sigma} \tag{2.40}$$

where$[I] = \operatorname{diag}(I_l, I_i, I_s)$, J is the spherical slug's inertia, μ is the non-negative viscous damping coefficient (a function of the slug radius and fluid viscosity), $\boldsymbol{\sigma}$ is the angular velocity of the slug

relative to the $\mathcal{B}$ frame, and $\boldsymbol{M}$ are the other external torques acting on the satellite. It should be noted that $\dot{\boldsymbol{\sigma}}$ is the time derivative with respect to the $\mathcal{B}$ frame. Taking the time derivative of the system's total kinetic energy T and plugging in Eqs. 2.39 and 2.40, we find that $\dot{T} = -\mu\sigma^2$. For non-zero μ, the system will dissipate energy whenever there is relative motion between the spacecraft and spherical slug. Conversely, energy is conserved when the spacecraft and slug are uniformly rotating with equal inertial angular velocities.

For this model, it is important to establish reasonable upper bounds for μ and J. Harvie et al. provide angular velocity information for a GOES 10 spin up maneuver in which all non-principal axis rotation was damped out in $\sim$28 hours [47]. So μ and J were varied to recreate this dissipation scenario with the initial spin state and inertias provided by Harvie et al. [47]. For this analysis is was assumed that complete damping corresponded to a norm off-axis angular velocity less than 0.1% of the angular velocity magnitude (i.e. $\sqrt{\omega_1^2 + \omega_3^2}/|\boldsymbol{\omega}| < $ 1e-3). $J = 18$ kg·m^2 approximately matched this dissipation rate at a critical ratio of $\mu/J = 0.01$ s^{-1}. Figure 2.8 shows the damping times for a grid of J and μ/J values, stopping simulations after 48 hr. GOES 10 had significant liquid propellant remaining during the spin up maneuver, so this dissipation rate is likely much larger than the current values since all five satellites were passivated of fuel at end of life. Therefore, the above value of J was taken as the extreme upper bound for all modeling with $\mu/J \approx 0.01$ s^{-1} providing the fastest dissipation for a given J.
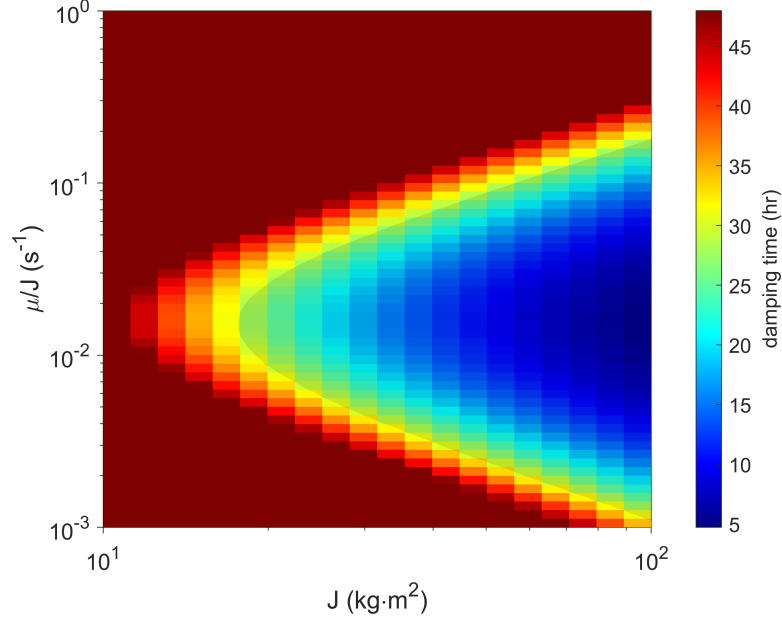
Figure 2.8: GOES 10 damping time vs. spherical slug inertia J and ratio μ/J.

2.6   Gravity Gradient Torque

Defining $\boldsymbol{R} = R\hat{\boldsymbol{R}}$ as the position vector from the earth center to the satellite, the gravity gradient torque is well approximated by the following [98],

$$\boldsymbol{L}_{gg} = \frac{3\mu_e}{R^3}[\tilde{\hat{\boldsymbol{R}}}][I]\hat{\boldsymbol{R}} \tag{2.41}$$

where μ_e is the gravitational parameter of the earth. We will assume that the satellite is in a circular earth orbit, so μ_e/R^3 can be replaced by the orbit mean motion $n_g^2 = \mu_e/R^3$. For satellites in or below GEO, gravity gradient contributions from the sun and moon are at least five orders of magnitude smaller than the earth gravity gradient, so they can be neglected.

In the inertially fixed satellite earth orbit frame $\mathcal{G}$,

$$^{\mathcal{G}}\hat{\boldsymbol{R}} = [-\cos\nu, -\sin\nu, 0]^{\mathrm{T}} \tag{2.42}$$

where ν is the true anomaly of the satellite on its earth-centered orbit.

Rotation from the $\mathcal{G}$ to the earth centered inertial equatorial frame $\mathcal{E}$ (i.e. J2000) is given

by,

$$EG = R_3(-\Omega)R_1(-i) \tag{2.43}$$

where Ω and i are the satellite earth orbit right ascension and inclination. Here we assume a circular orbit so the argument of periapse ω is neglected.

Then rotation from the $\mathcal{E}$ frame to $\mathcal{N}$ frame is given by,

$$NE = R_1(\delta_e) \tag{2.44}$$

where δ_e is earth's obliquity with respect to the ecliptic ($\sim$23.44°).

2.7   Magnetic and Eddy Current Torques

There are two additional environmental perturbations that we must discuss for completeness. The first are magnetic torques caused by interactions of magnetic materials in a spacecraft with earth's magnetic field. These torques are proportional to both a spacecraft's particular dipole moment (generated by permanent magnets and current loops) and earth's magnetic field strength which goes as $1/R^3$ [54]. Significant current loops generally require the spacecraft to be active and powered and therefore will be neglected for studies of defunct satellites. For permanent magnets, spacecraft designers can align them such that their net magnetic moment is as small as possible to minimize unwanted magnetic fields and torques [54]. So torques due to permanent magnets will be neglected as well. The second perturbation is the eddy current torque. For a conductive body rotating in a magnetic field, the body will experience a time-varying magnetic field, inducing currents that oppose the body's rotation [54, 76]. These torques are purely dissipative and will decrease the satellite's angular velocity component that is perpendicular to the magnetic field [54, 76]. Nevertheless, these torques are quite small at GEO since they are proportional to the square of earth's magnetic field strength (i.e proportional to $1/R^6$) [54, 76]. So eddy currents will also be neglected.

<div align="center">

Chapter 3

Full Dynamics

</div>

3.1   YORP only

We will now provide simulation results using the full dynamics model (Eqs. 2.4, 2.9, and 2.37) to illustrate the complex, yet structured YORP-driven dynamical evolution. This will motivate our development of the tumbling-averaged model. Again, we neglect the satellite's earth orbit and assume that the sun rotates in the inertial frame at earth's mean motion n ($\sim 0.986°$/day). The GOES 8 shape model and mass parameters given above are utilized. We will discuss two simulation runs, Run 1 and Run 2. Run 1 demonstrates uniform to tumbling transition, spin-orbit coupling, and tumbling cycles. Run 2 demonstrates these behaviors in addition to tumbling period resonances. Starting with Run 1, the satellite is placed in uniform rotation about $+\hat{\boldsymbol{b}}_2$ with $P_e = 2\pi/\omega_e = 20$ min and a pole direction with $\alpha_o = 202°$ and $\beta_o = 77°$. The initial evolution is provided in Figure 3.1. Starting in uniform rotation, Figure 3.1a shows that ω_e decreases rapidly over the first four days as the satellite spins down. During this initial spin down, Figure 3.1d shows that β decreases as the angular momentum vector (i.e. pole) moves towards the sun-line. Once ω_e reaches a sufficiently small value, the satellite transitions to non-principal axis rotation, apparent in Figure 3.1b. Here, I_d decreases as the rotation moves from uniform rotation to SAM to LAM, crossing the separatrix denoted by the horizontal dashed line. From approximately five days onward, ω_e increases and I_d decreases as the satellite spins up further about $+\hat{\boldsymbol{b}}_3$, the minimum inertia axis. During this time, α and β increase as the pole begins precessing about the sun-line with α taking roughly five days to complete each cycle.

(a) Effective Spin Rate

(b) Scaled Dynamic Moment of Inertia

(c) Clocking Angle

(d) Angle between $\boldsymbol{H}$ and $\hat{\boldsymbol{u}}$
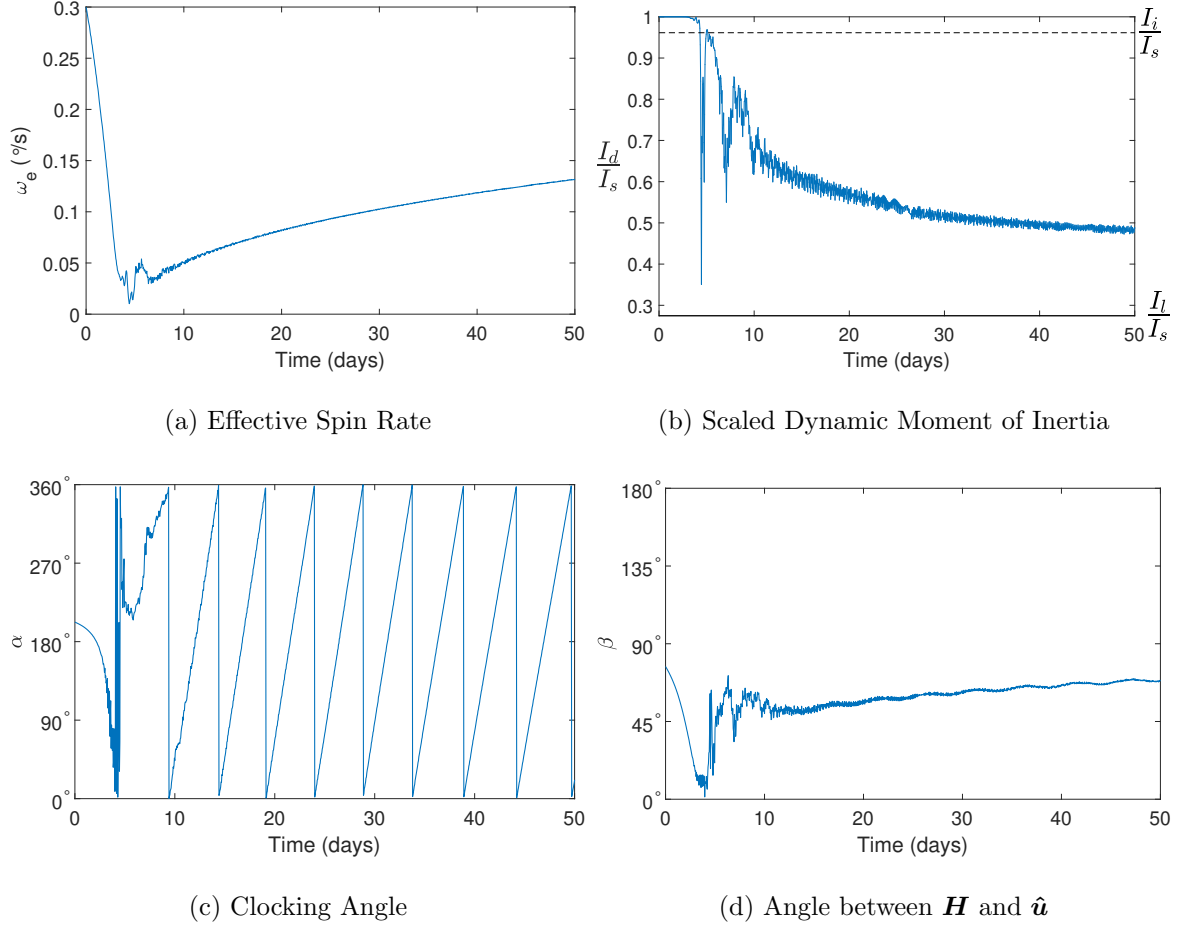
Figure 3.1: Run 1 - transition from uniform rotation to tumbling.

Proceeding further in time, Figure 3.2 shows evolution of the Run 1 solution over three years. On this timescale, we see that the satellite continues in this long axis spin up state until around 160 days when β reaches 90°. At this point, ω_e decreases and I_d increases as the satellite moves back towards uniform rotation. This trend continues until 285 days when the satellite is finally rotating slowly in near-uniform rotation with β approaching 180°. Given the small ω_e, β decreases rapidly towards 0°. During this time, ω_e briefly increases, then decreases with $I_d \approx I_s$. Once β nears 0°, the satellite again spins up about $+\hat{\boldsymbol{b}}_3$ and enters a second, much longer, tumbling cycle.

(a) Effective Spin Rate

(b) Scaled Dynamic Moment of Inertia

(c) Clocking Angle

(d) Angle between $\boldsymbol{H}$ and $\hat{\boldsymbol{u}}$
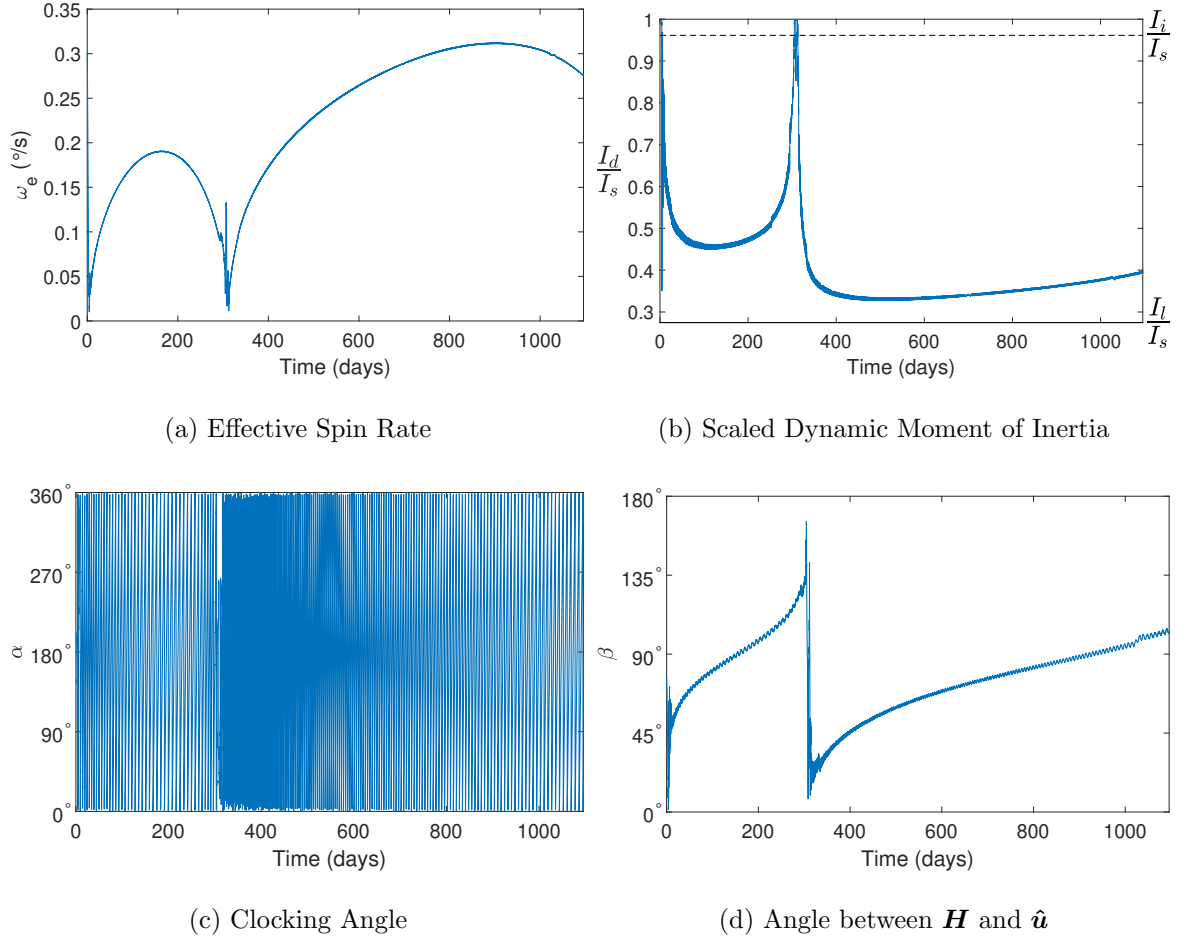
Figure 3.2: Run 1 - long-term dynamical evolution.

To better visualize the pole evolution during these tumbling cycles, Figure 3.3 shows the evolution of $\boldsymbol{H}$ in the $\mathcal{O}$ frame over the first tumbling cycle in Run 1 (from 0 to 309 days in Figure 3.2). The green section is the initial uniform spin down from 0 to 4 days as ω_e decreases and $\boldsymbol{H}$ moves towards the sun-line ($\hat{\boldsymbol{Z}}$). The blue tumbling segment from 4 days to 305 days, shows $\boldsymbol{H}$ precess about $\hat{\boldsymbol{Z}}$ while slowly moving in the $-\hat{\boldsymbol{Z}}$ direction. The red segment shows the return from β near 180° to 0°. The second tumbling cycle is not shown for clarity but follows this same general behavior.
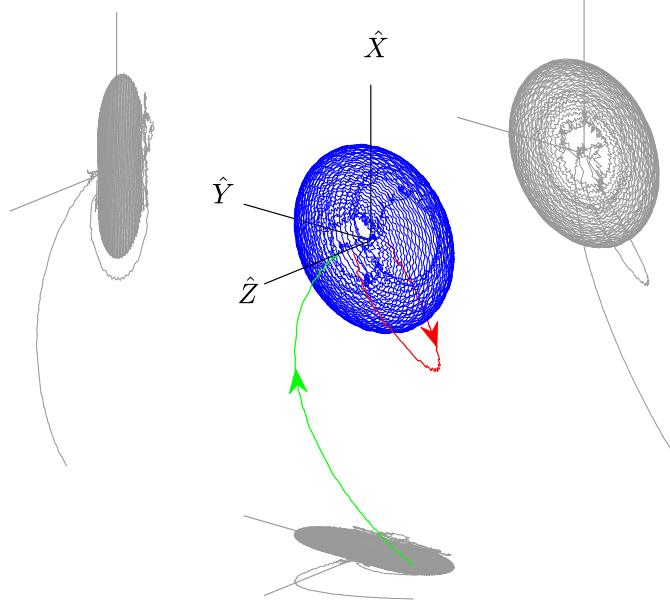
Figure 3.3: Run 1 - $\boldsymbol{H}$ evolution in $\mathcal{O}$ frame over the first tumbling cycle (0 to 308 days). The gray lines are projections of this evolution on the three orthogonal planes.

For Run 2, we illustrate tumbling period resonances. The satellite is again placed in uniform rotation with $P_e = 20$ min but now with a pole given by $\alpha_o = 202°$ and $\beta_o = 17°$. The resulting long-term evolution is provided in Figure 3.4. As with Run 1, ω_e decreases rapidly, the satellite transitions to tumbling, and it proceeds through a tumbling cycle. This first cycle is followed by a second, shorter cycle. After this tumbling cycle, the satellite again spins up about the minimum inertia axis but this time is captured in a $P_\psi/P_{\bar{\phi}} = 1$ tumbling period resonance at roughly 290 days rather than entering another cycle. $P_{\bar{\phi}}$ is the average precession period of the satellite's long axis ($\hat{\boldsymbol{b}}_3$) about $\boldsymbol{H}$ and P_ψ is the rotation period about $\hat{\boldsymbol{b}}_3$ itself. See Chapter 2 for the fundamental period expressions. Given the nearly axisymmetric mass distribution of GOES 8 ($I_s \approx I_i > I_l$), $\dot{\phi}$ is nearly constant and the average precession period $P_{\bar{\phi}}$ is essentially equal to the true precession period. So at this 1:1 resonance, the satellite returns to the same inertial attitude at multiples of $P_{\bar{\phi}}$ and P_ψ. Figure 3.4 shows that ω_e increases steadily while $P_{\bar{\phi}}$ and P_ψ remain in lock step with one another. Because the period ratio $P_\psi/P_{\bar{\phi}}$ is only a function of I_l, I_i, I_s, and I_d, constant $P_\psi/P_{\bar{\phi}}$ requires that I_d be constant as well. While in this resonance, β oscillates between 40° and 70° with

a slight secular increase over time. Carefully examining Figure 3.4c, the satellite's long axis spin up is briefly perturbed when passing through the 1:1 period resonance near 11 days. Also, the period ratio over the second tumbling cycle (from 260 to 285 days) oscillates around a 2:1 ratio. Tumbling resonances were often observed in other simulation runs with 1:1 and 2:1 resonances being most common. Other resonances were occasionally observed.

(a) Effective Spin Rate

(b) Scaled Dynamic Moment of Inertia

(c) Ratio of Fundamental Tumbling Periods

(d) Angle between $\boldsymbol{H}$ and $\hat{\boldsymbol{u}}$
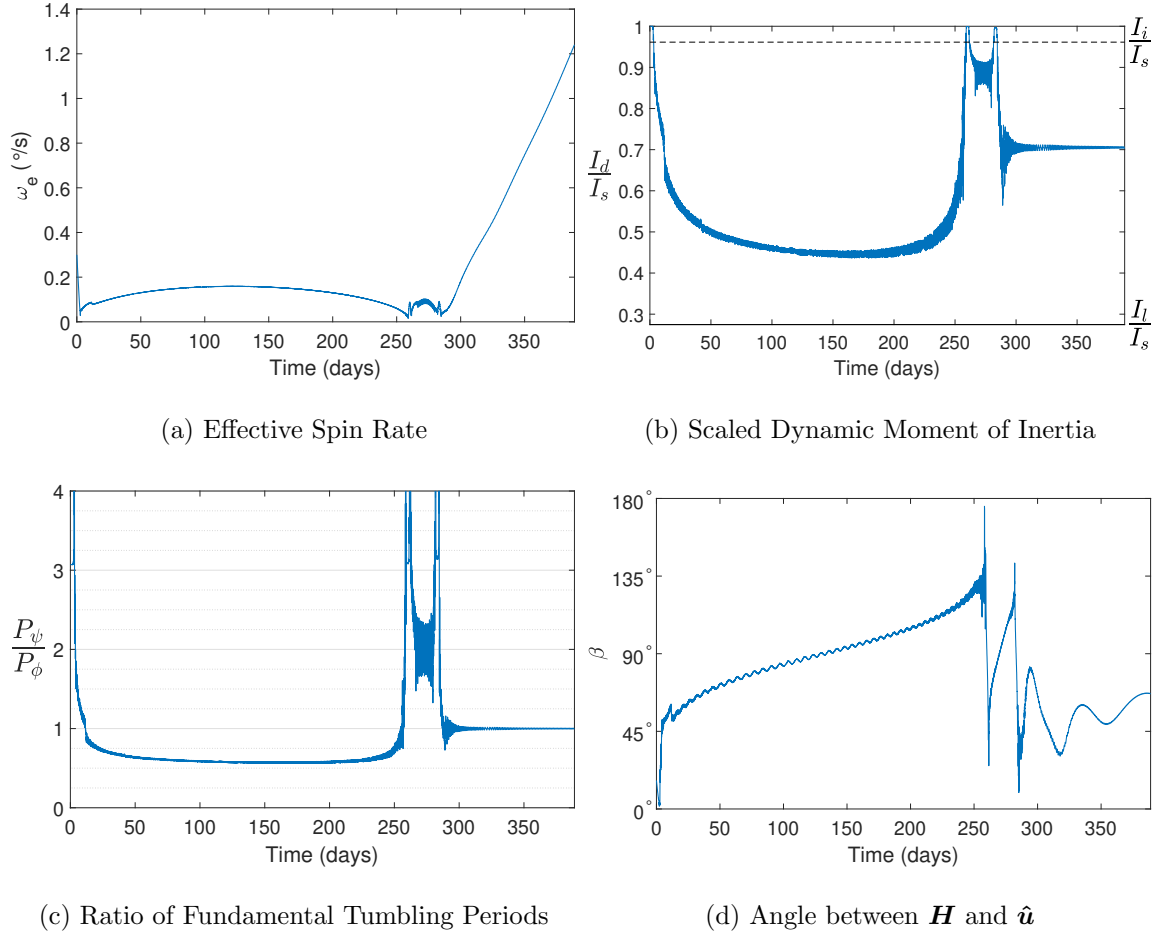
Figure 3.4: Run 2 - long-term dynamical evolution.

3.2   YORP with Internal Energy Dissipation

Using the full YORP dynamics model with the spherical slug energy dissipation model (Eqs. 2.39 and 2.40), long-term evolution for GOES 8 will now be explored. Figure 3.5 shows

the evolution with an initial state $\alpha = 0°$, $\beta = 15°$, $I_d/I_s = 0.98$ (SAM+), $P_e = 2\pi/\omega_e = 120$ min and spherical slug inertia $J = 0.1$ kg·m². As for the YORP-only cases in Figures 3.2 and 3.4, the satellite initially spins up tumbling and proceeds across the separatrix into LAM. But unlike those YORP only cases above, the satellite is pushed back towards uniform rotation (increasing I_d) after ~50 days due to internal energy dissipation. The satellite then proceeds through roughly five perturbed tumbling cycles before transitioning to uniform rotation at ~785 days and spinning up.

(a) Effective Spin Rate

(b) Scaled Dynamic Moment of Inertia

(c) clocking angle α

(d) Coning angle β
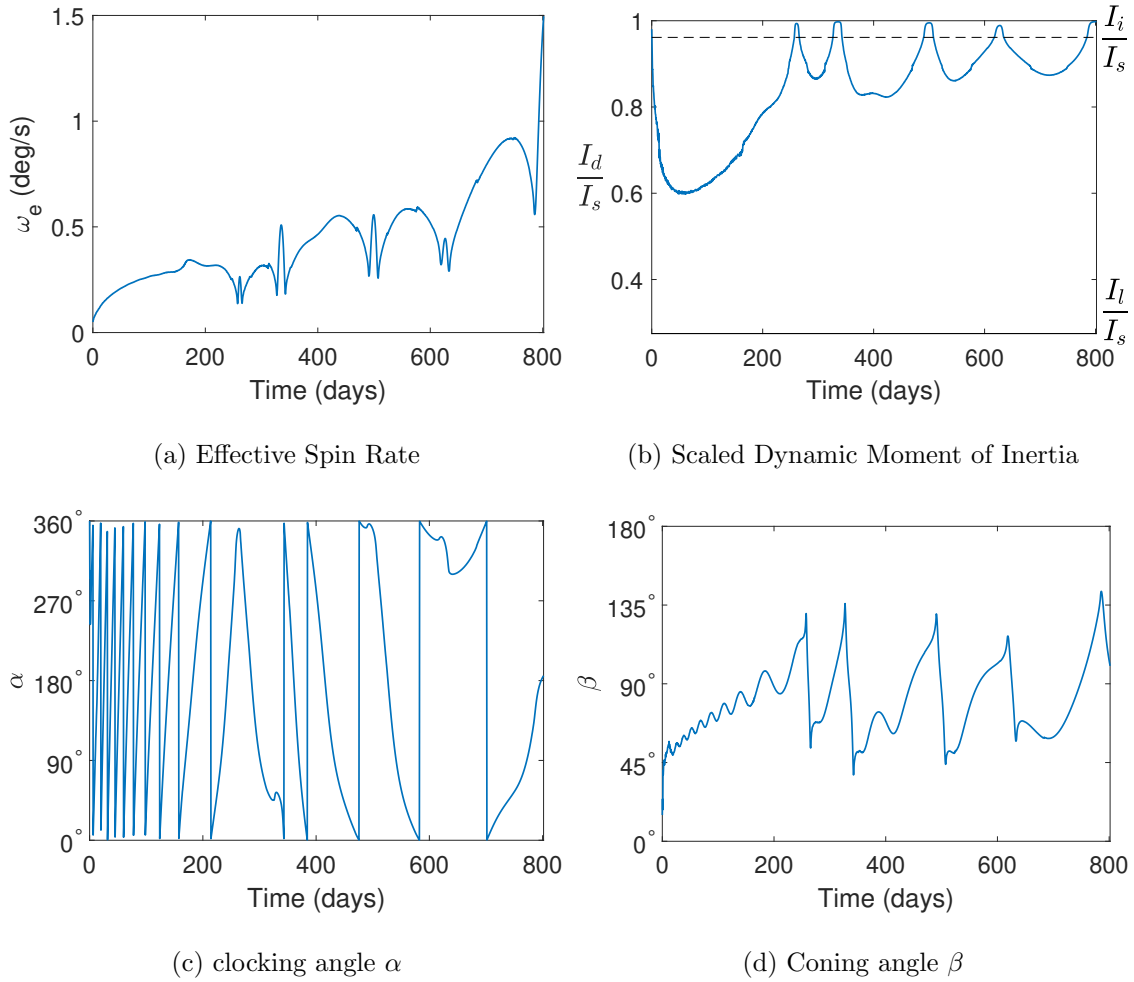
Figure 3.5: GOES 8 YORP + energy dissipation ($J = 0.1$ kg·m², $\mu/J = $ 1e-3 s^{-1})

Increasing the spherical slug inertia to $J = 1.8$ kg·m², Figure 3.6 shows the resulting evolution for the same initial spin state as for Figure 3.5. Again the satellite initially spins up tumbling and

proceeds into LAM. This time it is pushed back towards uniform rotation even more rapidly. Intriguingly, after some brief oscillation, I_d/I_s settles to a fixed value of ~ 0.97 on the SAM side of the separatrix. The remaining three osculating elements soon follow. The effective spin rate ω_e approaches a value of ~ 0.37 deg/s while α and β converge on $\sim 99°$ and $\sim 76°$ respectively. This indicates a tumbling state with constant fundamental tumbling periods and a pole direction fixed in the sun-satellite rotating orbit frame. In the absence of YORP, dissipation would ultimately push the satellite to uniform rotation. So this fixed tumbling state suggests a balance between YORP pushing the satellite further into tumbling and dissipation pushing it towards uniform rotation.

(a) Effective Spin Rate

(b) Scaled Dynamic Moment of Inertia

(c) clocking angle α

(d) Coning angle β
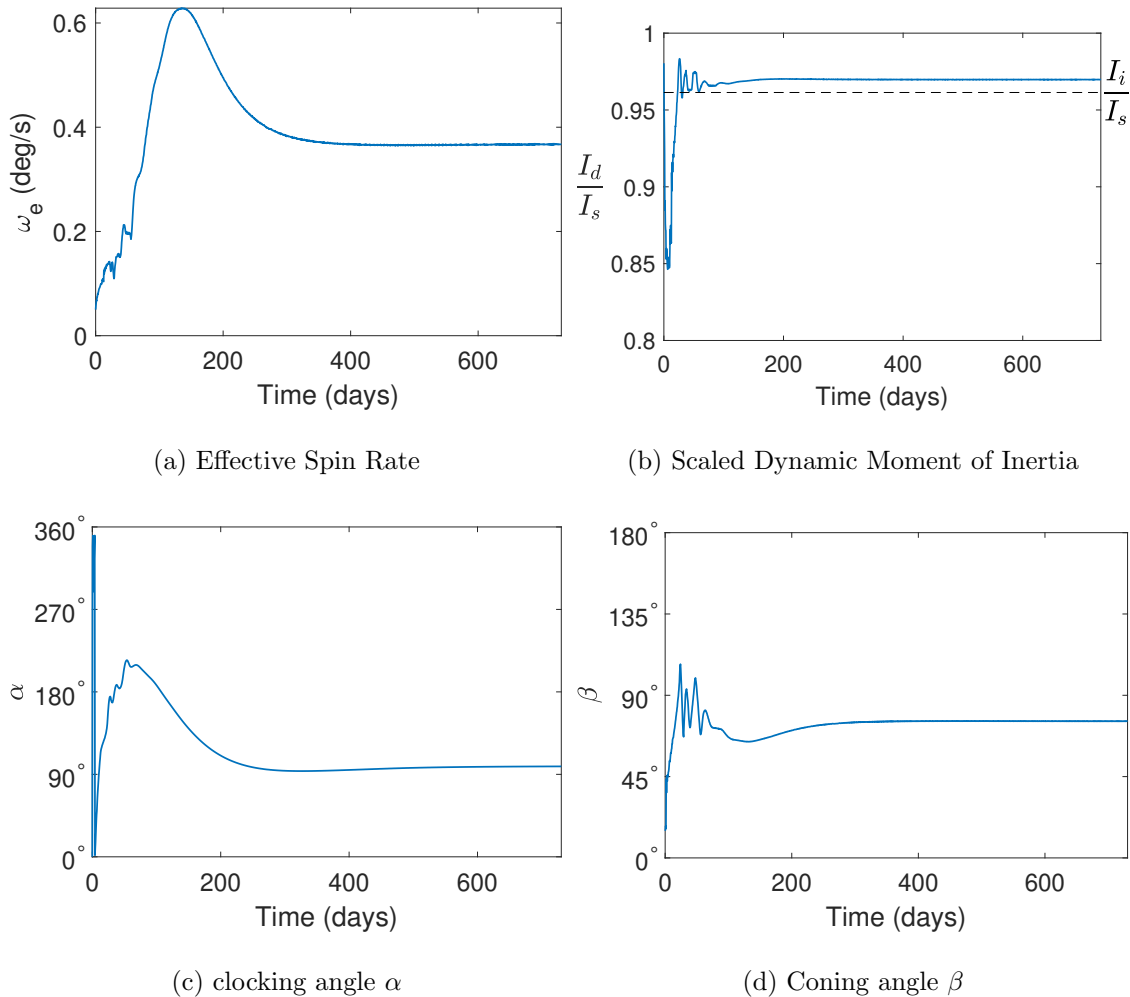
Figure 3.6: GOES 8 YORP + energy dissipation ($J = 1.8$ kg·m^2, $\mu/J = $ 1e-3 s^{-1})

3.3   YORP with Internal Energy Dissipation and Gravity Gradients

Full dynamical evolution will now be considered under the combined influences of YORP, internal energy dissipation, and gravity gradient torques. Figure 3.7 shows the evolution with an initial state $\alpha = 0°$, $\beta = 15°$, $I_d/I_s = 0.98$ (SAM+), $P_e = 2\pi/\omega_e = 120$ min and spherical slug inertia $J = 0.9$ kg·m^2. The satellite is assumed to be in the GEO graveyard with $R = 42575$ km and $i = \Omega = 0°$. Two cases are considered, 1) with just YORP and dissipation, and 2) accounting for all three perturbations. In both cases, the satellite initially proceeds further into tumbling and spins up. After some oscillation, case 1 approaches an equilibrium tumbling state rather quickly. For case 2, I_d also proceeds towards the separatrix where it undergoes significantly more oscillation. While evolving near the separatrix, Figure 3.7c shows for case 2 that the satellite is temporarily captured in the 5:1 SAM tumbling period resonance several times. Prior to 100 days, temporary 5:1 resonance capture is also observed for case 1 without gravity gradients, albeit to a lesser extent. For case 2, there is significantly more variation in ω_e and β as well. For case 2, after escaping the 5:1 tumbling resonance at $\sim$430 days, the satellite spins up quickly while remaining near the separatrix. Overall, these cases suggest that gravity gradient torques significantly perturb convergence to the equilibria observed for YORP with dissipation.

(a) Effective Spin Rate

(b) Scaled Dynamic Moment of Inertia

(c) tumbling period ratio

(d) Coning angle β
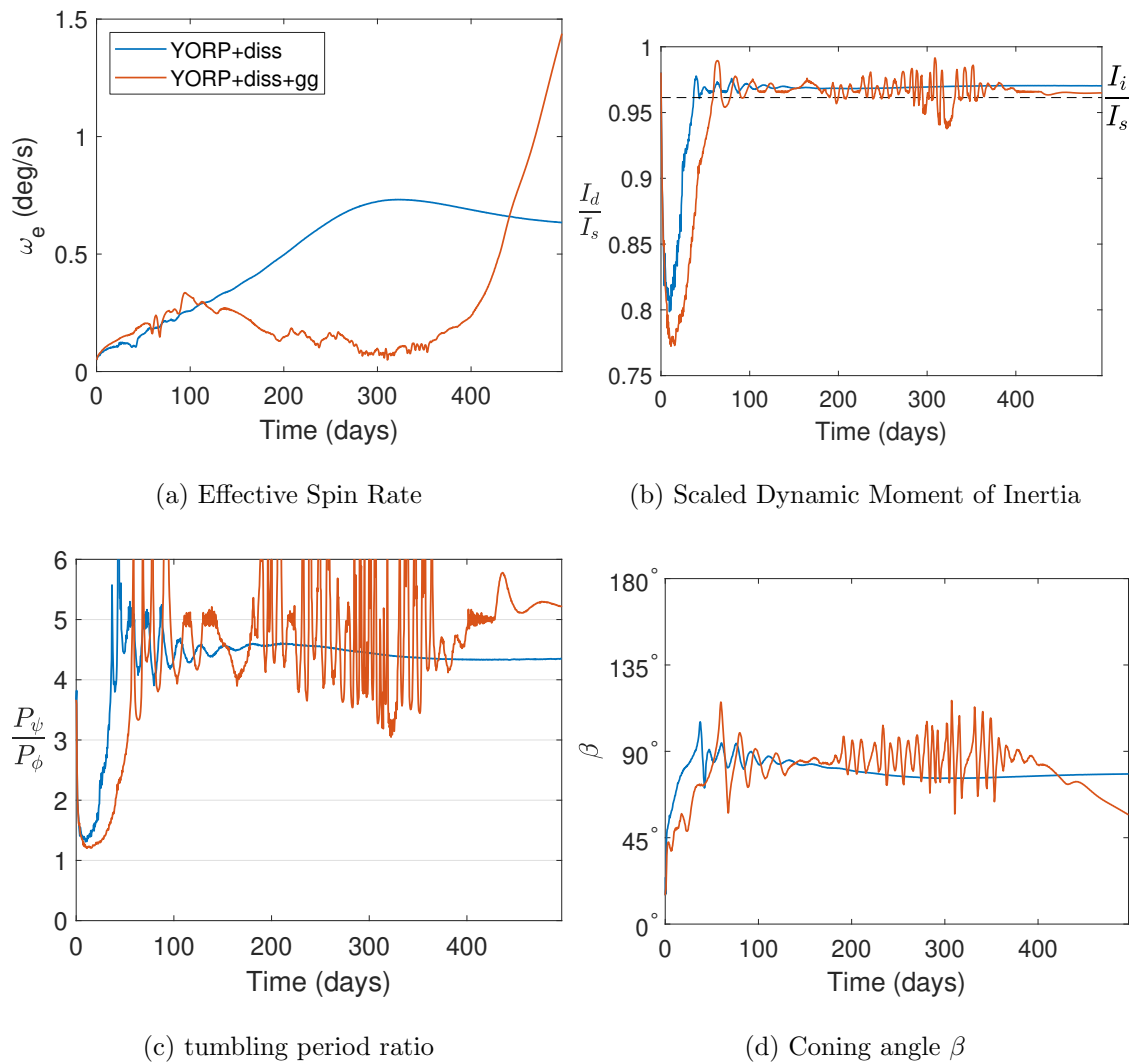
Figure 3.7: GOES 8 evolution for YORP + energy dissipation with and without gravity gradients ($J = 0.9$ kg·m^2, $\mu/J = $ 1e-3 s^{-1})

Chapter 4

Averaged Dynamics Theory

Accounting for YORP, internal energy dissipation, and gravity gradients, the full dynamics simulations presented in Chapter 3 revealed a number of intriguing behaviors including tumbling cycles, spin-orbit coupling, tumbling resonances, and equilibrium tumbling states. Unfortunately the full dynamics models do not explain the underlying mechanisms driving these behaviors. Furthermore, these dynamics are computationally expensive to propagate. This expense increases significantly with increasing satellite spin rate. As a result, these factors greatly limit the utility of the full dynamics for broad, long-term studies. This motivates development of tumbling averaged dynamical models which are the focus of the current chapter. These averaged models rely on the key assumption that all disturbances (external torques and dissipation) are small perturbations on the satellite's torque-free rigid body rotation. Also, the satellite's intrinsic rotation is assumed to be much faster than its orbit around the sun. We start by outlining the osculating elements that will form the foundation of the tumbling-averaged models. The averaging approaches for non-resonant and resonant tumbling are then presented. With these approaches in place, the semi-analytical and numerically averaged models for YORP, internal energy dissipation, and gravity gradients are derived and validated against the full dynamics.

4.1   Osculating Elements

Given the sun-tracking precession observed in the full model simulations, we are interested in developing our equations in the rotating $\mathcal{O}$ frame. Using the transport theorem [98], we find the

time derivative of $\boldsymbol{H}$ with respect to the $\mathcal{O}$ frame,

$$\frac{^{\mathcal{O}}d}{dt}(\boldsymbol{H}) = -\boldsymbol{\omega}_{\mathcal{O}/\mathcal{N}} \times \boldsymbol{H} + \boldsymbol{M} \tag{4.1}$$

where $\boldsymbol{M} = \dot{\boldsymbol{H}}$ is the net external torque. Then, expressing $\boldsymbol{H}$ in the $\mathcal{O}$ frame, we have

$$\begin{bmatrix} H_X \\ H_Y \\ H_Z \end{bmatrix} = \begin{bmatrix} H\cos\alpha\sin\beta \\ H\sin\alpha\sin\beta \\ H\cos\beta \end{bmatrix} \tag{4.2}$$

where (H_X, H_Y, H_Z) are the $\mathcal{O}$ frame components. Taking the time derivative of the Eq. 4.2, solving for $\dot{\alpha}$, $\dot{\beta}$, and $\dot{H}$, and substituting Eq. 4.1, we ultimately obtain,

$$\dot{\alpha} = \frac{M_y + Hn\cos\alpha\cos\beta}{H\sin\beta} \tag{4.3}$$

$$\dot{\beta} = \frac{M_x + Hn\sin\alpha}{H} \tag{4.4}$$

$$\dot{H} = M_z \tag{4.5}$$

where (M_x, M_y, M_z) denote the torque components in the angular momentum frame. Note that $\dot{\alpha}$ is singular for $\beta = 0°$ and $180°$ due to $\sin\beta$ in the denominator of Eq. 4.3.

These elements are complemented by the dynamic moment of inertia $I_d = H^2/2T$. Taking the time derivative of I_d, we obtain,

$$\dot{I}_d = \frac{2I_d}{H}\boldsymbol{M} \cdot \left(\mathbb{I}_{3\times3} - I_d[I]^{-1}\right)\hat{\boldsymbol{H}} \tag{4.6}$$

or equivalently,

$$\dot{I}_d = -\frac{2I_d}{H}\left[\frac{I_d - I_i}{I_i}a_{z1}M_1 + \frac{I_d - I_s}{I_s}a_{z2}M_2 + \frac{I_d - I_l}{I_l}a_{z3}M_3\right] \tag{4.7}$$

where (M_1, M_2, M_3) are the $\mathcal{B}$ frame torque components.

4.2   Non-Resonant Averaging Approach

Following Cicalo and Scheeres [26], we aim to average Eqs. 4.3 - 4.7 over the satellite's

tumbling motion. For this approach, we assume that the variables α, β, H and I_d vary slowly

compared to the satellite's intrinsic rotation. We also assume that all disturbances are relatively

small perturbations on the satellite's torque-free motion. So we average over the torque-free motion

(i.e. with respect to ϕ, θ, and ψ) assuming constant values for the average parameters $\overline{\alpha}$, $\overline{\beta}$, $\overline{H}$ and

$\overline{I}_d$.

Assuming the fundamental tumbling periods $P_{\overline{\phi}}$ and P_ψ are non-resonant, the precession (ϕ)

and coupled nutation (θ) and rotation (ψ) motions are driven by different irrational frequencies.

Note that θ and ψ are directly driven by the linearly scaled time parameter τ (see Chapter 2). So

over a relatively short period of time, the satellite attitude will uniformly cover the (τ, ϕ) phase

space. Figure 4.1 provides a graphical example of this. So in this non-resonant case, averaging over

the torque-free rotation can be reduced to an area average over the (τ, ϕ) phase space.

(a) inertially-fixed direction in body frame   (b) Attitude in (τ, ϕ) space
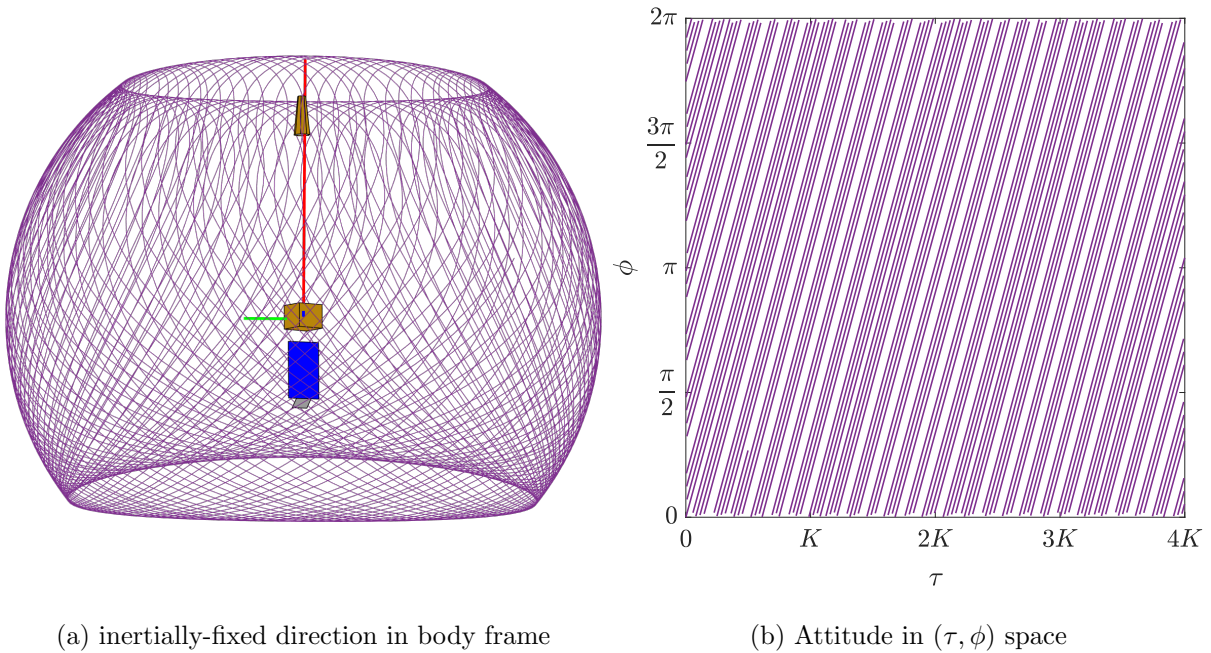
Figure 4.1: Example of non-resonant rotation

For the general variable F, this non-resonant average can be expressed mathematically as,

$$\dot{\overline{F}} = \frac{1}{4K}\frac{1}{2\pi}\int_0^{4K}\int_0^{2\pi}\dot{F}\Big(\phi,\theta(\tau),\psi(\tau)\Big)d\phi\,d\tau \tag{4.8}$$

Averaging over τ involves the Jacobi elliptic functions $\operatorname{cn}\tau$, $\operatorname{sn}\tau$, and $\operatorname{dn}\tau$.

The tumbling-averaged equations of motion are then given by,

$$\dot{\overline{\alpha}} = \frac{\overline{M_y} + \overline{H}n\cos\overline{\alpha}\cos\overline{\beta}}{\overline{H}\sin\overline{\beta}} \tag{4.9}$$

$$\dot{\overline{\beta}} = \frac{\overline{M_x} + \overline{H}n\sin\overline{\alpha}}{\overline{H}} \tag{4.10}$$

$$\dot{\overline{H}} = \overline{M_z} \tag{4.11}$$

$$\dot{\overline{I}_d} = -\frac{2\overline{I}_d}{\overline{H}}\left[\frac{\overline{I}_d - I_i}{I_i}\overline{a_{z1}M_1} + \frac{\overline{I}_d - I_s}{I_s}\overline{a_{z2}M_2} + \frac{\overline{I}_d - I_l}{I_l}\overline{a_{z3}M_3}\right] \tag{4.12}$$

The redundant averaged equation of motion for ω_e is given by,

$$\dot{\overline{\omega}}_e = \frac{1}{\overline{I}_d}\left[\overline{M_z} - \frac{\overline{H}}{\overline{I}_d}\dot{\overline{I}_d}\right] \tag{4.13}$$

We must evaluate the six averaged torque components $\overline{M_x}$, $\overline{M_y}$, $\overline{M_z}$, $\overline{a_{z1}M_1}$, $\overline{a_{z2}M_2}$, and $\overline{a_{z3}M_3}$. Note that at this stage, these are arbitrary torques.

4.3 Resonant Averaging Approach

When the fundamental tumbling period ratio satisfies the following equation where m and n are positive, non-zero integers, the tumbling spin state is considered to be resonant,

$$\frac{P_\psi}{P_{\overline{\phi}}} = \frac{m}{n} \tag{4.14}$$

In a resonant case, the satellite periodically returns to approximately the same inertial attitude with period $P_r = nP_\psi = mP_{\overline{\phi}}$. Again, this motion is approximately periodic because ϕ is not

generally periodic in time. An example of resonant motion is provided in Figure 4.2 for the LAM $\frac{P_\psi}{P_{\bar\phi}} = 1$ resonance assuming $I_l/I_s = 1/6$ and $I_i/I_s = 1/3$. Note in Figure 4.2a that the inertially fixed point takes an approximately periodic trajectory through the body frame compared to the quasi-periodic trajectory for the non-resonant case in Figure 4.1a. Figure 4.2b shows the trajectory in (τ, ϕ) phase space where it is also approximately periodic.

(a) inertially fixed point in body-fixed frame

(b) Attitude in (τ,ϕ) space
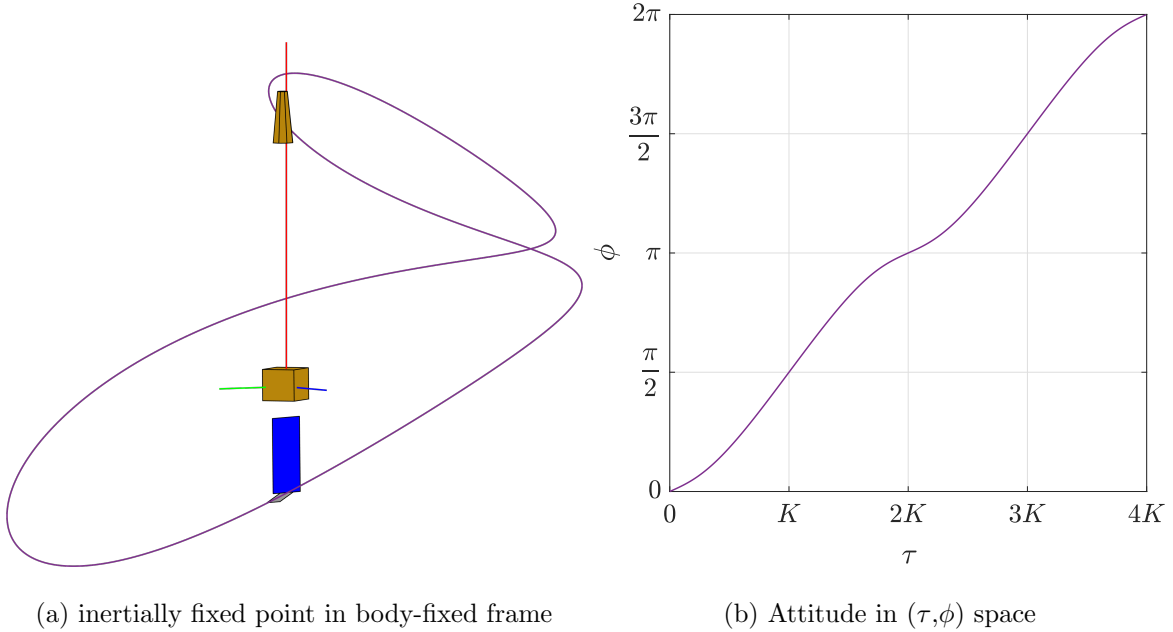
Figure 4.2: Resonant motion with $P_\psi/P_{\bar\phi} = 1$ (LAM)

To study the resonant dynamics, we desire an angle γ that captures the relative offset between the fast-varying Euler angles yet varies slowly in the vicinity of a given resonance and is constant directly on the unperturbed resonant motion. With a slow variable, we can then average over the Euler angles using a similar approach to the non-resonant case. One might assume this could be achieved by taking γ as $n\phi - m\psi$. Unfortunately, even on a resonance, $\dot\phi$ and $\dot\psi$ are not constant for triaxial bodies, and as stated earlier, ϕ is also non-periodic in the triaxial case. Furthermore, for SAM states in the long axis convention, ψ librates rather than circulates. So for any triaxial case, γ would fluctuate on the resonance using this definition. Taking a different approach, we define $\dot\varphi$

as the average rate of change of ϕ. And instead of ψ, we use the constant-rate angle τ_r. We then have,

$$\dot{\varphi} = \frac{2\pi}{P_{\bar{\phi}}} \qquad \dot{\tau}_r = \frac{2\pi}{P_\psi} \qquad (4.15)$$

where $\tau_r = 2\pi\tau/4K$. So τ_r is essentially τ converted to angle space. With the combined θ and ψ motion periodic on $\Delta t = P_\psi$ and $\Delta\tau = 4K$, it is therefore periodic on $\Delta\tau_r = 2\pi$ as well.

Rearranging Eq. 4.14 and modifying it to accounting for the relative phase angle γ, then substituting Eq. 4.15, we have,

$$\dot{\gamma} = n\dot{\varphi} - m\dot{\tau}_r \qquad (4.16)$$

Since $P_{\bar{\phi}}$ and P_ψ are constants of motion for torque-free rigid body rotation, so is $\dot{\gamma}$. Also, on a given resonance, $\dot{\gamma}$ is zero. Just off of that resonance, Eq. 4.14 is no longer satisfied for the given m and n, so $\dot{\gamma}$ will be non-zero.

Taking the time derivative of Eq. 4.16, we obtain an equation for how γ will evolve in the presence of internal/external perturbations,

$$\ddot{\gamma} = n\ddot{\varphi} - m\ddot{\tau}_r \qquad (4.17)$$

Expressions for $\ddot{\varphi}$ and $\ddot{\tau}_r$ are provided in Appendix C. Note that Eq. 4.17 depends on the the external torque $\boldsymbol{M}$ through $\dot{I}_d$ and $\dot{H}$. Following through the expressions in Appendix C, we also find that H cancels in $\ddot{\varphi}$, $\ddot{\tau}_r$, and $\dot{I}_d$. So $\ddot{\gamma}$ is independent of H (i.e. the satellite rotation rate).

Since γ evolves slowly compared to the satellite's intrinsic rotation in the vicinity of a given resonance, we can apply the same assumptions as for the non-resonant case. Taking constant "average" values for $\bar{\alpha}$, $\bar{\beta}$, $\bar{H}$, $\bar{\gamma}$, and $\overline{I_d}(m, n)$ we numerically average Eqs. 4.3 - 4.6, and 4.17 over one cycle of the torque-free resonant motion defined by the Euler angles $\phi(t)$, $\theta(t)$, and $\psi(t)$. Analytical averaging for the resonant case would require evaluating a number of non-trivial integrals involving various products of cos, sin, cn, sn, and dn. These required integrals would change for each resonance. So only numerically averaged resonant dynamics are developed here. The I_d value

corresponding to the given period ratio m/n is calculated using the bisection method with Eqs. 2.34 and 2.35 for LAMs and SAMs respectively. The duration of this resonance cycle is $\Delta t = P_r$ where P_r is the resonance period $P_r = nP_\psi = mP_{\bar\phi}$. Note that the averaging kernel here is distinct from the non-resonant case where we instead took an area average over the entire (τ, ϕ) phase space.

For consistency with the average sense of φ, one would like $\Delta\phi(\Delta t = P_r) = \dot\varphi P_r = 2\pi m$. This is very nearly satisfied for roughly prolate bodies which includes many box-wing satellites, rocket bodies, and the GOES 8-12 satellites. Interestingly, for triaxial bodies in resonances satisfying $P_\psi/P_{\bar\phi} = 2/i$ where $i = [1, 2, 3, ...]$, $\Delta\phi(\Delta t) = \dot\varphi\Delta t = 2\pi m$ for any $\Delta t = P_r$. This can be shown using the equations for ϕ in Chapter 2. Otherwise, $\phi(t)$ is only periodic for triaxial bodies on average. Nevertheless, we neglect this complication and simply assume the cycle over which the average is taken has $\Delta\phi(P_r) = 2\pi m$. So for the non-averaged equation given arbitrarily by $\dot F$, the resonance-averaged equation $\overline{\dot F}$ is,

$$\overline{\dot F}\left(\overline\alpha, \overline\beta, \overline H, \overline\gamma\right) = \frac{1}{P_r}\int_0^{P_r} \dot F\left(\overline\alpha, \overline\beta, \overline H, \overline{I_d}, \phi(t), \theta(t), \psi(t)\right)dt \tag{4.18}$$

Following this notation, the fundamental resonance-averaged equations of motion for the system $(\overline\alpha, \overline\beta, \overline H, \overline\gamma)$ are given by,

$$\overline{\dot\alpha} = \frac{\overline M_y + \overline H n\cos\overline\alpha\cos\overline\beta}{\overline H\sin\overline\beta} \tag{4.19}$$

$$\overline{\dot\beta} = \frac{\overline M_x + \overline H n\sin\overline\alpha}{\overline H} \tag{4.20}$$

$$\overline{\dot H} = \overline M_z \tag{4.21}$$

$$\overline{\ddot\gamma} = n\overline{\ddot\varphi} - m\overline{\ddot\tau}_r \tag{4.22}$$

where $\overline{\ddot\gamma}$ in turn depends on $\overline{\dot I_d}$,

$$\overline{\dot I_d} = \frac{2\overline{I_d}}{\overline H}\overline{M\cdot\left(\mathbb{I}_{3\times3} - \overline{I_d}[I]^{-1}\right)\hat H} \tag{4.23}$$

Since we are averaging in the vicinity of a particular resonance, $\overline{I_d}$ is held constant.

The resonant motion is best propagated with the analytical torque-free solutions for $\phi(t)$, $\theta(t)$, and $\psi(t)$ which do not suffer from numerical integration errors (see Chapter 2 for these solutions). To propagate the motion, we must determine the initial values for τ_r and ϕ, given by τ_{r_o} and ϕ_o. Our approach is to assume $\gamma_o = n\phi_o - m\tau_{r_o}$, select a value for τ_{r_o}, and solve for the corresponding ϕ_o. For consistency with the averaged sense of our dynamics, we would like the unperturbed resonant trajectory over which we average to satisfy $\gamma(t) = n\phi(t) - m\tau_r(t) \approx \overline{\gamma} = \gamma_o$. Since $\phi(t)$ depends non-linearly on τ_{r_o}, Figure 4.3 shows that the resonant trajectories will differ slightly for different values of τ_{r_o}. Taking τ_{r_o} as any multiple of $\pi/2$ yields one trajectory in (τ_r, ϕ) space that tracks $\overline{\gamma} = \gamma_o$ on average. Also, trajectories for all possible τ_{r_o} values are equally spread about this "center" trajectory, with those for τ_{r_o} equal to odd multiples of $\pi/4$ located farthest away. With this in mind, we simply take $\tau_{r_o} = 0$, reasonably assuming that the averaged equation values for this "center" trajectory approximately equal the collective mean of the averaged equation values taken over all trajectories (i.e. all possible τ_{r_o} values). To clearly illustrate the trajectory differences in Figure 4.3, we selected roughly oblate principal inertias (i.e., $I_l \approx I_i < I_s$). Using the long axis convention for bodies that are progressively more prolate (i.e., $I_l < I_i \approx I_s$), dispersion of trajectories around $\overline{\gamma} = \gamma_o$ becomes smaller and smaller and the "center" trajectory values converge on the collective mean values. For the GOES satellites, the four lines in Figure 4.3 are nearly coincident.
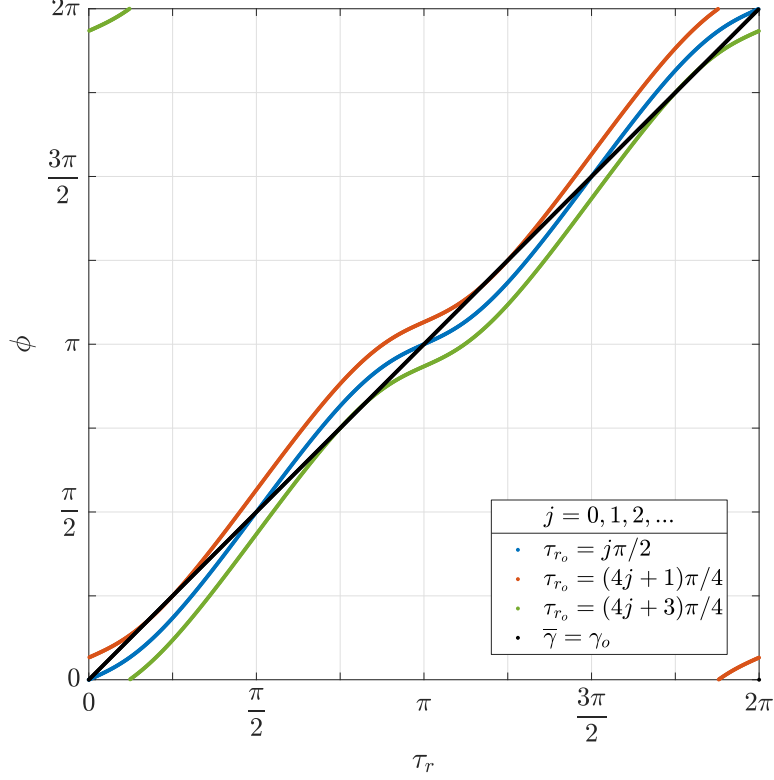
Figure 4.3: $P_\psi/P_{\bar\phi} = 1$ trajectories for different τ_{r_o} values with $\gamma_o = 0$ $\left(I_l/Is = 1/6,\ I_i/I_s = 1/3\right)$

So, in summary we have,

$$\tau_{r_o} = 0 \qquad\qquad \phi_o = \overline{\gamma}/n \tag{4.24}$$

The range of $\overline{\gamma}$ is $[0, 2\pi n]$, but one can consider just the sub-interval $\overline{\gamma} = [0, 2\pi]$ because the trajectories for $\phi_o \geq 2\pi/n$ overlap those for $0 \leq \phi_o < 2\pi/n$.

After averaging over the resonant motion, $\ddot{\overline{\gamma}}$, $\overline{M_x}$, $\overline{M_y}$, and $\overline{M_z}$ only depend on $\overline{\beta}$ and $\overline{\gamma}$. So for a given resonance, 2-D $(\overline{\beta}, \overline{\gamma})$ lookup tables can be generated. When numerically propagating Eqs. 4.9 - 4.22, one can simply interpolate between lookup table points. It is valuable to note that the resonance-averaged equations of motion are generalized for any small perturbing torque.

4.4   Non-Resonant Averaged YORP

The non-resonant, semi-analytical tumbling-averaged YORP model will now be developed. To obtain analytical solutions for $\overline{M_x}$, $\overline{M_y}$, $\overline{M_z}$, $\overline{a_{z1}M_1}$, $\overline{a_{z2}M_2}$, and $\overline{a_{z3}M_3}$ in Eqs. 4.9 - 4.12, we

follow Ref. [26] and approximate $\max(0, \hat{\boldsymbol{u}} \cdot \hat{\boldsymbol{n}}_i)$ in Eq. 2.36 using its second order Fourier series expansion,

$$\max(0, \hat{\boldsymbol{u}} \cdot \hat{\boldsymbol{n}}_i) \approx g_i = \frac{1}{3\pi} + \frac{1}{2}(\hat{\boldsymbol{u}} \cdot \hat{\boldsymbol{n}}_i) + \frac{4}{3\pi}(\hat{\boldsymbol{u}} \cdot \hat{\boldsymbol{n}}_i)^2 \tag{4.25}$$

where, given our frame definitions, $u_x = -\sin\beta$, $u_y = 0$, and $u_z = \cos\beta$. So $\hat{\boldsymbol{u}} \cdot \hat{\boldsymbol{n}} = u_x n_x + u_z n_z$. This illumination function approximation is shown graphically in Figure 4.4.
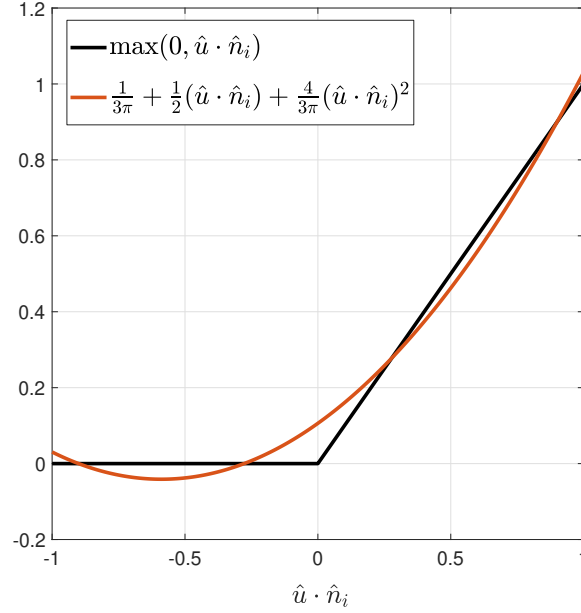
Figure 4.4: 2nd Order Fourier Series Illumination Function Approximation

With this approximation,

$$\begin{bmatrix} \overline{M_x} \\ \overline{M_y} \\ \overline{M_z} \end{bmatrix} = -P_{SRP} \sum_{i=1}^{n_f} \left[c_{si}\overline{(\hat{\boldsymbol{u}} \cdot \hat{\boldsymbol{n}}_i)g_i\boldsymbol{d}_i} + c_{ai}\overline{g_i\boldsymbol{r}_i \times \hat{\boldsymbol{u}}} + c_{di}\overline{g_i\boldsymbol{d}_i} \right] A_i \tag{4.26}$$

where $\boldsymbol{d}_i = \boldsymbol{r}_i \times \hat{\boldsymbol{n}}_i$ and the constants $c_{si} = 2\rho_i s_i$ and $c_{ai} = (1 - \rho_i s_i)$.

From Eqs. 2.5 and 2.6, we see that all $\mathcal{H}$ frame x and y vector components will contain either $\cos\phi$ or $\sin\phi$. So products with odd combined powers of x and y will average to zero over ϕ. Expanding Eq. 4.26, including only non-zero terms, and dropping the ith facet indices from the averaged products for brevity, $\overline{M_x}$, $\overline{M_y}$, and $\overline{M_z}$ are then given by,

$$\overline{M_x} = -P_{SRP}\sum_{i=1}^{n_f}\left[u_x\left(\frac{1}{2}c_{di} + \frac{1}{3\pi}c_{si}\right)\overline{d_x n_x} + u_x u_z\left(c_{si} + \frac{8}{3\pi}c_{di}\right)\overline{d_x n_x n_z} + \frac{4}{3\pi}c_{si}u_x^3\overline{d_x n_x^3}\right.$$
$$\left. + \frac{4}{\pi}c_{si}u_x u_z^2\overline{d_x n_x n_z^2} + \frac{1}{2}c_{ai}u_x u_z\overline{r_y n_x} + \frac{8}{3\pi}c_{ai}u_x u_z^2\overline{r_y n_x n_z}\right]A_i$$

(4.27)

$$\overline{M_y} = -P_{SRP}\sum_{i=1}^{n_f}\left[u_x\left(\frac{1}{2}c_{di} + \frac{1}{3\pi}c_{si}\right)\overline{d_y n_x} + u_x u_z\left(c_{si} + \frac{8}{3\pi}c_{di}\right)\overline{d_y n_x n_z} + \frac{4}{3\pi}c_{si}u_x^3\overline{d_y n_x^3}\right.$$
$$+ \frac{4}{\pi}c_{si}u_x u_z^2\overline{d_y n_x n_z^2} + \frac{1}{3\pi}c_{ai}u_x\overline{r_z} - \frac{1}{2}c_{ai}u_x u_z\overline{r_x n_x} + \frac{1}{2}c_{ai}u_x u_z\overline{r_z n_z}$$
$$\left. - \frac{8}{3\pi}c_{ai}u_x u_z^2\overline{r_x n_x n_z} + \frac{4}{3\pi}c_{ai}u_x^3\overline{r_z n_x^2} + \frac{4}{3\pi}c_{ai}u_x u_z^2\overline{r_z n_z^2}\right]A_i$$

(4.28)

$$\overline{M_z} = -P_{SRP}\sum_{i=1}^{n_f}\left[\frac{1}{3\pi}c_{di}\overline{d_z} + u_z\left(\frac{1}{2}c_{di} + \frac{1}{3\pi}c_{si}\right)\overline{d_z n_z} + \left(\frac{1}{2}c_{si} + \frac{4}{3\pi}c_{di}\right)\left(u_x^2\overline{d_z n_x^2} + u_z^2\overline{d_z n_z^2}\right)\right.$$
$$\left. + \frac{4}{\pi}c_{si}u_x^2 u_z\overline{d_z n_x^2 n_z} + \frac{4}{3\pi}c_{si}u_z^3\overline{d_z n_z^3} - \frac{1}{2}c_{ai}u_x^2\overline{r_y n_x} - \frac{8}{3\pi}c_{ai}u_x^2 u_z\overline{r_y n_x n_z}\right]A_i$$

(4.29)

Solutions for the various averaged quantities in Eqs. 4.27, 4.28, and 4.29 are provided in Appendix A. Note that these quantities are implicitly dependent on $\overline{I}_d$.

The terms $\overline{a_{z1}M_1}$, $\overline{a_{z2}M_2}$, and $\overline{a_{z3}M_3}$ are given by,

$$\overline{a_{z*}M_*} = -P_{SRP}\sum_{i=1}^{n_f}\left[\frac{1}{3\pi}c_{di}\overline{a_{z*}d_*} + u_z\left(\frac{1}{2}c_{di} + \frac{1}{3\pi}c_{si}\right)\overline{a_{z*}d_* n_z}\right.$$
$$+ \left(\frac{1}{2}c_{si} + \frac{4}{3\pi}c_{di}\right)\left(u_x^2\overline{a_{z*}d_* n_x^2} + u_z^2\overline{a_{z*}d_* n_z^2}\right)$$
$$\left. + \frac{4}{\pi}c_{si}u_x^2 u_z\overline{a_{z*}d_* n_x^2 n_z} + \frac{4}{3\pi}c_{si}u_z^3\overline{a_{z*}d_* n_z^3} + c_{ai}\overline{ga_{z*}\delta_*}\right]A_i$$

(4.30)

where $* = 1, 2, 3$. Also, $\delta_1 = (r_2 u_3 - r_3 u_2)$, $\delta_2 = (r_3 u_1 - r_1 u_3)$, and $\delta_3 = (r_1 u_2 - r_2 u_1)$. To calculate $\overline{a_{z*}d_*}$, $\overline{a_{z*}d_* n_z}$, etc., we note that $d_z = a_{z1}d_1 + a_{z2}d_2 + a_{z3}d_3$. From the averaged Appendix A equations that include d_z (Eqs. A.16, A.19, A.22, A.23, A.28, A.29 for LAMs and Eqs. A.33, A.36, A.39, A.40, A.45, A.46 for SAMs), we retain just the terms containing d_*. Solutions for $\overline{ga_{z*}\delta_*}$ are provided separately in Appendix A. Overall, Eqs. 4.27 - 4.30 depend on $\overline{I}_d$ and $\overline{\beta}$ but are independent of $\overline{\alpha}$ and $\overline{H}$.

With the semi-analytical averaged model developed, the analytically averaged components can now be validated against the numerically averaged modle. For the numerically averaged model, $\overline{M_x}$, $\overline{M_y}$, $\overline{M_z}$, $\overline{a_{z1}M_1}$, $\overline{a_{z2}M_2}$, and $\overline{a_{z3}M_3}$ are obtained by numerically averaging over a uniformly spaced (τ,ϕ) grid for each I_d and β combination. Here, the full Eq. 2.36 is used without assuming the 2nd order Fourier series illumination function approximation.

Figure 4.5 shows the average torques in the $\mathcal{H}$ frame for the analytically and numerically averaged models. Both SAM and LAM states are tested. We see that in all cases, the models only differ quantitatively, sharing the same general structure. For the SAM cases, we see that $\overline{M_z}$ is negative for $\beta < 90°$ and positive for $\beta > 90°$. So the satellite will spin down when $\beta < 90°$. Also, $\overline{M_x} \leq 0$ across all β, so $\boldsymbol{H}$ will tend to be pushed towards the sun line. For the LAM cases in Figure 4.5, $\overline{M_y}$ has the largest magnitude of the three torque components. $\overline{M_y}$ drives $\dot{\bar{\alpha}}$ and therefore precession of $\boldsymbol{H}$ around the sun line. The precession rate $\dot{\bar{\alpha}}$ varies significantly with β. Also, $\overline{M_x} \geq 0$ for all β, pushing $\boldsymbol{H}$ away from the sun line. $\overline{M_z}$ changes sign at $\beta = 90°$, so the satellite will first spin up and then down as β increases. Continuing the comparison, Figure 4.6 shows $\dot{\bar{I}}_d$ for the analytically and numerically averaged models assuming an arbitrary $\omega_e = 2\pi$ rad/s. Again, they differ only quantitatively. We see that for both the SAM and LAM states the satellite will be pushed towards more excited tumbling (smaller I_d) for $\beta < 90°$ and towards uniform rotation (larger I_d) for $\beta > 90°$. $\dot{\bar{I}}_d$ solutions for LAM/SAM $-$ were virtually indistinguishable from the $+$ solutions and have been excluded from Figure 4.6 for brevity. Overall, the $+/-$ solutions for both LAMs and SAMs differ insignificantly for all components except $\overline{M_y}$, where the solution is mirrored around $\beta = 90°$ and has an opposite sign. So for the $+$ and $-$ solutions, $\dot{\bar{\alpha}}$ will have opposite signs and $\boldsymbol{H}$ will precess about the sun line in opposite directions. This symmetric structure is due to the particular satellite geometry. For a fixed $\boldsymbol{H}$, the $+/-$ LAM/SAM spin states essentially flip the satellite model 180° while maintaining the same inertial precession direction. As a result, some averaged torque contributions from the GOES solar array will change for $+/-$ LAM/SAM due to different reflective properties for the front and back array faces. On the other hand, contributions from the axisymmetric solar sail will not change.

(a) SAM+ $I_d = 3500$ kg·m^2

(b) LAM+ $I_d = 3000$ kg·m^2

(c) SAM- $I_d = 3500$ kg·m^2

(d) LAM- $I_d = 3000$ kg·m^2
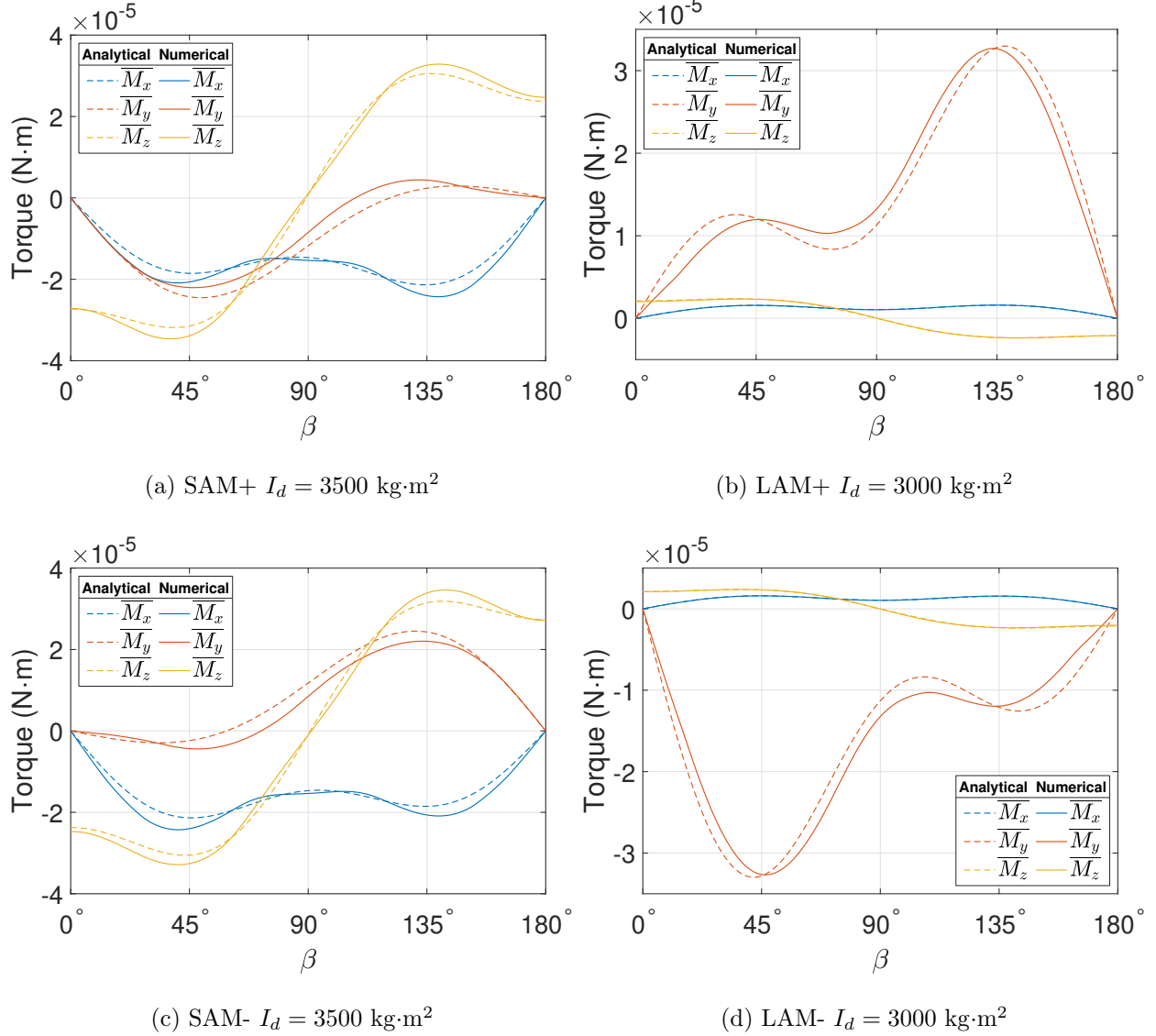
Figure 4.5: Comparison of GOES 8 analytically and numerically averaged torques.

We will now compare the dynamical evolution for the full, numerically averaged, and analytically averaged models by numerically integrating Eqs. 4.9 - 4.12. For all three models, the same initial spin state is prescribed with $\alpha_o = 95°$, $\beta_o = 50°$, $I_d/I_s = 0.62$ (SAM+), $2\pi/\omega_e = 40$ min. For the numerically averaged model, 2-D $\overline{M_x}$, $\overline{M_y}$, $\overline{M_z}$, and $\dot{\overline{I}}_d$ lookup tables are generated vs. β and I_d (180×150 point grid). Using MATLAB's ode113 numerical integrator with 1e-12 absolute and relative tolerances for the models, they were propagated for 3 years. The resulting evolution

(a) SAM+ $I_d = 3500$ kg·m^2

(b) LAM+ $I_d = 3000$ kg·m^2
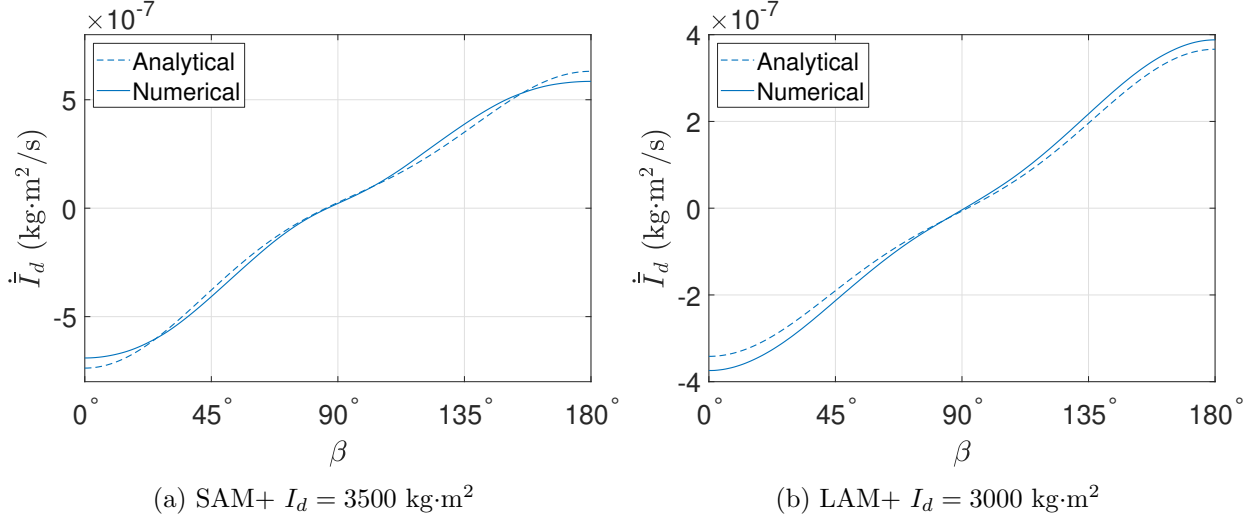
Figure 4.6: Comparison of analytically and numerically averaged $\dot{\bar{I}}_d$ for GOES 8

is provided in Figure 4.7. Overall, both averaged models follow the full model evolution well. Given the illumination function approximation for the analytically averaged model, it does start to diverge from the numerically averaged model. Also, the full model is slightly perturbed while passing through the $P_\psi/P_{\bar\phi} = 1{:}1$ resonance at $\sim$670 days (just prior to the brief return to uniform rotation). This resonance perturbation is most clearly observed in Figure 4.7a. The non-resonant averaged models do not account for these resonances. So this provides some of the discrepancy between the full and averaged models towards the end of the simulation. The computation times for the averaged models were both $\sim$4 seconds, compared to 70 minutes for the full model. This corresponds to a roughly three order of magnitude decrease in computation time.

(a) effective spin rate ω_e

(b) normalized dynamic moment of inertia I_d

(c) clocking angle α

(d) coning angle β
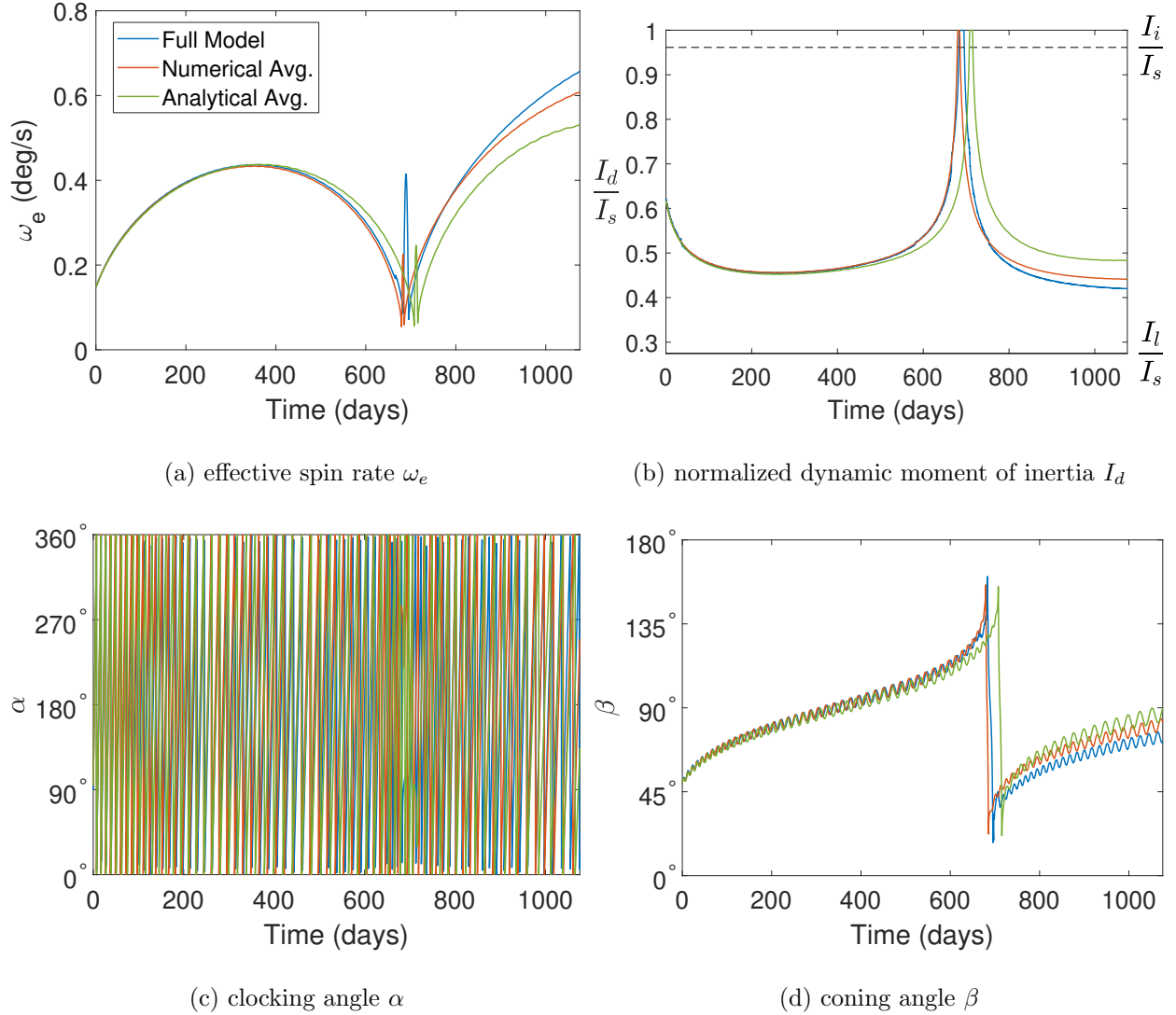
Figure 4.7: Non-resonant analytically averaged model validation ($\alpha_o = 95°$, $\beta_o = 50°$, $I_d/I_s = 0.62$, $2\pi/\omega_e = 40$ min)

4.5 Resonance Averaged YORP

With the resonance-averaged model outlined, we will now validate it against the full dynamics model in the vicinity of the $P_\psi/P_{\bar\phi} = 1$ LAM resonance observed in full dynamics simulations. For the resonance-averaged model, lookup tables are generated for $\ddot{\bar\gamma}$, $\overline{M_x}$, $\overline{M_y}$, and $\overline{M_z}$ over the (γ, β) phase space with $1° \times 1°$ grid spacing. Figure 4.8 shows the full and averaged model evolution over

30 days for the following initial conditions: $\alpha_o = 0°$, $\beta_o = 45°$, $\gamma_o = 300°$, and $P_e = 2\pi/\omega_e = 20$ min ($\omega_e = 0.3$ deg/s). For the full model results in Figure 4.8, γ is calculated directly from $\gamma = n\phi - m\tau_r$. The angle ϕ is obtained by equating Eq. 2.5 expressed in terms of quaternions and Euler angles. On the other hand, τ_r is obtained from the instantaneous angular velocity $\boldsymbol{\omega}$ using the approach outlined by Scheeres [101]. Consulting Figure 4.8, we see that the averaged model evolution closely follows the full dynamics, particularly in terms of ω_e and β. Nevertheless, given the averaging assumptions, most prominently that the solar torques being are a small perturbation on the torque-free rotation and only considering the $\tau_{r_o} = 0$ trajectory when averaging, the models do begin to separate over time with α and γ diverging most rapidly. The simulation run time for the full dynamics model was $\sim$27 s compared to $\sim$1 s for resonance-averaged model. For parity, both models were propagated with MATLAB's ode113 numerical integrator using 1e-10 absolute and relative tolerances.

For more comprehensive validation, we now compare the aggregate evolution of both models over the (β, γ) phase space. In non-resonant motion, γ circulates rapidly. So upon encountering a resonance, γ can be thought of as random. To succinctly compare the full and resonance-averaged models, we investigate the probability of capture for a given β over all possible γ values. The satellite essentially escapes a resonance when γ changes from libration to circulation. Following this approach, we define escape when $|\gamma(t) - \gamma_o| > 6n\pi$ (i.e., 3 circulation cycles). A cutoff of 3 cycles is used rather than 1 or 2 to ensure that escape has occurred. To determine escape for the full model, the full dynamics are propagated alongside Eq. 4.17 using the expressions for $\ddot{\varphi}$ and $\ddot{\tau}_r$ provided in Appendix B with $\dot{H}$ and $\dot{I}_d$ obtained from Eqs. 4.5 and 4.6.

(a) Effective spin rate ω_e

(b) Resonance Angle γ

(c) "Clocking" angle α

(d) "Coning" angle β
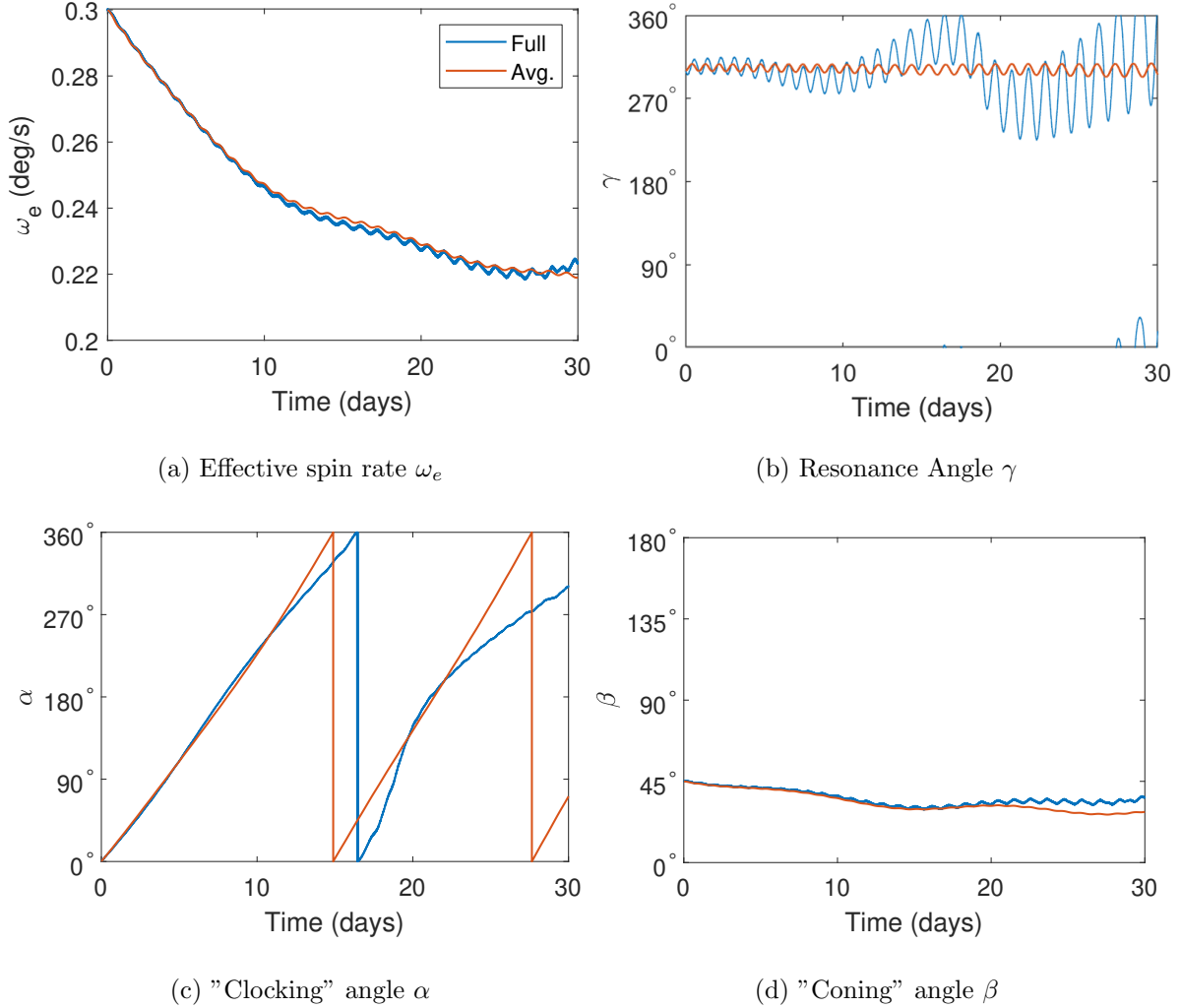
Figure 4.8: Comparison of full and resonance-averaged model evolution for GOES 8 ($P_\psi/P_{\bar\phi} = 1$ LAM+)

Again considering the $P_\psi/P_{\bar\phi} = 1$ resonance, we propagate the full and resonance-averaged dynamics models for 10 days, sampling γ_o and β_o on a $2° \times 2°$ grid assuming the same α_o and P_e as for the run above. The mean run time for the $\sim$16000 runs was $\sim$19 s/run for the full model compared to $\sim$1 s/run for the averaged model. Figure 4.9a shows the (β_o, γ_o) pairs where the satellite was either captured for ≥ 10 days or escaped prior to this. The full and averaged model results agree well, with no capture for β near $0°$ or $180°$ and for the horizontal strip around $\gamma \approx 160°$. For the averaged model, the capture area is somewhat larger than for the full model.

Taking the mean over all γ_o values for each β_o, Figure 4.9b summarizes the capture probabilities for both models. Here, the lower capture probabilities for the full model are clear to see, particularly around $\beta_o = 90°$. The increased escape rate for the full model can be attributed to short period variations in the dynamics which are often de-stabilizing. These variations are removed through averaging and are therefore not present in the averaged model, resulting in higher capture rates.

(a) capture contours (white denotes escape)

(b) capture probability (over all γ_o)
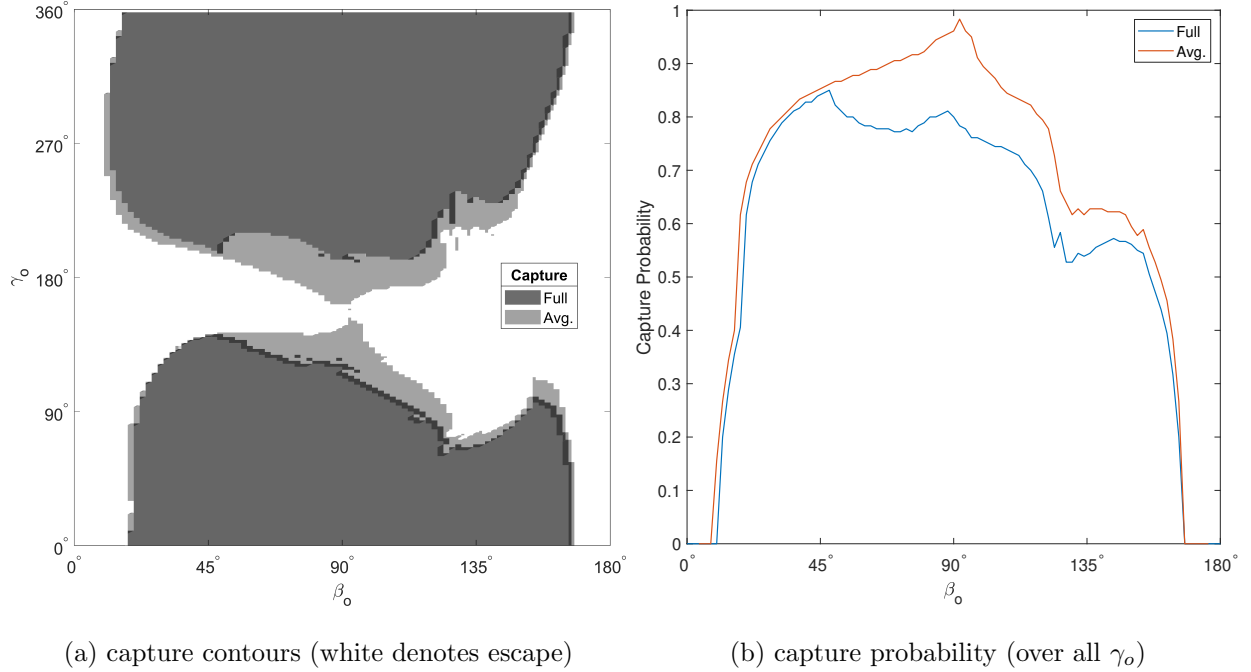
Figure 4.9: Full and averaged model probability of capture in $P_\psi/P_{\bar{\phi}} = 1$ (LAM+) resonance for ≥ 10 days

For further validation of the averaged model, we compare the spin states after 10 days or at the time of escape, whichever occurred first. Figure 4.10 shows the distributions of the final ω_e and $\Delta\beta$ for both models. The distributions for the full and averaged models are very similar. At extreme β_o values, resonant escape occurs rapidly and there is little time for the states to change. So ω_e and β differ insignificantly from their initial values. For intermediate β_o values on the other hand, there are significant spin state changes over this ≤ 10 day span. For the initial ω_e of 0.3 deg/s, we see more than a 50% decrease for some cases. Similarly, β changes by as much as $\pm 45°$. These

results illustrate that temporary resonance capture may yield significant spin state evolution over a relatively short period of time.

(a) Full ω_e

(b) Average ω_e

(c) Full $\Delta\beta$

(d) Average $\Delta\beta$

Figure 4.10: Full and average model spin state distributions after 10 days or at time of escape, whichever occurred first. ($P_\psi/P_{\bar{\phi}} = 1$ LAM+)

4.6   Non-Resonant Gravity Gradient Torque

The aim of this section is to analytically average the gravity gradient torque given by Eq. 2.41. Gravity gradient torques did not significantly affect resonant YORP-driven dynamics in GOES full model simulations. So only the non-resonant tumbling case will be considered.

Rotation from the $\mathcal{G}$ to $\mathcal{H}$ frame is given by the following,

$$HG = HO \begin{bmatrix} 0 & 0 & 1 \\ 0 & -1 & 0 \\ 1 & 0 & 0 \end{bmatrix} R_3(-\lambda)R_1(-\delta) = \begin{bmatrix} b_{x1} & b_{x2} & b_{x3} \\ b_{y1} & b_{y2} & b_{y3} \\ b_{z1} & b_{z2} & b_{z3} \end{bmatrix} \tag{4.31}$$

where λ and δ are the right ascension and inclination of the $\mathcal{G}$ frame with respect to the $\mathcal{O}$ frame. These angles are illustrated in Figure 4.11, where $\hat{\boldsymbol{H}}_G$ is the satellite's earth orbit angular momentum direction.
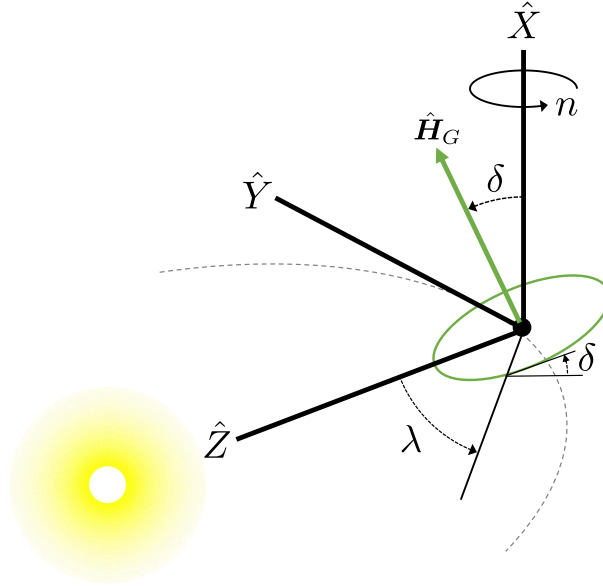
Figure 4.11: Orientation of the satellite's GEO orbit in the $\mathcal{O}$ frame

The angles λ and δ can be related to the traditional right ascension Ω and inclination i of the satellite's earth orbit. With the satellite's GEO orbital angular momentum direction in the $\mathcal{G}$

frame given by,

$$^{\mathcal{G}}\hat{\boldsymbol{H}}_G = [0, 0, 1]^{\mathrm{T}} \tag{4.32}$$

we have,

$$^{\mathcal{N}}\hat{\boldsymbol{H}}_G = NE\,EG\,^{\mathcal{G}}\hat{\boldsymbol{H}}_G \tag{4.33}$$

Then, δ is given by,

$$\cos \delta = \hat{\boldsymbol{n}}_3 \cdot {}^{\mathcal{N}}\hat{\boldsymbol{H}}_G = \cos \delta_e \cos i + \sin \delta_e \cos \Omega \sin i \tag{4.34}$$

Similarly, the ascending node $\boldsymbol{a} = [a_1, a_2, a_3]^{\mathrm{T}}$ of the satellite GEO orbit in the $\mathcal{N}$ frame is,

$$\boldsymbol{a} = \hat{\boldsymbol{n}}_3 \times {}^{\mathcal{N}}\hat{\boldsymbol{H}}_G \tag{4.35}$$

Assuming $\hat{\boldsymbol{Z}}$ and $\hat{\boldsymbol{n}}_1$ are initially aligned (i.e. the sun is along the equinox), the initial right ascension λ_o is,

$$\lambda_o = \mathrm{atan2}(a_2, a_1) \tag{4.36}$$

where $a_1 = \cos \Omega \cos \delta_e \sin i - \cos i \sin \delta_e$ and $a_2 = \sin \Omega \sin i$.

Since the $\mathcal{O}$ frame is rotating, $\lambda(t)$ is time-varying,

$$\lambda(t) = -nt + \lambda_o \tag{4.37}$$

Expressing the earth-satellite unit vector $\hat{\boldsymbol{R}}$ in the $\mathcal{H}$ frame, we simply have,

$$^{\mathcal{H}}\hat{\boldsymbol{R}} = HG\,^{\mathcal{G}}\hat{\boldsymbol{R}} \tag{4.38}$$

Similarly for $[I]$,

$$^{\mathcal{H}}[I] = HB\,^{\mathcal{B}}[I]BH \tag{4.39}$$

We will make the strong assumption that the gravity gradient torque is a small perturbation on the satellite's torque-free motion. We will further assume that the Euler angles ϕ, θ, ψ, and the GEO orbit true anomaly ν vary much faster than α, β, H, and I_d. Finally, assuming that the GEO

orbit period and two fundamental tumbling periods are all non-resonant, we average the gravity gradient torque (Eq. 2.41) over these three independent motions,

$$
{}^{\mathcal{H}}\overline{\boldsymbol{L}}_{gg} = \begin{bmatrix} \overline{L}_x \\ \overline{L}_y \\ \overline{L}_z \end{bmatrix} = 3n_g^2 \frac{1}{2\pi} \frac{1}{4K} \frac{1}{2\pi} \int_0^{2\pi} \int_0^{4K} \int_0^{2\pi} {}^{\mathcal{H}}[\tilde{\hat{\boldsymbol{R}}}]^{\mathcal{H}}[I]^{\mathcal{H}}\hat{\boldsymbol{R}} \, d\phi \, d\tau \, d\nu
$$
(4.40)

and since ${}^{\mathcal{H}}\hat{\boldsymbol{R}}$ is independent of ϕ and τ,

$$
{}^{\mathcal{H}}\overline{\boldsymbol{L}}_{gg} = \frac{3n_g^2}{2\pi} \int_0^{2\pi} {}^{\mathcal{H}}[\tilde{\hat{\boldsymbol{R}}}] \left(\frac{1}{4K} \frac{1}{2\pi} \int_0^{4K} \int_0^{2\pi} {}^{\mathcal{H}}[I] d\phi d\tau \right) {}^{\mathcal{H}}\hat{\boldsymbol{R}} d\nu
$$
(4.41)

or more compactly,

$$
{}^{\mathcal{H}}\overline{\boldsymbol{L}}_{gg} = \frac{3n_g^2}{2\pi} \int_0^{2\pi} {}^{\mathcal{H}}[\tilde{\hat{\boldsymbol{R}}}]^{\mathcal{H}}[\overline{I}]^{\mathcal{H}}\hat{\boldsymbol{R}} d\nu
$$
(4.42)

where the average inertia tensor,

$$
{}^{\mathcal{H}}[\overline{I}] = \frac{1}{4K} \frac{1}{2\pi} \int_0^{4K} \int_0^{2\pi} {}^{\mathcal{H}}[I] d\phi d\tau = \mathrm{diag}(\overline{I_x}, \overline{I_y}, \overline{I_z})
$$
(4.43)

The average inertias are simply given by,

$$
\overline{I_x} = \overline{I_y} = \frac{1}{2}\left[I_i\left(1 - \overline{a_{z1}^2}\right) + I_s\left(1 - \overline{a_{z2}^2}\right) + I_l\left(1 - \overline{a_{z3}^2}\right) \right]
$$
(4.44)

and

$$
\overline{I_z} = I_i\overline{a_{z1}^2} + I_s\overline{a_{z2}^2} + I_l\overline{a_{z3}^2}
$$
(4.45)

Finally, averaging Eq. 4.42 over the GEO orbit true anomaly ν, we find,

$$
\overline{L}_x = \frac{3n_g^2}{2}\left(\overline{I_z} - \overline{I_y}\right)(b_{y1}b_{z1} + b_{y2}b_{z2})
$$
(4.46)

$$
\overline{L}_y = -\frac{3n_g^2}{2}\left(\overline{I_z} - \overline{I_x}\right)(b_{x1}b_{z1} + b_{x2}b_{z2})
$$
(4.47)

$$
\overline{L}_z = -\frac{3n_g^2}{2}\left(\overline{I_x} - \overline{I_y}\right)(b_{x1}b_{y1} + b_{x2}b_{y2}) = 0
$$
(4.48)

Since gravity gradient torques are conservative, their net effect on H over the averaged orbit and rotation motions should be zero. So $\overline{L}_z = 0$ in Eq. 4.48 is expected. Similarly, excluding the intermediate calculations for brevity, $\dot{T} = \boldsymbol{L}_{gg} \cdot \boldsymbol{\omega}$ averaged over these motions is also zero.

Figure 4.12 shows a validation case for the non-resonant averaged gravity gradient torques against the full dynamics. Both models are started with $I_d = 3000$ kg·m^2, $P_e = 2\pi/\omega_e = 20$ min assuming a circular earth orbit with $R = 42575$ km. The initial $\mathcal{G}$ frame pole latitude and longitude are set to $45°$ and $180°$ respectively and the averaged model is set to the corresponding average values over the full model short period oscillation ($44.858°$ for latitude). Figure 4.12 shows that the averaged model closely follows the full model. Note that the $\mathcal{G}$ frame pole longitude steadily decreases while its latitude remains constant on average. In general, the gravity gradient torque will cause $\hat{\boldsymbol{H}}$ to precess about $\hat{\boldsymbol{H}}_G$. For prograde rotation ($\hat{\boldsymbol{H}} \cdot \hat{\boldsymbol{H}}_G > 0$) precession will be in the clockwise direction around $\hat{\boldsymbol{H}}_G$. For retrograde rotation ($\hat{\boldsymbol{H}} \cdot \hat{\boldsymbol{H}}_G < 0$) precession will instead be counter-clockwise.

(a) $\mathcal{G}$ frame latitude

(b) $\mathcal{G}$ frame longitude
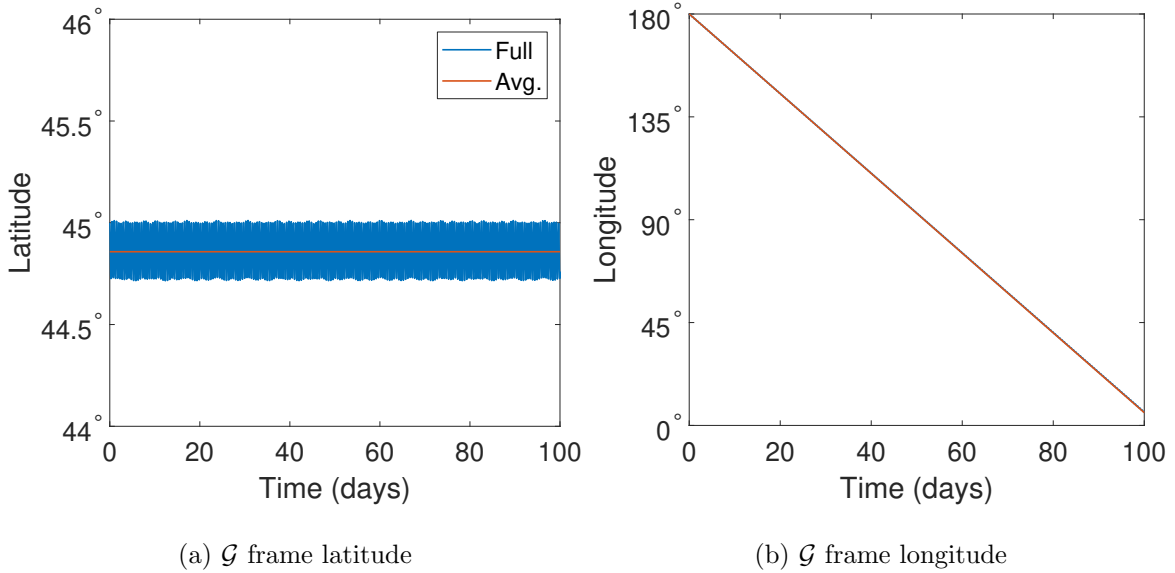
Figure 4.12: GOES 8 Tumbling Averaged Gravity Gradient Validation ($I_d = 3000$ kg·m^2, $P_e = 2\pi/\omega_e = 20$ min)

4.7 Averaged Internal Energy Dissipation

An analytically averaged internal energy dissipation model will now be developed from the full spherical slug model given by Eqs. 2.39 and 2.40. Figure 4.13 shows a simulation of the full spherical slug model for GOES 8. The initial simulation parameters are $\boldsymbol{\omega} = [0,\ 0.971,\ 0.985]^{\mathrm{T}}$ deg/s (corresponding to $I_d = 3000$ kg·m^2 and $P_e = 5$ min) and $\boldsymbol{\sigma} = [0,\ 0,\ 0]^{\mathrm{T}}$ with dissipation parameters $J = 10$ kg·m^2, and $\mu/J = $ 1e-4 s^{-1}. Figure 4.13a shows that $\boldsymbol{\sigma}$ converges to steady state behavior within 100 long axis rotation periods. This convergence was observed for a wide array of initial spin states with 1e-5 s$^{-1} < \mu/J < 1$ s^{-1} . Larger μ/J values generally resulted in faster convergence to steady state. Figure 4.13b shows that for the given dissipation parameters, $\boldsymbol{\sigma} \approx [A]\boldsymbol{\omega}$ in steady state where $[A] = \mathrm{diag}(a,b,c)$ and a,b,c are specific constants that depend on I_d, ω_e, $[I]$, μ, and J. For the GOES satellites with P_e on the order of 5-20 min, $\boldsymbol{\sigma} \approx [A]\boldsymbol{\omega}$ in steady state was observed for $\mu/J < \sim$1e-3 s^{-1}. For larger μ/J values, the steady state $\boldsymbol{\sigma}$ moved progressively out of phase with $\boldsymbol{\omega}$ while retaining the same shape. Also, $\boldsymbol{\omega}$ in Figure 4.13b closely follows the torque-free solutions. This was observed for a wide range of spin states and dissipation parameters because, in these cases, $\mu\boldsymbol{\sigma}$ is much smaller in magnitude than $[\tilde{\boldsymbol{\omega}}][I]\boldsymbol{\omega}$ in Eq. 2.39.

(a) $\boldsymbol{\sigma}$

(b) $\boldsymbol{\sigma}$ and $\boldsymbol{\sigma} \approx [A]\boldsymbol{\omega}$
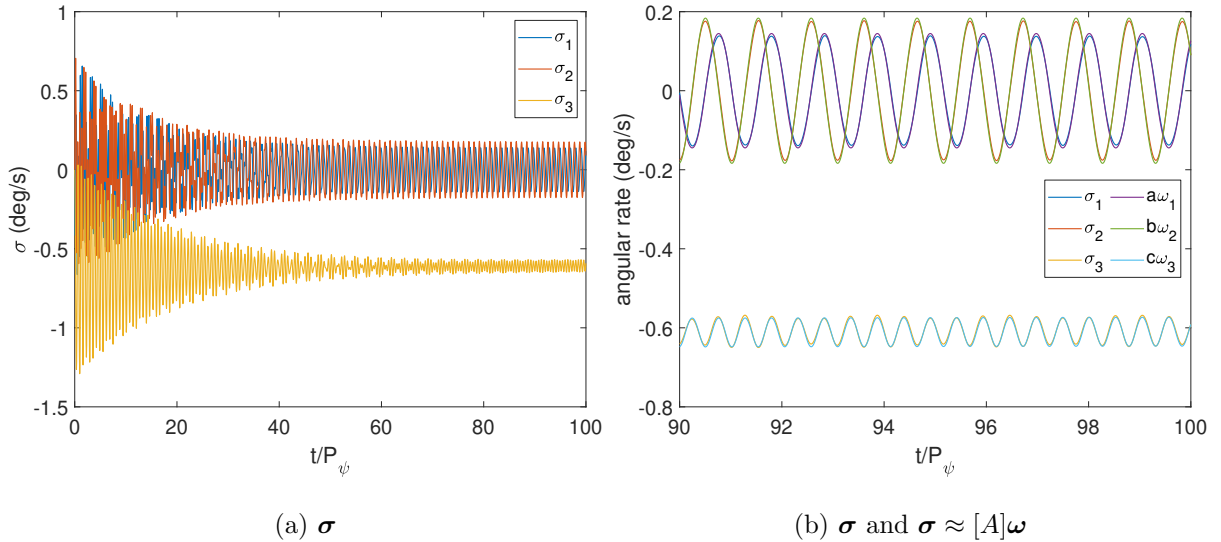
Figure 4.13: GOES 8 steady state $\boldsymbol{\sigma}$ convergence

To facilitate development of the averaged model, μ/J will be limited to smaller values where $\boldsymbol{\sigma} \approx [A]\boldsymbol{\omega}$. With the initial transient $\boldsymbol{\sigma}$ motion damping out, it will reasonably be assumed that $\boldsymbol{\sigma}$ always tracks the instantaneous steady state solution which slowly changes as the system evolves due to dissipation and external torques. Apart from the trivial $\boldsymbol{\omega} = 0$ case, the only time $\boldsymbol{\sigma} \approx [A]\boldsymbol{\omega}$ is consistent with the full dynamics is at the steady state solution. So, assuming $\boldsymbol{\sigma} = [A]\boldsymbol{\omega}$, we aim to find $[A]$ that is most consistent with the full dynamics given by Eqs. 2.39 and 2.40. With these assumptions,

$$\dot{\boldsymbol{\sigma}} = [A]\dot{\boldsymbol{\omega}} \tag{4.49}$$

We would like to investigate the difference between the left and right hand sides of Eq. 4.49,

$$\boldsymbol{D} = \dot{\boldsymbol{\sigma}} - [A]\dot{\boldsymbol{\omega}} \tag{4.50}$$

Assuming torque-free dynamics for the spacecraft (i.e. $\dot{\boldsymbol{\omega}} = -[I]^{-1}[\tilde{\omega}][I]\boldsymbol{\omega}$) and substituting Eq. 2.40 with $\boldsymbol{\sigma} = [A]\boldsymbol{\omega}$,

$$\boldsymbol{D} = ([A] + \mathbb{I})[I]^{-1}[\tilde{\omega}][I]\boldsymbol{\omega} - \left([\tilde{\omega}] + \frac{\mu}{J}\mathbb{I}\right)[A]\boldsymbol{\omega} \tag{4.51}$$

we aim to find $[A]$ that minimizes $\overline{D^2}$, where $\overline{D^2}$ is $D^2 = \boldsymbol{D} \cdot \boldsymbol{D}$ averaged over one $\boldsymbol{\omega}$ cycle in the body frame (i.e., $\tau = [0, 4K]$). We can substitute the torque-free solutions for $\boldsymbol{\omega}$ (provided in Chapter 2) into Eq. 4.51 and analytically average over $\tau = [0, 4K]$. Then taking the derivatives of $\overline{D^2}$ with respect to (a, b, c), we find equations with the following form,

$$\frac{d\overline{D^2}}{da} = t_{11}a + t_{12}b + t_{13}c + t_{14} = 0 \tag{4.52}$$

$$\frac{d\overline{D^2}}{db} = t_{21}a + t_{22}b + t_{23}c + t_{24} = 0 \tag{4.53}$$

$$\frac{d\overline{D^2}}{dc} = t_{31}a + t_{32}b + t_{33}c + +t_{34} = 0 \tag{4.54}$$

where the coefficients t_{ij} are functions of I_l, I_i, I_s, I_d, ω_e, μ, and J (see Appendix C). Solving the linear system of equations yields (a, b, c) approximating the steady state $\boldsymbol{\sigma}$ solution.

The averaged steady state energy dissipation rate is then,

$$\dot{\overline{T}} = -\mu\overline{\sigma^2} = -\mu\overline{\boldsymbol{\omega}^T[A][A]\boldsymbol{\omega}} = -\mu\left(a^2\overline{\omega_1^2} + b^2\overline{\omega_2^2} + c^2\overline{\omega_3^2}\right) \tag{4.55}$$

with the corresponding $\dot{\overline{I}}_d$ (denoted as h_d) given by,

$$h_d = -\frac{2\dot{\overline{T}}}{\overline{\omega}_e^2} \tag{4.56}$$

Note here that $\dot{\overline{T}} \leq 0$, so $h_d \geq 0$. Therefore dissipation can only cause $\overline{I}_d$ to increase.

Figure 4.14a provides an example contour of the averaged spherical slug dissipation rate h_d for GOES 8 with $J = 1$ kg·m^2 and $\mu/J = $ 1e-3 s^{-1}. Figure 4.14b compares the averaged results to the full model steady state dissipation rate. For the full model, MATLAB's fmincon is used to find $[A]$ that best satisfies $\boldsymbol{\sigma}(t) = [A]\boldsymbol{\omega}(t)$ over P_ψ. For the majority of the (ω_e, I_d) space, absolute relative errors for the averaged model are at most several percent and much lower in some cases. Only for slow rotation near the minimum inertia axis do the errors rise to 10's of percent.

(a) h_d vs. ω_e and I_d

(b) Absolute relative error of averaged model h_d
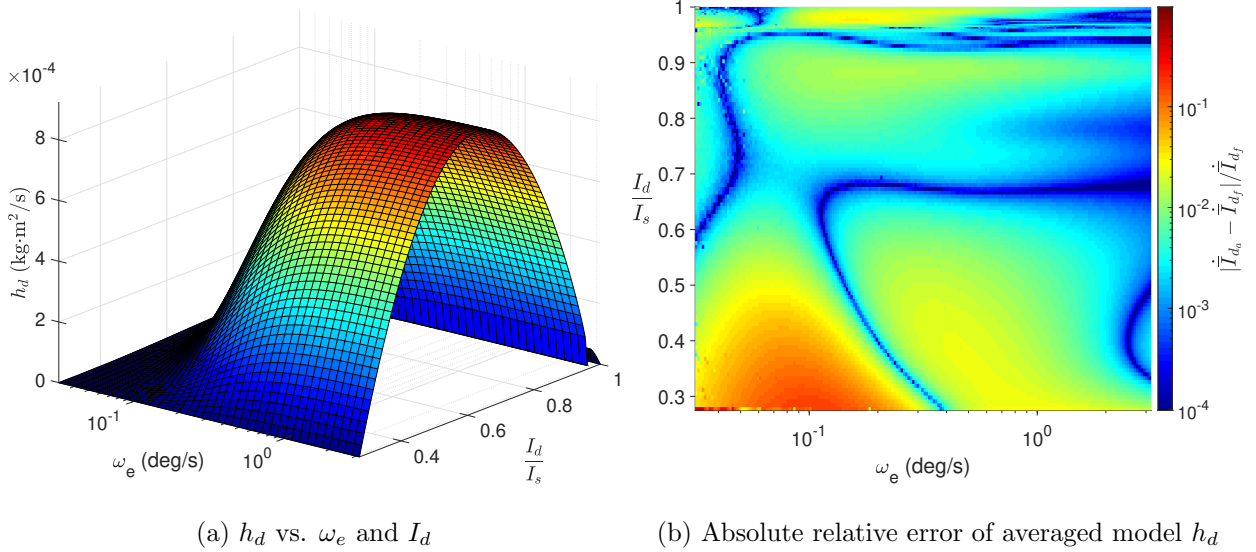
Figure 4.14: GOES 8 averaged spherical slug dissipation model ($J = 1$ kg·m^2, $\mu/J = $ 1e-3 s^{-1})

4.8   Non-Resonant YORP + Dissipation

To validate the averaged YORP + dissipation model, Figure 4.15 shows the full and averaged model evolution over two years for the initial state $I_d/I_s = 0.98$ (SAM-), $P_e = 2\pi/\omega_e = 120$ min, $\alpha = 0°$, $\beta = 15°$, $J = 1.8$ kg·m^2, and $\mu/J = $ 1e-3 s^{-1}. The numerically averaged YORP model is used. In both cases the satellite initially spins up about the long axis into LAM. Dissipation then pushes the satellite back across the separatrix into SAM where all four state variables approach constant values. Overall, the averaged model agrees well with the full model, approaching a very similar asymptotic spin state. Using 1e-12 absolute and relative tolerances, the full model and averaged models required 73 min and 19 s for propagation respectively.

(a) effective spin rate ω_e

(b) normalized dynamic moment of inertia I_d

(c) clocking angle α

(d) coning angle β
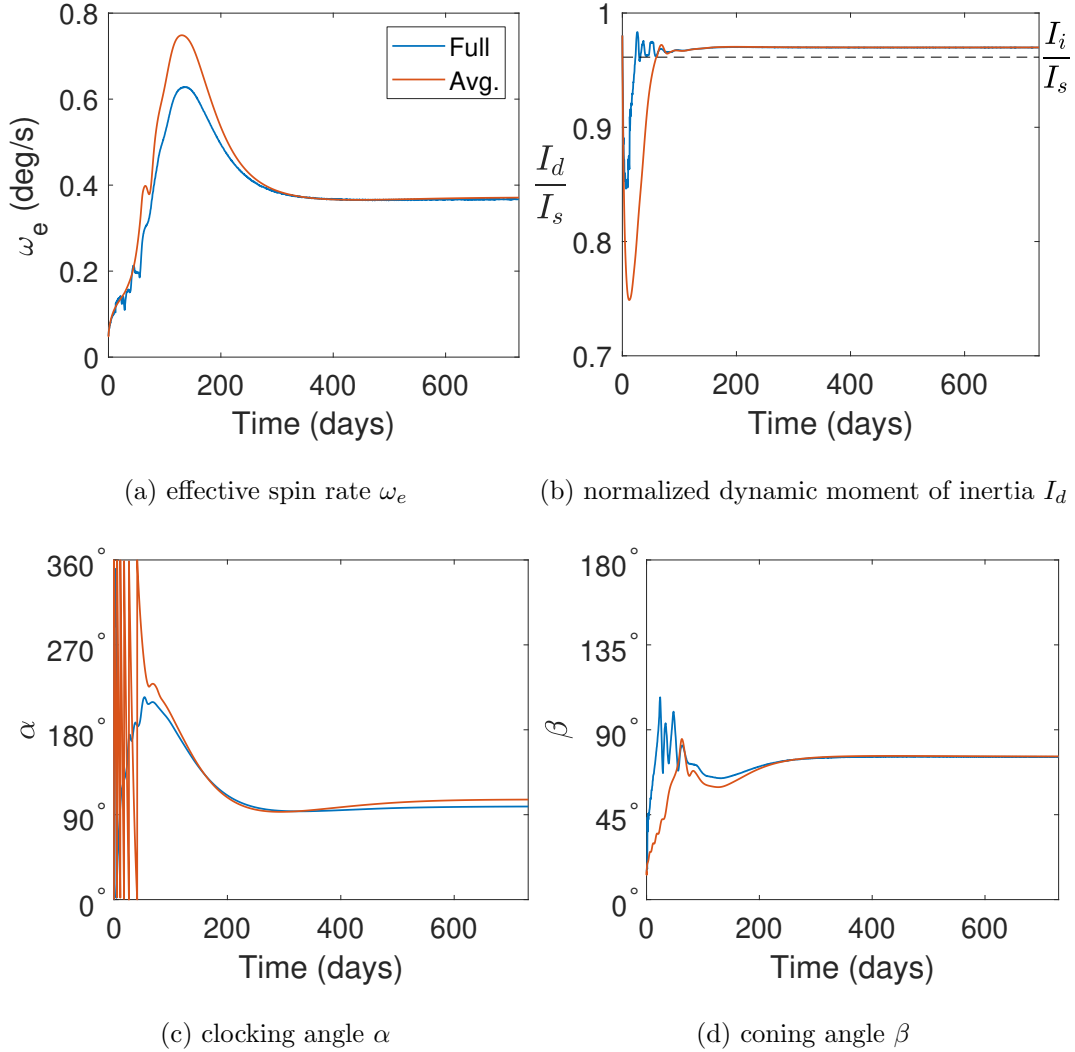
Figure 4.15: GOES 8 averaged YORP and dissipation validation

4.9 Non-Resonant YORP + Dissipation + Gravity Gradients

Figure 4.16 compares full and non-resonant numerically averaged models accounting for YORP, dissipation, and gravity gradients. The initial state is given by $I_d = 3500$ kg·m^2, $P_e = 2\pi/\omega_e = 120$ min, $\alpha = 0°$, $\beta = 15°$, $J = 0.1$ kg·m^2, $\mu/J = $ 1e-3 s^{-1}. Propagation times were 85 min for the full model and 4 s for the averaged model. The average model closely follows the full model for most of the simulation, particularly over the first two tumbling cycles covering roughly 500 days. Figure 4.16c shows that the full model is perturbed by 1:1 and 2:1 resonances throughout the

simulation, particularly around 550 days. The averaged model does not account for these, resulting in divergence towards the end of the simulation. Note that the full model escapes to uniform rotation. Propagating the averaged model further in time (not shown), it temporarily escapes to uniform rotation at 3.6 years, reaching a peak $\omega_e = 3.8$ deg/s before returning to tumbling.

(a) effective spin rate ω_e

(b) normalized dynamic moment of inertia I_d

(c) tumbling period ratio

(d) coning angle β
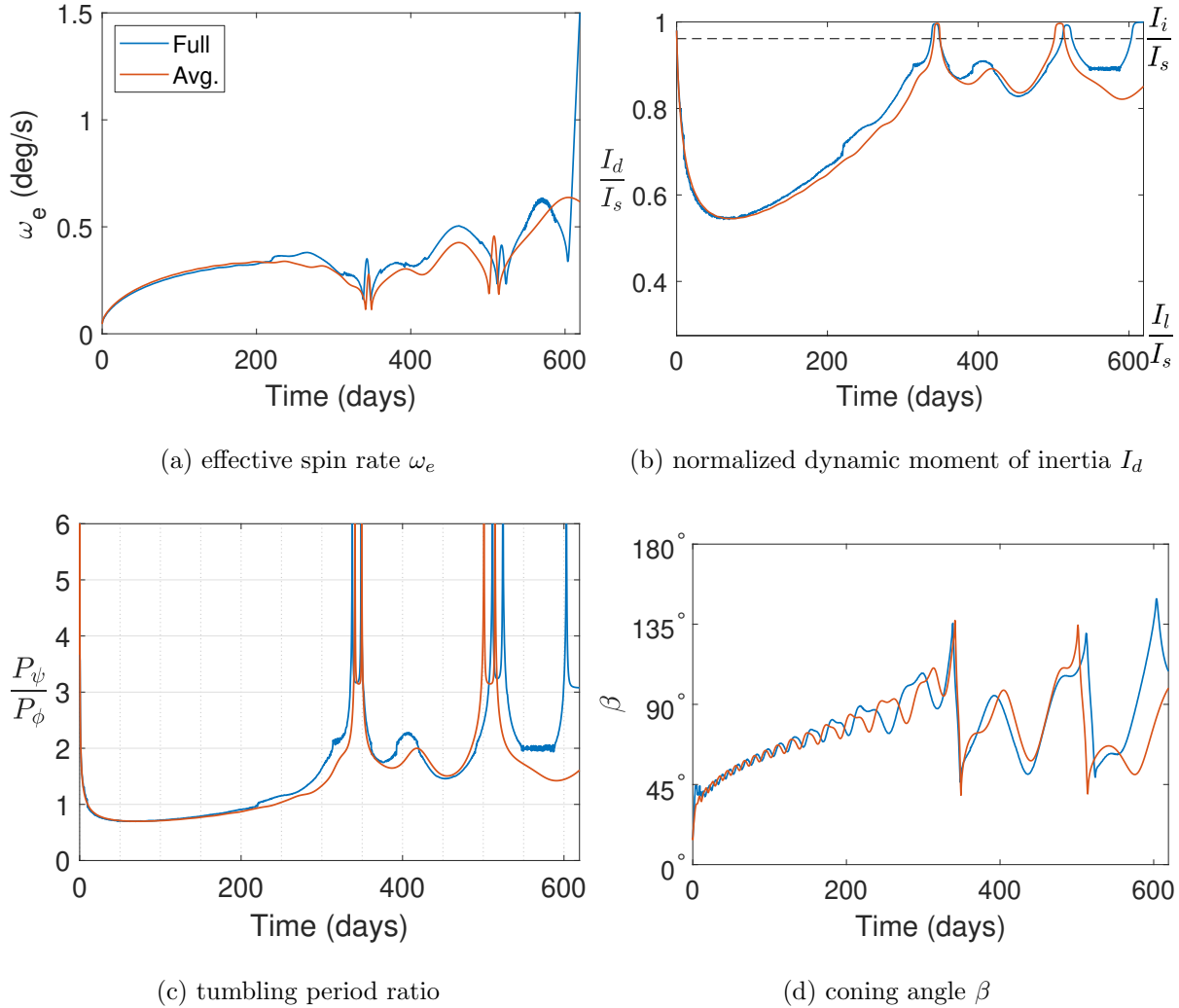
Figure 4.16: GOES 8 full and average YORP + dissipation + gravity gradient comparison ($J = 0.1$ kg·m^2, $\mu/J = $ 1e-3 s^{-1})

Chapter 5

Averaged Dynamics

5.1 Uniform Rotation YORP

We start our exploration of the averaged dynamics for the GOES satellites with uniform rotation YORP. The tumbling-averaged model essentially extends the uniform spin-averaged model explored by Scheeres [100] and Albuja et al. [1, 2] to general tumbling motion. Figure 2.6 illustrates that the fundamental periods are generally incommensurate for uniform rotation. So in the framework of the tumbling-averaged models, uniform rotation is technically non-resonant. Nevertheless, in major axis uniform rotation, the amplitude of the motion associated with P_ψ is zero since $\theta = 90°$ and $\psi = 0°$ or $180°$. Figure 5.1 shows the numerically averaged $\dot{\bar{\omega}}_e = \overline{M_z}/I_s$ for the GOES 8-12 satellites in uniform rotation about the maximum inertia axis. Here $\dot{\bar{\omega}}_e$ is directly comparable to $\dot{\bar{\omega}}_z$ for the Scheeres uniform spin-averaged model where the body frame solar latitude $\delta_s = 90° - \beta$ [100]. For the GOES satellites, $\dot{\bar{\omega}}_e$ changes sign at roughly $90°$. For GOES 8, 9, 10, and 12, ω_e will increase for $\beta < {\sim}90°$ and decrease for $\beta > {\sim}90°$. For GOES 11, the behavior is reversed. Given their different end of life solar array and trim tab angles (see Table 2.1) and slightly different mass properties, the $\dot{\bar{\omega}}_e$ curves differ for each satellite. Of the five, GOES 10 has the smallest overall $\dot{\bar{\omega}}_e$.
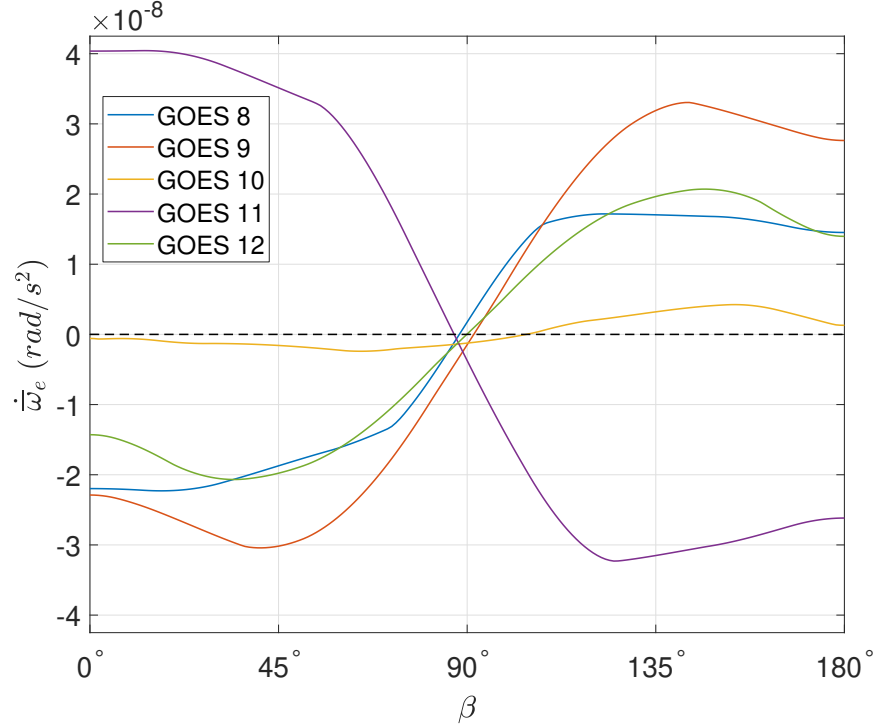
Figure 5.1: $\dot{\bar{\omega}}_e = \overline{M_z}/I_s$ for the GOES 8-12 satellites in major axis uniform rotation about $+\hat{\boldsymbol{b}}_2$

To further illustrate the differences in $\dot{\bar{\omega}}_e$, the numerically averaged uniform spin rate evolution for GOES 8 and 10 are provided in Figure 5.2. Starting with an initial spin period $P_e = 2\pi/\omega_e = 30$ s, 200 runs are conducted with uniformly distributed initial pole directions. Here we assume an initial long axis rotation angle amplitude $\psi_{\max} = 0.01°$ which corresponds to $I_d/I_s \approx 1 - 10^{-9}$. This slight negative offset from uniform rotation prevents I_d from exceeding I_s during propagation due to truncation error. For GOES 8, ω_e evolution varies significantly with some runs spinning down rapidly towards zero while others double or nearly triple the initial spin rate within three years. For GOES 10 on the other hand, the spin rate variation is much lower with no runs reaching zero spin rate after 3 years. Some runs do exhibit secular decrease in spin rate, suggesting eventual spin down to zero for these runs.

(a) GOES 8   (b) GOES 10
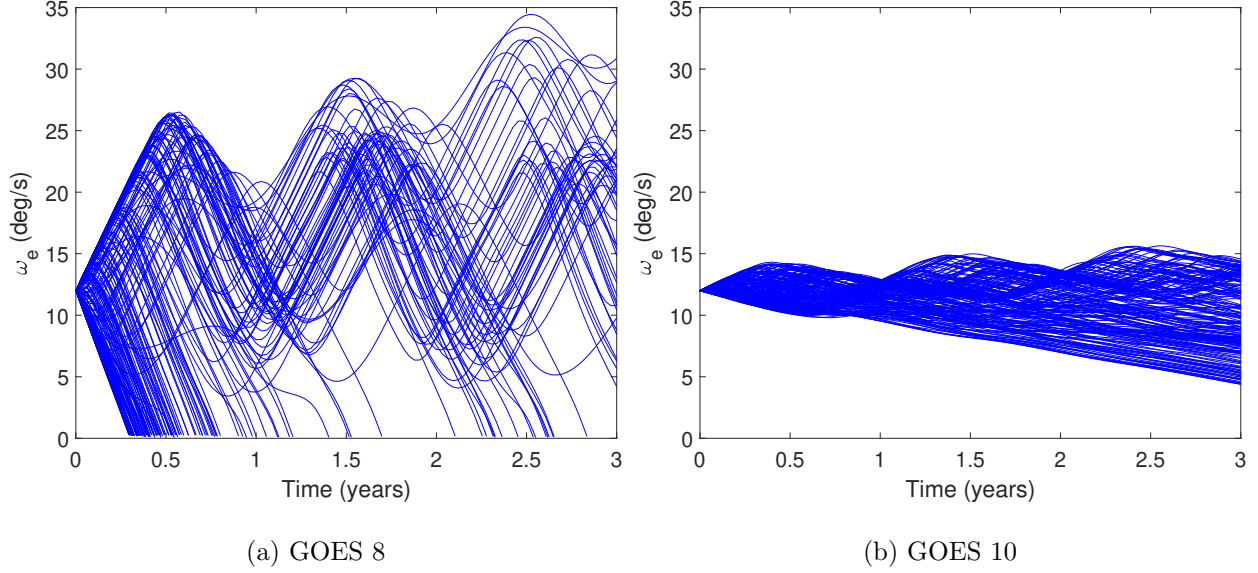
Figure 5.2: Uniform spin rate evolution ($P_e = 30$ s, $\overline{I}_d/I_s \approx 1 - 10^{-9}$, 200 runs each).

5.2   Non-Resonant YORP

5.2.1   Uniform Rotation to Tumbling

Being much faster than the full dynamics model, the tumbling-averaged model readily allows for exploration of the transition from uniform rotation to tumbling. Figure 5.3 shows the six year numerically averaged model evolution for GOES 8 starting in nearly uniform major axis rotation. Here we again assume an initial $P_e = 30$ s and $I_d/I_s \approx 1 - 10^{-9}$. For the first 3.5 years, the satellite remains in uniform rotation and exhibits a roughly one year periodicity in ω_e. This is due to $\overline{M_z}$ and $\dot{\overline{\omega}}_e$ changing sign at $\beta = 90°$ (see Figure 4.5a and Figure 5.4c) as $\boldsymbol{H}$ remains nearly inertially fixed due to the fast spin rate. Defunct satellites including Telstar 401 and retired Glonass satellites exhibit similar yearly spin rate oscillations [34, 86]. During this initial 3.5 year period, there is also a secular decrease in $\overline{\omega}_e$. After roughly 3.5 years, the satellite reaches a maximum P_e of approximately 40 min with $\overline{\beta}$ approaching 0°. At this point, the satellite loses sufficient spin stability and transitions to tumbling. It then spins up about the long axis and progresses into a tumbling cycle with $\boldsymbol{H}$ precessing around the sun line.

(a) Effective Spin Rate

(b) Scaled Dynamic Moment of Inertia

(c) Clocking Angle

(d) Angle between $\boldsymbol{H}$ and $\hat{\boldsymbol{u}}$
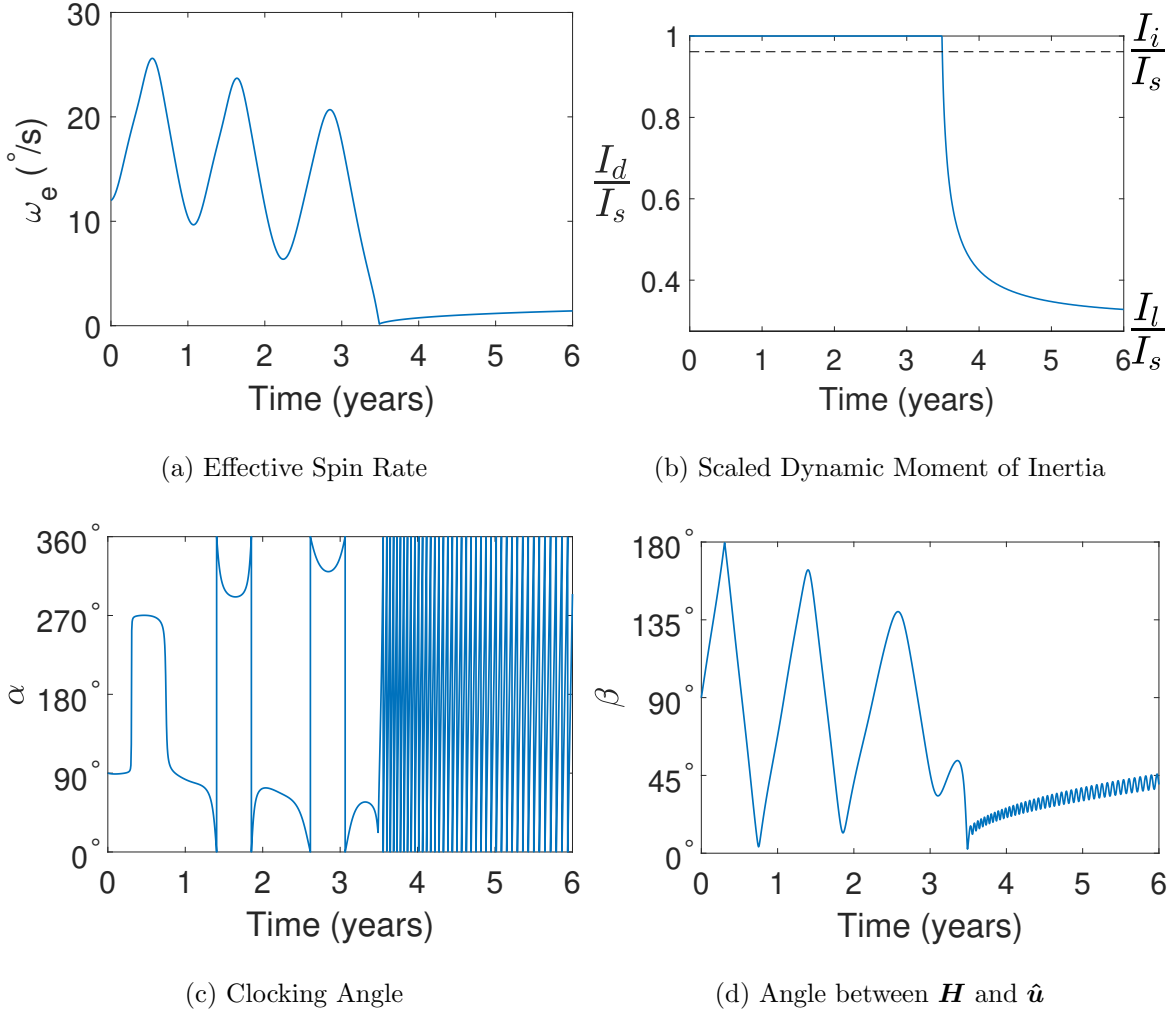
Figure 5.3: Averaged model transition from uniform rotation to tumbling for GOES 8 (initial conditions: $\overline{\alpha} = 90°$, $\overline{\beta} = 90°$, $P_e = 30$ s, $\overline{I}_d/I_s \approx 1 - 10^{-9}$).

5.2.2   Tumbling Cycles

We will now leverage the averaged model to better understand the observed tumbling cycles. Figure 5.4 shows the signs of $\dot{\overline{I}}_d$, $\dot{\overline{\beta}}$, and $\dot{\overline{\omega}}_e$ computed over I_d and β (the sign contours for $\dot{\overline{H}}$ are nearly identical to those for $\dot{\overline{\omega}}_e$). The black regions denote negative values and the white regions denote positive values. To simplify analysis, $\dot{\overline{\beta}}$ (Eq. 4.10) has been averaged over $\overline{\alpha}$ to remove dependency. This is valid because $\overline{\alpha}$ is a fast variable compared to $\overline{I}_d$, $\overline{\beta}$, and $\overline{\omega}_e$ during the

tumbling cycles. Example analytically averaged model evolution has been overlaid in red with an initial $P_e = 2\pi/\overline{\omega}_e = 120$ min. Starting at the green dot, Figure 5.4a shows that $\overline{I}_d$ will initially decrease as the satellite is pushed into more excited tumbling. As we near the separatrix (the dashed grey line), Figure 5.4b shows that β will start increasing. At the same time, the satellite effective spin rate $(\overline{\omega}_e)$ will begin increasing as well. These combined effects cause the satellite to proceed into more excited tumbling with a faster spin rate and the pole moving away from the sun. Once β increases past 90° (i.e. pole perpendicular to the sun) the satellite begins spinning down and moving back towards uniform rotation. Upon crossing the separatrix, the signs of $\dot{\overline{\beta}}$ and $\dot{\overline{\omega}}_e$ flip. So, the satellite then spins up, entering a nearly uniform rotation phase with the pole moving back towards the sun direction. Finally, passing through $\beta = 90°$, $\dot{\overline{I}}_d$ and $\dot{\overline{\omega}}_e$ flip signs resulting in spin down and progression back towards tumbling. At this point, the next tumbling cycle can begin. From Eqs. 4.9, 4.10, and 4.12, we note that the tumbling cycle duration will be driven directly by $\overline{H}$. The larger the initial $\overline{H}$, the slower the satellite will progress through the tumbling cycle. For GOES 8, any escape to long-term uniform rotation from these tumbling cycles will likely occur in the upper right (after passing upward across the separatrix). To escape, the satellite must spin up sufficiently before β decreases below 90°. Alternatively, capture into these tumbling cycles from uniform rotation $(I_d = I_s)$ requires $\beta < 90°$ so that $\dot{\overline{I}}_d$ and $\dot{\overline{\omega}}_e$ are negative. If the spin rate is small enough, $\boldsymbol{H}$ will be pulled towards the sun line and the satellite will spin down and transition into a tumbling cycle.

(a) $\dot{\overline{I}}_d$

(b) $\dot{\overline{\beta}}$

(c) $\dot{\overline{\omega}}_e$
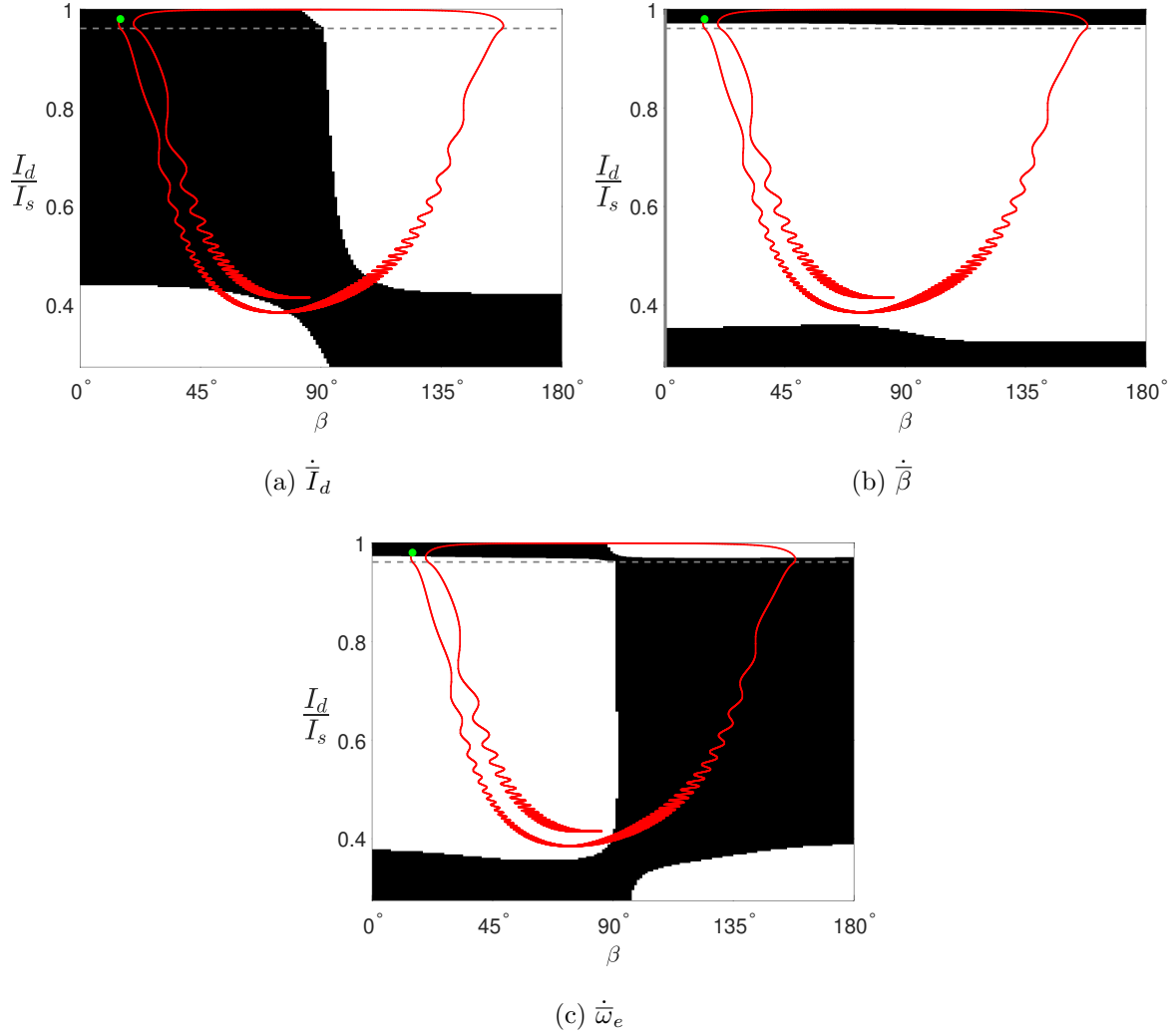
Figure 5.4: Signs of averaged parameter derivatives vs. I_d and β (SAM+/LAM+) for GOES 8 with example averaged evolution overlaid in red, starting at the green dot.

5.2.3 Sun-Tracking Behavior

We will now discuss the sun-tracking precession behavior observed during tumbling cycles. Plotting $\overline{M_y}/\sqrt{\overline{M_x}^2 + \overline{M_y}^2 + \overline{M_z}^2}$ over I_d and β, the resulting values are provided in Figure 5.5a for GOES 8. From the values near $+1$, we see that $\overline{\boldsymbol{M}} \approx \overline{M_y}\hat{\boldsymbol{y}}$ for most LAM I_d, β values. This makes sense given the large relative magnitude of $\overline{M_y}$ compared to $\overline{M_x}$ and $\overline{M_z}$ in Figures 4.5b,d. Calculating $\overline{M_y}$ for a number of LAM I_d values for GOES 8, Figure 5.5b shows that $\overline{M_y} \approx M \sin \beta$

for I_d/I_s values near 0.4 - 0.5 (where M is the arbitrary torque amplitude). From Figure 4.7b, we see that the satellite spends most of the tumbling cycle near $I_d/I_s = 0.45$, where this $M \sin \beta$ approximation agrees best.

(a) $\overline{M_y}/\sqrt{\overline{M_x}^2 + \overline{M_y}^2 + \overline{M_z}^2}$ (b) $\overline{M_y}$ and $M \sin \beta$ Approximation
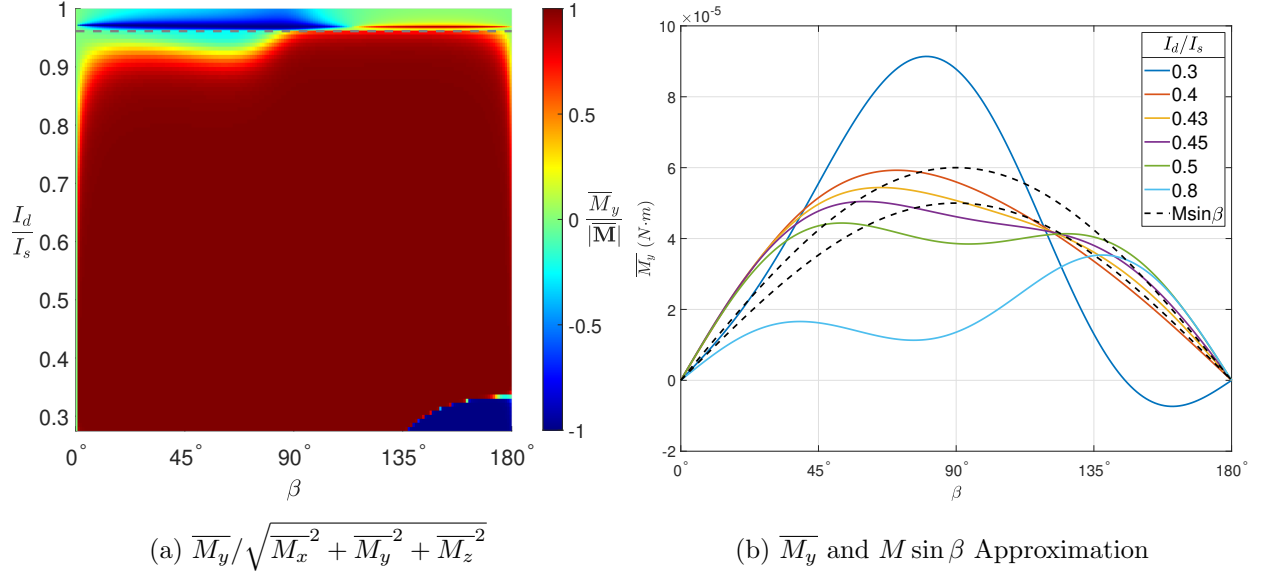
Figure 5.5: Structure of $\overline{M_y}$ for GOES 8 (SAM+/LAM+).

Given this, we can develop an approximate system to better understand sun-tracking precession. Assuming $\overline{M} = \overline{M_y} \hat{y}$, we can calculate $\frac{^{\mathcal{O}}d}{dt}(H)$ using the transport theorem,

$$\frac{^{\mathcal{O}}d}{dt}(H) = \overline{M_y}\hat{y} - \omega_{\mathcal{O}/\mathcal{N}} \times H \tag{5.1}$$

Then assuming $\overline{M_y} = M \sin \beta$ and noting $\sin \beta = |\hat{Z} \times \hat{H}|$, Eq. 5.1 can be written as,

$$\frac{^{\mathcal{O}}d}{dt}(H) = \left(\frac{M}{H}\hat{Z} - n\hat{X} \right) \times H \tag{5.2}$$

Since we assume $M \cdot H = 0$, H is constant. Therefore, Eq. 5.2 is a linear system with constant coefficients. Solving the initial value problem with $H(t=0) = H[\sin \beta_o, 0, \cos \beta_o]^T$,

$$H(t) = \frac{H}{\omega^2} \begin{bmatrix} \delta(n \cos \beta_o + \delta \sin \beta_o) \cos \omega t - n(\delta \cos \beta_o - n \sin \beta_o) \\ \omega(n \cos \beta_o + \delta \sin \beta_o) \sin \omega t \\ n(n \cos \beta_o + \delta \sin \beta_o) \cos \omega t + \delta(\delta \cos \beta_o - n \sin \beta_o) \end{bmatrix} \tag{5.3}$$

where $\delta = M/H$ and $\omega = \sqrt{\delta^2 + n^2}$. Note that $\boldsymbol{H}(t)$ is periodic with period $2\pi/\omega$. Taking the time derivative of Eq. 5.3, we find,

$$\frac{{}^{\mathcal{O}}d}{dt}(\boldsymbol{H}) = H(n\cos\beta_o + \delta\sin\beta_o) \begin{bmatrix} -\frac{\delta}{\omega}\sin\omega t \\ \cos\omega t \\ -\frac{n}{\omega}\sin\omega t \end{bmatrix} \tag{5.4}$$

For $\delta >> n$, $\omega \approx \delta$, so $\dot{H}_Z$ is relatively small and evolution occurs mostly parallel to the the $\hat{\boldsymbol{X}}$ - $\hat{\boldsymbol{Y}}$ plane (i.e. sun-tracking precession). Here, precession occurs much faster than the mean motion n because $\omega >> n$. As δ/n decreases, the precession rate slows and motion transitions more towards the $\hat{\boldsymbol{Y}}$ - $\hat{\boldsymbol{Z}}$ plane. As $\delta/n \to 0$, $\dot{H}_X \to 0$ and motion becomes confined parallel to the $\hat{\boldsymbol{Y}}$ - $\hat{\boldsymbol{Z}}$ plane with $\omega \to n$. Here, the torque is not sufficient to turn $\boldsymbol{H}$ which remains inertially fixed. Figure 5.6 illustrates this transition from sun-tracking precession to inertially fixed $\boldsymbol{H}$ for a number of δ/n values. Proceeding clockwise from lower right to upper left, δ/n decreases and circulation gradually transitions from $\hat{\boldsymbol{Z}}$ to $\hat{\boldsymbol{X}}$.
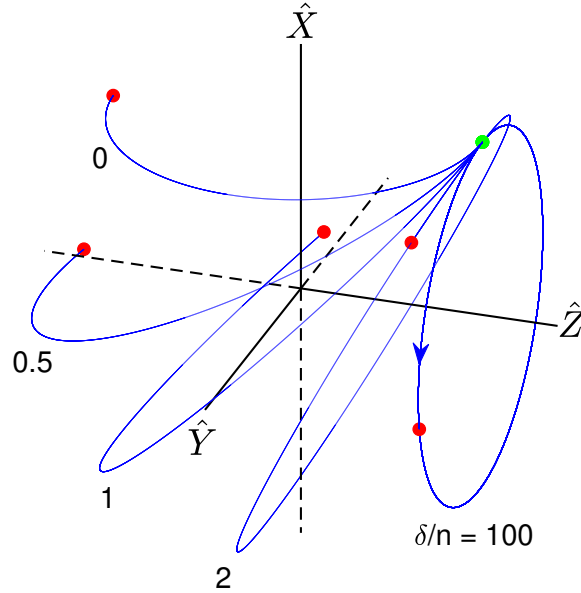
Figure 5.6: $\hat{\boldsymbol{H}}(t)$ from Eq. 5.3 over 180 days with varying δ/n (0, 0.5, 1, 2, 100). The green dot denotes the initial state ($\alpha = 0°$, $\beta = 45°$) and the red dots denote the final states for each δ/n.

5.2.4   Influence of Optical Properties

Given the assumption of instant Lambertian thermal re-emission, there is no distinction in the current model between diffuse reflection and thermal re-emission. So changing the reflectivity of surfaces that are assumed to be strictly diffuse, like the back sides of the solar array and trim tab, will not affect the solar torques. Instead, the amount of specular reflection must be changed. Here we will focus on surfaces assumed to have only specular reflection and thermal re-emission, namely the bus, cell-side of the solar array, trim tab front, and solar sail. The reflectivities of MLI, Kapton, and solar cells can change significantly over time due to space weathering. Figure 5.7 shows the analytically averaged model ω_e evolution for different reflectivities, holding the specular fraction s_i of these surfaces equal to 1. The initial spin state for all cases is given by $I_d = 3500$ kg·m^2, $\alpha = 0°$, $\beta = 15°$, and $P_e = 2\pi/\omega_e = 120$ min. The cases in red correspond to the nominal values from Table 2.2. In all cases, the satellite proceeds through roughly 1.5 tumbling cycles. For the bus, trim tab, and solar solar sail, changing the reflectivity has a negligible impact on evolution over the first tumbling cycle. Proceeding into the second cycle after ∼4 years, there are slight differences in evolution, likely due to increased spin state sensitivity during the brief transition to and from near-uniform rotation. For the solar array on the other hand, the first tumbling cycle duration decreases notably as the reflectivity is increased. Investigating the averaged torque contours, $\overline{M_x}$ is progressively larger for increasing ρ, resulting in faster pole motion and shorter tumbling cycles for the higher reflectivities. Overall, varying the reflectivities of these specular surfaces within reasonable bounds only has a quantitative impact on the dynamical evolution.
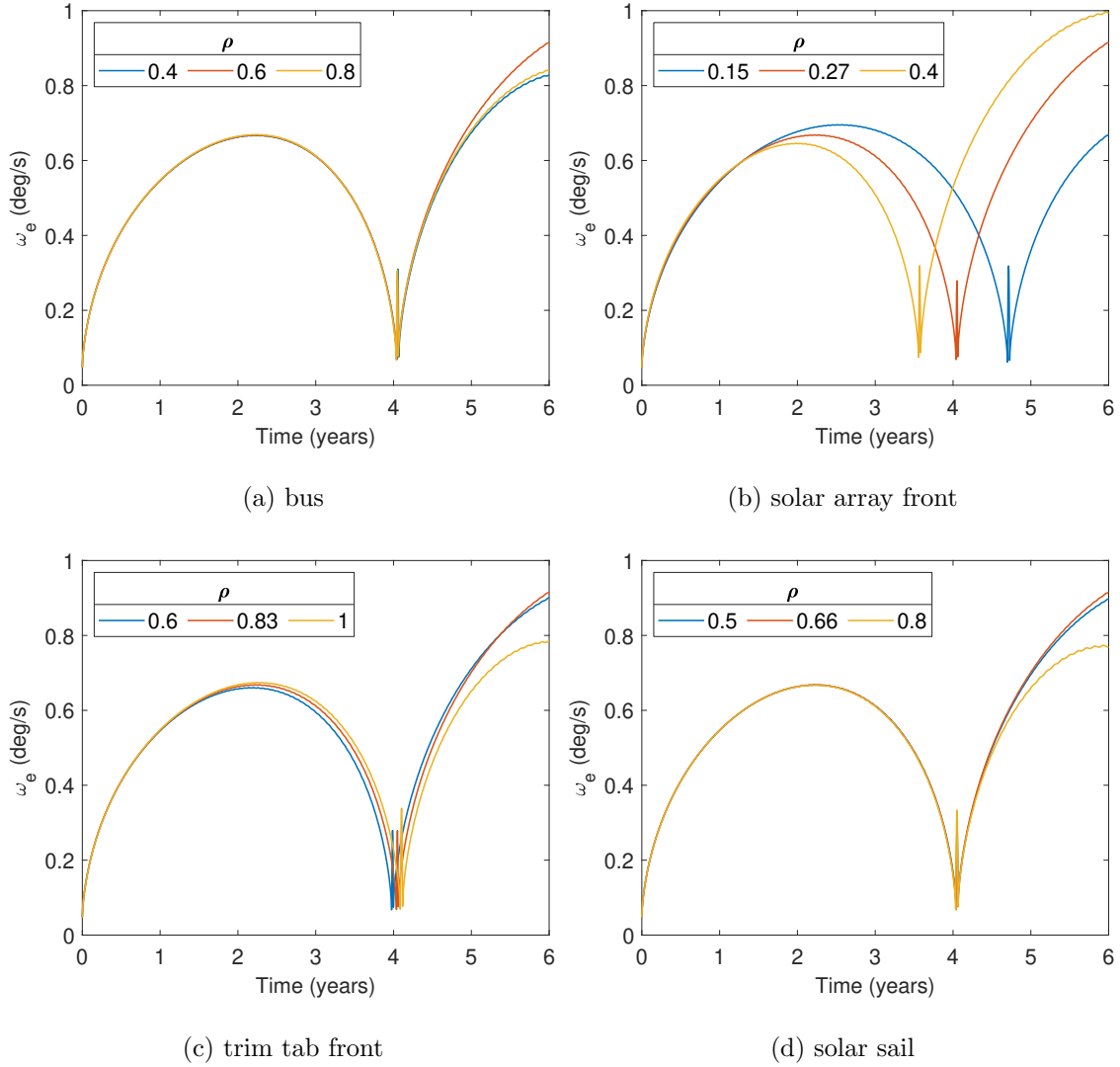
Figure 5.7: GOES 8 evolution dependence on component reflectivity properties

5.2.5 Influence of End of Life Configurations

It is important to note that the counter-clockwise (I_d, β) motion in Figure 5.4 is just one of the possible evolutionary scenarios. Figures 5.1 and 5.2 show that long-term uniform GOES evolution strongly depends on the end of life solar array angle θ_{sa}. Computing $\overline{M_x}$, $\overline{M_y}$, $\overline{M_z}$, and $\dot{\overline{I}}_d$ over all possible end of life GOES 8 solar array angles with the analytically averaged model, we find the following contours in Figure 5.8. For $\dot{\overline{I}}_d$, $\omega_e = 2\pi$ rad/s was again assumed. Sweeping over θ_{sa},

the averaged components change significantly in sign and magnitude, indicating that θ_{sa} greatly affects general long-term satellite evolution. In addition, for θ_{sa} near odd multiples of $42°$, we find that $\overline{M_x}$, $\overline{M_z}$, and $\dot{\overline{I}}_d$ are approximately zero. These critical θ_{sa} values also hold for the major axis uniform rotation contours (not shown). Obviously, these negligible torque configurations are specific to GOES 8's geometry and mass distribution. For other satellites, the averaged framework will allow for fast and efficient studies of the parameter space to identify any similar configurations. These GOES findings illustrate the potential to reduce long-term spin state variation by properly setting end of life configurations.

(a) $\overline{M_x}$

(b) $\overline{M_y}$

(c) $\overline{M_z}$

(d) $\dot{\overline{I}}_d$
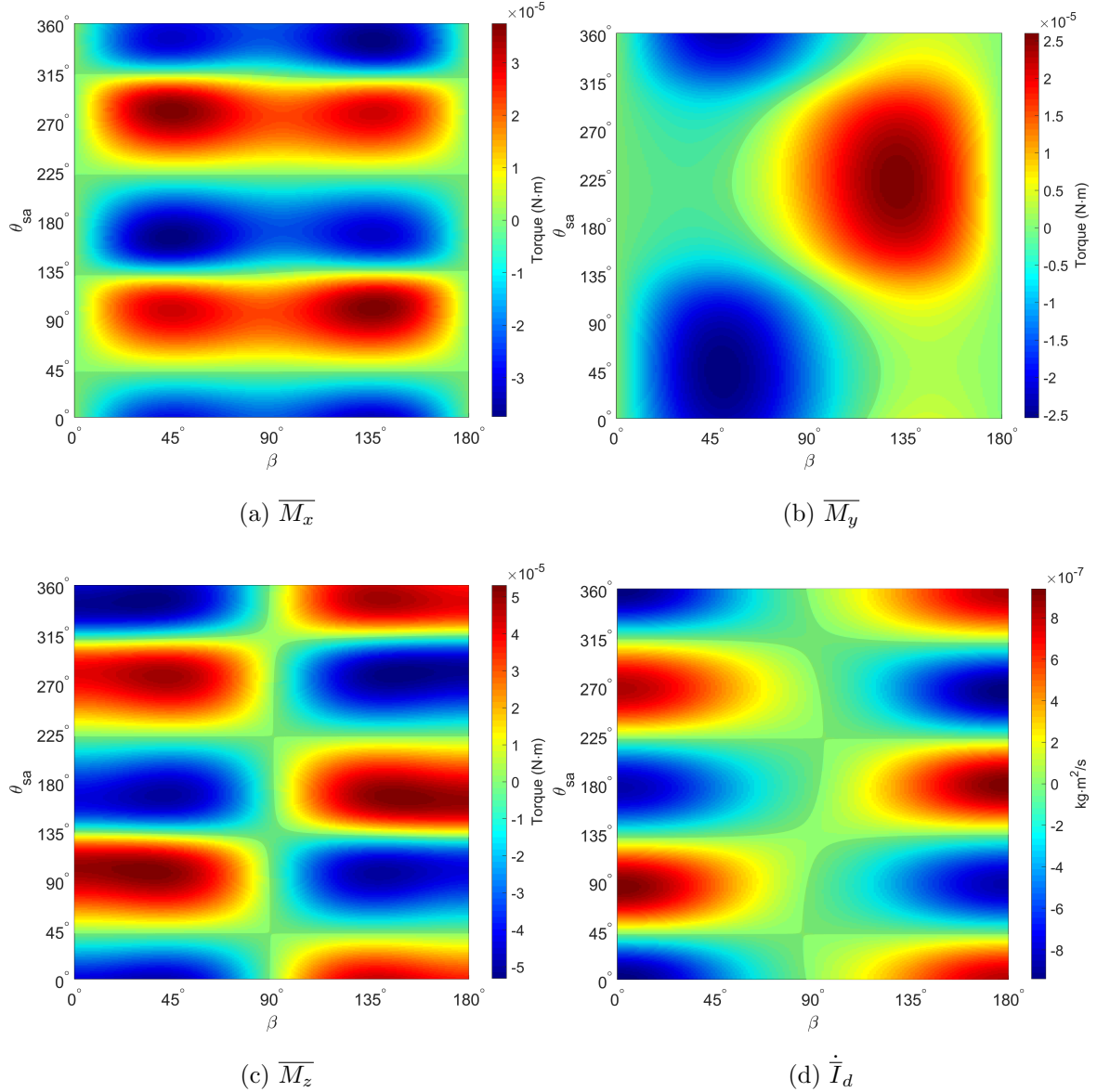
Figure 5.8: GOES 8 Averaged Terms vs. β and Solar Array Angle θ_{sa} (SAM+ $I_d = 3500$ kg·m^2)

We will now briefly consider the long-term evolution for GOES 8 with a different solar array angle. Changing GOES 8's θ_{sa} from 17° to 70° yields the contours in Figure 5.9. Here, the signs of $\dot{\overline{I}}_d$ and $\dot{\overline{\omega}}_e$ are essentially mirrored about $\beta = 90°$ as compared to Figure 5.4. For $\dot{\overline{\beta}}$, the sign is mirrored about the separatrix. Complementing the contours is the six year averaged evolution given by the following initial conditions: $\overline{\alpha} = 0°$, $\overline{\beta} = 165°$, $I_d/I_s = 0.98$ (SAM+), and $P_e =$

240 min. The satellite goes through several tumbling cycles as in Figure 5.4 except that (I_d, β) evolution instead proceeds clockwise with β now decreasing over the course of each tumbling cycle.

(a) $\dot{\overline{I}}_d$

(b) $\dot{\overline{\beta}}$

(c) $\dot{\overline{\omega}}_e$
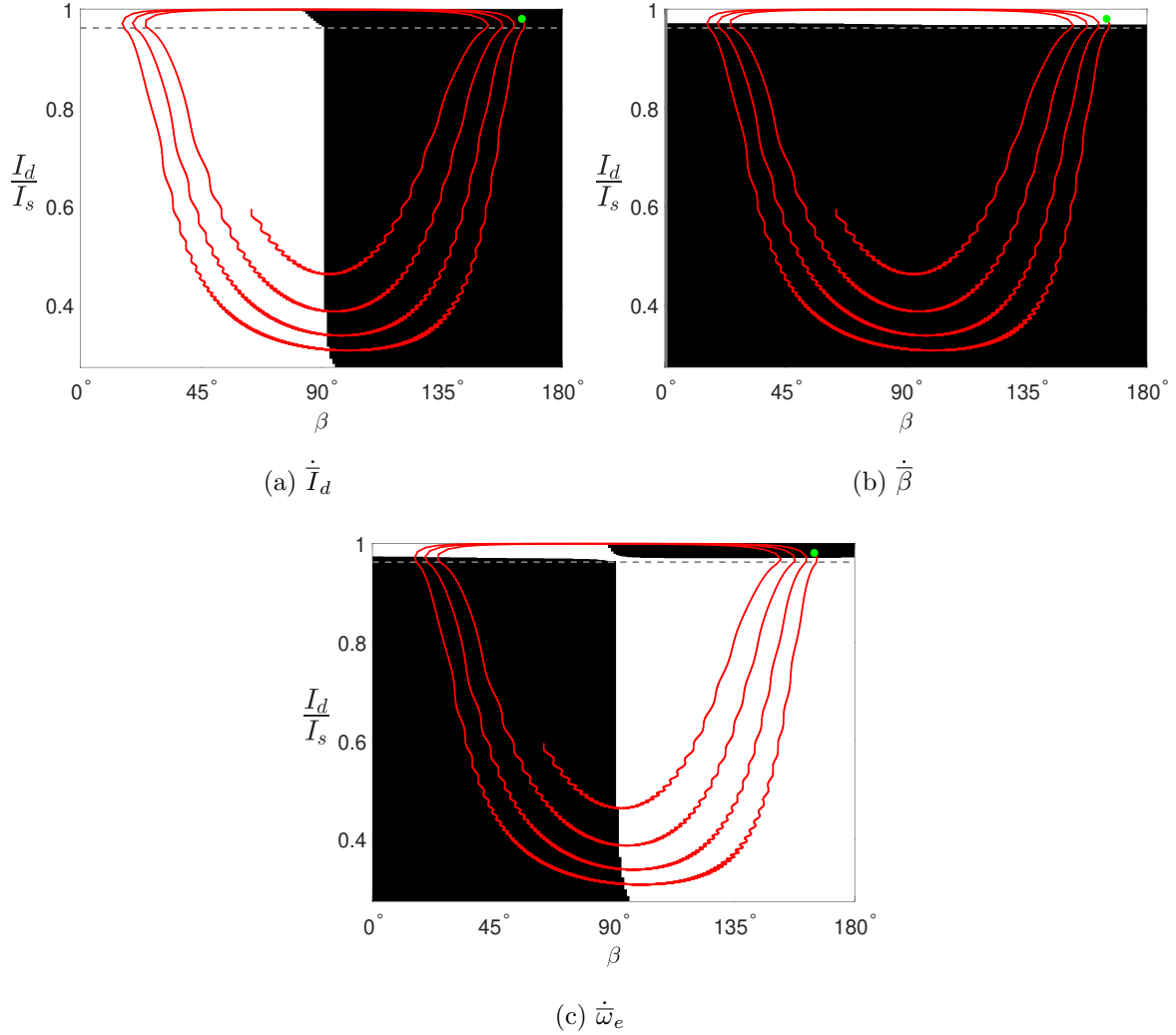
Figure 5.9: Same as Figure 5.4 except with $\theta_{sa} = 70°$ and corresponding averaged evolution.

5.3   Resonant YORP

5.3.1   1:1 LAM Resonance

Figure 5.10 shows the contours of $\ddot{\overline{\gamma}}$, $\overline{M}_x$, $\overline{M}_y$, and $\overline{M}_z$ with example 10 day trajectories overlaid for the $P_\psi/P_{\overline{\phi}} = 1$ LAM resonance. From from left to right, the trajectory initial conditions

are given by: 1) $\beta_o = 10°$, $\gamma_o = 180°$, 2) $\beta_o = 45°$, $\gamma_o = 300°$, 3) $\beta_o = 90°$, $\gamma_o = 250°$, 4) $\beta_o = 130°$, $\gamma_o = 150°$, and 5) $\beta_o = 170°$, $\gamma_o = 180°$ all with $\alpha_o = 0°$ and an initial $P_e = 20$ min. Looking first at $\beta \leq 10°$ and $\geq 170°$, Figure 5.10a shows that $\ddot{\gamma}$ does not change sign in these regions. So at these extreme β values, γ strictly increases or decreases and begins circulating as illustrated by trajectories 1 and 5. This explains why capture was not observed for these β values in Figure 4.9. Moving on to trajectory 2 which shares initial conditions with the Figure 4.8 example, we see that γ instead oscillates about the stable $\bar{\ddot{\gamma}} = 0$ manifold. Since $d\bar{\ddot{\gamma}}/d\gamma < 0$ along this manifold, nearby trajectories will remain close for an extended period and be captured in the resonance. Consulting the contours in Figures 5.10b-d, we see that trajectory 2 will have $\overline{M}_x < 0$, $\overline{M}_y > 0$, and $\overline{M}_z < 0$. With $\overline{M}_x$, $\overline{M}_y$, and $\overline{M}_z$ driving β, α, and ω_e respectively, this explains the initial secular decrease in ω_e and β as well as the increase in α observed in Figure 4.8.

For trajectory 3, the satellite is placed a bit farther from the stable $\bar{\ddot{\gamma}} = 0$ manifold. Nevertheless, it is captured for at least 10 days albeit with larger γ oscillations. Here β slowly increases due to net positive $\overline{M}_x$ over one γ oscillation. Now considering trajectory 4, it is initialized near the unstable $\bar{\ddot{\gamma}} = 0$ manifold where $d\bar{\ddot{\gamma}}/d\gamma > 0$. So γ and $\dot{\gamma}$ steadily increase until reaching the stable manifold near $\gamma = 360°$. At this point, $\dot{\gamma}$ is too large to be sufficiently slowed in the narrower $\bar{\ddot{\gamma}} < 0$ region. As a result, $\dot{\gamma}$ remains positive and γ begins circulating with the satellite escaping from the resonance. Generalizing the trajectory 4 results, the asymmetry between the positive and negative $\ddot{\gamma}$ regions over one γ cycle for moderate β values (i.e. near $45°$ and $135°$) reduces the capture rate. Moving towards $\beta = 90°$, capture will occur for more γ values due to greater symmetry in the $\bar{\ddot{\gamma}}$ regions over one γ cycle. Near $\beta = 90°$, rapid escape only occurs near the unstable $\bar{\ddot{\gamma}} = 0$ manifold (i.e. for $\gamma \approx 160°$). So the $\bar{\ddot{\gamma}}$ asymmetries help explain the convergent-divergent shaped capture contours and centrally-peaked capture probability in Figure 4.9.
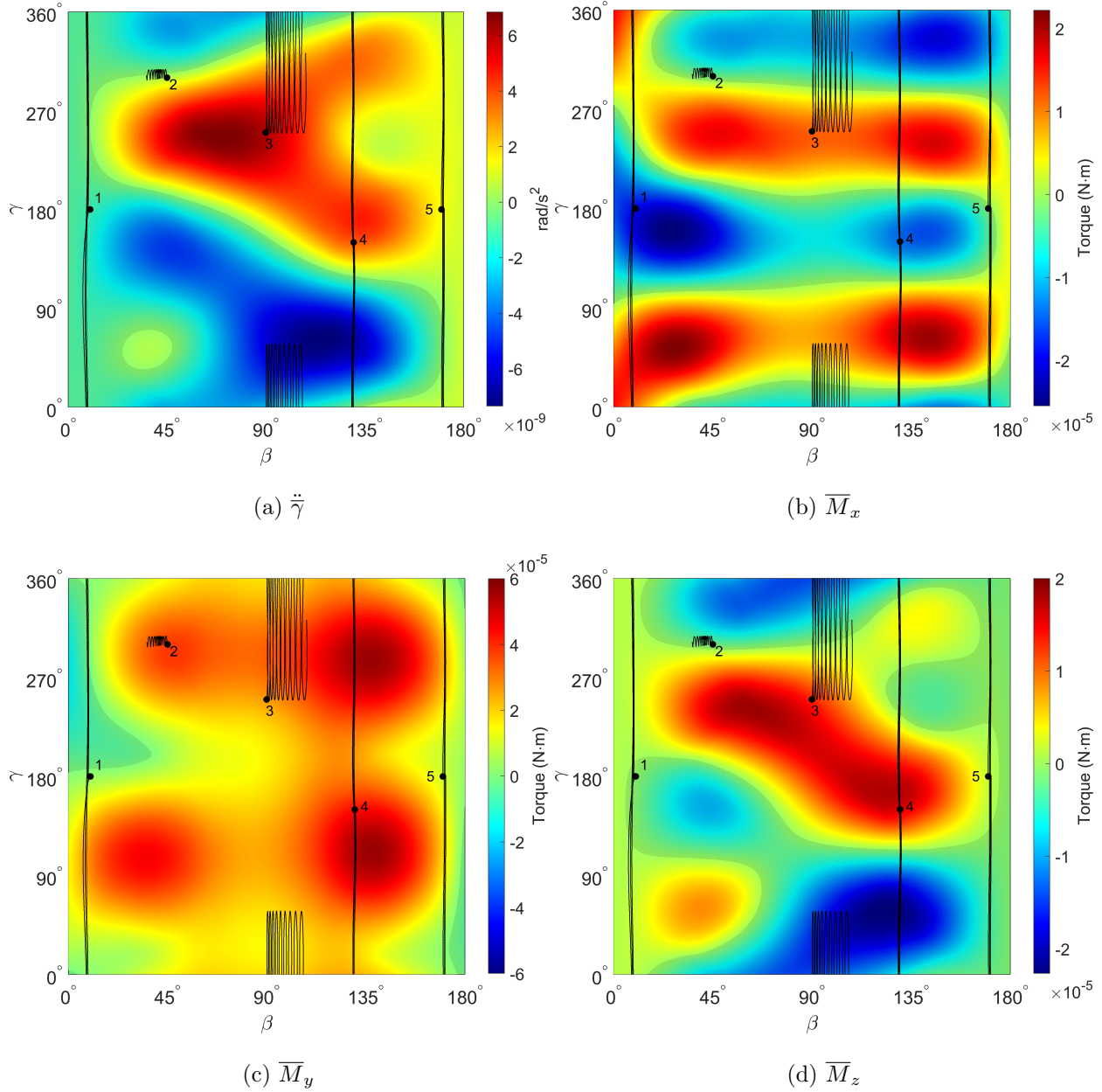
Figure 5.10: GOES 8 $P_\psi/P_{\bar\phi} = 1$ (LAM+) resonance-averaged contours with five overlaid runs.

One fundamental question is how long a satellite will remain captured in a given resonance. Investigating capture duration with the full dynamics over the entire (β, γ) phase space would be computationally expensive. Given that the resonance averaged model provides a speed up of at least $20\times$, it is much better suited to this task. Nevertheless, the larger capture rates for the

averaged model in Figure 4.9 indicate that these capture durations will likely be an upper bound for the full model. Continuing with our exploration of the 1:1 LAM+ resonance, Figure 5.11 shows the capture duration over the (β, γ) phase space for an initial $P_e = 20$ min ($\omega_e = 0.3$ deg/s). This is essentially Figure 4.9a stratified in terms of capture time. Many of the captured trajectories in Figure 5.11 have dwell times longer than 50 days. Note that full model simulation in Figure 3.4 exhibited 1:1 capture for at least 80 days. For the averaged model, we see that the longest capture durations occur along the stable $\ddot{\bar{\gamma}} = 0$ manifold with a maximum of about 283 days near $\beta = 30°$, $\gamma = 300°$. Consulting Figures 5.10a,b this is approximately where the $\ddot{\bar{\gamma}} = 0$ and $\overline{M}_x = 0$ manifolds intersect. So β and γ will evolve slowly in this vicinity and the satellite will remain captured for an extended period of time. Even at the $\ddot{\bar{\gamma}} = \overline{M}_x = 0$ intersection, β will vary due to frame rotation and α circulation (see Eq. 4.10). So one cannot expect indefinite capture. The 1:1 resonance was also investigated for the LAM- case. We found that in general the capture probabilities were slightly higher for LAM+ than LAM-, with maximum capture durations somewhat longer for LAM-.
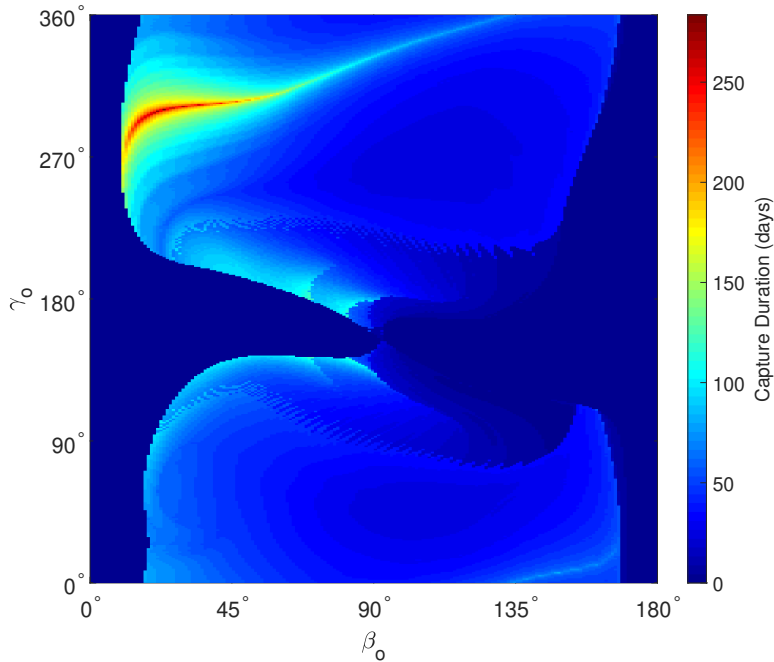
Figure 5.11: GOES 8 capture duration in $P_\psi/P_{\bar{\phi}} = 1$ resonance (LAM+)

Also of interest is how much the satellite spin state changes while captured. Figure 5.12 shows the corresponding states at the time of escape from the 1:1 (LAM+) resonance. For trajectories that are not captured, the final ω_e and β values are essentially unchanged from the initial values. For most captured trajectories, notably the longest duration ones in Figure 5.11, the final ω_e values have gone to zero. In fact, most extended capture duration trajectories were stopped when $\overline{H}$ approached zero rather than when γ began circulating. From Eqs. 4.10 and 4.12, $\dot{\overline{\beta}}$ and $\dot{\overline{I_d}}$ go to infinity as $\overline{H} \to 0$. Rapid $\overline{\beta}$ and $\overline{I_d}$ evolution will likely cause the satellite to escape the resonance. The validity of this reasoning was confirmed by propagating several trajectories with the full model. Holding β_o and γ_o constant while increasing P_e from 20 to 60 and then 120 min, the time until γ began circulating decreased notably. Now considering Figure 5.12b, there is significant local variation in final β values. This is driven in part by the horizontally banded structure in Figure 5.10b, where β evolution will be very sensitive to the γ libration amplitude. A prominent feature in Figure 5.12b is the concentration of high $\Delta\beta$ values on the two mirrored lobes for $\beta_o < 90\,°$. Here escape occurs because β is pushed far enough to the right that γ begins circulating.

(a) Final ω_e (b) $\Delta\beta$
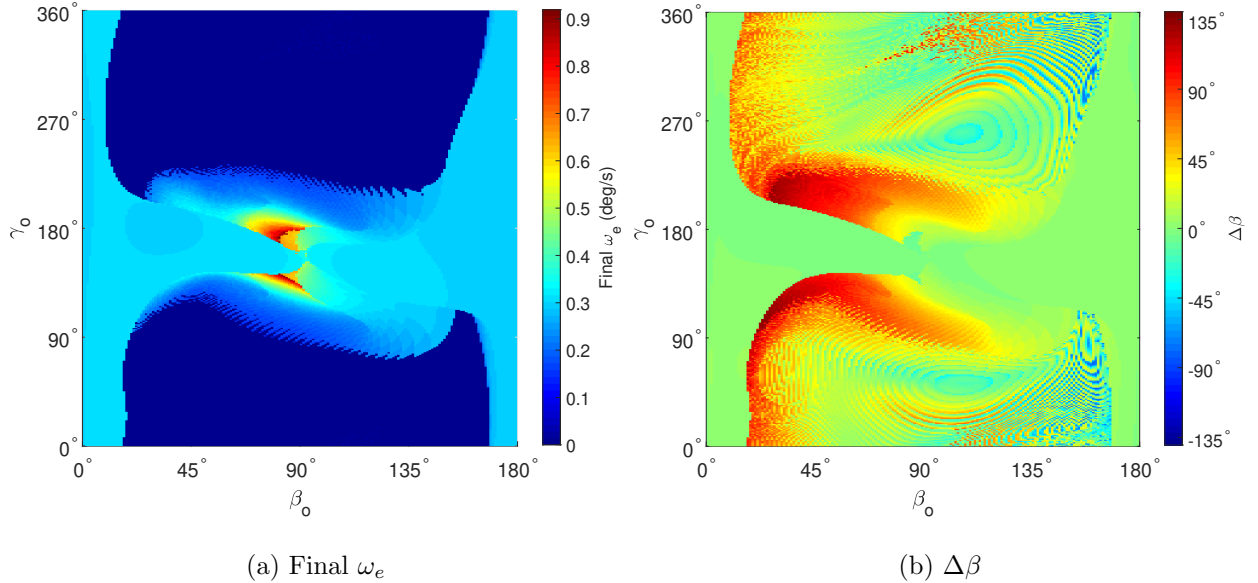
Figure 5.12: GOES 8 states at $P_\psi/P_{\bar{\phi}} = 1$ resonance escape (LAM+)

To explore the dependence of capture probability on spin rate, Figure 5.13 shows the 1:1 LAM+ capture probabilities for increasing effective spin periods. Capture probabilities rise for $\beta < 45°$ as P_e is increased. On the other hand, they steadily decrease with increased P_e for $\beta > 90°$. For $P_e = 60$ min, the large drop in capture probability for β between $70°$ and $160°$ is primarily due to $\overline{H} \to 0$. Obviously, as the initial spin rate is decreased, less time is needed to reach $\overline{H} \approx 0$, and escape via this avenue becomes more likely.
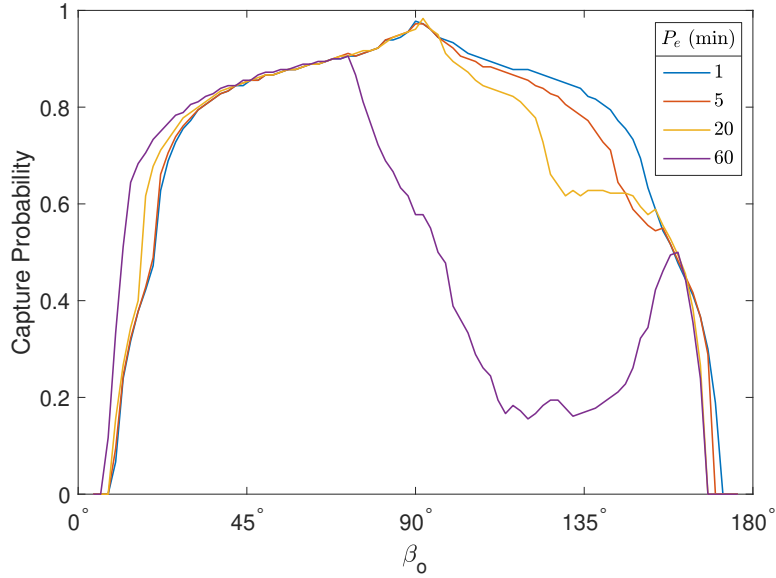
Figure 5.13: GOES 8 capture probability in $P_\psi / P_{\bar{\phi}} = 1$ resonance for ≥ 10 days for different effective spin periods (LAM+).

5.3.2   Higher Order Resonances

We will now investigate higher order LAM resonances with the averaged model, specifically $P_\psi / P_{\bar{\phi}} = 3:2, 2:1, 3:1, 4:1$. Tying these back to the physical motion using the 3:2 resonance as an example, for every 3 precession periods of the long axis $\hat{\boldsymbol{b}}_3$ around $\boldsymbol{H}$, the satellite rotates about $\hat{\boldsymbol{b}}_3$ twice. Recall from Figure 2.6 that these higher order resonances are all possible for GOES 8 LAM states, while only the 4:1 resonance is possible for SAMs. The 4:1 SAM resonance structure was similar to that for the following higher order LAM resonances and has been excluded for brevity.

Figure 5.14 shows the $\ddot{\bar{\gamma}}$ contours for the higher order LAM resonances. The most apparent trait across these contours is that the $\ddot{\bar{\gamma}} = 0$ manifolds span considerably narrower ranges of β compared to the 1:1 resonance contour in Figure 5.10a. This suggests that capture into these resonances will only be possible for smaller fractions of the phase space. Of the four resonances, the 2:1 contour shares the most similarity with the 1:1 resonance in terms of structure.

(a) 3:2

(b) 2:1

(c) 3:1

(d) 4:1
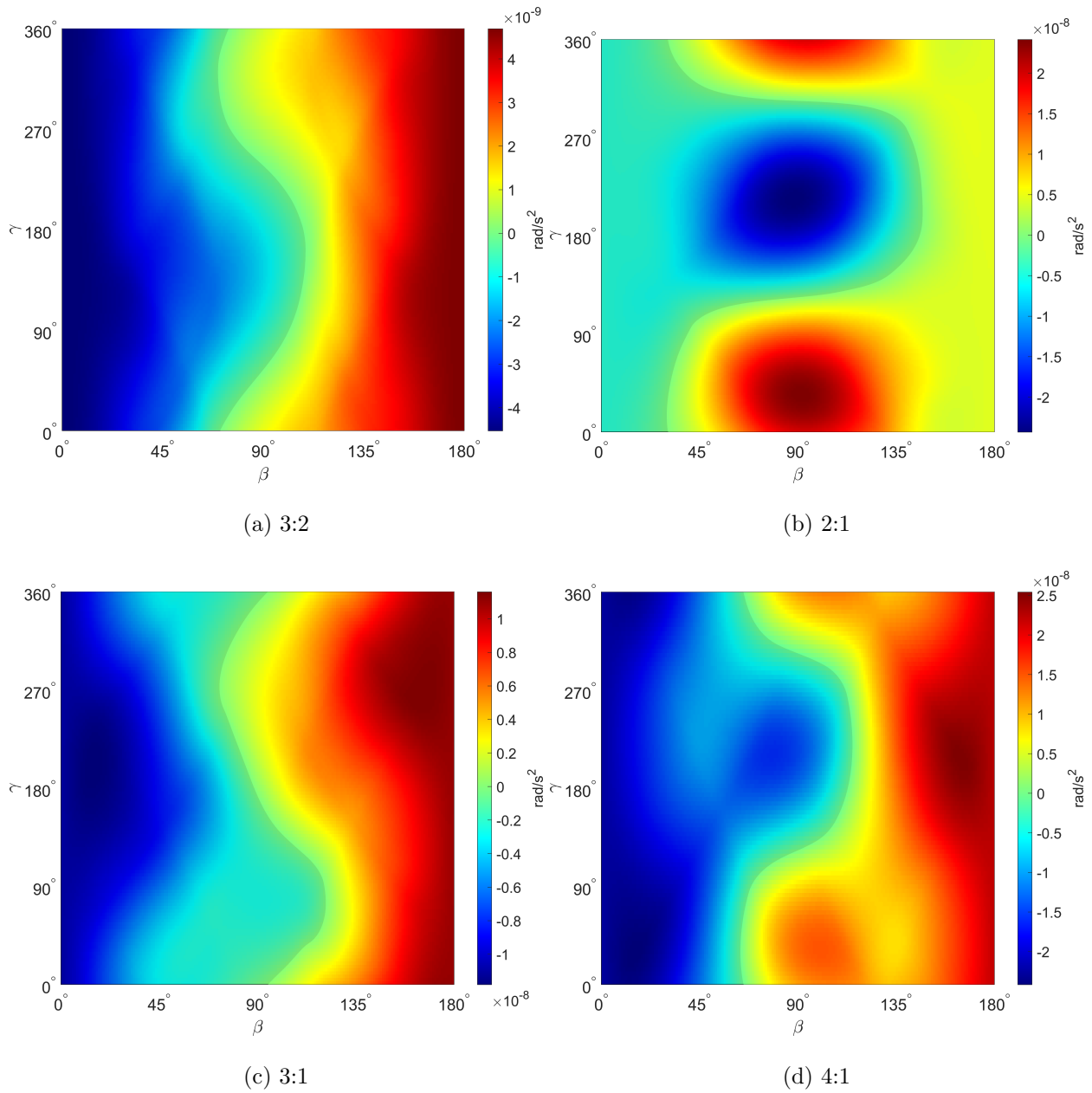
Figure 5.14: GOES 8 $\ddddot{\bar{\gamma}}$ for higher order resonances (LAM+)

Propagating trajectories for these resonances using $2° \times 2°$ grid spacing for β and γ, the resulting 10 day capture probabilities are shown in Figure 5.15. Consistent with the contour discussion above, resonance capture occurs for smaller ranges of β compared to the 1:1 resonance, with probabilities peaking around 90°. Also, the capture probabilities themselves are generally

lower than for the 1:1 resonance. These findings help explain why the 1:1 and 2:1 resonances were observed most frequently in the long-term full YORP dynamics simulations, as they have the highest capture "area" of the resonances shown. It is also worthy to note that for the YORP-driven tumbling cycles observed in Chapter 3 and Figure 5.4 for example, the satellite generally passes through these higher order resonances at extreme values of β where the capture probabilities are negligible. This further explains why they were not encountered frequently in long-term full YORP dynamics simulations.
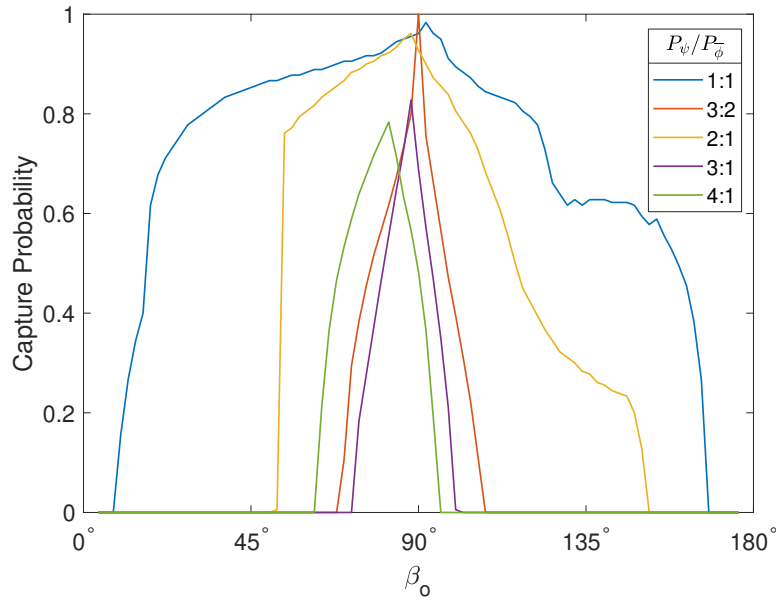
Figure 5.15: GOES 8 probability of capture in various resonances for ≥ 10 days (LAM+)

5.4   Non-Resonant YORP + Gravity Gradients

Full dynamics simulations showed that gravity gradients alone did not significantly affect YORP-only tumbling evolution or resonant capture for the GOES satellites. But, gravity gradients were found to impact long-term uniform spin rate evolution in a non-negligible way. Figure 5.16 shows the uniform spin rate evolution for GOES 10 accounting for averaged solar radiation and gravity gradient torques assuming $\alpha_o = 90°$, $\beta_o = 90°$, $P_e = 30$ s, $R = 42500$ km. Here, the numerically averaged model was used assuming $I_d/I_s \approx 1 - 10^{-9}$. Several different simulations are

included: 1) assuming solar torques only, 2) for GOES 10's orbit in April 2021 with approximate inclination $i = 11°$ and right ascension $\Omega = 33°$, and 3) the classical GEO Laplace plane with $i \approx 7°$ and $\Omega = 0°$ [4]. Due to luni-solar gravitational perturbations, the orbit planes of uncontrolled GEO satellites will oscillate about the classical Laplace plane every $\sim$53 years [4]. Figure 5.16 illustrates that gravity gradient torques can have a non-negligible impact on uniform spin rate evolution over long timescales with dependence on the satellite orbit.
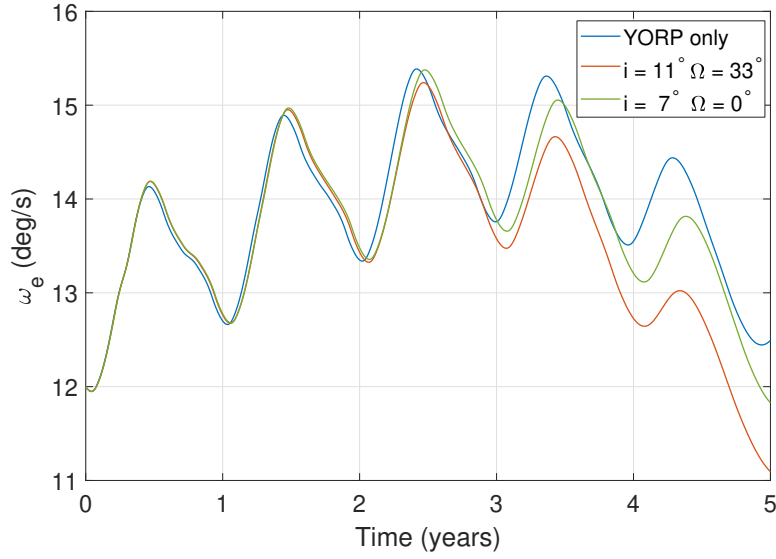
Figure 5.16: GOES 10 averaged uniform spin rate evolution for YORP and gravity gradients

5.5 Non-Resonant YORP + Dissipation

5.5.1 Equilibria

Using the averaged model, we would like to investigate the YORP + dissipation equilibria observed with the full dynamics. The aim is to find $\overline{\alpha}$, $\overline{\beta}$, $\overline{H}$, and $\overline{I_d}$ such that,

$$\dot{\overline{\alpha}} = \frac{\overline{M_y} + \overline{H} n \cos \overline{\alpha} \cos \overline{\beta}}{\overline{H} \sin \overline{\beta}} = 0 \tag{5.5}$$

$$\dot{\overline{\beta}} = \frac{\overline{M_x} + \overline{H} n \sin \overline{\alpha}}{\overline{H}} = 0 \tag{5.6}$$

$$\dot{\overline{H}} = \overline{M_z} = 0 \tag{5.7}$$

$$\dot{\overline{I_d}} = \frac{2\overline{I_d}}{\overline{H}} \overline{\boldsymbol{M} \cdot \left(\mathbb{1}_{3\times3} - I_d[I]^{-1}\right)\hat{\boldsymbol{H}}} + h_d = 0 \tag{5.8}$$

We start by prescribing $\overline{\beta}$ and finding the $\overline{I_d}$ value(s) that satisfy Eq. 5.7. Since $\overline{I_d}$ is bounded, this can be done with the simple bisection method. $\overline{M_x}$ and $\overline{M_y}$ are then calculated for the $(\overline{\beta}, \overline{I_d})$ pair(s). Setting the numerators of Eqs. 5.5 and 5.6 equal to zero and solving for $\sin\overline{\alpha}$ and $\cos\overline{\alpha}$, we obtain $\overline{\alpha}$,

$$\overline{\alpha} = \text{atan2}\left(-\overline{M_x}, -\overline{M_y}/\cos\overline{\beta}\right) \tag{5.9}$$

Note that we can solve for $\overline{\alpha}$ in this way by canceling out $\overline{H}n$ because it equally scales both terms and is positive (i.e. will not change their signs). On the other hand, removing the negative signs in Eq. 5.9 would change the quadrant, yielding an incorrect solution for $\overline{\alpha}$. We can then obtain $\overline{H}$ from Eq. 5.5 or 5.6. Finally, the value of J satisfying Eq. 5.8 is calculated (assuming a prescribed value for μ/J). Again, bisection can be used with a wide initial search range constrained to positive J values. Note that the equilibrium state is essentially solved for in reverse, since J and μ/J actually dictate the equilibrium values for $\overline{\alpha}$, $\overline{\beta}$, $\overline{H}$, and $\overline{I_d}$. Figure 5.17 shows the YORP + dissipation equilibria for GOES 8 computed with this approach, using numerically averaged lookup tables for the solar torque evaluation. These solutions place the satellite on the SAM side of the separatrix, consistent with earlier full and averaged model results. The solutions differ considerably for SAM+ and SAM- states, largely due to differences in the averaged torque components and the sensitivity of $\overline{\alpha}$ solutions in Eq. 5.9 to changes in these components.

(a) effective spin rate ω_e

(b) normalized dynamic moment of inertia I_d

(c) clocking angle α

(d) spherical slug inertia J
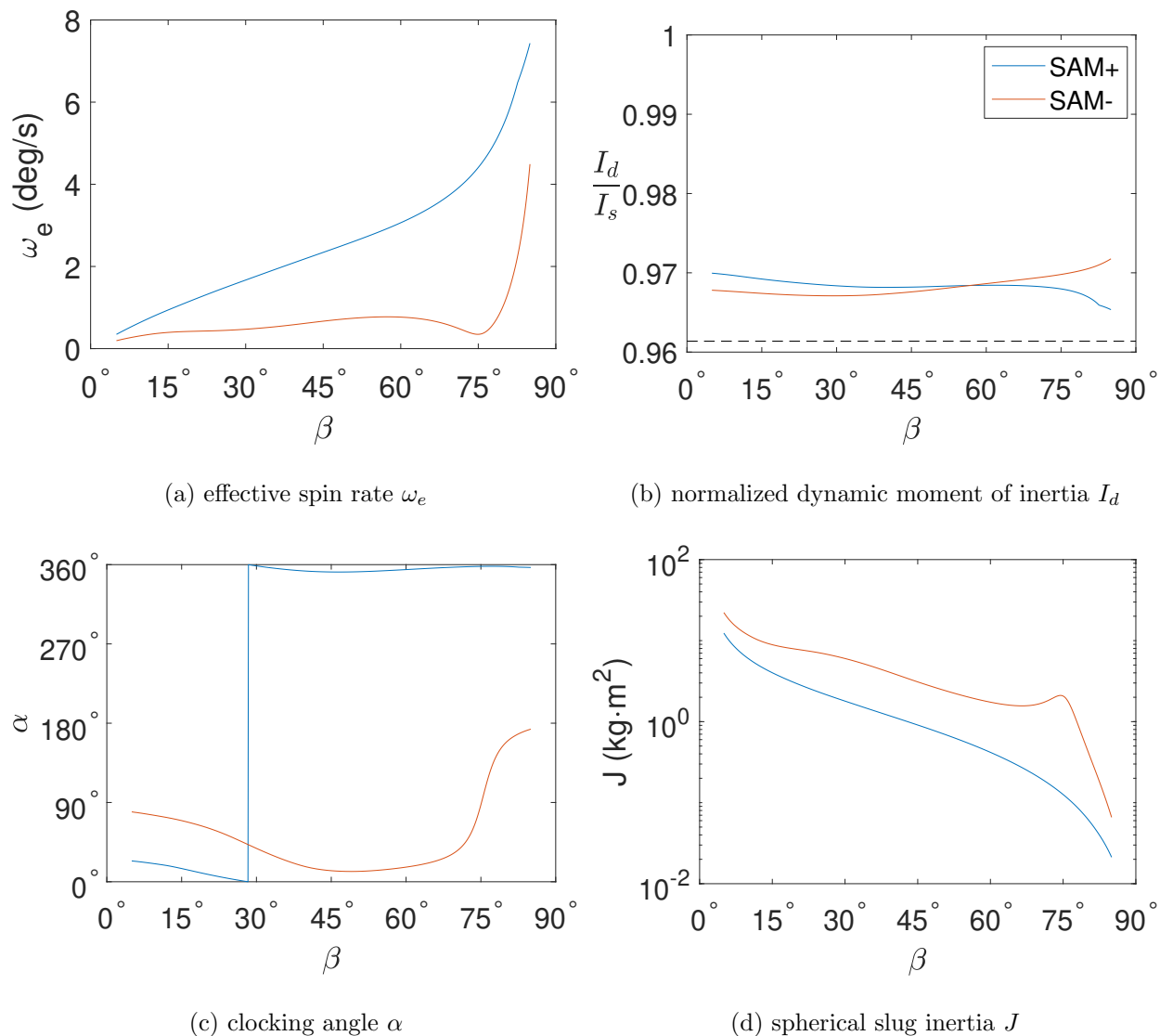
Figure 5.17: GOES 8 YORP + dissipation equilibria ($\mu/J = $ 1e-3 s^{-1})

Figure 5.17 shows the corresponding $P_\psi = P_{\bar{\phi}}$ period ratios. For both SAM+ and SAM-, these equilibrium period ratios are in the vicinity of the 4:1 and 5:1 resonances which has implications for resonant capture.
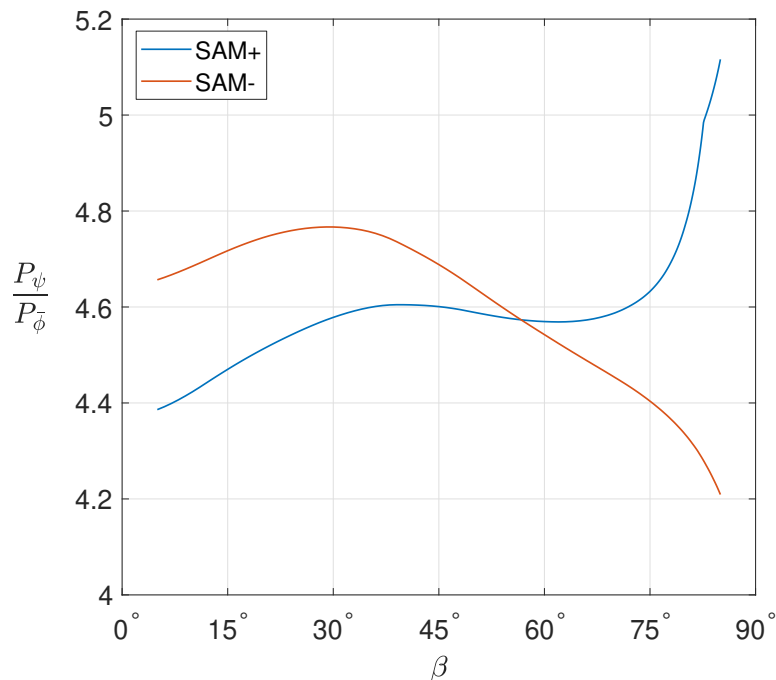
Figure 5.18: GOES 8 YORP + dissipation equilibrium period ratios corresponding to Figure 5.17

Figure 5.19 is an extension of Figure 5.17 over the range of end of life solar array angles θ_{sa} for the SAM- equilibria. Here, the torques are evaluated with the analytically averaged model. Sweeping through θ_{sa}, the equilibrium solutions change significantly. Note that equilibria only exist one side of $\beta \approx 90°$ for a given θ_{sa} since YORP-induced $\dot{\bar{I}}_d$ changes sign here (see Figures 5.4 and 5.9). Dissipation-induced $\dot{\bar{I}}_d$ is always positive, so for an equilibrium to exist, YORP-induced $\dot{\bar{I}}_d$ must be negative.

(a) effective spin rate ω_e

(b) normalized dynamic moment of inertia I_d

(c) clocking angle α

(d) spherical slug inertia J
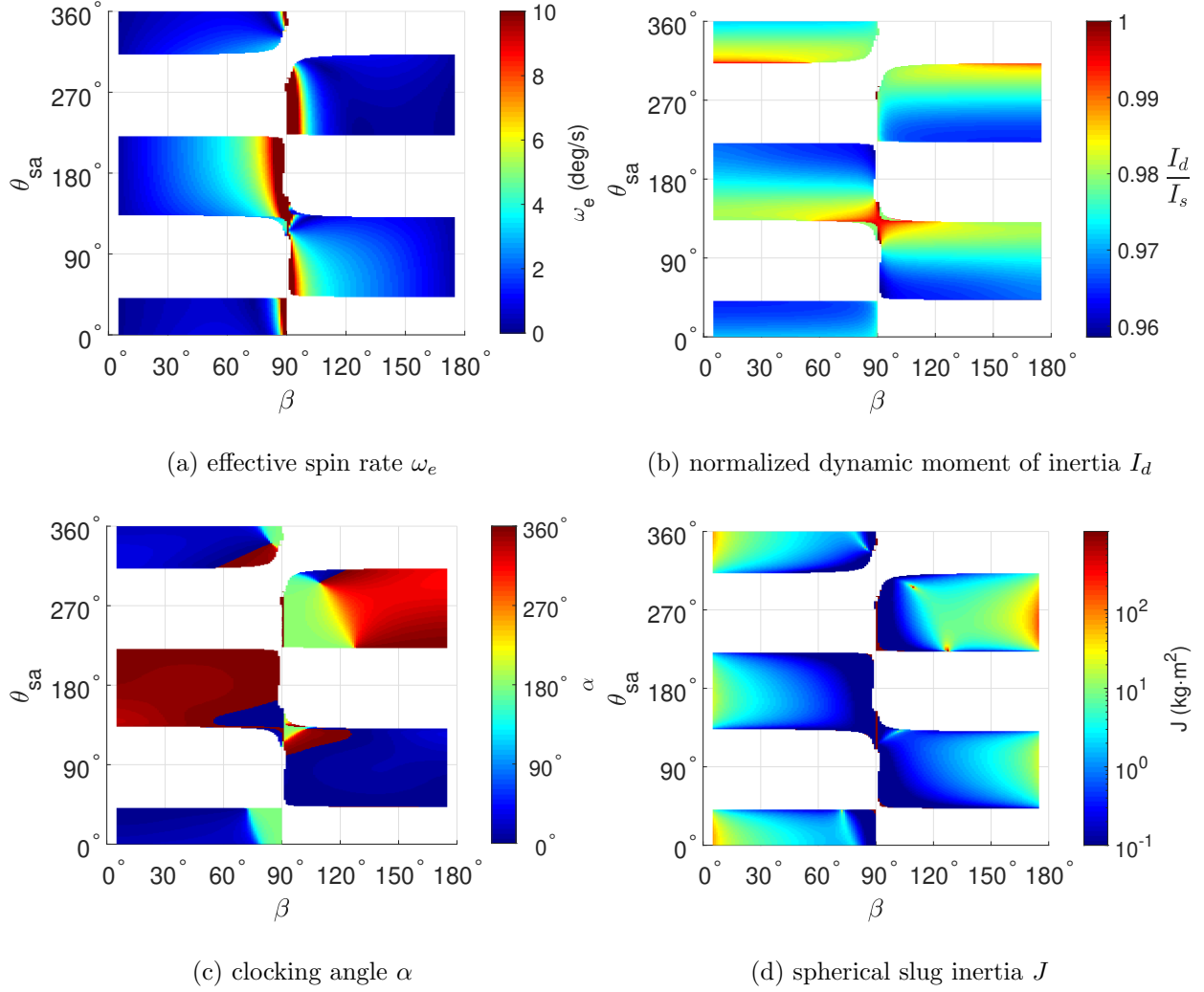
Figure 5.19: GOES 8 YORP and dissipation SAM- equilibria vs. array angle θ_{sa} ($\boldsymbol{\mu/J} = $ 1e-3 s$^{\boldsymbol{-1}}$)

5.5.2   Stability

To evaluate the linear stability of these equilibria, we analyze the eigenvalues of the dynamics matrix B at a given equilibrium state $\boldsymbol{X}_e$,

$$B = \frac{\partial \dot{\boldsymbol{X}}}{\partial \boldsymbol{X}}\bigg|_{\boldsymbol{X}_e} \tag{5.10}$$

where $\boldsymbol{X} = \left[\overline{\alpha}, \overline{\beta}, \overline{H}, \overline{I}_d\right]^{\mathrm{T}}$. Partial derivatives involving $\overline{M}_x$, $\overline{M}_y$, $\overline{M}_z$, and $\dot{\overline{I}}_d$ are evaluated with finite difference of the corresponding lookup tables, selecting the finite difference deltas small enough such that the partials converge.

Figure 5.20 shows the stability corresponding to the equilibria in Figure 5.17. While the existence of local asymptotic stability depends on the given J, note that the SAM- equilibria all have lower associated kinetic energy than the SAM+ states. For a subset of J values, there are also several possible SAM- equilibria, some being locally asymptotically stable or unstable. For both SAM± equilibria, the least stable eigenvalues (i.e. those with the largest real components) generally corresponded to the angular momentum direction, indicating the equilibria are least stable in this direction. For unstable equilibrium points, averaged model simulations showed that divergence in H (and ω_e) generally occurred well before the other state variables, supporting this eigenvalue/eigenvector analysis.

(a) maximum real eigenvalue component

(b) total kinetic energy
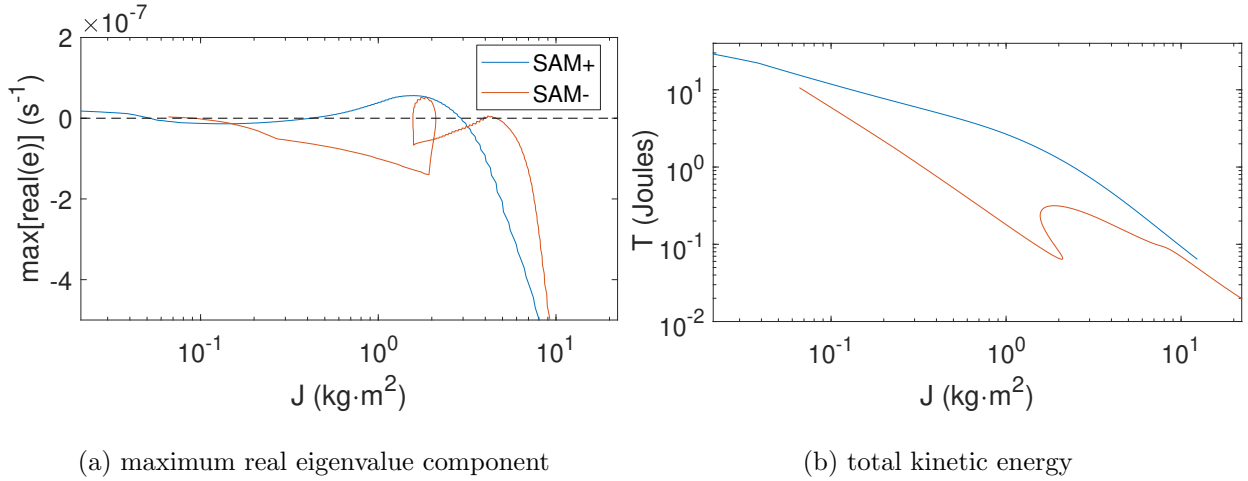
Figure 5.20: GOES 8 YORP + dissipation equilibria stability ($\boldsymbol{\mu/J} = $ 1e-3 s$^{\boldsymbol{-1}}$)

Using the numerically averaged model, we will briefly investigate the asymptotic stability for a case where J has multiple SAM- equilibria. We will consider $J = 1.8$ kg·m^2 which has two stable and one unstable equilibria as shown in Figure 5.20a. The two stable equilibria have corresponding system kinetic energies of $\sim$0.07 and $\sim$0.3 Joules respectively. We propagate 200 runs, uniformly drawing initial values for α from $[0°, 360°]$, β from $[0°, 90°]$, I_d from $[I_i, I_s]$, and $P_e = 2\pi/\omega_e$ from $[5, 20]$ min. The resulting evolution is shown in Figure 5.21. All states converge to the stable equilibria, but the histogram in Figure 5.21b indicates the satellite is roughly 2.5$\times$ more likely to

settle in the lower energy equilibrium.

(a) kinetic energy

(b) histogram of final kinetic energy
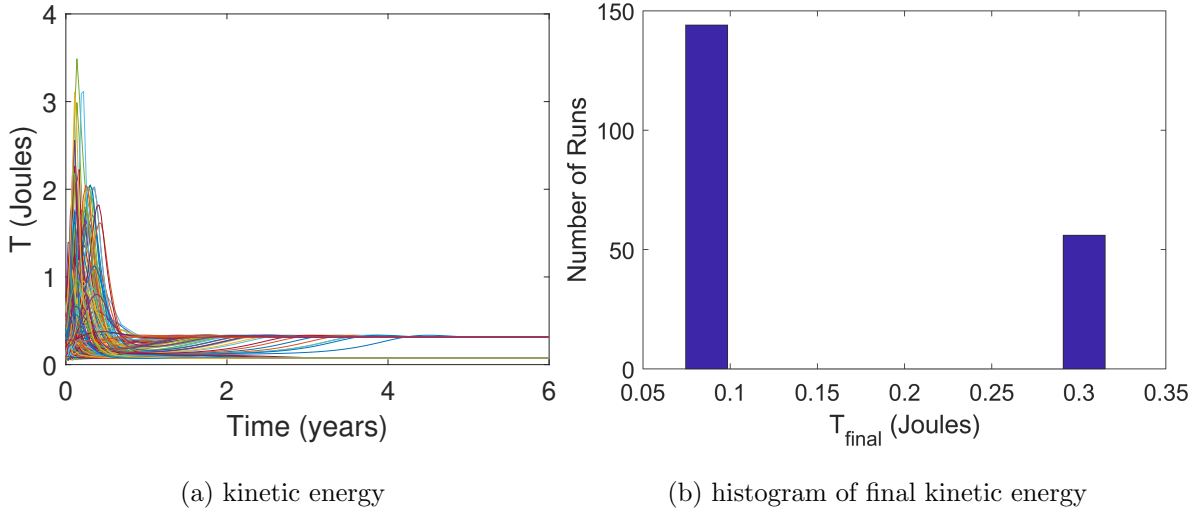
Figure 5.21: GOES 8 YORP + dissipation preferred convergence to minimum energy SAM- equilibrium ($J = 1.8$ kg·m^2, $\mu/J = $ 1e-3 s^{-1}, 200 runs)

Extending this analysis to the combined SAM± equilibria, which both exist for a given J, we conduct simulation runs with the full model to naturally handle switching between SAM+ and SAM-. Starting the GOES 8 model with $I_d/I_s = 0.98$, $P_e = 2\pi/\omega_e = 120$ min, $\alpha = 0°$, $\beta = 15°$, we vary J from 0.5 to 10 kg·m^2 over 13 runs for SAM- and SAM+ states. Figure 5.22 shows the resulting evolution for the 26 total runs. In all cases, I_d settles on the SAM side of the separatrix within roughly one year. Similarly, ω_e is in the process of converging in almost all cases, albeit a bit more slowly given the aforementioned negative real eigenvalue components being closer to zero. Nevertheless, in each run shown, the short axis spin rate ω_s is converging a negative value, indicating SAM-. The averaged analysis from Figure 5.20 shows that the stable SAM- equilibria have lower energy than SAM+. As the satellite is perturbed by YORP and dissipation, it repeatedly transitions between LAM and SAM, having the opportunity to switch from SAM+ and SAM-. So as it dissipates energy, the satellite will tend to settle in equilibria with the minimum energy, which for the GOES 8 model and prescribed J values correspond to SAM- states. Investigating stable

SAM+ equilibria from Figure 5.20 with the averaged model, they were only locally asymptotically stable, diverging from the equilibria for sufficiently large initial state offsets.

(a) effective spin rate ω_e and short axis rate ω_s (b) normalized dynamic moment of inertia I_d
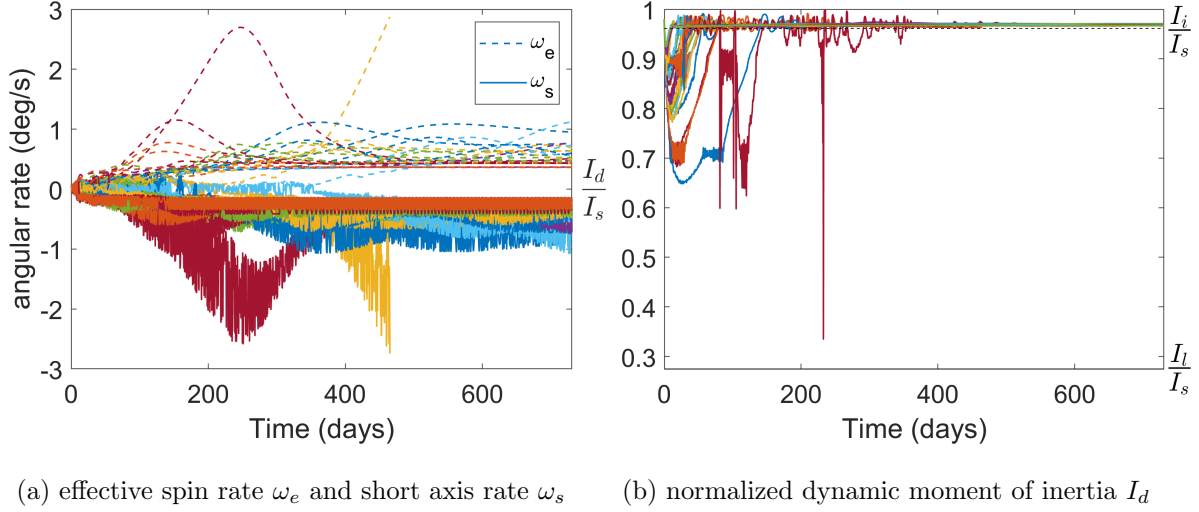
Figure 5.22: GOES 8 full model YORP and dissipation SAM- convergence ($\mu/J = $ 1e-3 s^{-1})

5.6   Resonant YORP + Dissipation

With $\dot{\overline{I_d}}$ for YORP + dissipation given by Eq. 5.11,

$$\dot{\overline{I_d}} = \frac{2\overline{I_d}}{H}\overline{\boldsymbol{M} \cdot \left(\mathbb{I}_{3\times3} - \overline{I_d}[I]^{-1}\right)\hat{\boldsymbol{H}}} + h_d \tag{5.11}$$

we can write $\ddot{\overline{\gamma}}$ as,

$$\ddot{\overline{\gamma}} = \ddot{\overline{\gamma}}_{\text{YORP}} + \ddot{\overline{\gamma}}_{\text{diss}} \tag{5.12}$$

where $\ddot{\overline{\gamma}}$ in turn depends on $\dot{\overline{I_d}}$ through the expressions provided in C.

Considering the 1:1 LAM resonance, Figure 5.23 shows that $\ddot{\overline{\gamma}}$ shifts upwards as ω_e (and therefore the dissipation rate) increases. This is because $\ddot{\overline{\gamma}}_{\text{diss}} \geq 0$ in LAM. As a result, the $\ddot{\overline{\gamma}} = 0$ manifolds shrink with increasing dissipation. For Figure 5.23d, dissipation becomes sufficiently large that $\ddot{\overline{\gamma}}$ is strictly positive and resonance capture is no longer possible. As a reminder, $\ddot{\overline{\gamma}}_{\text{YORP}}$ is independent of H (and ω_e), so the YORP only contour in Figure 5.23a holds for all spin rates.

(a) YORP only

(b) $\omega_e = 0.3$ deg/s

(c) $\omega_e = 0.6$ deg/s

(d) $\omega_e = 1.2$ deg/s
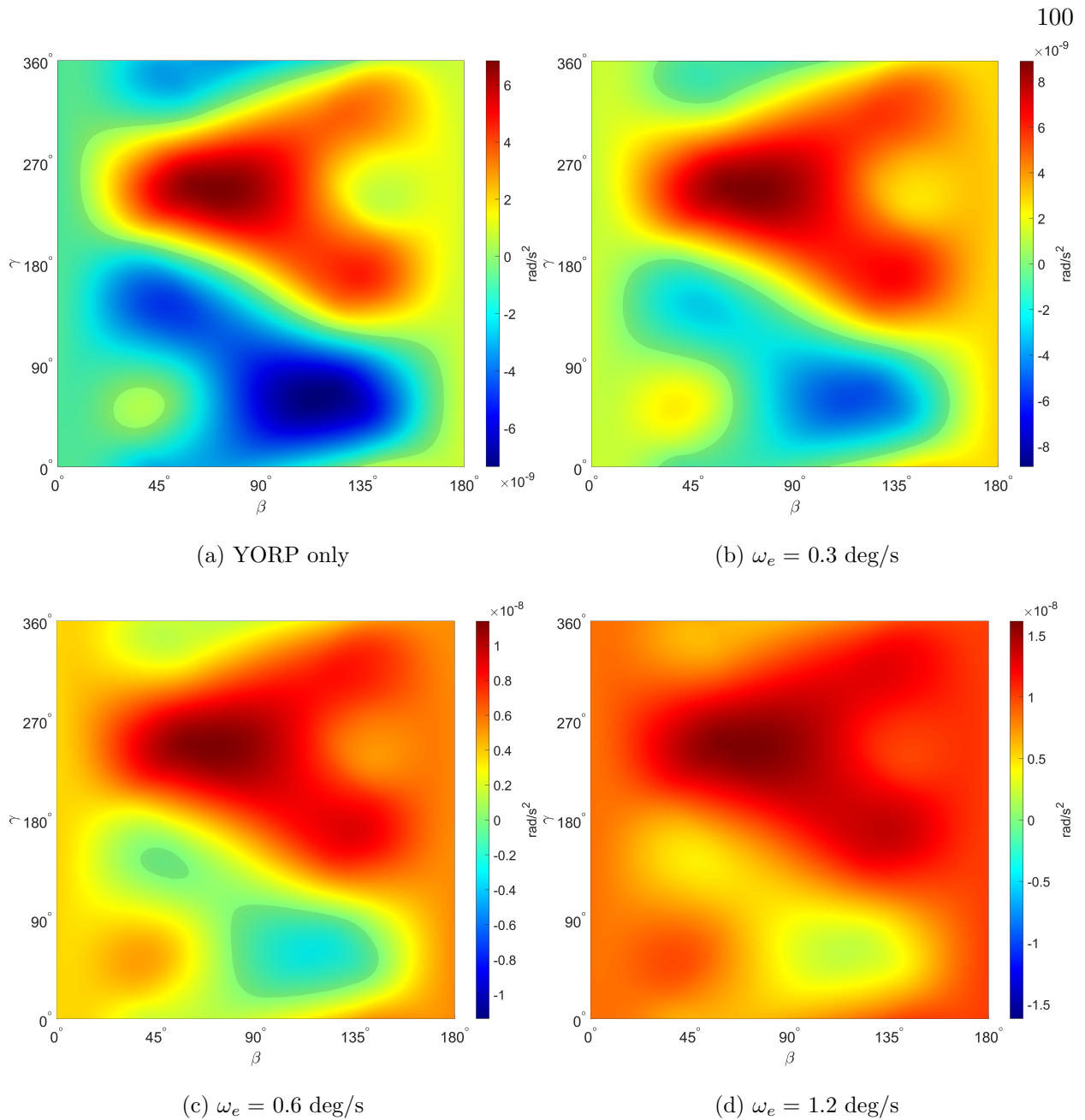
Figure 5.23: GOES 8 YORP + dissipation $\ddot{\bar{\gamma}}$ for $P_\psi/P_{\bar{\phi}} = 1{:}1$ resonance (LAM+) with various spin rates ($J = 1$ kg·m^2, $\mu/J = $ 1e-3 s^{-1})

Figure 5.24 shows the LAM+ 1:1 resonance capture duration with dissipation $J = 1.8$ kg·m^2, and $\mu/J = $ 1e-3 s^{-1}, $P_e = 20$ min ($\omega_e = 0.3$ deg/s). Compared to Figure 5.11 for the YORP only case, there are significantly fewer regions that result in extended capture and the maximum capture

duration (219 days) is about 25% lower. This is consistent with the shrinking $\ddot{\bar{\gamma}} = 0$ manifolds in Figure 5.23 with increasing spin rates.
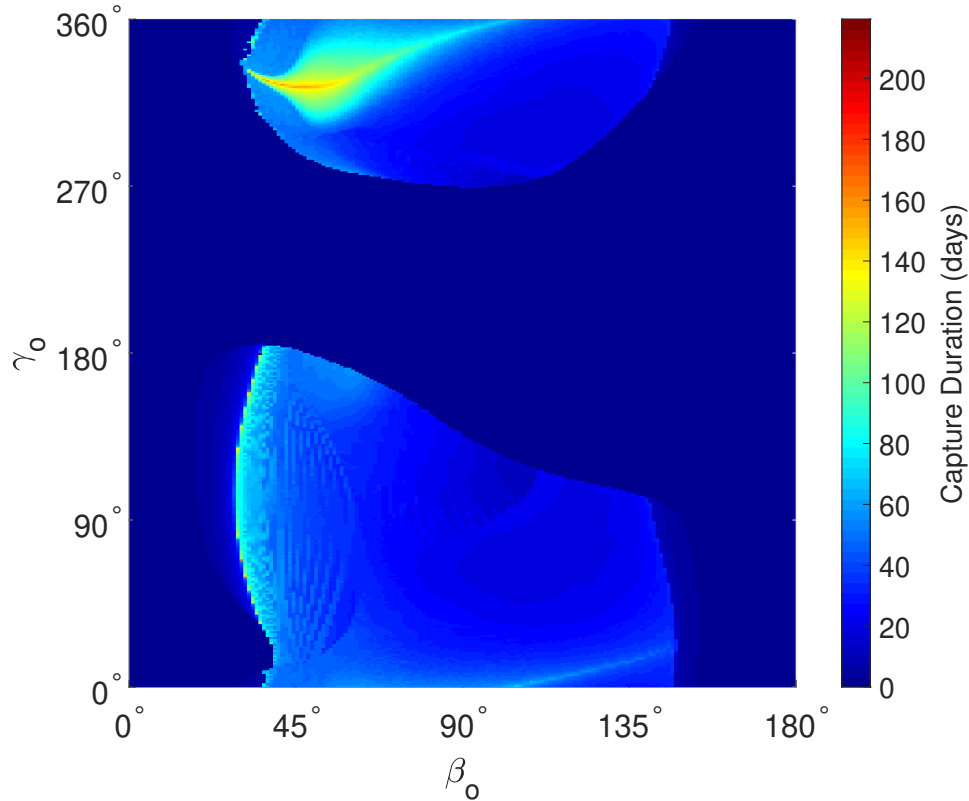
Figure 5.24: GOES 8 capture duration in $P_\psi/P_{\bar{\phi}} = 1$ resonance for YORP + dissipation ($\omega_e = 0.3$ deg/s, $J = 1$ kg·m^2, $\mu/J = $ 1e-3 s^{-1}))

Figure 5.25a demonstrates the reduction in capture probability for increased initial spin rate. Starting with Figure 5.25a, capture probabilities decrease steadily with increased ω_e, with no capture for $\omega_e = 1.2$ deg/s. This behavior is consistent with the interpretation of the contours in Figure 5.23. Similarly, the dissipation rate can be increased by increasing J for a fixed ω_e. Figure 5.25b shows the resulting reduction in capture probability for increasing J.

(a) varying ω_e with $\boldsymbol{J} = 1$ kg·m^2

(b) varying $\boldsymbol{J}$ with $\omega_e = 0.3$ deg/s
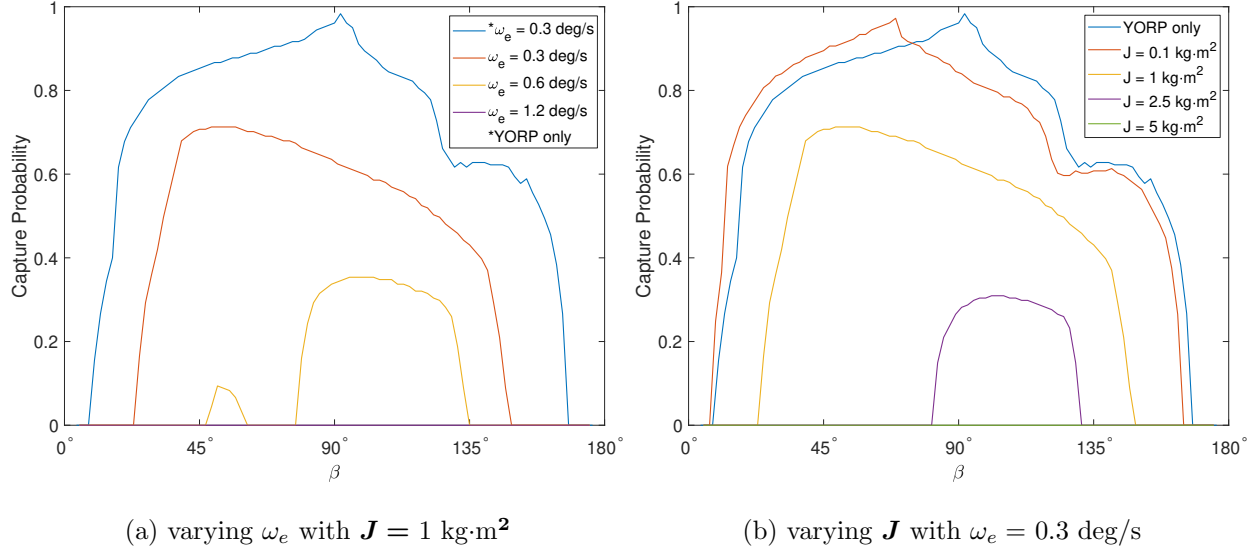
Figure 5.25: GOES 8 YORP + dissipation $P_\psi/P_{\bar\phi} = 1{:}1$ (LAM+) probability of resonance capture for ≥ 10 days ($\mu/J = 1$e-3 s^{-1})

Figure 5.26 shows $\ddot{\bar\gamma}$ for the 5:1 SAM- resonance for YORP with and without dissipation. In SAM, $\ddot{\bar\gamma}_{\mathrm{diss}} \leq 0$, so the $\ddot{\bar\gamma} = 0$ manifold shifts leftward to smaller values of β. Overall, the 4:1 and 5:1 SAM$\pm$ $\ddot{\bar\gamma}$ contours have similar structure and follow the same behavior. As noted above, the 4:1 and 5:1 SAM resonances will be near the period ratios corresponding to the equilibria in Figures 5.17 and 5.18. The $\ddot{\bar\gamma} = 0$ manifold does not span nearly as wide a β range compared to the LAM 1:1 and 2:1 resonances, suggesting low capture probability. Nevertheless, for particular dissipation rates, the β value centered on $\ddot{\bar\gamma} = 0$ will be near the corresponding equilibrium β. With β evolving in the vicinity of the $\ddot{\bar\gamma} = 0$ manifold, probability of capture probability in the SAM 4:1 and 5:1 resonances will likely be greater for YORP + dissipation than for YORP alone. This is consistent with the full YORP dynamics simulations from Chapter 2, where 5:1 SAM resonance capture was generally observed only when dissipation was considered.

(a) YORP only

(b) $\omega_e = 1.2$ deg/s
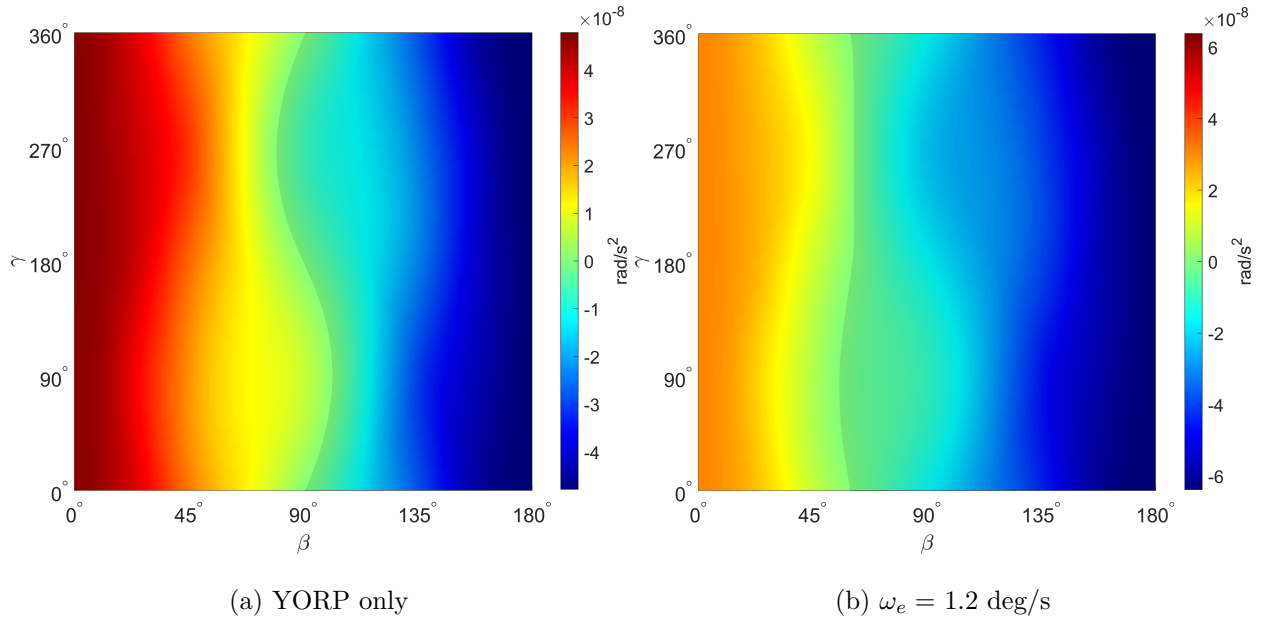
Figure 5.26: GOES 8 YORP + dissipation $\ddot{\bar{\gamma}}$ for $P_\psi/P_{\bar{\phi}} = 5{:}1$ resonance (SAM-) ($J = 1$ kg·m^2, $\mu/J = $ 1e-3 s^{-1})

5.7 Non-Resonant YORP + Dissipation + Gravity Gradients

The influence of gravity gradient torques on the averaged model YORP + dissipation equilibria will now be investigated. Figure 5.27 shows the evolution when gravity gradient torques are considered in addition to YORP and dissipation for $J = 1$ kg·m^2. Here, the satellite is assumed to be in the GEO Laplace plane ($i = 7°$, $\Omega = 0°$). For the YORP + dissipation case, the satellite converges to the stable equilibrium in roughly two years. Adding gravity gradients, the satellite spin state begins oscillating about steady state values that are offset from the YORP + dissipation equilibrium. Propagation for 20+ years showed no damping, indicating the satellite is captured in a limit cycle. These oscillations have a 1 year periodicity, consistent with the annual rotation of $\lambda(t)$ in the $\mathcal{O}$ frame.

(a) effective spin rate ω_e

(b) normalized dynamic moment of inertia I_d

(c) clocking angle α

(d) coning angle β
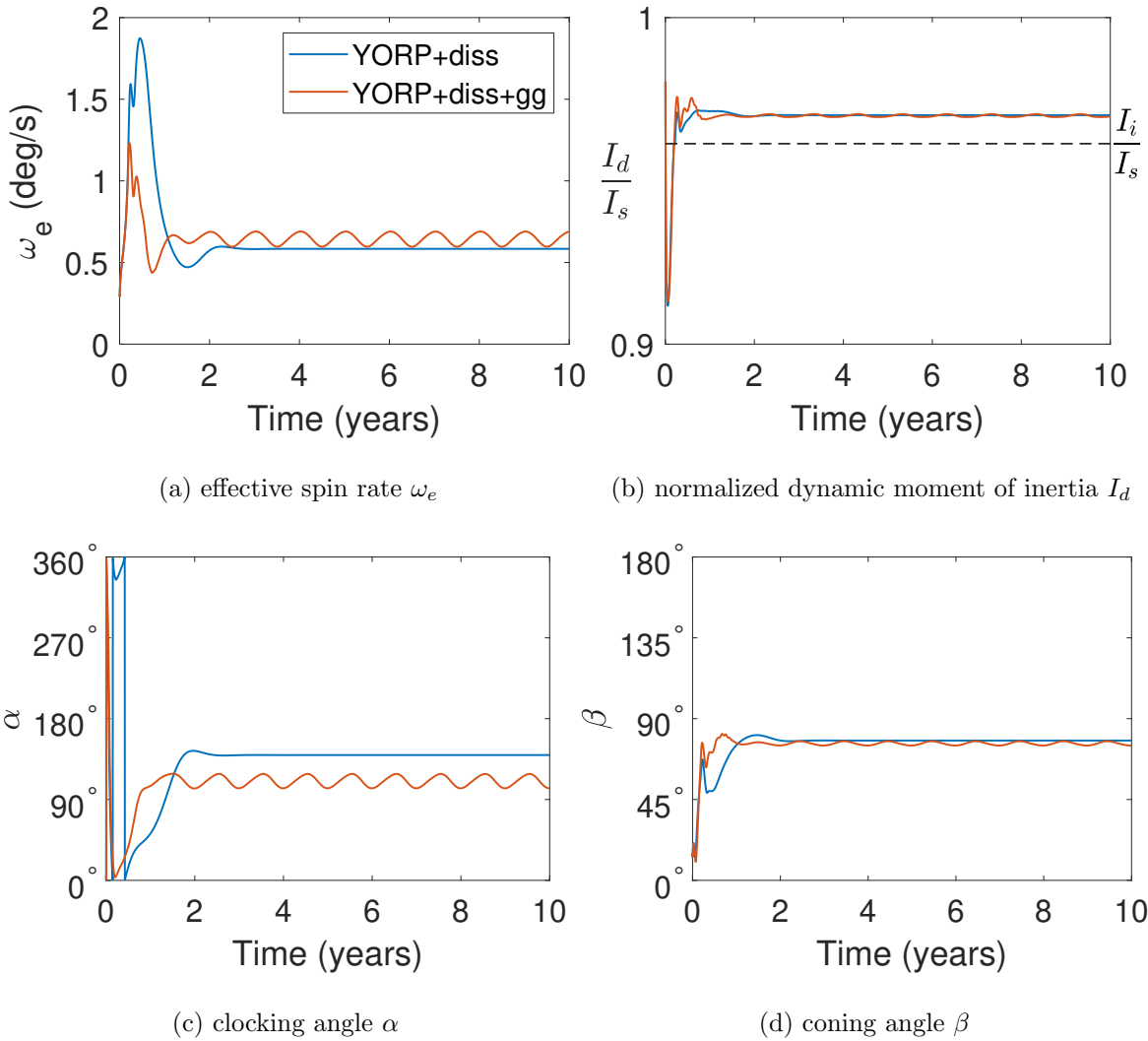
Figure 5.27: GOES 8 averaged YORP + dissipation + gravity gradient limit cycle (SAM-, $J = 1$ kg·m^2, $\mu/J = $ 1e-3 s^{-1}, $i = 7°$)

Considering a higher dissipation rate with $J = 10$ kg·m^2, Figure 5.28 shows that the difference between the YORP + dissipation equilibrium and steady state gravity gradient limit cycle spin states are much greater, particularly in terms of ω_e and β. This shift in steady state values is due to the gravity gradient tendency to precess $\boldsymbol{H}$ around the GEO orbital angular momentum direction $\hat{\boldsymbol{H}}_G$ which affects the YORP-driven sun-tracking.

(a) effective spin rate ω_e

(b) normalized dynamic moment of inertia I_d

(c) clocking angle α

(d) coning angle β
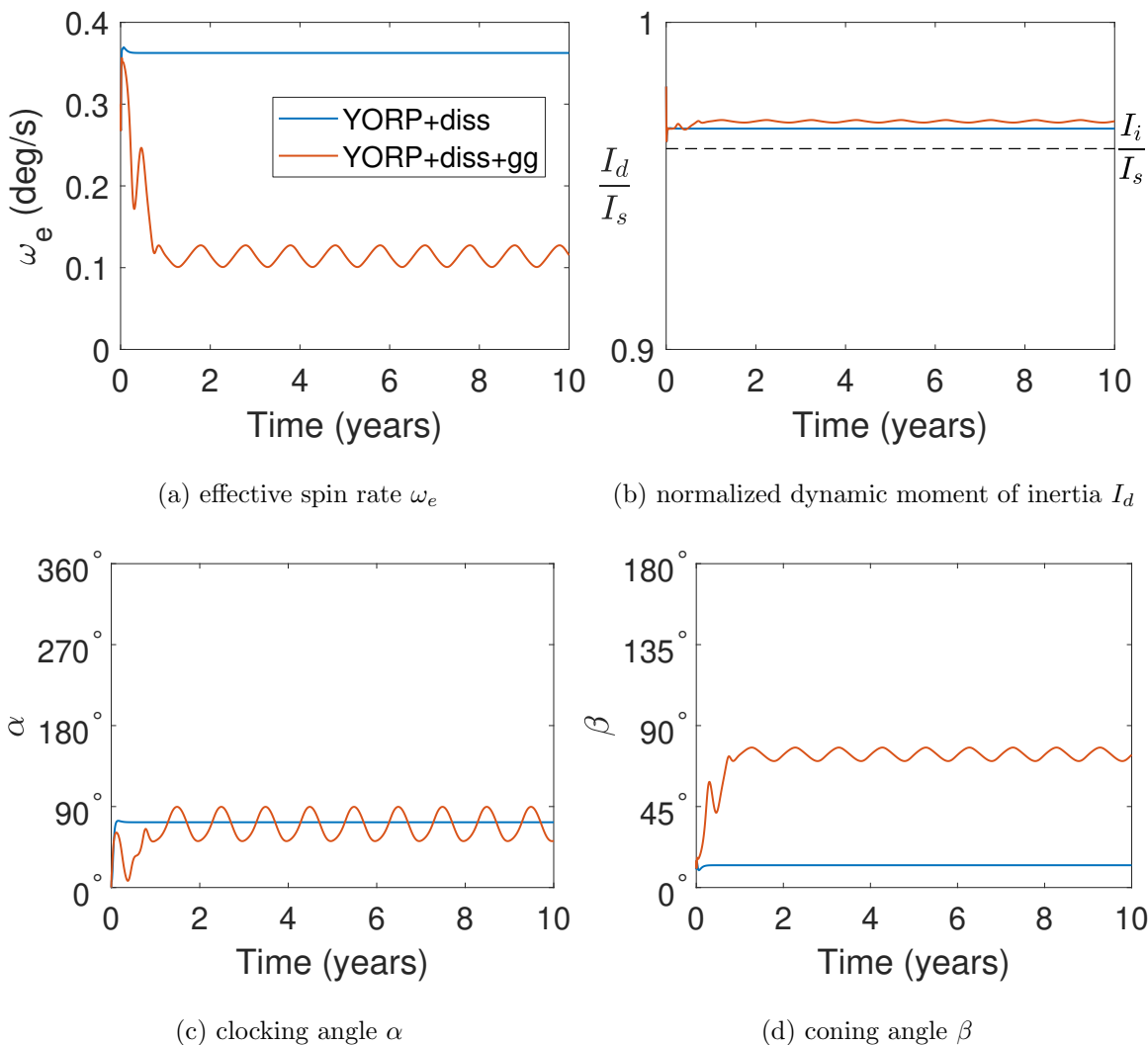
Figure 5.28: GOES 8 averaged YORP + dissipation + gravity gradient limit cycle (SAM-, $J = 10$ kg·m^2, $\mu/J = $ 1e-3 s^{-1}, $i = 7°$)

Figure 5.29 compares averaged model simulations for YORP + dissipation with gravity gradients on and off. For both cases, the satellite initial approaches the asymptotically stable equilibrium. For the small prescribed $J = 0.1$ kg·m^2, the equilibrium is very near $\beta = 90°$. Note that for GOES 8, $\dot{I}_d$ in the SAM region switches from negative to positive as $\beta > $ increases past 90°. For the case without gravity gradients, the satellite state remains near this equilibrium. For the case with gravity gradients, β is perturbed significantly enough beyond 90° that the satellite escapes to

rapid uniform rotation. It then undergoes successive tumbling cycles. The peak uniform rotation precession period is roughly 16 s near the end of the simulation.

(a) effective spin rate ω_e

(b) normalized dynamic moment of inertia I_d

(c) clocking angle α

(d) coning angle β
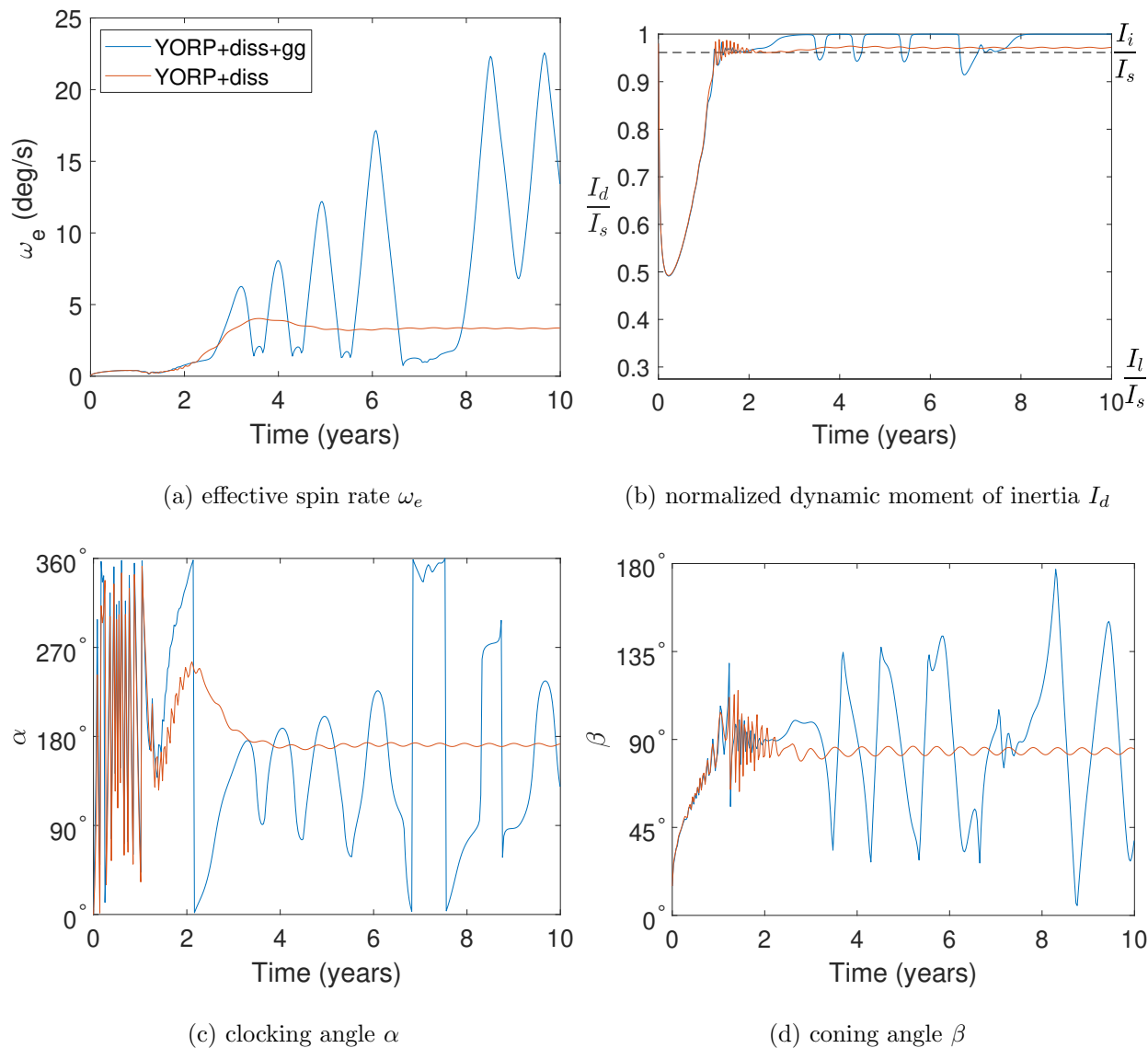
Figure 5.29: GOES 8 averaged model tumbling escape due to gravity gradient torques (SAM-, $J = 0.1$ kg·m^2, $\mu/J = $ 1e-3 s^{-1}, $i = 0°$)

Chapter 6

Observation Analysis

While dynamical modeling provides the opportunity to explore various perturbations and their effects on long-term rotational dynamics, it is important that these simulations agree with observed satellite spin state evolution. So it is useful to validate simulation results against satellite spin state estimates extracted from real observations. Observations also provide direct insight into ongoing dynamical evolution. There are several types of observations often used to investigate space debris spin states. Measurements of an object's time-varying photometric brightness due to reflected sunlight (i.e. light curves) are the most prevalent observation type [80, 57, 105]. There are two other notable observation types, both relying on active approaches. The first is satellite laser ranging (SLR). Here, short laser pulses transmitted from a ground-based laser reflect off of an object and back to the observer. The round-trip light time then provides precise ranging information which can be used to infer an object's spin state [63]. SLR requires an object to be fitted with retro-reflectors which are not common, especially on older spacecraft. Therefore, SLR is not applicable to the general space debris population. The second notable active observation type is radar. Radio waves with carefully engineered properties (e.g. frequency, phase, polarization) are transmitted from a ground-based antenna towards an object [77]. The reflected echoes have different properties, providing insights about the object. The primary limitation for radar is the $1/R^4$ dependence of echo power, compared to $1/R^2$ dependence for brightness measurements [77, 104]. So large, high power antennas are needed to obtain sufficiently high signal to noise, particularly for distant objects [77].

In this work, we will focus on extracting satellite spin state information from light curves and Doppler radar observations with a particular emphasis on the tumbling regime. Here, analysis is limited to period and pole extraction rather than complete spin state estimation (i.e. instantaneous attitude and angular velocity). Various methods for light curve based complete spin state estimation for satellites have been explored (e.g. [116, 51, 66, 82]). These methods are significantly aided by *a priori* information. The approaches outlined in this chapter have the potential to greatly constrain possible solutions for subsequent complete spin state estimation, especially for tumbling rotation where there can be many candidate tumbling period pairs. For the following spin state analyses, we make the important assumption that the satellite is in torque-free rigid body rotation. Since solar radiation torques, gravity gradients, and dissipation are generally small perturbations on torque-free rotation for high-altitude satellites, this is a good approximation over relatively short timescales.

6.1   Photometric Light Curves

Given the small angular size of GEO satellites from earth, resolved images are generally not obtainable with current ground-based optical telescopes. So spin state information must be inferred from non-resolved brightness measurements. As a satellite rotates, different surfaces are exposed to the sun and reflect light towards the observer, resulting in time-varying brightness known as a light curve. An object's instantaneous brightness is a function of many parameters including it's shape, reflective properties, and attitude (as well as the sun-satellite-observer phase angle and relative distances which are assumed to be known).

For uniformly rotating satellites with inertially fixed sun-satellite-observer geometry, light curves are periodic in the satellite precession (i.e. spin) period $P_{\bar{\phi}}$. In this case, a number of methods can be employed to estimate the precession period. For observations that are equally spaced in time, fast Fourier transforms (FFTs) can be used to determine the precession period [56]. Observation gaps and data points contaminated by background stars often result in uneven spacing. For these cases, traditional FFT analysis will yield spurious frequencies. So it is instead

more appropriate to use Lomb-Scargle periodograms or single period Fourier series fitting which can handle these gaps [46]. A particularly robust alternative is minimum dispersion phase-folding. For this technique, one folds the data in time over a candidate period. The folded light curve is then divided into a number of discrete bins. Calculating and summing the brightness variation of the data points in each bin, the candidate period minimizing overall variation is selected. Phase-folding is particularly advantageous for cases where the light curve sampling rate is low compared to the satellite rotation period. Time-varying geometry introduces differences between this extracted synodic period $P_{\bar{\phi}}^{\text{syn}}$ and the sidereal (inertial) period $P_{\bar{\phi}}$. This difference is approximately [83, 11],

$$\Delta P \approx \frac{d(PAB)}{dt} P_{\bar{\phi}}^2 \qquad (6.1)$$

where $d(PAB)/dt$ is the rate of change of the phase angle bisector (vector halfway between the satellite-sun and satellite-observer vectors). For GEO observing, $d(PAB)/dt$ is roughly half of earth's spin rate ($\sim$3.5e-4 rev/min^{-1}). So for $P_{\bar{\phi}} = 10$ min, ΔP would be approximately ± 2 s.

Due to the general incommensurability of $P_{\bar{\phi}}$ and P_{ψ}, tumbling light curves are generally non-periodic. So frequency analysis becomes significantly more challenging. For tumbling asteroids, dominant light curve frequencies are generally a priori unknown integer linear combinations (i.e. harmonics) of the two fundamental frequencies $f_{\bar{\phi}} = 1/P_{\bar{\phi}}$ and $f_{\psi} = 1/P_{\psi}$ [56, 71, 83, 96]. In other words,

$$f_i = a f_{\bar{\phi}} + b f_{\psi} \qquad (6.2)$$

where f_i is a dominant frequency and a and b are different integers $[..., -2, -1, 0, 1, 2, ...]$.

These frequency harmonics are generally low orders (e.g. $2f_{\bar{\phi}}$, $f_{\bar{\phi}} + f_{\psi}$, $f_{\bar{\phi}} - f_{\psi}$) given the relative simplicity of asteroid shapes and their roughly homogeneous reflective properties dominated by diffuse reflection [56, 71, 83, 96]. Nevertheless, there will be many potential assignments for a given tumbling light curve. So correctly interpreting the dominant frequencies in tumbling asteroid light curves is challenging. For tumbling defunct satellites with more complex geometry, varying surface materials, and specular reflections, it is important to determine if these low order harmonics

still dominate. No studies of how fundamental tumbling periods appear in satellite light curves have been conducted. Binz et al. [13] attempted place upper limits on "tumble rates" of defunct GEO satellites from light curves using a simple correlation function. Piergentili et al. [82] looked at the dominant Fourier transform frequencies in observed and simulated light curves. Neither discussed how these "tumble rates" or dominant frequencies connect with the underlying tumbling periods.

6.1.1   Light Curve Simulator

In order to explore how the fundamental periods manifest themselves in tumbling light curves of defunct satellites, a light curve simulator was needed. Given the complexity of observed light curves, a model was desired that could generate specular, glossy, and diffuse reflections as well as shadows and indirect illumination (i.e. multi-bounce reflections). So a light curve simulator was developed in the NASA Goddard Space Flight Center (GSFC) Freespace dynamics toolbox using the built in stochastic (Monte Carlo) ray tracer [33]. The three channel (red, green, blue) ray tracer employs a bidirectional reflectance distribution function (BRDF) based on the model by Ashikhmin and Shirley [5]. This energy conserving BRDF can generate diffuse, glossy, and specular reflections through a microfacet formulation to simulate small-scale surface roughness.

Another important aspect of the light curve simulator was an accurate GOES shape model. An existing GSFC model was updated to include an articulating solar array and trim tab. End of life orientations for these surfaces were provided by John Tsui of NOAA's satellite operations office. With the various surface materials of the GOES satellites well documented [107], their reflective properties in each color band were set to plausible pre-launch values. However, the true properties have likely been altered by space weathering effects. The bus and solar sail are covered in multi-layer insulation (MLI) and aluminized Kapton, materials that generate almost exclusively specular/glossy reflections. So macroscopic roughness was added to these surfaces better match the true material appearance and observed light curves. A ray traced image of the GOES shape model is shown in Figure 6.1 and illustrates the complex reflections and shadows possible with the

light curve simulator. The surface roughness of the bus MLI is also visible.
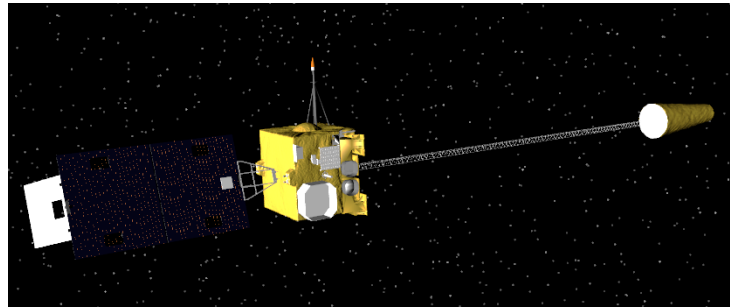
(a) high fidelity GOES shape model
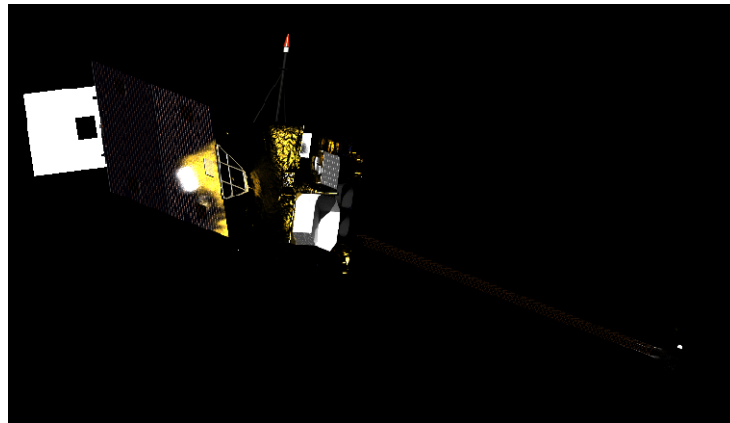
(b) ray traced image of shape model

Figure 6.1: Freespace GOES 8 shape model for light curve simulator

To generate more accurate simulated data and facilitate comparison with observed light curves, the correct time-varying positions of the satellite, sun, and earth-based observer were accounted for. The satellite's orbit was propagated from two line element (TLE) data obtained from the Joint Space Operations Center's Space-Track database. JPL Horizons ephemerides were used to determine the correct sun and earth positions. Finally, WGS 84 coordinates were used for the observation site. The raw output of the ray tracer is an image with three radiance values per pixel (one for each waveband). The simulated photometry was determined by integrating the radiance values (W/m2/sr) over all pixels in the image and multiplying by each pixel's solid angle. Each of

the three radiance values was pre-multiplied by the prescribed photometric filter's average trans-mittance in that waveband. This yielded a total irradiance (W/m2) at the observing location. Finally, this irradiance value was calibrated to the prescribed filter's corresponding zero point flux and converted to magnitudes. Successive reduced images constitute a simulated light curve.

An example tumbling GOES light curve generated with the ray traced simulator is provided in Figure 6.2. This light curve illustrates several notable features. First of all is the lack of clean periodicity with several frequencies seemingly present. There are short period variations on the order of several minutes superimposed on longer period variations of more than 20 minutes. The light curve also exhibits a trend in decreasing magnitude (increasing brightness) due to time-varying viewing geometry and the resulting change in sun-satellite-observer phase angle.
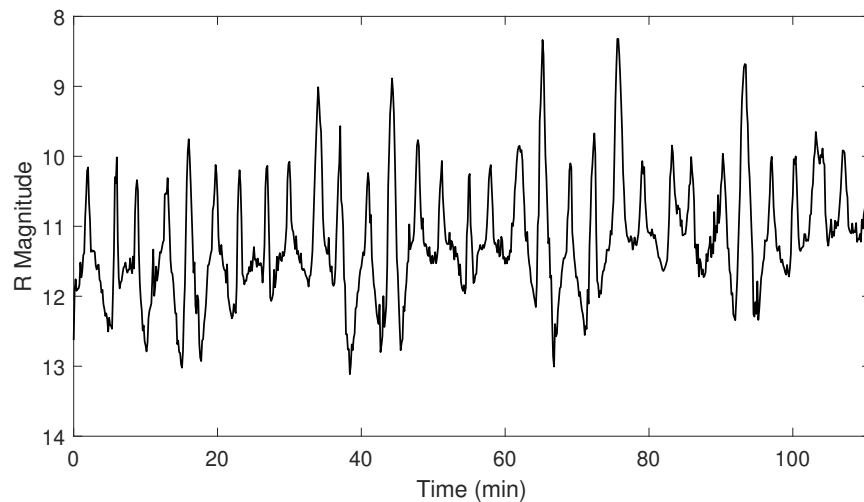
Figure 6.2: Simulated GOES Light Curve ($I_d = 3520$ kg·m^2, $P_{\bar{\phi}} = 7.04$ min, $P_\psi = 25.83$ min, phase angle: 49°-27°)

6.1.2 Tumbling Light Curve Frequency Analysis

We will now discuss methodologies to extract the fundamental periods from tumbling light curves. Generally, tumbling light curves can be approximated by a 2-D Fourier series [83],

$$
\begin{aligned}
B(t) \;=\; & C_0 + \sum_{i=1}^{m}\Big[C_{i0}\cos i\omega_{\bar{\phi}}t + S_{i0}\sin i\omega_{\bar{\phi}}t\Big] \\
& + \sum_{j=1}^{m}\sum_{i=-m}^{m}\Big[C_{ij}\cos\left(i\omega_{\bar{\phi}}+j\omega_{\psi}\right)t + S_{ij}\sin\left(i\omega_{\bar{\phi}}+j\omega_{\psi}\right)t\Big]
\end{aligned}
\tag{6.3}
$$

where C_0 is the mean light-curve brightness, m is the Fourier series order, $\omega_{\bar{\phi}} = \frac{2\pi}{P_{\bar{\phi}}} = 2\pi f_{\bar{\phi}}$, and $\omega_{\psi} = \frac{2\pi}{P_{\psi}} = 2\pi f_{\psi}$, and C_{ij} and S_{ij} are the Fourier coefficients for a particular frequency harmonic. Note that there are $(2m+1)^2$ coefficients. So the number of parameters grows very large with increasing m.

Given Equation 6.3, the most obvious and straightforward extraction technique would be to choose candidate values for $P_{\bar{\phi}}$ and P_{ψ} and perform a least-squares fit of the Fourier coefficients with the goal of finding the period pair with the lowest root mean square (rms) residual. The rms residual ϵ is given by,

$$
\epsilon^2 = \frac{1}{n}\sum_{k=1}^{n}\Big(B(t_k) - L(t_k)\Big)^2
\tag{6.4}
$$

where $B(t_k)$ and $L(t_k)$ are the modeled and observed light-curve brightness values at a particular time t_k and n is the number of observations. The candidate periods could be chosen by systematically searching a grid. While simple, this type of 'blind' grid search has a number of disadvantages. First, it will generally require a finely spaced grid to locate well-fitting period pairs. This grid needs to be made large enough to ensure it contains the true pair. More importantly, this approach is likely to yield a number of similarly well-fitting, harmonically related solutions. This is because these harmonically related solutions will share many of the same $i\omega_{\bar{\phi}}+j\omega_{\psi}$ Fourier series frequency terms. As a result, it is often more useful to first compute the fast Fourier transform or Lomb-Scargle periodogram of the light curve and determine the dominant frequencies. Then, a Fourier series containing consisting of just these frequencies can be fit to the light curve to improve the estimates of these dominant frequencies.

Frequency analysis of the Figure 6.2 light curve is provided in Figure 6.3. The top plot shows the FFT light curve power spectrum. The power spectrum peaks are labeled with their corresponding frequency harmonic. Note that $2f_{\bar{\phi}}$ is the dominant frequency. Also note the prominent left-most peak due to the secular decrease in magnitude. This peak is also adjacent to the f_ψ peak. For rotation near the separatrix where P_ψ becomes large (and f_ψ small), discerning between light curve variations due to long-period rotation and changing phase angle becomes quite challenging. So de-trending a light curve to zero mean magnitude may result in removal of long-period rotation information. The bottom plot shows the iterated Fourier series fit to the light curve using the power spectrum frequencies for initial guesses. The iterated Fourier series provides improved frequency estimates given the limited resolution of the power spectrum.
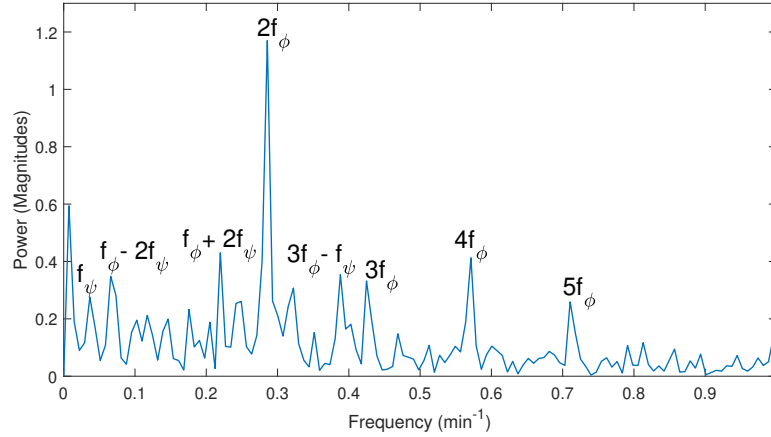
(a) light curve power spectrum and dominant frequencies
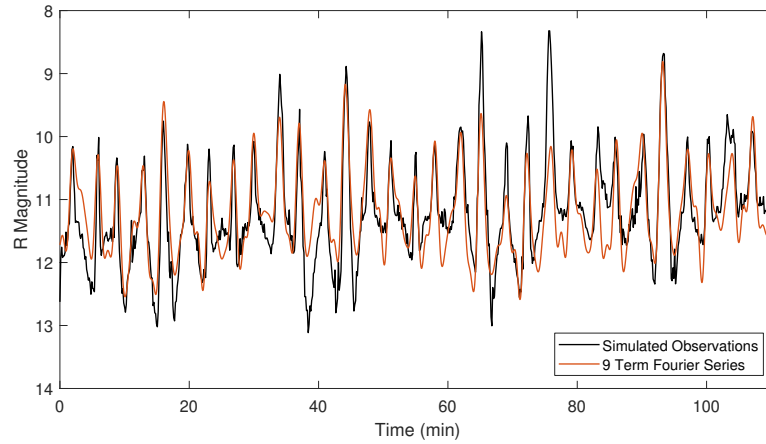
(b) light curve and Fourier series fit

Figure 6.3: Simulated GOES light curve frequency analysis ($I_d = 3520$ kg·m^2, $P_{\bar{\phi}} = 7.04$ min, $P_{\psi} = 25.83$ min, phase angle: 49°-27°)

To develop a better understanding of the dominant frequencies in tumbling GOES light curves, Figure 6.4 shows the histograms of dominant frequencies in an ensemble of 400 SAM light curves with pole directions spread across the celestial sphere. The largest amplitude frequency in each light curve is almost always 2 or $4f_{\bar{\phi}}$ and the second largest peak is most often a multiple of $f_{\bar{\phi}}$ as well.

(a) largest amplitude frequency   (b) 2nd largest amplitude frequency
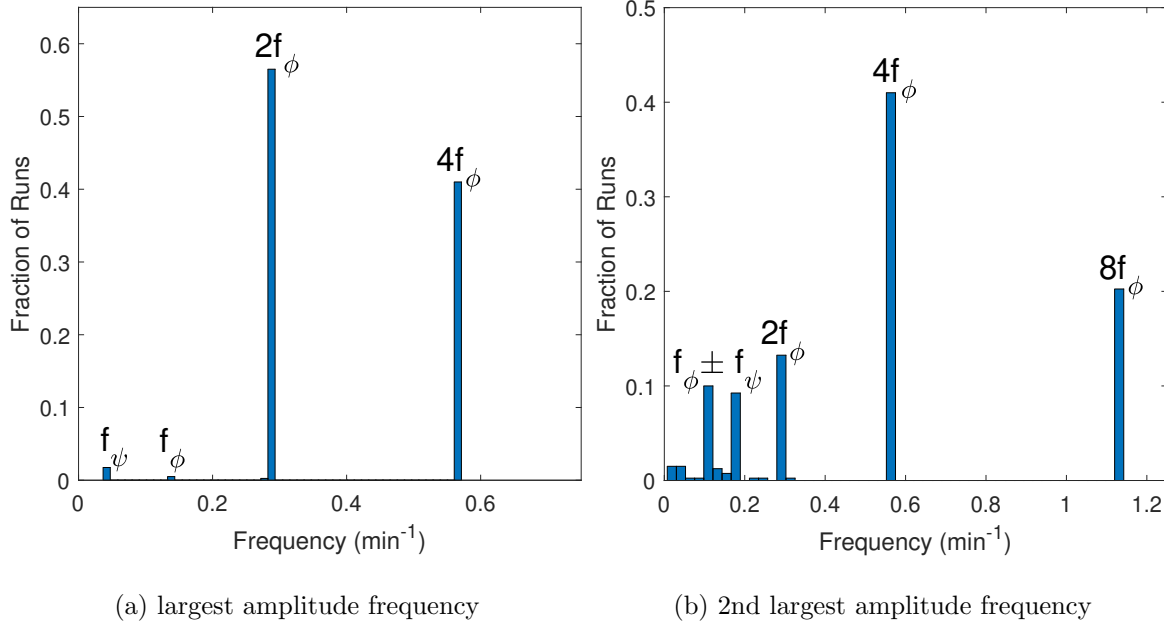
Figure 6.4: Histograms of dominant frequencies in 400 simulated GOES light curves ($I_d = 3520$ kg·m^2, $P_{\bar{\phi}} = 7.04$ min, $P_\psi = 25.83$ min, phase angle: 49°-27°)

The final test case provided concerns resonant tumbling and how that manifests itself in a tumbling light curve. A SAM state with $P_{\bar{\phi}} = 4.43$ min, $P_\psi = 15.55$ min ($P_\psi/P_{\bar{\phi}} = 3.51 \sim 7/2$) was tested. Figure 6.5 shows a sample light curve folded on the best-fit synodic $P_r = 30.85$ min. Note that the sidereal $P_r = 31.01$ min, so the difference due to time-varying geometry is roughly 9 s. The light curve covers roughly 3.5 resonance periods and almost exactly repeats, demonstrating that the satellite periodically returns to nearly the same attitude. The light curve variation over this resonant cycle is very complex with a total of 14 peaks. No more than 4 peaks per cycle were observed for uniform rotation GOES light curves [11].
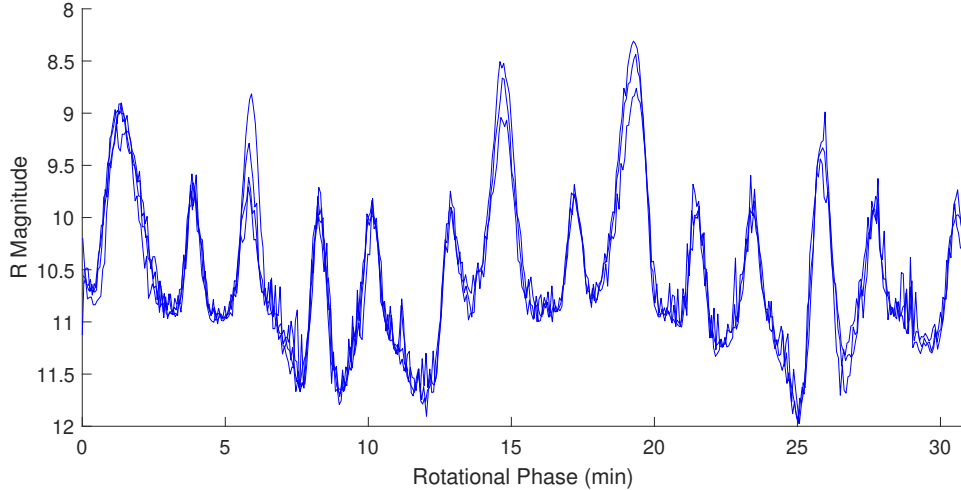
Figure 6.5: Simulated phase-folded resonant tumbling GOES light curve (SAM $P_{\bar{\phi}} = 4.43$ min, $P_\psi = 15.55$ min, $P_\psi/P_{\bar{\phi}} \sim 7/2$, Phase angle: $20°$ - $9°$)

Additional surveys are provided in Benson et al. [11]. Overall, the simulated light curve surveys provided a number of insights about light curve frequency content. First of all, integer linear combinations of the tumbling fundamental frequencies $f_{\bar{\phi}}$ and f_ψ account for the overwhelming majority of observed GOES light curve frequencies. Furthermore multiples of the precession frequency $f_{\bar{\phi}}$ tend to dominate GOES light curve power spectra with three or more different multiples often observed. This is likely due in part to the large, axisymmetric solar sail which provides frequent precessional reflections but is unaffected by long axis rotation and therefore f_ψ. As a further constraint, the most dominant frequency in any simulated light curve was never higher than $4f_{\bar{\phi}}$, likely constrained by the cube-shaped bus and solar sail not providing more than four broad reflections per precession period. For GEO observing conditions with slowly time-varying phase and viewing geometry, the dominant light curve frequencies still closely agreed with tumbling frequency combinations apart from low frequency phase change aliases sometimes included. For slower complex rotation, the low frequency f_ψ terms were often obscured by long period phase change aliases, making identification of f_ψ more difficult. Finally, light curves for resonant tumbling states folded cleanly on the synodic resonance period P_r, even in the presence of time-varying viewing geometry. This encourages the use of long-period phase folding to identify potential resonant tumbling states.

While these results show that for GOES, $f_{\bar{\phi}}$ can often be narrowed to a few possibilities, they also showed that identification of f_ψ is much more challenging. So ultimately, after conducting Fourier analysis, there are often a number of plausible solutions for the pair $(f_{\bar{\phi}}, f_\psi)$. Only $P_\psi/P_{\bar{\phi}}$ ratios greater than specific values are viable. In general all physical bodies require $P_\psi/P_{\bar{\phi}} \geq 0$ for LAMs and $P_\psi/P_{\bar{\phi}} \geq 1$ for SAMs [95]. For objects with well-known moments of inertia such as GOES, possible period pairs can be further constrained. Considering Eq. 2.34 and 2.35 for the limiting case of uniform rotation, we have the following inequality for LAMs [95],

$$\frac{P_\psi}{P_{\bar{\phi}}} > \sqrt{\frac{I_i I_s}{(I_i - I_l)(I_s - I_l)}} - 1 \tag{6.5}$$

whereas for SAMs,

$$\frac{P_\psi}{P_{\bar{\phi}}} > \sqrt{\frac{I_l I_i}{(I_s - I_i)(I_s - I_l)}} \tag{6.6}$$

So for a given body, potential period pairs obtained from frequency analysis can be discarded if they do not meet these criteria. Even with these general and body-specific inertia constraints, one will likely have a handful of candidate period pairs remaining. Also, these pairs could correspond to both LAM± and SAM± states. Candidate solutions can then be tested with optimization [56, 83, 82] or statistical filtering [116, 51, 66] approaches with representative satellite and measurement models to determine the best-fitting solution. This requires considering the sphere of possible pole directions and the initial attitude phasing. Even using high fidelity ray tracing for objects with well-constrained mass properties, geometry, and optical properties, this often results in many similarly well-fitting solutions within model uncertainty and measurement noise.

6.2 Doppler Radar

To help reduce light curve spin state ambiguity, especially for tumbling objects, Doppler radar measurements can be incorporated. Unlike non-resolved photometric light curves, Doppler radar provides spatial resolution due to differences in radial velocity across a spinning object. The radar antenna transmits an electromagnetic wave towards the target body which is then reflected back to

the antenna. Assuming a single transmitting/receiving radar antenna, the Doppler frequency shift f_d of the reflected signal is given by,

$$f_d = -2\dot{R}/\lambda_t \tag{6.7}$$

where $\dot{R}$ is the range-rate of the target relative to the antenna and λ_t is the transmitted radar wavelength [77]. Since the inertial radial velocity of a rotating body increases with distance from its center of mass, $\dot{R}$ will vary across the body. Therefore the radar echoes reflected back to the antenna will be spread in frequency. An example of this is provided in Figure 6.6 showing the Doppler shift of the rotating target along the horizontal axis.
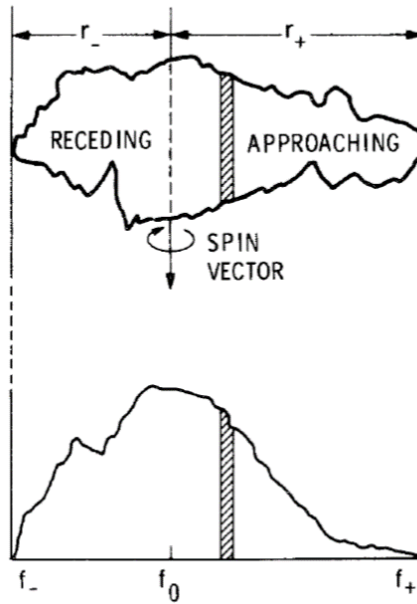
Figure 6.6: Illustration of Doppler shift for a rotating body [77]

For elongated objects, the Doppler frequency spread (i.e. bandwidth) will vary significantly as the object rotates. This allows for unambiguous identification of the long axis precession period $P_{\bar{\phi}}$ for elongated uniform rotators and tumblers. Furthermore, compared to light curves, Doppler provides pole information that is much easier to interpret and a potentially unambiguous pole solution given advantageous geometry. Overall, radar and optical data are complementary. Optical provides rich period harmonics and detailed attitude information, while radar provides the preces-

sion period and greatly constrains the pole. These constraints can be used to significantly narrow the search space for the light curve fitting process, potentially yielding an unambiguous complete spin state solution (i.e. instantaneous attitude and angular velocity).

6.2.1   Doppler Radar Model

We will start by discussing the simulated radar model used to test spin state estimation techniques. To calculate simulated Doppler echoes, the vector $\boldsymbol{R}_i$ from the ith satellite facet to radar antenna is given by,

$$\boldsymbol{R} = \boldsymbol{s} - \boldsymbol{r}_i \tag{6.8}$$

where $\boldsymbol{r}_i$ is the position vector from the satellite center of mass to the facet centroid, and $\boldsymbol{s} = s\hat{\boldsymbol{s}}$ is the vector from the satellite center of mass to the radar antenna (calculated using JPL NAIF SPICE ephemerides for the antenna and TLEs for the satellite orbit). Then, assuming $|\boldsymbol{r}_i| << s$, the facet's range-rate $\dot{R}_i$ due solely to satellite rotation is given by,

$$\dot{R}_i = -\left[(\boldsymbol{\omega} - \boldsymbol{\omega}_{S/N}) \times \boldsymbol{r}_i\right] \cdot \hat{\boldsymbol{s}} \tag{6.9}$$

where $\boldsymbol{\omega}$ is the satellite's inertial angular velocity and $\boldsymbol{\omega}_{S/N} = -\frac{1}{s}\dot{\boldsymbol{s}} \times \hat{\boldsymbol{s}}$ is the angular velocity of $\hat{\boldsymbol{s}}$ with respect to inertial space (roughly 15°/hr for GEO satellites). The spacecraft attitude and angular velocity are obtained from the analytical solutions for torque-free rotation in Chapter 2. Neglecting distance and constant antenna parameters and assuming Lambertian reflection, the facet echo power P_i is simply given by,

$$P_i = \rho_i A_i \max(\hat{\boldsymbol{s}} \cdot \hat{\boldsymbol{n}}_i, 0)^2 \tag{6.10}$$

where ρ_i is the facet radar reflectivity, A_i is its area, and $\hat{\boldsymbol{n}}_i$ is its outward unit normal vector. The max() function ensures that facets only provide echoes when $\hat{\boldsymbol{s}}$ is above the facet horizon. To obtain the Doppler power spectrum, the facet power is then discretely binned by its corresponding Doppler shift f_d.

Figure 6.7 shows the radar shape model of the defunct GOES 8 satellite in the principal axis frame consisting of roughly 1000 facets. The large number of facets helps fill the Doppler spectrum. The thin solar sail boom is only shown for effect and not included in the actual model.
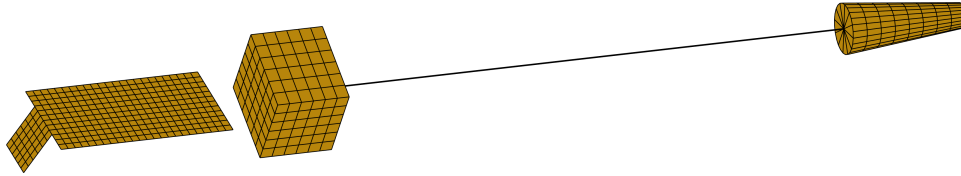
Figure 6.7: GOES radar shape model

Simulating Doppler echoes, the satellite model is placed in uniform rotation about the maximum inertia axis with $P_{\bar{\phi}} = 216$ s. The radar reflectivity of all facets is set equal. Figure 6.8 shows simulated Doppler echoes vs. time with brighter regions denoting higher echo power, here simply expressed in terms of area. The sinusoidal ± 15 Hz amplitude echoes correspond to the conical solar sail as this is farthest from the satellite center of mass and therefore has the largest radial velocity. The ± 5 Hz solar panel echoes are directly out of phase with the solar sail echoes since these components are on opposite sides of the satellite. The 216 s periodicity is clearly evident from the sail and solar panel echoes. This extracted synodic period $P_{\bar{\phi}}^{\text{syn}}$ will differ slightly from the true period $P_{\bar{\phi}}$ due to non-zero $\boldsymbol{\omega}_{S/N}$. Finally, around ± 1 Hz are the bright bus echoes. With significant implications for pole estimation, we see a notable increase in Doppler echo frequency range (i.e. bandwidth) over time. Since the satellite's pole is inertially fixed, the projection of the satellite's rotational velocity along the time-varying $\hat{\boldsymbol{s}}$ changes as it orbits, resulting in increasing Doppler bandwidth.
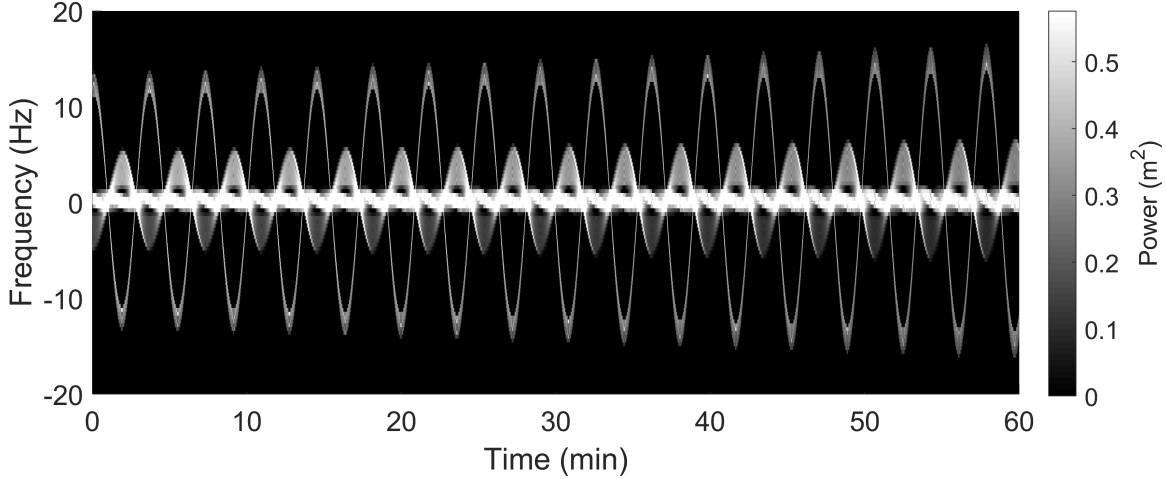
Figure 6.8: Example GOES Doppler echoes (uniform rotation with $P_{\bar{\phi}} = 216$ s)

6.2.2 Doppler Bandwidth Pole Estimation

We will now discuss the first and simplest pole estimation technique considered in this work, called Doppler bandwidth. This method only requires knowledge of the satellite's maximum radial extent from the center of mass (known for the GOES satellites). First, with r denoting the satellite's maximum radial extent and α the angle between $\hat{\boldsymbol{H}}$ and $\hat{\boldsymbol{s}}$ (see Figure 6.9), the maximum range-rate of a facet (assuming uniform rotation with $\boldsymbol{\omega}_{S/N} << \boldsymbol{\omega}$) is,

$$\dot{R}_{\max} = \frac{2\pi r \sin \alpha}{P_{\bar{\phi}}} \tag{6.11}$$

With Eqs. 6.7 and 6.11, we can solve for α in terms of the observed maximum Doppler half-bandwidth b,

$$\sin \alpha = \frac{\lambda_t P_{\bar{\phi}} b}{4\pi r} \tag{6.12}$$

This equation is illustrated in Figure 6.9 where $\boldsymbol{v}$ is the inertial velocity of the satellite at its maximum radial extent.
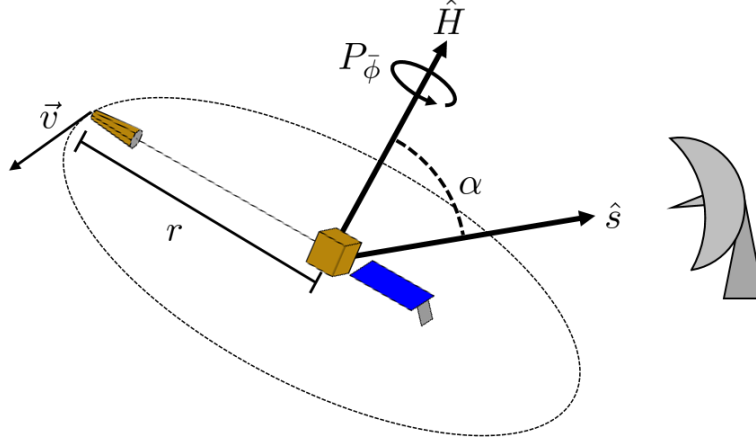
Figure 6.9: Doppler bandwidth illustration

For Doppler bandwidth, we assume $P_{\bar{\phi}} = P_{\bar{\phi}}^{\mathrm{syn}}$ (a good approximation if $\boldsymbol{\omega}_{S/N} << \boldsymbol{\omega}$). To estimate $P_{\bar{\phi}}^{\mathrm{syn}}$ from radar, we simply phase fold the Doppler echoes in time. Binning the time steps by rotational phase for each candidate $P_{\bar{\phi}}^{\mathrm{syn}}$, the dispersion over successive periods in each Doppler frequency/rotational phase bin is calculated. Sweeping over a range of candidate periods in small increments, the one minimizing overall dispersion is taken as $P_{\bar{\phi}}^{\mathrm{syn}}$.

At a given epoch, Eq. 6.12 yields two cones on which $\hat{\boldsymbol{H}}$ lies (only one if $\sin\alpha = 1$). Echoes obtained from significantly different $\hat{\boldsymbol{s}}$ directions yield additional cones. Assuming the pole is inertially fixed, viable pole solutions must lie on the intersection of cones from all epochs. With a single or two closely spaced transmitting/receiving antennas, the well-spaced $\hat{\boldsymbol{s}}$ directions can be obtained by observing a GEO target every several hours or at different local times on subsequent days.

Sample GOES 8 Doppler bandwidth analysis is provided in Figure 6.10. The simulated Doppler echoes are provided in the top plot. The dashed white lines denotes the maximum possible bandwidth for the given $P_{\bar{\phi}} = 216$ s and maximum radial extent. The colored time stamps denote the observation times with the corresponding half-bandwidths marked. Proceeding from t_1 to t_3, b decreases from $\sim$23 Hz to $\sim$15 Hz. Solving Eq. 6.12 and plotting the resulting cones, we obtain four candidate poles shown in Figure 6.10b. Note that the upper left solution with R.A. $= 90°$

and declination $= 45°$ is the correct one. In general, Doppler bandwidth yields at least two pole solutions and often four.
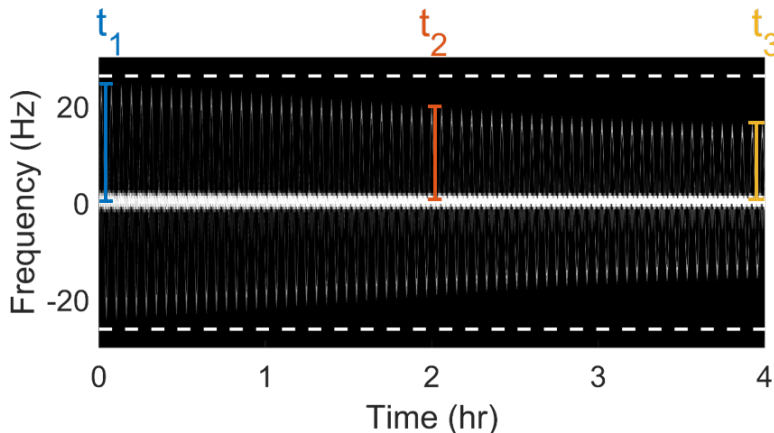
(a) Doppler echoes with half-bandwidth b at different times
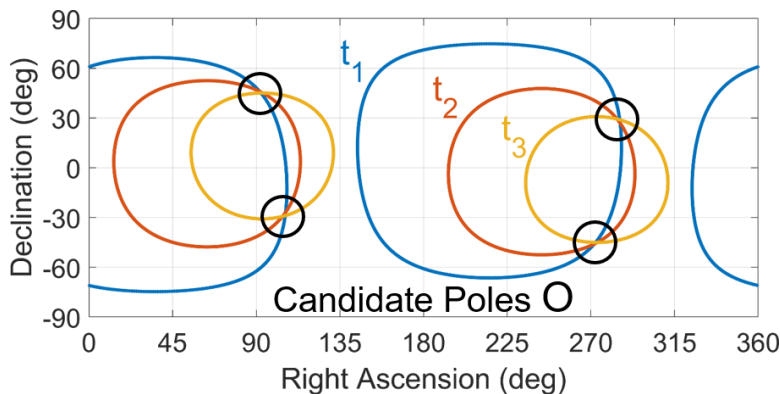
(b) Candidate pole solutions (true solution is R.A.= 90° and declination = 45°)

Figure 6.10: Doppler bandwidth example ($P_{\bar{\phi}} = 216$ s)

6.2.3   3D Rotationally Phased Doppler Pole Estimation

While straightforward, the Doppler bandwidth approach yields at least two candidate pole solutions and requires knowledge about the satellite's maximum radial extent. To hopefully overcome these limitations, we explore another technique. With three or more receiving antennas in a

well-spaced, non-planar configuration, one can directly solve for an object's instantaneous velocity. Assuming $|\boldsymbol{r}_i| \ll s$ and $\boldsymbol{\omega}_{S/N} \ll \boldsymbol{\omega}$, both strong assumptions for GEO satellites, Eq. 6.7 can be written in matrix form for three (or more) receiving antennas denoted 1, 2, and 3,

$$\begin{bmatrix} f_{d_1} \\ f_{d_2} \\ f_{d_3} \end{bmatrix} = \frac{2}{\lambda_t} \begin{bmatrix} \hat{\boldsymbol{s}}_1^{\mathrm{T}} \\ \hat{\boldsymbol{s}}_1^{\mathrm{T}} \\ \hat{\boldsymbol{s}}_1^{\mathrm{T}} \end{bmatrix} \boldsymbol{v}(\tau) \tag{6.13}$$

where $\boldsymbol{v}(\tau)$ is the inertial rotational velocity of a part of the satellite and $\hat{\boldsymbol{s}}_1$, $\hat{\boldsymbol{s}}_2$, and $\hat{\boldsymbol{s}}_3$ denote the unit vectors from the satellite to each receiving antenna (see Figure 6.11). With $\hat{\boldsymbol{s}}_1$, $\hat{\boldsymbol{s}}_2$, and $\hat{\boldsymbol{s}}_3$ well-spaced and non-planar, we can invert Eq. 6.13 to solve directly for $\boldsymbol{v}$.
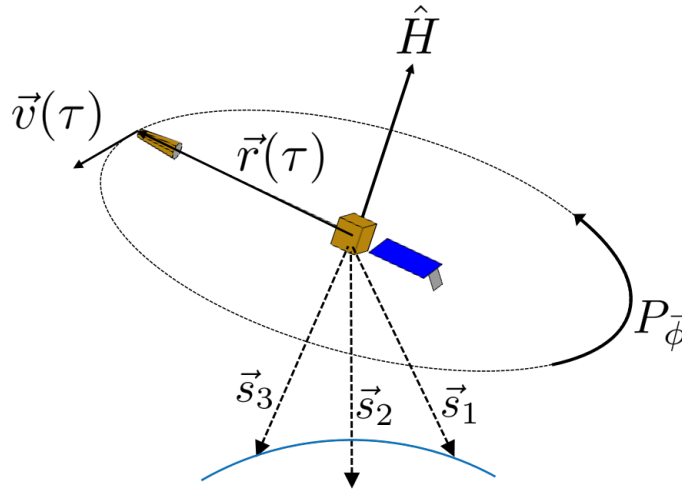
Figure 6.11: Rotationally phased Doppler illustration

Unfortunately for GEO observation, the receiving antennas must be in a non-planar configuration 1000s of km apart. In most practical scenarios, obtaining and coordinating three or more large antennas separated by these distances is not possible. For example, at NASA Goldstone, the antennas are separated by no more than 20 km (angular separation at GEO of 0.03°). This is not sufficient for the above inversion.

To overcome this practical limitation for the case of a single transmitting/receiving antenna, we leverage the periodicity of the satellite's rotation. Assuming the satellite is in uniform rotation

with a fixed $P_{\bar{\phi}}$ and pole direction, the inertial position $\boldsymbol{r}(\tau)$ and velocity $\boldsymbol{v}(\tau)$ of a part of the satellite (e.g. GOES 8's solar sail in Figure 6.11) with respect to the center of mass are periodic in $P_{\bar{\phi}}$. In other words,

$$\boldsymbol{r}(\tau + nP_{\bar{\phi}}) = \boldsymbol{r}(\tau) \qquad \boldsymbol{v}(\tau + nP_{\bar{\phi}}) = \boldsymbol{v}(\tau)$$

where n is an integer. So now, instead of $\hat{\boldsymbol{s}}_1$, $\hat{\boldsymbol{s}}_2$, and $\hat{\boldsymbol{s}}_3$ being the directions to each of three antennas at the same time, they are the directions from the satellite to a single receiving antenna at three different times spaced by multiples of $P_{\bar{\phi}}$,

$$\hat{\boldsymbol{s}}_1(\tau) = \hat{\boldsymbol{s}}(\tau + n_1 P_{\bar{\phi}}) \qquad \hat{\boldsymbol{s}}_2(\tau) = \hat{\boldsymbol{s}}(\tau + n_2 P_{\bar{\phi}}) \qquad \hat{\boldsymbol{s}}_3(\tau) = \hat{\boldsymbol{s}}(\tau + n_3 P_{\bar{\phi}})$$

Observations in phase with the satellite's rotation are used so that the "same" velocity vector is viewed at each time. Provided the observer lines of sight are sufficiently well-spaced and non-planar over time, one can directly solve for $\boldsymbol{v}(\tau)$ using Eq. 6.13. Repeating this analysis for successive rotational phases (i.e. times spanning $\Delta\tau = P_{\bar{\phi}}$), one can trace out the $\boldsymbol{v}(\tau)$ rotational plane and therefore the pole direction $\hat{\boldsymbol{H}}$ with the right hand rule.

There is a complication for this rotationally phased Doppler (RPD) approach, namely estimation of $P_{\bar{\phi}}$. Solutions for $\boldsymbol{v}(\tau)$ will be very sensitive to the estimated value for $P_{\bar{\phi}}$. As noted above, the extracted synodic period $P_{\bar{\phi}}^{\text{syn}}$ will likely differ slightly from the true inertial value $P_{\bar{\phi}}$. For uniform rotation with a fixed spin rate, the velocity magnitude $|\boldsymbol{v}(\tau)|$ is constant. So with the Doppler echo phase-folding technique we obtain $P_{\bar{\phi}}^{\text{syn}}$. From there, we sweep over candidate $P_{\bar{\phi}}$ values around $P_{\bar{\phi}}^{\text{syn}}$, obtaining solutions for $\boldsymbol{v}(\tau)$ for a number of phases spanning one complete satellite rotation. We then find the candidate $P_{\bar{\phi}}$ that yields the smallest dispersion in $|\boldsymbol{v}(\tau)|$ over one satellite rotation. This $P_{\bar{\phi}}$ estimate can then be used to obtain our pole solution.

To illustrate this RPD approach, we will now provide simulated analysis. We use the GOES 8 model and place it in the 14.9° inclination orbit of defunct GEO satellite Telstar 401 on Apr. 30, 2020. Assuming an arbitrary and precise $P_{\bar{\phi}} = 216.4493$ s and pole right ascension and declination of 0° and 45° respectively, Doppler spectra are recorded at a 2 s cadence over the course of 8 hr

assuming a single antenna located in Goldstone, California. Phase-folding the initial 30 min of data, we obtain a minimum dispersion $P_{\bar{\phi}}^{\text{syn}} = 217$ s. Analyzing observations at the beginning, middle, and end of this 8 hr arc (see Figure 6.12), we manually fit local sinusoids to the outermost (i.e. solar sail) Doppler echoes, shown as red lines in Figure 6.12. Continuous local fits are useful since we sweep over candidate $P_{\bar{\phi}}$ values, sampling the Doppler at different times.

(a) t = 0 hr

(b) t = 4 hr

(c) t = 7.9 hr
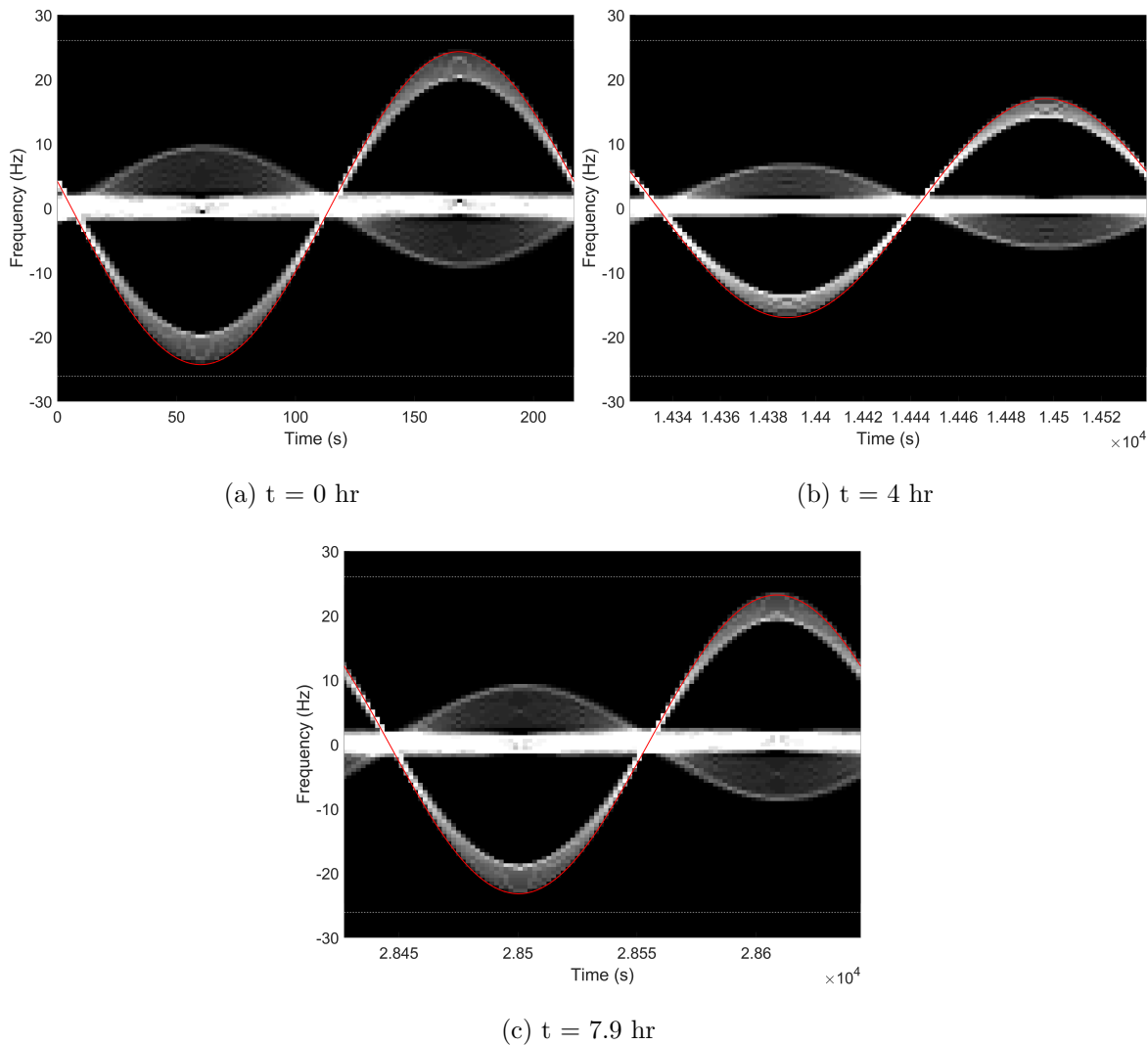
Figure 6.12: Doppler echoes at multiples of $P_{\bar{\phi}}^{\text{syn}}$. The red lines are locally fit sinusoids.
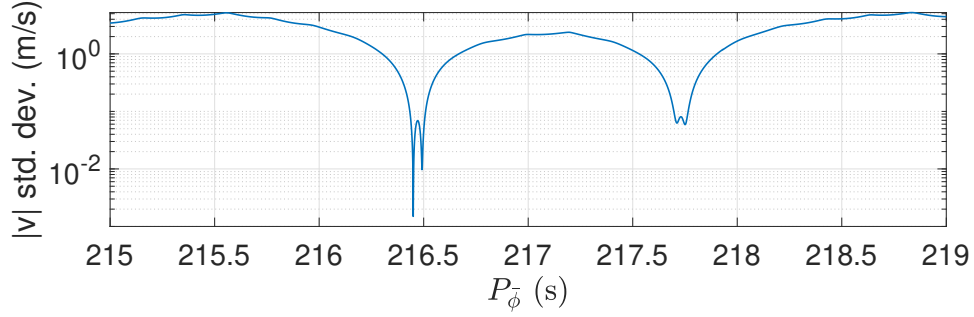
(a) $|\boldsymbol{v}|$ standard deviation over rotational phase vs. candidate $P_{\bar{\phi}}$
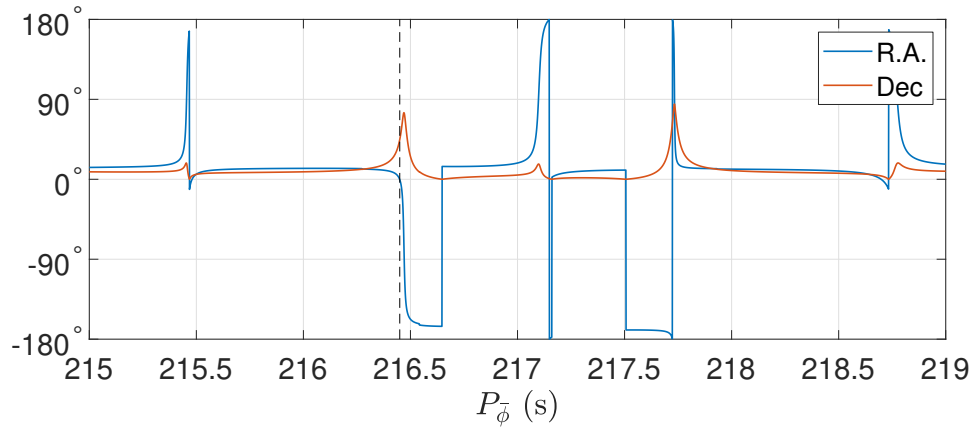
(b) Pole right ascension and declination vs. candidate $P_{\bar{\phi}}$ with the dashed line denoting the minimum dispersion $P_{\bar{\phi}}$ value (216.450 s)

Figure 6.13: 3D rotationally phased Doppler example solution

Solving for $\boldsymbol{v}(\tau)$ using Eq. 6.13 at 22.5° increments of rotational phase from 0° to 360° using the locally fit sinusoids from Figure 6.12, the resulting velocity magnitude standard deviation for candidate $P_{\bar{\phi}}$ values are provided in the top plot of Figure 6.13. Note that the $P_{\bar{\phi}}$ resolution is 0.001 s. Here, we see the lowest dispersion at 216.450 s where the standard deviation in $|\boldsymbol{v}(\tau)|$ over these 22.5° increments is 1.5 mm/s, 0.3% of the nominal $|\boldsymbol{v}(\tau)|$, and nearly an order of magnitude smaller than the next best solution. Taking this as our $P_{\bar{\phi}}$ estimate, Figure 6.13b provides the pole estimate. We can see that the pole estimate is very sensitive to the assumed $P_{\bar{\phi}}$ value. The resulting spin state estimates are provided in Table 6.1 along with the prescribed truth values. Since the GOES satellites have known radial extents (e.g. 18.87 m for GOES 8 from the center of

mass to the end of the solar sail[107]), this can also be compared to the derived extent given by $|\boldsymbol{v}|_{\mathrm{mean}} P_{\bar{\phi}}/2\pi$. All parameters agree well for our simulated case.

	$P_{\bar{\phi}}$	RA	Dec	Radial Extent
Truth	216.4493 s	0°	45°	18.87 m
Estimate	216.450 s	-0.4°	44.75°	18.997 m

Table 6.1: Results for 3D Rotationally Phased Doppler Example

Summarizing this 3D rotationally phased Doppler (RPD) pole estimation approach, with sufficiently well-spaced and non-planar observation directions, a precise $P_{\bar{\phi}}$ estimate can be obtained along with an unambiguous pole estimate using Doppler echoes from a single transmitting/receiving antenna. Importantly, we assume that the satellite's pole and inertial precession period $P_{\bar{\phi}}$ are fixed. Assuming spin state perturbations are small, the former is a reasonable assumption over relatively short timespans. For rigid torque-free tumblers, $P_{\bar{\phi}}$ is only constant for uniform rotation or when the object has axisymmetric moments of inertia. For nearly axisymmetric tumblers like GOES and many other satellites, $P_{\bar{\phi}}$ oscillations may be small enough for this approach to work. In addition, the RPD approach does not employ a satellite model in the solution process. So detailed knowledge of an object's geometry and reflective properties are not required, only the presence of distinguishing features far from the center of mass that can be identified over successive rotations (e.g. solar sail, solar panel outer edge, upper stage rocket nozzle). For GEO objects, high inclinations are advantageous as they provide the necessary non-planar observation geometry. Once a sufficiently accurate $P_{\bar{\phi}}^{\mathrm{syn}}$ is obtained, observations are only needed every several hours covering 1-2 rotation periods each. So the antennas can be cycled between several targets over one observing session. For MEO and geostationary transfer orbit (GTO) objects, the smaller semi-major axes and often large inclinations allow for shorter observation arcs to yield the same line of sight variation with only marginal increase in $\boldsymbol{\omega}_{S/N}$. Shorter arcs are useful as the satellite's spin state could be slowly changing due to environmental torques.

6.2.4   2D Rotationally Phased Doppler Pole Estimation

For shorter observing arcs and/or low inclination satellites where 3D RPD is not possible, the approach can be reduced to two dimensions for satellites with known radial extent r, yielding two candidate pole solutions (because the sign of the out of plane velocity component is unconstrained). Denoting $\beta_i(\tau)$ as the angle between the instantaneous velocity $\boldsymbol{v}(\tau)$ and the antenna direction $\hat{\boldsymbol{s}}_i(\tau)$ we have,

$$\cos \beta_i(\tau) = \frac{\lambda_t P_{\bar{\phi}} f_{d_i}(\tau)}{4\pi r} \tag{6.14}$$

Eq. 6.14 yields a single cone around $\hat{\boldsymbol{s}}_i(\tau)$ on which $\boldsymbol{v}(\tau)$ lies. Using three or more observations spaced at multiples of the candidate $P_{\bar{\phi}}$, we find the value of $P_{\bar{\phi}}$ where all cones mutually intersect (i.e. self-consistent inertial velocity directions). This provides the two possible solutions for the velocity direction at that rotational phase. Solving at successive rotational phases yields additional velocities, providing the two candidate rotation planes and pole directions.

Chapter 7

Observation Results

The five GOES 8-12 satellites have been observed periodically between 2013 and 2020. Optical light curves were collected at the Maui Research and Technology Center (MRTC) [27], the US Naval Observatory (USNO) Flagstaff Station, Magdalena Ridge Observatory [94, 11], and Lowell Observatory [11]. Subsets of these GOES satellites were observed using Doppler radar at NASA Goldstone Deep Space Communications Complex on Dec. 6, 2019 and Feb. 18 - 20, 2020. Two of Goldstone's 34 meter Deep Space Network (DSN) antennas were used in a bi-static configuration with one antenna transmitting and the second receiving the reflected echoes. The transmitted signal consisted of fixed frequency, continuous wave carrier at X-band ($\sim$7150 MHz). We cycled periodically between targets over the course of the night to sample different inertial viewing directions for each. On several radar nights, near-simultaneous photometry was collected using a 12 inch aperture f/6.6 Schmidt Cassegrain telescope at Magdalena Ridge Observatory (MRO) in New Mexico.

7.1 GOES 8

Of the five GOES satellites, observations collected from 2013 to 2020 have shown GOES 8 to exhibit the most significant dynamical evolution. Optical light curves indicate its uniform spin period ($P_{\bar{\phi}}$) steadily increased from 16.48 s to 75.66 s between February and July 2014 [27, 94]. Optical light curves and Doppler radar echoes collected between 2014 and 2020 will now be analyzed and discussed to better understand the satellite's subsequent spin state evolution.

7.1.1 September 2014

In September 2014, the USNO COTS instrument obtained the following observations in Figure 7.1. These data were collected at a 37 s sampling cadence with 32 s exposures and have been calibrated to apparent V magnitude (courtesy Dave Monet). Both light curves in Fig 7.1 fold well on periods of ∼40 min, suggesting that the satellite is in fact rotating slowly and that a much faster spin period is not being under sampled. The variations in light curve structure over successive rotations may be caused by one-time glints, under sampling of features, or mild non-principal axis tumbling. So no definitive conclusions can be drawn about uniform rotation vs. tumbling.

(a) Sept. 22 2014 light curve   (b) phase-folded (P = 41.05 min)

(c) Sept. 25 2014 light curve   (d) phase-folded (P = 39.80 min)
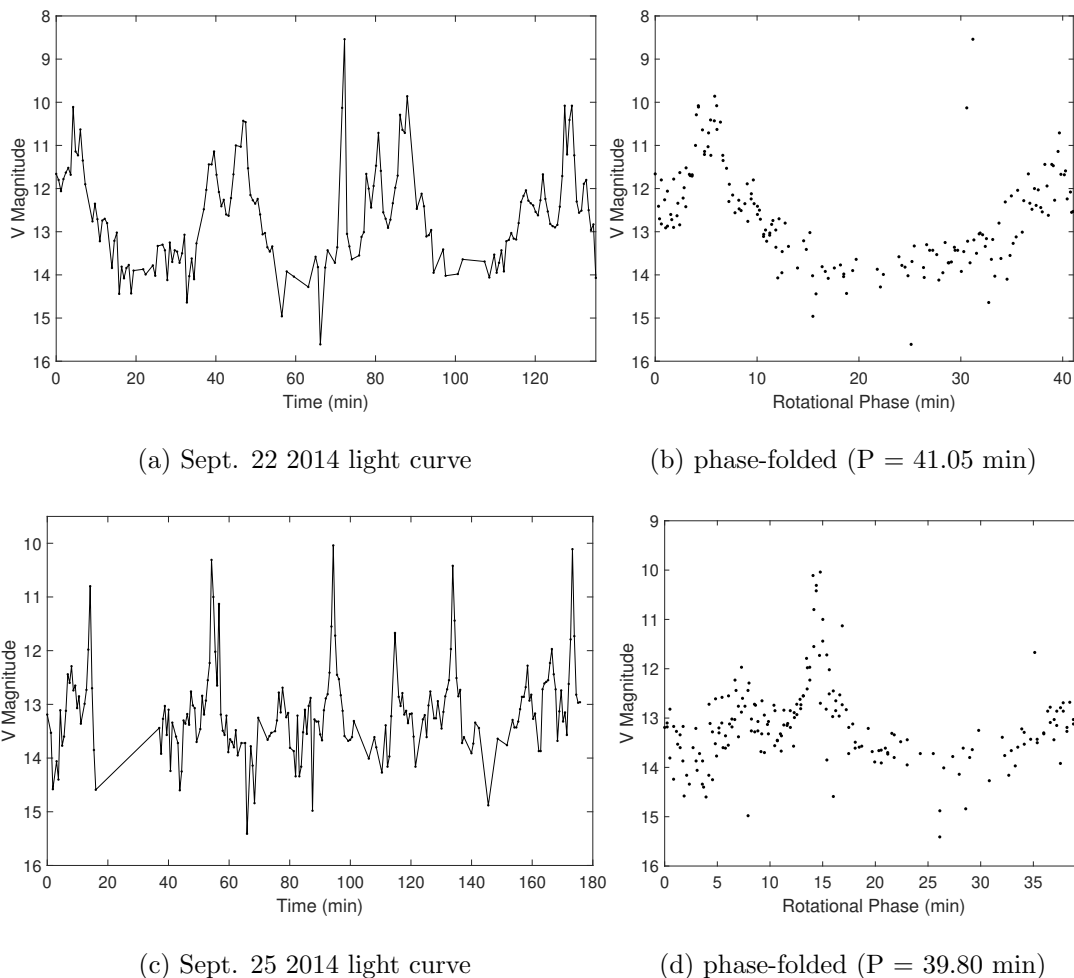
Figure 7.1: September 2014 GOES 8 light curves and minimum dispersion phase-folded solutions.

7.1.2   September 2015

Figure 7.2 shows a light curve obtained with the Magdalena Ridge Observatory (MRO) 2.4 m telescope on 28 September 2015. All MRO observations were taken using an Andor iKon 936 CCD camera and Bessel VR or R filter. Images were taken at a rate of 1 Hz with 0.6 s exposures and reduced using the IRAF phot task, yielding instrumental magnitudes. These observations suggest significantly faster rotation than a year before. The 28 September observations fold on a period of 14.46 ± 0.05 min. Nevertheless, the alignment and amplitude of the peaks is quite variable, suggesting complex rotation. Simulated GOES 8 uniform rotation light curves generally folded more cleanly than this light curve, particularly in terms of peak alignment.

Given the observation gap in the middle of the light curve, a Lomb-Scargle frequency analysis was conducted. It showed the two most dominant frequencies were 0.2772 min^{-1} and 0.5544 min^{-1}. Several peaks at additional multiples of 0.069 min^{-1} were also present. These dominant frequencies, the phase folding results, and light curve survey findings strongly point to the dominant frequency of 0.2772 min^{-1} being $4f_{\bar{\phi}}$ (i.e. $P_{\bar{\phi}} \approx 14.46$ min).
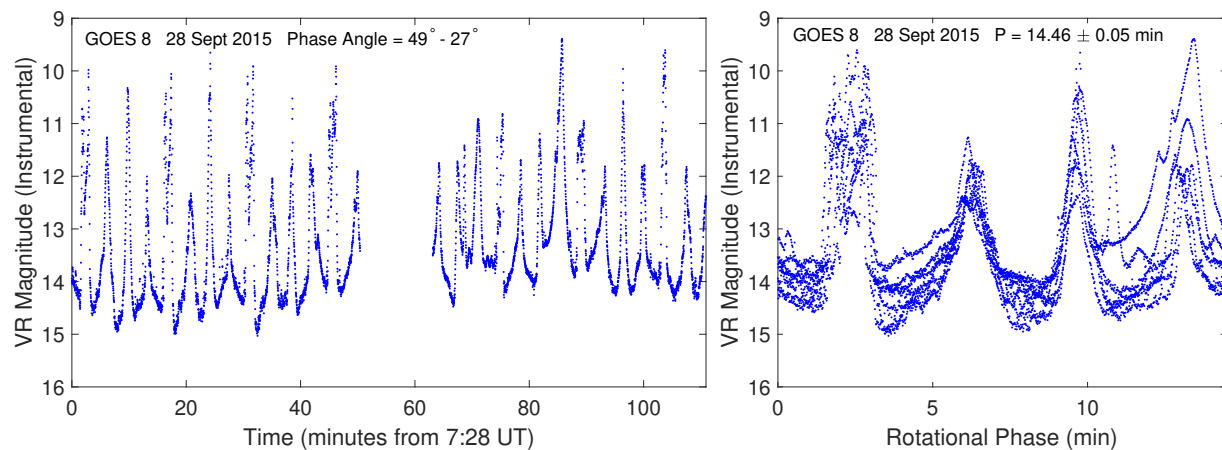
Figure 7.2: Sequential and phase-folded September 28, 2015 GOES 8 light curve (MRO 2.4 m)

7.1.3   April 2018

The GOES 8 light curve in the top plot of Figure 7.3 was obtained on 19 April 2018 with the MRO 2.4 m telescope. These data were collected using a Bessel R filter and processed in the same fashion as the previous MRO observations except that they were calibrated to apparent R magnitude. The high frequency of this light curve suggests rapid rotation but there is no clearly visible periodicity.
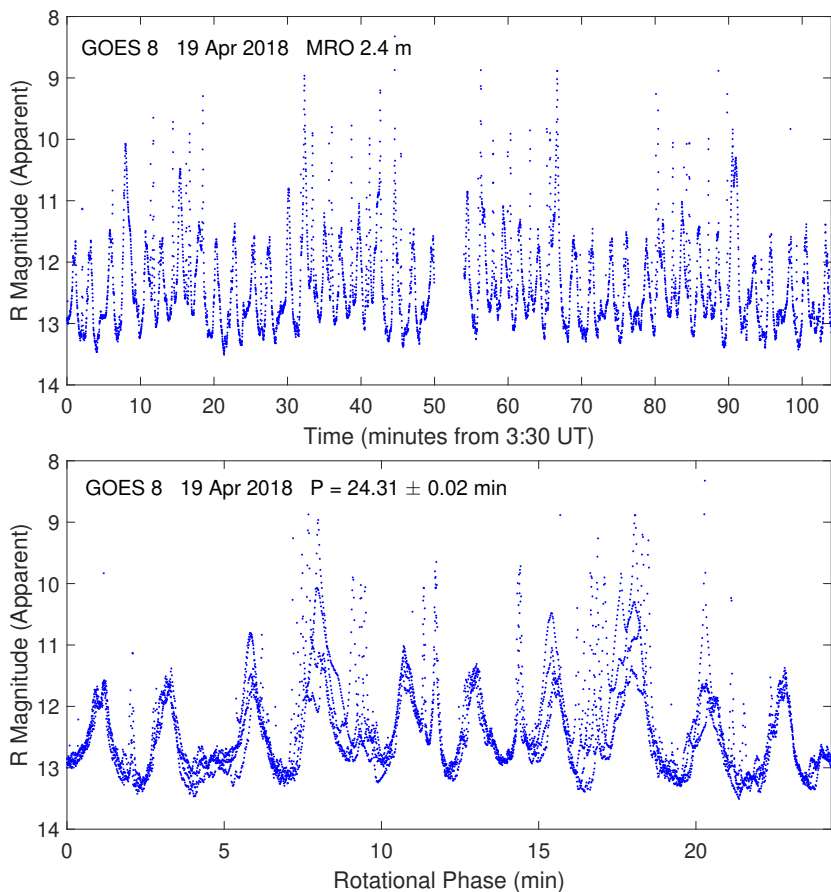
Figure 7.3: Sequential and phase-folded April 19, 2018 GOES 8 light curve (MRO 2.4 m)

An intriguing result is obtained when the 19 April 2018 light curve is phase folded over a large range of candidate periods. In the bottom plot of Figure 7.3, the data are folded on the minimum dispersion period of 24.31 min, showing clear repetition in the 10 broad peaks and many of the

sharper glints (particularly at 2, 11, and 14 minutes of phase). While there are differences in peak amplitudes and misaligned glints, these would not be unexpected for uniform rotation given the varying geometry over the ∼100 min observation arc. The clean folding suggests that the satellite could be in uniform rotation with a 24.31 min spin period. On the other hand, all previous periodic GOES 8 and GOES 10 light curves have had no more than four broad peaks per rotation [27, 94]. Simulated uniform rotation light curve surveys showed the same four peak limit [11]. This light curve would have at least 10 main peaks.
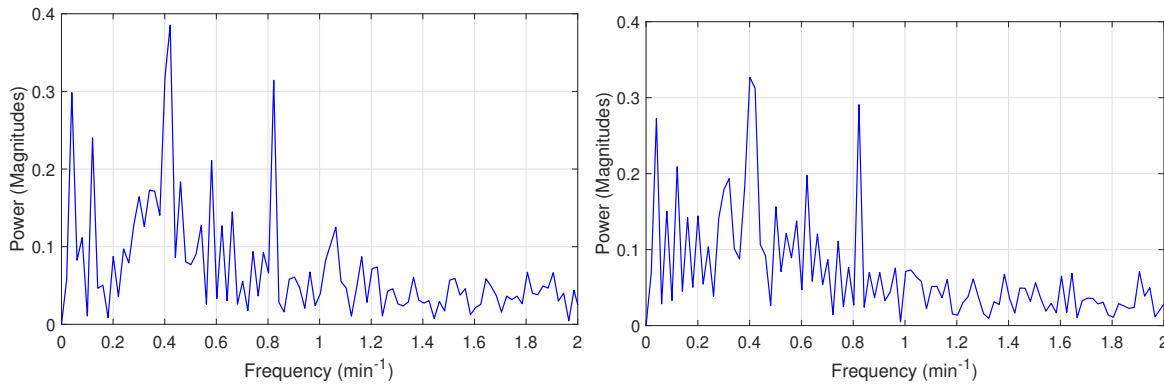
Figure 7.4: April 19, 2018 GOES 8 light curve Power Spectra (Part A and Part B)

Figure 7.4 shows the power spectra for parts A and B of the light curve, generated separately to avoid observation gap aliasing. From left to right, both power spectra show clearly dominant frequencies of 0.04 min^{-1}, 0.12 min^{-1}, 0.41 min^{-1}, and 0.82 min^{-1}, all of which are approximately multiples of 0.04 min^{-1}. This common denominator corresponds to the 24.31 min best fold period from Figure 7.3b. Folding the observations on the next best-fitting periods of 4.88 min and 9.76 min showed significant variation in peak alignment. This suggests that the satellite is actually in a tumbling period resonance with $P_r = 24.31$ min. The frequencies present in the power spectra suggest 0.41 min^{-1} is 2 or $4f_{\bar{\phi}}$, making $P_{\bar{\phi}} \approx 4.88$ min or 9.76 min. This would mean that $m = P_r/P_{\bar{\phi}} = 5$ or 2.5 respectively. Given m for the 9.76 min period is not an integer, the satellite would be half a precession cycle off in 24.31 min and the light curve would likely not fold as cleanly. No clear improvement was made when folding the observed light curve on a 48.62 min period.

Given this, $P_{\bar{\phi}} \approx 4.88$ min is the most likely solution. From simulated tumbling light curve surveys, the left most clean power spectrum frequency was most often f_ψ. This suggests that $f_\psi \approx 0.04$ min^{-1} and $P_\psi = 24.31$ min. Overall, these period assignments would mean the satellite is in a $P_\psi/P_{\bar{\phi}} = 5{:}1$ tumbling resonance which is possible for both LAMs and SAMs.

7.1.4 December 2019

Doppler radar echoes for GOES collected were collected on Dec. 6, 2019. With the echoes recorded, windowed FFT analysis was conducted to obtain Doppler spectra vs. time. Adjustment of the FFT integration time allowed for trade off between temporal and frequency resolution. To maintain roughly equal Doppler and rotational phase resolution for all observations, FFT integration times were adjusted for the extracted precession periods. With a fixed frequency carrier, orbital Doppler was removed in post-processing using TLEs for the satellites and JPL NAIF SPICE ephemerides for the antennas.

Figure 7.5 shows the resulting Doppler spectra vs. time, collected roughly three hours apart. Comparing with the simulated Doppler echoes in Figure 6.8, we can clearly identify the solar sail, solar panel, and bus echoes. Phase-folding the observations yielded $P_{\bar{\phi}}^{\mathrm{syn}} = 353$ s (5.9 min). There are additional rotating features visible that lag roughly $45°$ behind the solar sail sinusoid (e.g. at $+4$ Hz at $\sim$700 s and $\sim$1100 s in the top plot and 400s and 2500 s in the bottom plot). These are likely due to the satellite's magnetometer boom and/or telemetry and control antenna which protrude several meters from the bus (see Figure 2.5). Tracing these features through both plots, we see that their amplitudes vary over successive precession periods, indicating long axis rotation and therefore non-principal axis tumbling. With long axis rotation, the projected area of the solar panel along the satellite to antenna line of sight $\hat{s}$ would change, likely affecting the panel's echo power. Examination of the top plot in Figure 7.5 shows that the echo power (brightness) within the $+/-$ 5 Hz amplitude solar array sinusoid (i.e. the sinusoid directly out of phase with the large amplitude boom echoes) varies over successive rotations. This is consistent with the varying projected area associated with long axis rotation. Also, we see that the observed Doppler bandwidth in the top

plot is nearly equal to the maximum expected bandwidth for the extracted spin period, indicating we are viewing the pole roughly side-on. Moving to the bottom plot, we see a notable decrease in Doppler bandwidth indicating a somewhat more pole-on view.
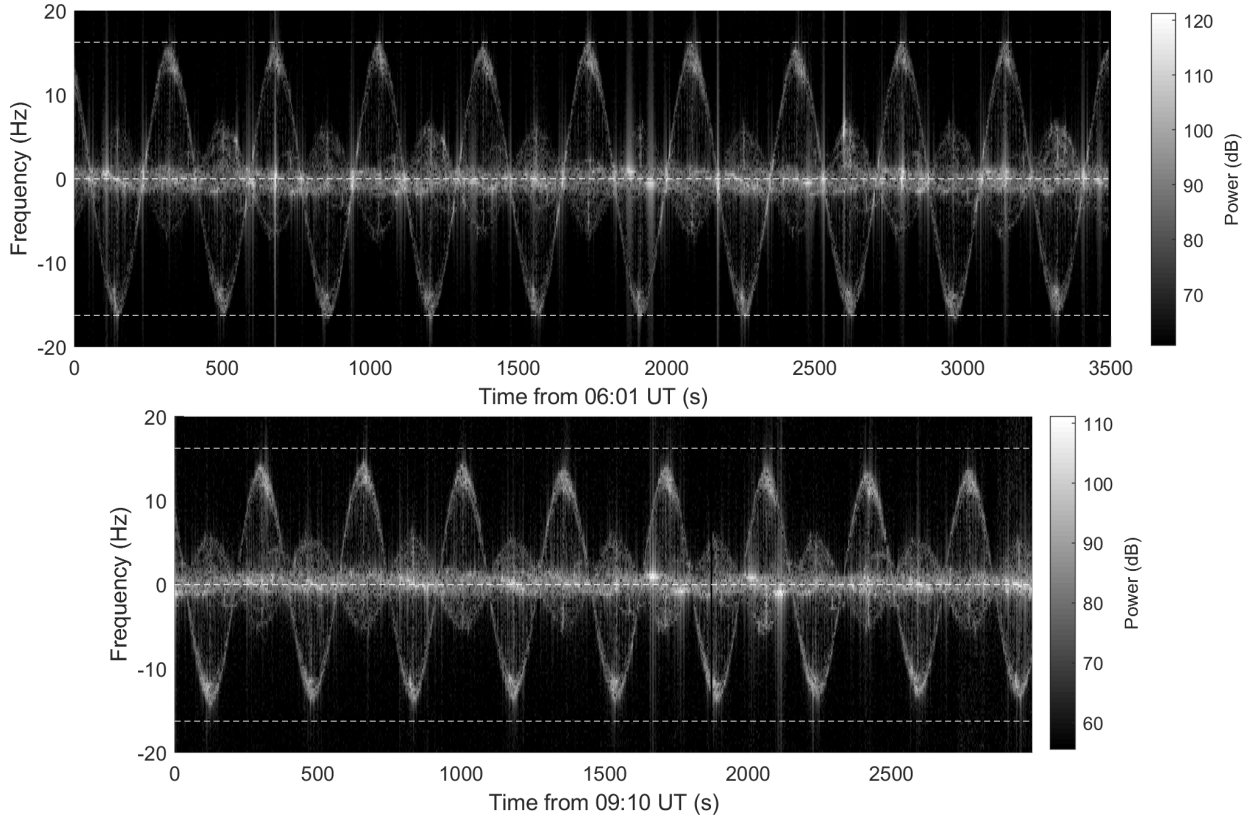
Figure 7.5: Dec. 6, 2019 GOES 8 Doppler echoes. The outer dashed lines denote the maximum expected bandwidth for the extracted precession period $P_{\bar{\phi}}^{\mathrm{syn}} = 353$ (5.9 min)

We analyzed the Dec. 6, 2019 GOES 8 echoes with the Doppler bandwidth and 2D RPD techniques to obtain candidate poles, leveraging GOES 8's known radial extent. The relatively short arc and resulting near-planar observing geometry made the 3D RPD approach infeasible. $P_{\bar{\phi}}$ is almost constant for the tumbling GOES satellites since their mass distributions are nearly prolate. So GOES 8's rotation was assumed to be uniform, allowing us to use the Doppler bandwidth and 2D RPD approaches. The resulting solutions are provided in Figure 7.6 in the J2000 ecliptic frame to allow for natural comparison with the sun and anti-sun directions (shown as filled and open

circles respectively). The Doppler bandwidth approach yields eight possible pole solutions (in four compact regions). 2D RPD eliminates two of these regions. Overall, this analysis suggests GOES 8's pole is below the ecliptic plane with either ecliptic longitude of $\sim$150° and ecliptic latitude of $\sim$-30° or alternatively $\sim$300° and $\sim$-23°.
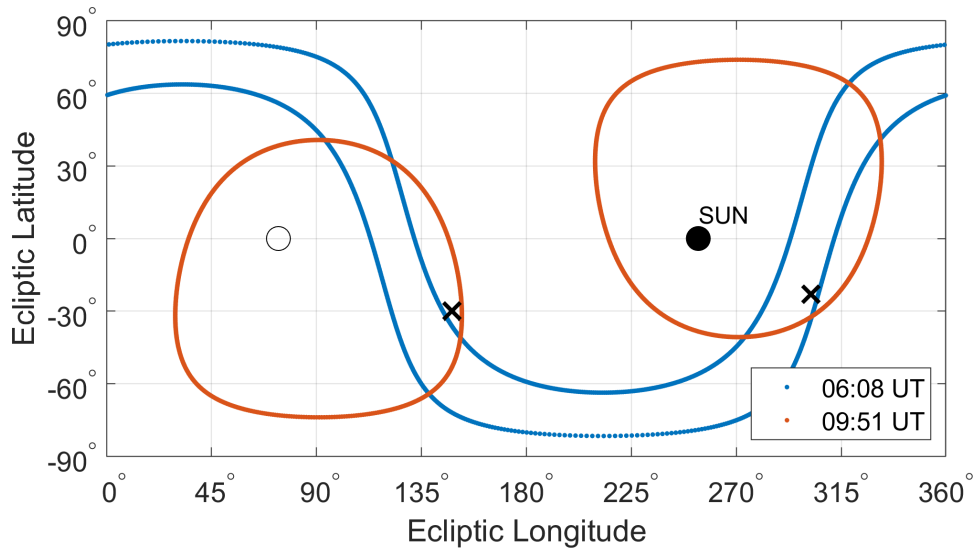
Figure 7.6: Dec. 6, 2019 GOES 8 Candidate Poles in the J2000 Ecliptic Frame. The colored lines and crosses are the Doppler bandwidth and 2D RPD solutions respectively. The open circle is the anti-sun direction.

7.1.5   February 2020

Figure 7.7 shows GOES 8 Doppler echoes obtained on Feb. 18, 2020. Initially, the echoes beginning at 02:42 UT fill nearly the maximum expected Doppler bandwidth for the best-fit phased folded $P_{\bar{\phi}}^{\text{syn}} = 216$ s (3.60 min). This indicates a nearly side on view of the pole (i.e. roughly along GOES 8's equator). Continuing through time over the remaining three plots there is a significant decrease in Doppler bandwidth indicates a progressively more pole on view.
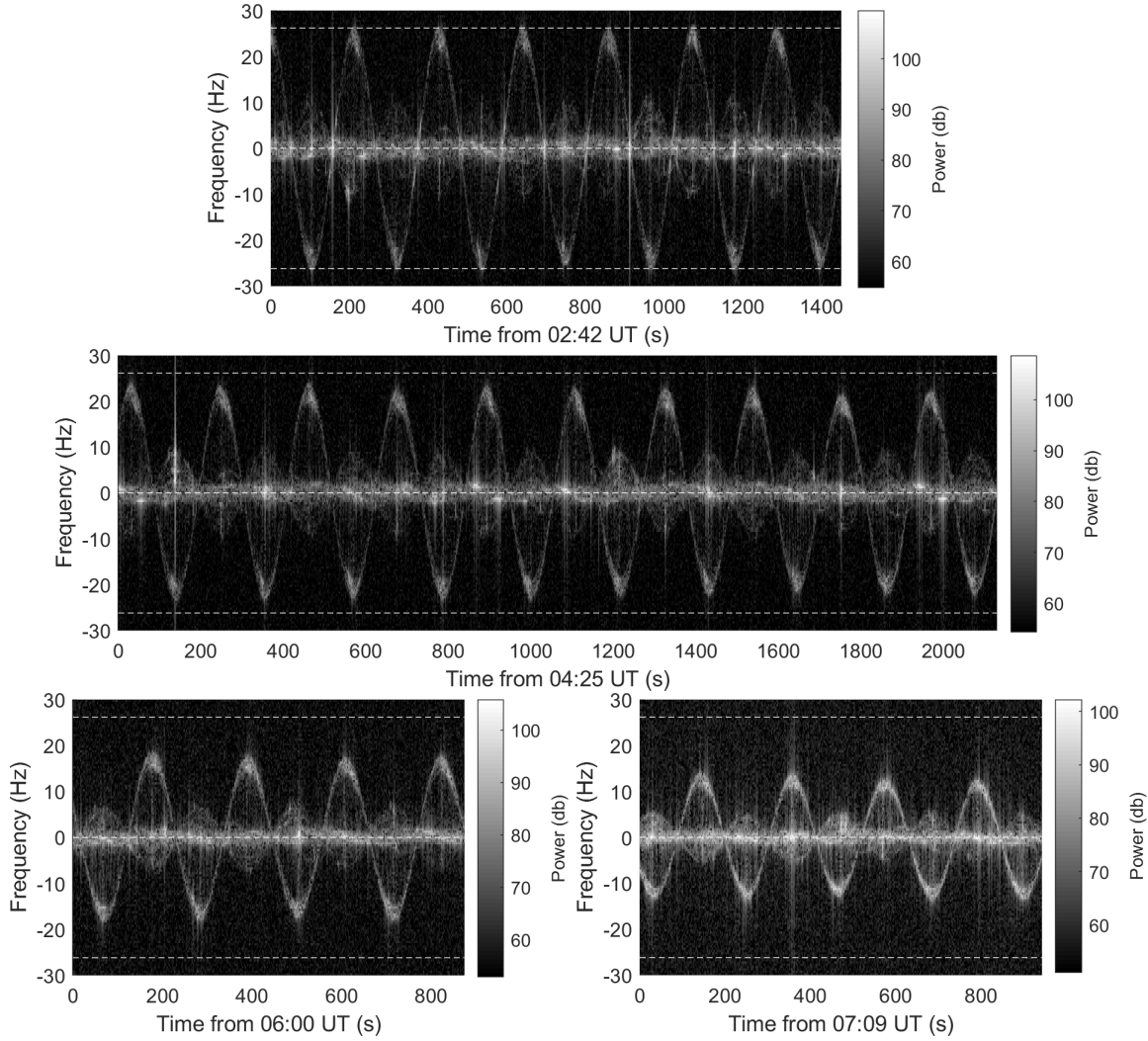
Figure 7.7: Feb. 18, 2020 GOES 8 Doppler echoes. The extracted $P_{\bar{\phi}}^{\text{syn}} = 216$ s (3.6 min).

Figure 7.8 shows the candidate poles for GOES 8 on Feb, 18, 2020. We see that the Doppler bandwidth solutions and 2D RPD solutions are consistent with one another indicating the pole has ecliptic longitude ~135° and latitude ~15° or ~325° and ~25°. Fortunately, the GOES 8 observation geometry was well-enough spaced on this day to attempt 3D RPD analysis. The tentative 3D RPD solution is shown as a black diamond in Figure 7.8 and is near the left-most Doppler bandwidth/2D RPD solution. We are somewhat confident in this 3D RPD solution because it yielded almost exactly the same $P_{\bar{\phi}}$ estimate as the 2D RPD solution (215.0 s) with a derived radial extent of 22 m (slightly more than GOES 8's known boom length). Regardless, both

candidate solutions place GOES 8's pole within 30° of the sun/anti-sun line. Furthermore, the two pole solutions obtained from Feb. 20, 2020 GOES 8 Doppler echoes were virtually the same as for Feb. 18, increasing our confidence in these candidate solutions.
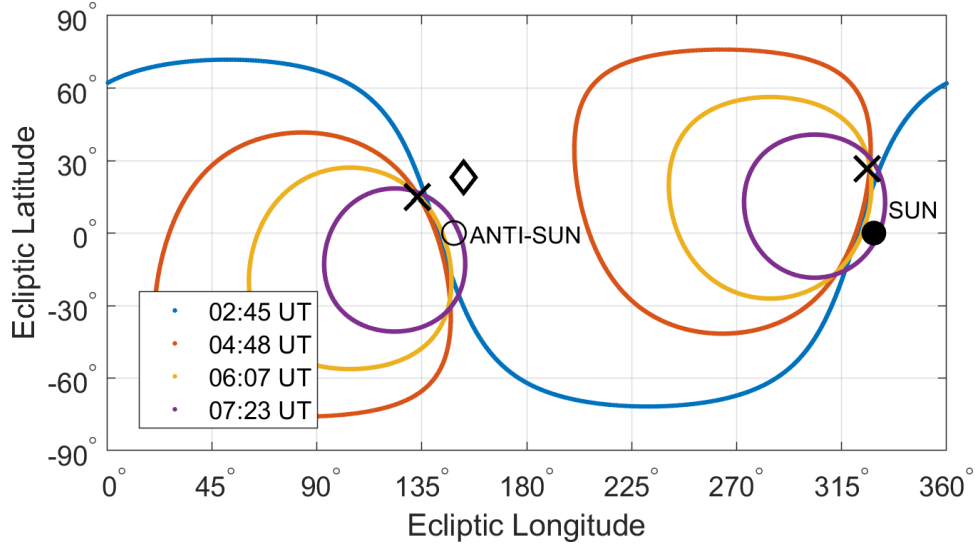
Figure 7.8: Feb. 18, 2020 GOES 8 Candidate Poles. The colored lines and crosses are the Doppler bandwidth and 2D RPD solutions respectively. The black diamond denotes the tentative 3D RPD solution.

On Feb. 18, GOES 8 photometry was also obtained at Magdalena Ridge Observatory (MRO). With images contaminated by background stars removed, the reduced light curve is provided in Figure 7.9. The complexity of this light curve is clear indication of non-principal axis tumbling. With $P_{\bar{\phi}}^{\text{syn}}$ unambiguously provided by radar, we would like to estimate the long axis rotation period P_ψ. Fitting the light curve with a fourth order (m = 4) two dimensional Fourier series across a range of candidate P_ψ values, we obtain the best-fitting solution with $P_\psi = 17.94$ min. Interestingly, this is almost exactly 5 times $P_{\bar{\phi}}^{\text{syn}}$. Similar to the April 2018 observations, the light curve is much too complex for uniform rotation. Furthermore, Lomb-Scargle periodogram analysis provided in Figure 7.10b (used instead of FFT analysis due to observation gaps) showed significant frequencies at 0.057, 0.34, 0.39, and 0.56 min^{-1}. These would correspond to f_ψ, $f_{\bar{\phi}} + f_\psi$, $f_{\bar{\phi}} + 2f_\psi$, and $2f_{\bar{\phi}}$,

with $2f_{\bar{\phi}}$ having the highest Lomb-Scargle significance by a factor of two. These harmonics were commonly observed in the simulated tumbling GOES light curve surveys in Chapter 6 and Benson et al. [11]. Phase-folding the light curve (Figure 7.9a), we find that it repeats almost exactly on this candidate P_ψ. Folding on $P_{\bar{\phi}}$ yielded significantly poorer peak alignment. Since GOES 8 is nearly prolate, if the two fundamental tumbling periods $P_{\bar{\phi}}$ and P_ψ are multiples of each other, the satellite will periodically return to approximately the same inertial attitude. Closely inspecting the 04:25 UT plot in Figure 7.7, the magnetometer/antenna echoes repeat after five precession periods, suggesting the satellite has returned to the same inertial attitude. The first appearance is at 260 s and +5 Hz and they return to the same spot relative to the solar sail echoes at 1340 s and +5 Hz. Overall, these findings strongly suggest the satellite is in a $P_\psi/P_{\bar{\phi}} = 5{:}1$ tumbling resonance with tumbling periods $P_{\bar{\phi}} \sim 3.60$ min and $P_\psi \sim 17.94$ min.
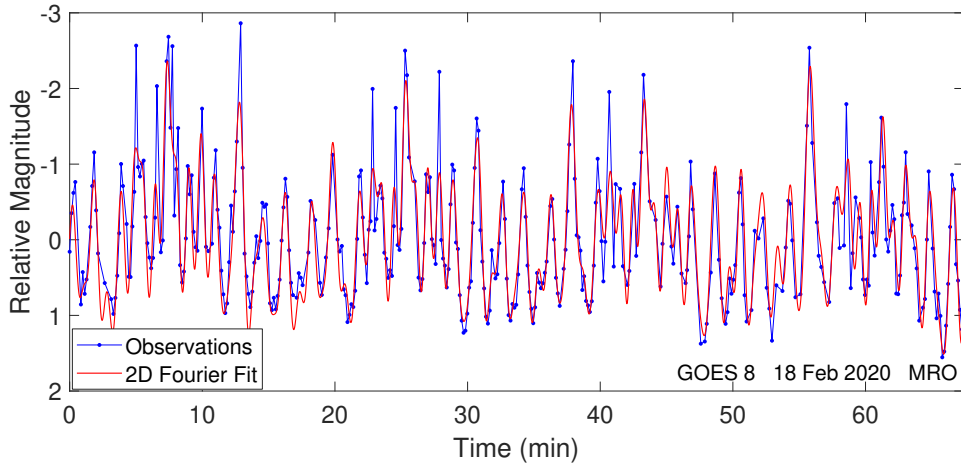
Figure 7.9: Feb. 18, 2020 GOES 8 light curve and 2D Fourier series fit ($m = 4$, $P_1 = 3.60$ min, $P_2 = 17.94$ min)

(a) phase-folded light curve ($P = 17.92$ min)   (b) Lomb-Scargle Periodogram
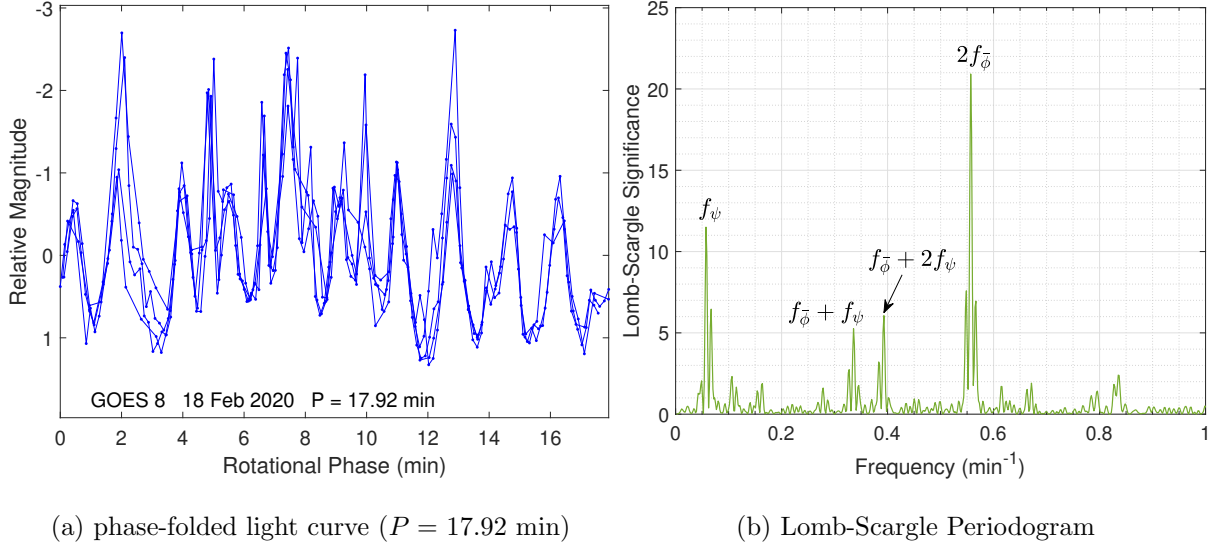
Figure 7.10: Feb. 18, 2020 GOES 8 light curve analysis

7.2   GOES 9

GOES 9 was observed on July 4, 2014 at MRTC revealing slow complex rotation with best-fit phase folded periods of 22.7 min and 9.1 min corresponding to five and two broad peaks respectively [27]. These data are provided in Figure 7.12. Also, an ensemble of USNO COTS light curves were collected between late 2014 and early 2018 and did not show evidence for significant changes in spin rate. Combined with the July 3, 2016 results below, this suggests that GOES 9 remained in the tumbling regime between 2014 and 2018.

GOES 9 optical photometry was obtained using Lowell Observatory's 1.1 m Hall telescope on July 3, 2016. The resulting light curve and Lomb-Scargle periodogram are provided in Figure 7.11. The lack of clear periodicity in the light curve indicates tumbling. From left to right, the dominant Lomb-Scargle frequencies are 0.0464, 0.131, 0.215, and 0.422 min^{-1}. From the simulated light curve trends, the 0.215 min^{-1} peak likely corresponds to $2f_{\bar{\phi}}$ or somewhat less likely $4f_{\bar{\phi}}$ and the 0.422 min^{-1} peak to 4 or $8f_{\bar{\phi}}$ respectively. This corresponds to $P_{\bar{\phi}} \sim 9.3$ min or ~ 18.6 min. Assuming $P_{\bar{\phi}} \sim 9.3$ min, we can consider possible f_{ψ} assignments with the two left-most peaks which are not sub-harmonics of the others. If the left-most peak at 0.0464 min^{-1} is f_{ψ}, then the 0.131 min^{-1} peak

would not align with any low order harmonics (e.g. $f_{\bar{\phi}} + f_\psi$ or $f_{\bar{\phi}} - 2f_\psi$). So instead, a plausible assignment for 0.0464 min^{-1} is $2f_\psi$ (i.e. $f_\psi \sim 0.0232$ min^{-1}). Then the 0.131 min^{-1} peak would correspond to $f_{\bar{\phi}} + f_\psi$, a harmonic often having the second largest amplitude in simulated light curve surveys (see Figure 6.4). Overall, these assignments would imply $P_{\bar{\phi}} \sim 9.3$ min and $P_\psi \sim 43.1$ min and $P_\psi/P_{\bar{\phi}} \sim 4.7$.
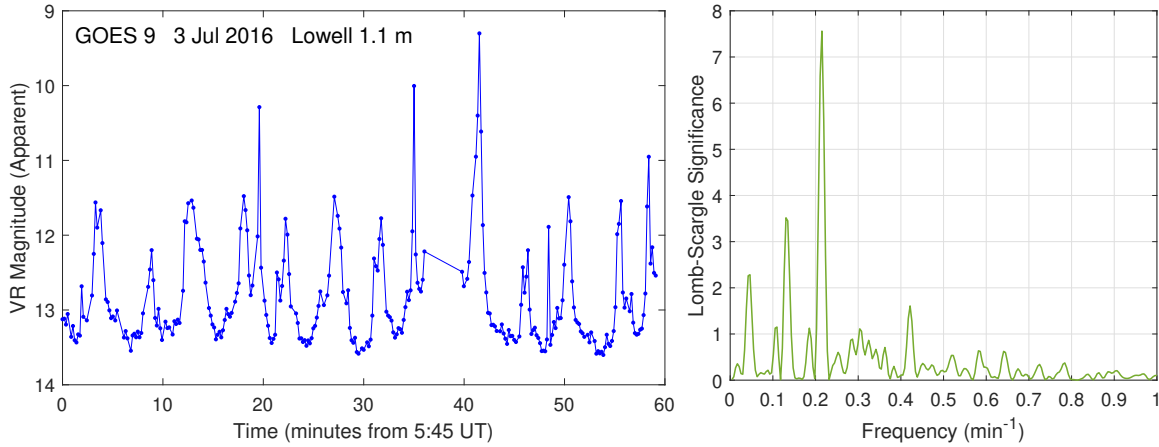
Figure 7.11: July 3, 2016 GOES 9 light curve and Lomb-Scargle Periodogram

The best-fit phase folded periods from July 4, 2014 are very similar to the likely $P_{\bar{\phi}} \sim 9.3$ min assignment for the July 3, 2016 light curve where $2f_{\bar{\phi}}$ would be the dominant frequency and $5P_{\bar{\phi}}/2$ $\sim$22.7 min. Furthermore, the final 25 min of the 2014 light curve and the first part of the 2016 light curve closely overlap as shown in Figure 7.12, suggesting very similar tumbling periods. With pole direction significantly affecting light curve structure, the similarity of the two light curves also suggests nearly the same pole direction at these two epochs.
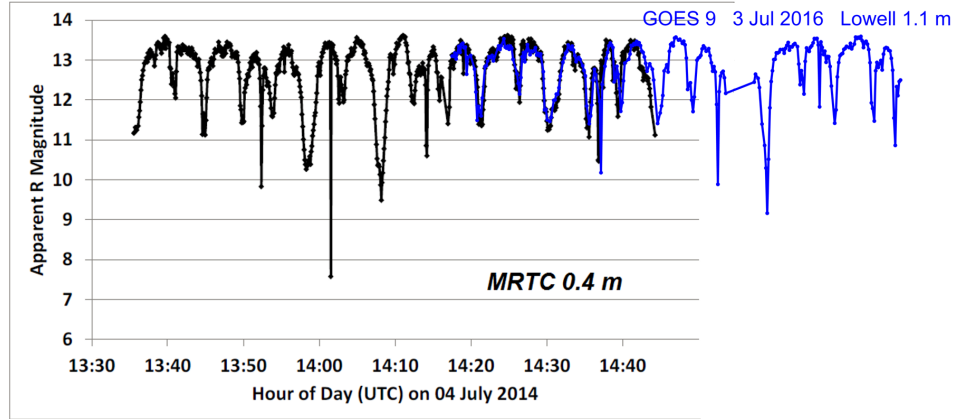
Figure 7.12: July 4, 2014 and July 3, 2016 GOES 9 light curves (black from [27])

7.3   GOES 10

GOES 10 was observed on several ocassions between February and August 2014, revealing a uniform spin period that decreased from 31.1 s to 26.2 s [27]. Additional observations were obtained on June 5, 2018 with the USNO 1.3 m telescope. These observations were collected at an 8.6 s sampling cadence with 5 s exposures and reduced to instrumental magnitudes. A 130 min subset of the data is provided in Fig. 7.13 phase folded on a period of 25.18 s. The data fold well, indicating uniform rotation. The outlying points are likely due to background field star contamination and one-time glints as formal uncertainties on the data were all below 0.05 magnitudes. The corresponding Lomb-Scargle periodogram is provided in Figure 7.13 with a lone significant peak at 2.381 min^{-1} (period of $\sim$25.20 s), further indicating $P_{\phi}^{-} \sim 25.2$ s.
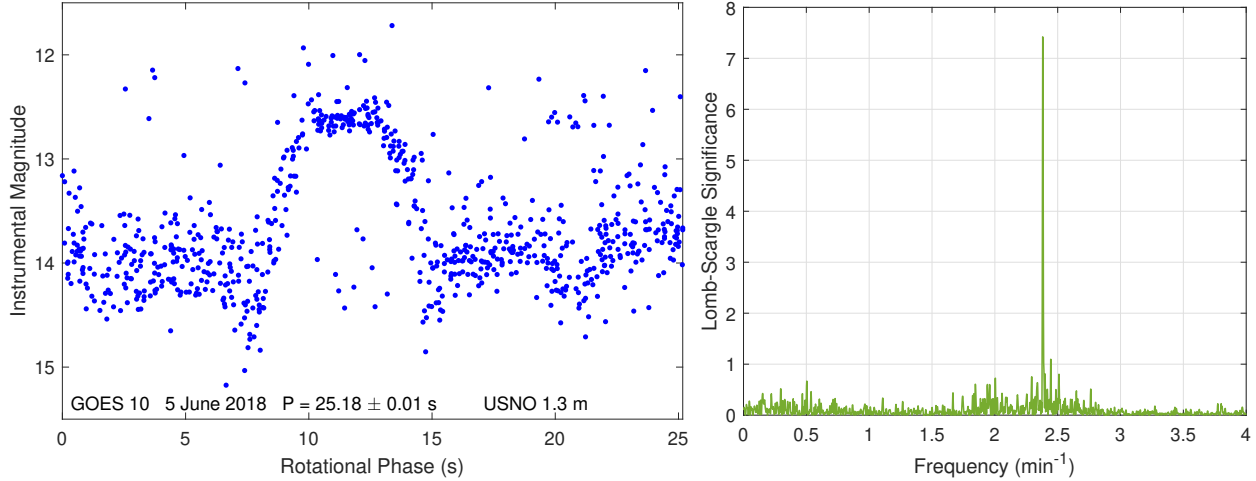
Figure 7.13: Phase-Folded June 5, 2018 GOES 10 light curve and Lomb-Scargle Periodogram

In addition, a number of GOES 10 light curves were collected with the USNO COTS array from late 2014 through mid 2018. While sparsely sampled at a cadence of 37 s with 32 s exposures, all light curves showed high frequency brightness variations. These findings combined with the results in Fig. 7.13 suggest that GOES 10 remained in rapid uniform rotation over this roughly four year span.

GOES 10 Doppler echoes were obtained on February 18, 2020. A subset of the data are provided in Figure 7.14. We see rapid rotation with $P_{\bar{\phi}}^{\text{syn}} \sim 30.5$ s and Doppler bandwidth exceeding ± 150 Hz. Utilizing observations spanning roughly three hours, the four Doppler bandwidth candidate pole estimates are provided in Figure 7.15 along with the two possible solutions provided by 2D RPD. Each 2D RPD solution is near a Doppler bandwidth solution, both differing slightly in longitude. The Doppler bandwidth solutions indicate the pole has either ecliptic longitude and latitude of $\sim 45°$ and $\sim 40°$ or alternatively $\sim 180°$ and $\sim 67°$.
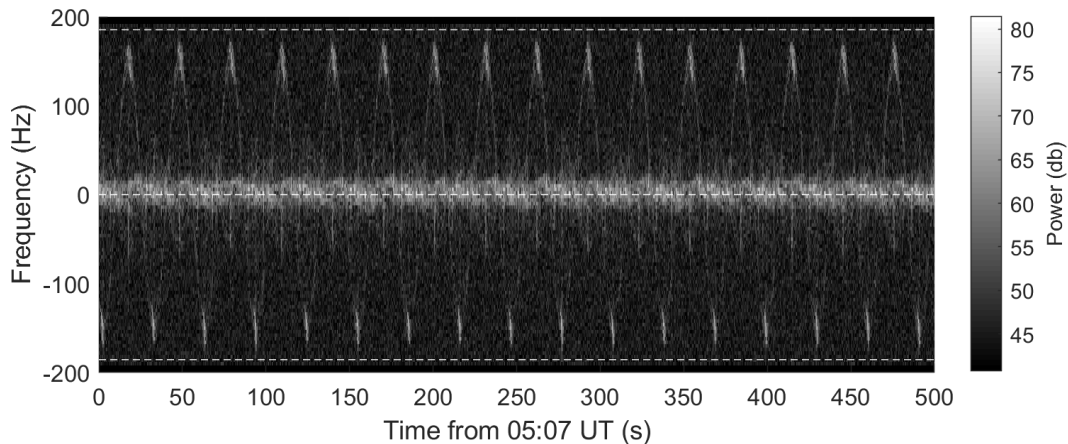
Figure 7.14: Feb. 18, 2020 GOES 10 Doppler echoes. The extracted $P_{\bar{\phi}}^{\mathrm{syn}} = 30.5$ s.
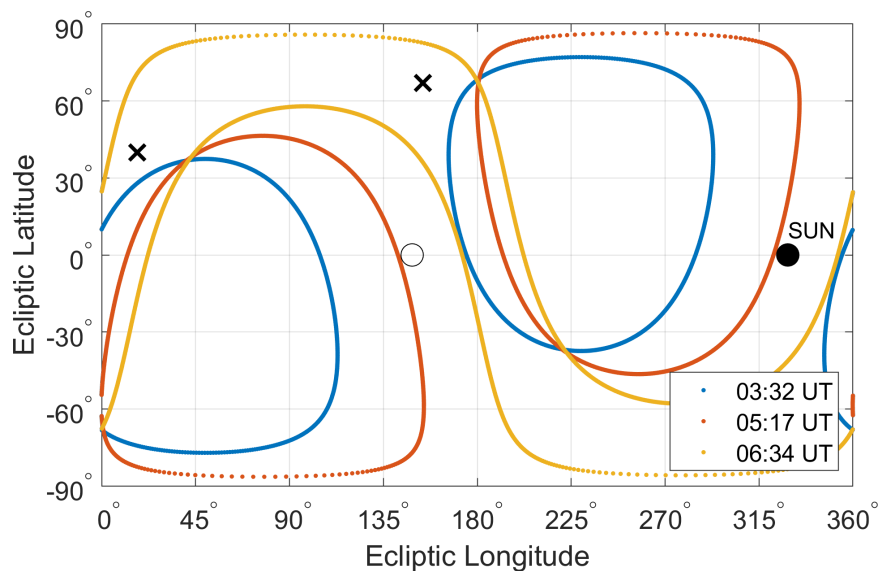
Figure 7.15: Feb. 18, 2020 GOES 10 Candidate Poles.

7.4   GOES 11

GOES 11 was observed in August 2014 with the light curve showing a best-fit phase folded period of 20.9 min [27]. The observations folded poorly on this period, suggesting the satellite was in complex rotation. High fidelity simulated GOES light curve surveys showed that slow uniform rotation light curves still fold well, indicating the poor GOES 11 light curve folding is likely due to

complex rotation rather than changing sun-satellite-observer phase angle [11]. Additional GOES 11 observations were collected with the USNO COTS array. These data consist of over 100 light curves obtained between 2014 and 2018. Each light curve was analyzed with a Lomb-Scargle periodogram and minimum dispersion phase folding to obtain strong periodicities. The top ten most significant Lomb-Scargle periods for each light curve are plotted in Figure 7.16. The size of each data point scales with the period's significance (i.e. the larger, the more significant). There is clear variation in these periods with hints of a yearly cycle. The light curves did not show clear periodicity, suggesting the satellite remained in complex rotation. From the high fidelity GOES light curve simulations, the top Lomb-Scargle frequencies of 2 or $4f_{\bar{\phi}}$ suggest precession periods between 5 and 25 min. This suggests that GOES 11 was in relatively slow, complex rotation with a varying spin rate between 2014 and 2018.
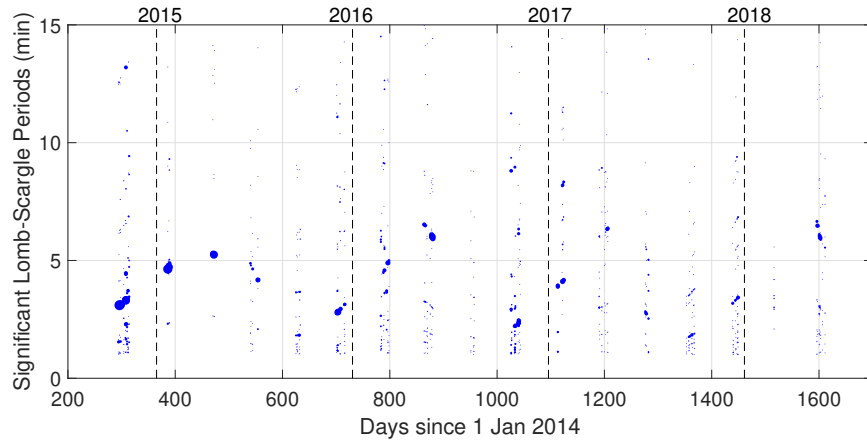
Figure 7.16: GOES 11 Significant Lomb-Scargle Periods

GOES 11 Doppler echoes obtained on Dec. 6, 2019 are provided in Figure 16. Phase-folding the echoes indicated $P_{\bar{\phi}}^{\text{syn}} = 775$ s (12.9 min). Comparing the top and bottom plots in Figure 7.17, we see a significant decrease in Doppler bandwidth over the three hour observation span. The small bandwidth of the 11:10 UT plot suggests a near pole-on view. Photometry collected on Dec. 17, 2019 did not fold cleanly on any candidate rotation period, indicating non-principal axis rotation. Given only 11 days between collection of the photometry and radar, it is very likely

that GOES 11 was also tumbling on Dec. 6. Lomb-Scargle analysis of the photometry suggested $P_{\bar{\phi}}^{\text{syn}} \sim 13$ min. This value is comparable to that obtained from our radar observations 11 days prior. Approximating GOES 11 in uniform rotation and computing the Doppler bandwidth and 2D RPD pole estimates, the resulting solutions are provided in Figure 17. The 2D RPD solutions are in the vicinity of two Doppler bandwidth solutions. These solutions place the pole within $\sim$45° of the sun/anti-sun directions.
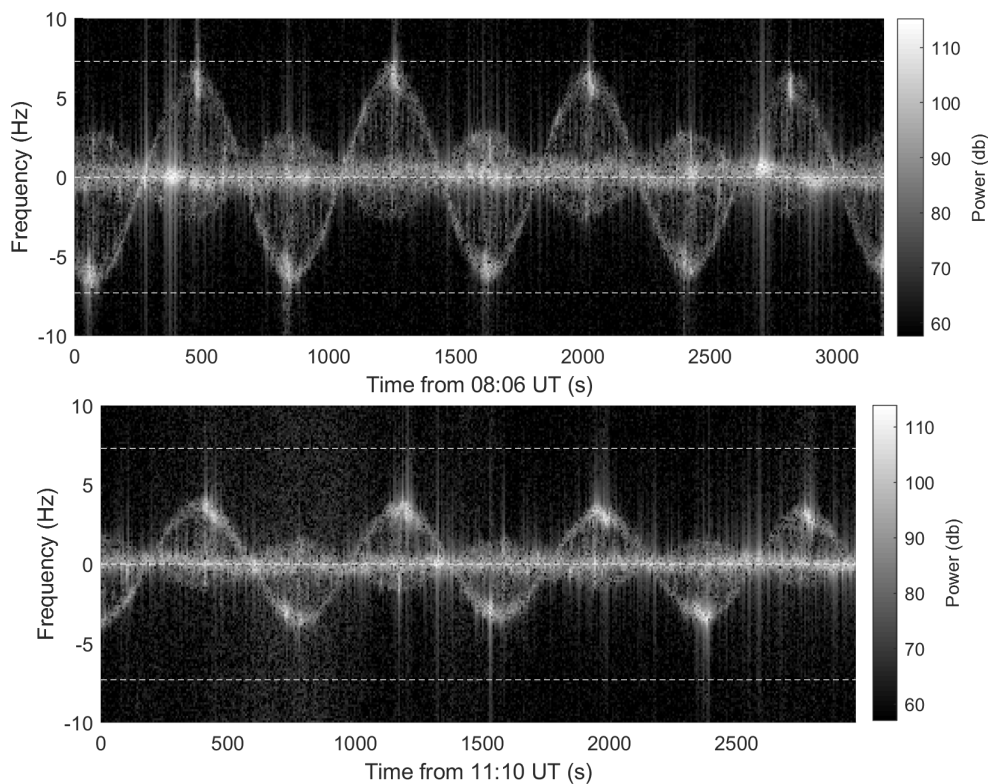
Figure 7.17: Dec. 6, 2019 GOES 11 Doppler echoes. The extracted $P_{\bar{\phi}}^{\text{syn}} = 775$ s (12.9 min).
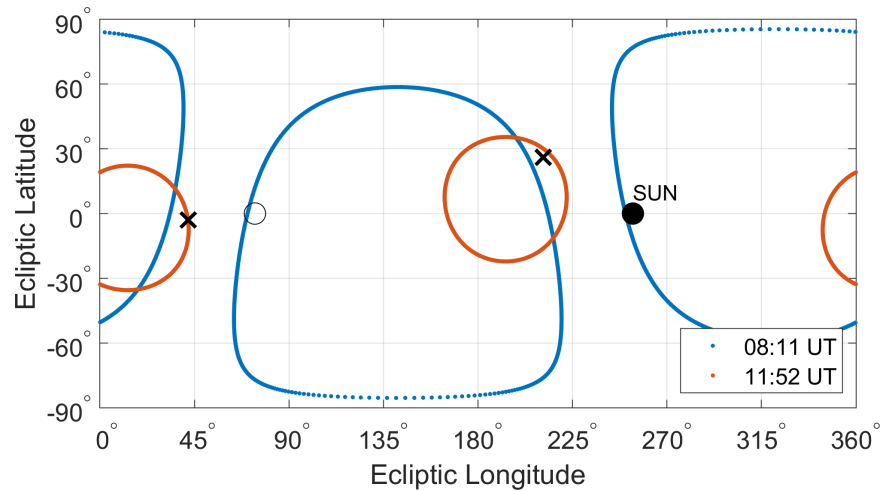
Figure 7.18: Dec. 6, 2019 GOES 11 Candidate Poles.

7.5   GOES 12

GOES 12 was observed on three occasions in 2014 with each light curve showing slow, complex rotation with best-fit phase folded periods between 9.75 and 13.8 min [27]. USNO COTS data for GOES 12 were also collected between 2014 and 2018, but were too sparse to provide significant insight about the satellite's subsequent evolution.

7.5.1   December 2019

GOES 12 was observed with Doppler radar on Dec. 6, 2019 and Feb. 18-20, 2020. The Dec. 6 echoes indicated $P_{\bar{\phi}}^{\text{syn}} = 882$ s (14.7 min). Calculating the Doppler bandwidth and 2D RPD pole estimates, the resulting solutions on Dec. 6, 2019 are provided in Figure 7.19. The December solutions indicate the pole has ecliptic latitude near -45°.
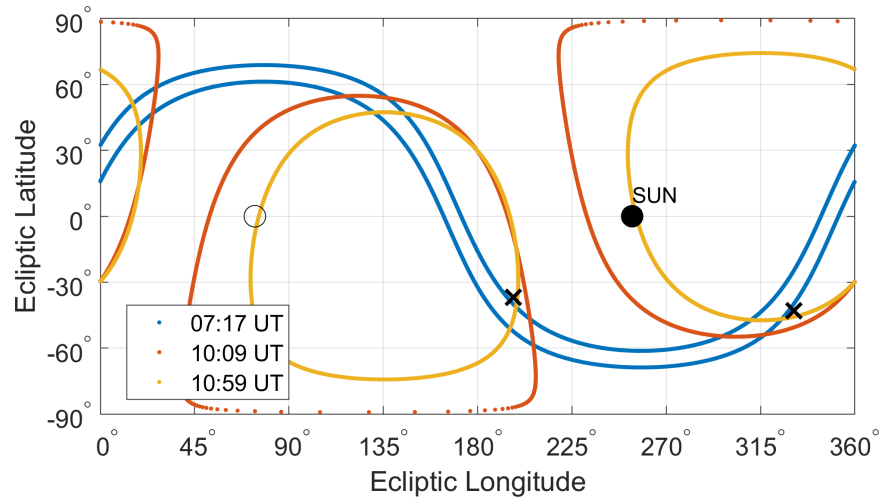
Figure 7.19: Dec. 6, 2019 GOES 12 Candidate Poles.

7.5.2   February 2020

The Feb. 18-20 Doppler echoes indicated $P_{\vec{\phi}}^{\text{syn}}$ decreasing from 462 s (7.7 min) to 454 s (7.6 min). Photometry collected from Feb. 18-20 at MRO indicated GOES 12 was in uniform rotation with a best-fit phase-folded period of $P_{\vec{\phi}}^{\text{syn}} = 7.66$ min, consistent with the radar findings. These data are provided in Figure 7.20, showing four peaks per rotation. The right plot shows the clean folding on the best-fit period. Given the relatively short time span between these observations and those on Dec. 6, 2019, the satellite was likely uniformly rotating on Dec. 6, 2019 as well.
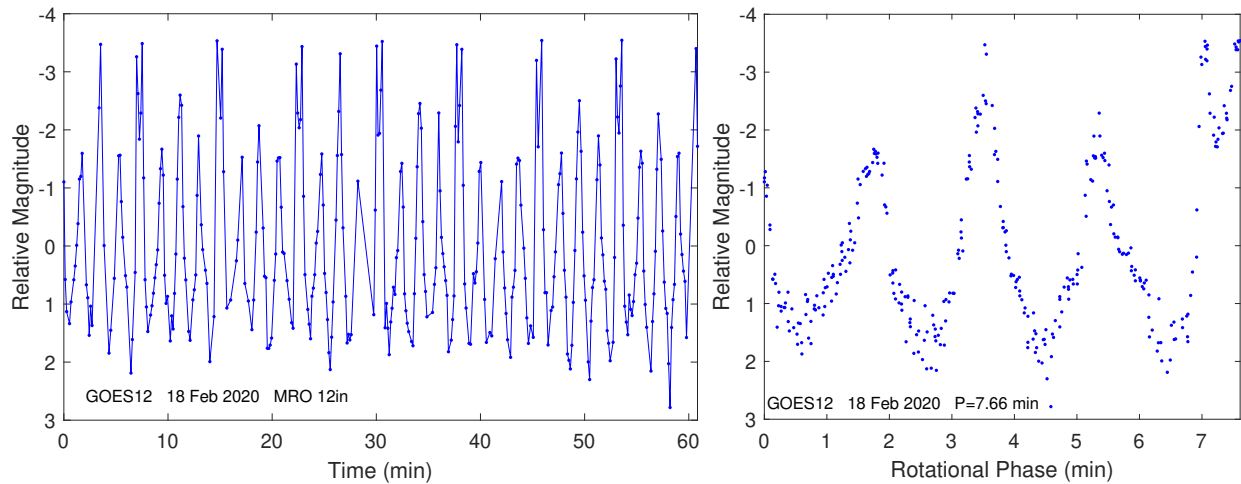
Figure 7.20: Sequential and phase-folded Feb. 18, 2020 GOES 12 light curve

Calculating the Doppler bandwidth and 2D RPD pole estimates, the resulting solutions on Feb. 20, 2020 are provided in Figure 7.21. With the December solutions indicating the pole is below the ecliptic plane, the closest Feb. 18 solution and therefore most likely, has ecliptic longitude $\sim$265° and latitude $\sim$-70°. The two candidate poles on Feb. 18, 2020 were virtually identical to those from Feb. 20.
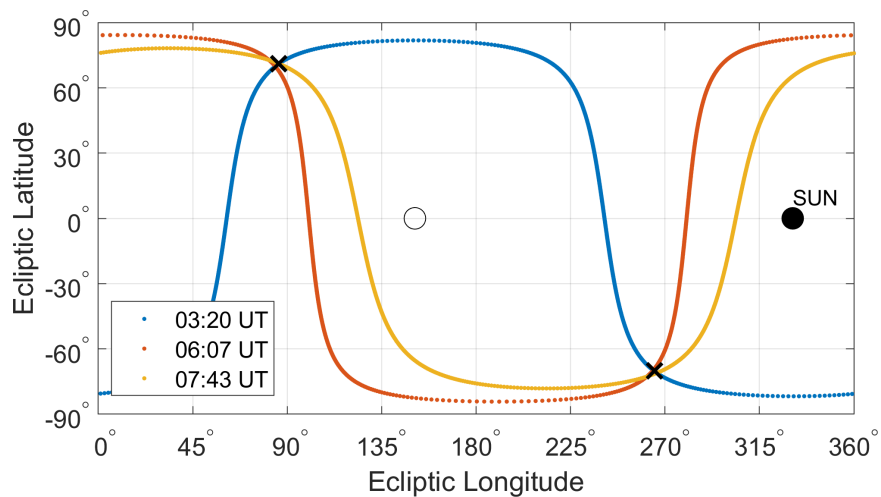
Figure 7.21: Feb. 20, 2020 GOES 12 Candidate Poles.

7.6   Comparisons with Dynamical Modeling

Overall, analysis of light curve and Doppler radar observations of the GOES 8-12 satellites showed diverse spin states and significant evolution over time. This diversity is illustrated by Table 7.1 and Figure 7.23 which summarizes the radar-derived precession periods and pole directions.

Date	GOES 8	GOES 10	GOES 11	GOES 12
Dec. 6, 2019	353 s (5.9 min)	-	775 s (12.9 min)	882 s (14.7 min)
Feb. 18, 2020	215 s (3.58 min)	30.5 s	-	462 s (7.7 min)
Feb. 20, 2020	216 s (3.6 min)	30.5 s	-	452 s (7.6 min)

Table 7.1: Summary of radar-derived GOES $P_{\bar{\phi}}$ Estimates

The evolution of GOES 8's long axis precession rate $f_{\bar{\phi}} = 1/P_{\bar{\phi}}$ from 2013 to 2020 is summarized in Figure 7.22. The satellite spun down rapidly in uniform rotation through 2014, reaching a $P_{\bar{\phi}}$ of at least 40 min in mid-late 2014. The satellite then transitioned to tumbling and has subsequently spun up again while tumbling. The most recent confirmed $P_{\bar{\phi}}$ is ~3.6 min on February 18, 2020. The circled stars in Figure 7.22 denote resonant tumbling states. Also included in Figure 7.22 are two example GOES 8 runs computed with the non-resonant averaged model accounting for YORP, energy dissipation, and gravity gradient torques. Numerically averaged lookup tables were used for the solar torque evaluation. For both runs, the initial precession period was set to GOES 8's December 12, 2013 extracted value of $P_{\bar{\phi}} = 16.83$ s [27]. The initial value of $I_d/I_s = $ 1e-8 (SAM+) was assumed. The dissipation parameters were set to $J = 0.1$ kg·m^2 and $\mu/J = $ 1e-3 s^{-1}. GOES 8's January 1, 2017 inclination and right ascension ($i = 11.2°$ and $\Omega = 40.5°$) were used for the gravity gradient torque evaluation. Simulating 5000 runs with poles randomly drawn from a uniform distribution, the range of initial values yielding spin down matching the September 2014 periods was limited to $\alpha \sim [260°, 330°]$ and $\beta \sim [65°, 110°]$. For all other pole directions, the satellite did not decelerate sufficiently for tumbling transition until at least mid-late 2015. Two of the most consistent examples, denoted Run 1 and 2 in Figure 7.22 have initial values of $\alpha = 297.8°$, $\beta = 104.0°$ and $\alpha = 317.9°$, $\beta = 98.7°$ respectively. The overwhelming majority of runs matching

the observed spin down followed the same general behavior as these two runs. In both Runs 1 and 2, the averaged evolution follows the satellite's observed deceleration, tumbling transition, and tumbling spin up. From early 2017 onward, the averaged runs evolve near the separatrix and the extracted precession rates, taking temporary excursions to uniform rotation, most notably for Run 1. During this time, the tumbling period ratios for both runs frequently pass through 5:1. Overall, GOES 8's evolution since late 2014 is only loosely constrained. There are many pathways it could have taken including one or more intervening tumbling cycles. In any case, the averaged model runs are consistent with the three key aspects of GOES 8's observed evolution: 1) spin down in uniform rotation through mid 2014, 2) subsequent transition to tumbling spin up, and 3) eventual evolution near the separatrix and extracted precession periods.
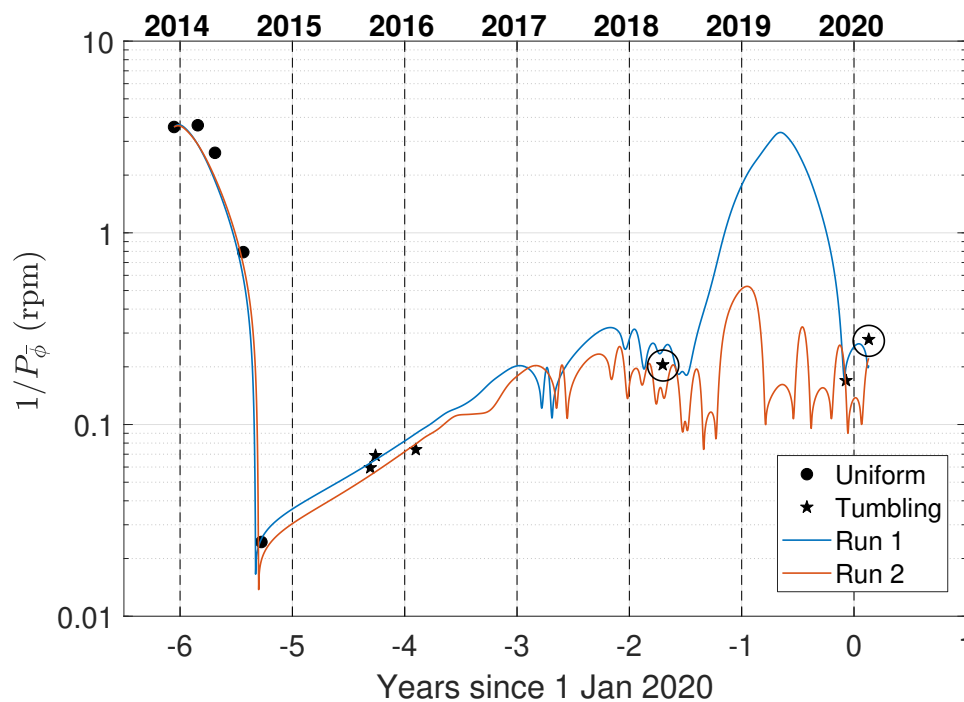
Figure 7.22: Evolution of GOES 8's long axis precession rate $f_{\bar{\phi}} = 1/P_{\bar{\phi}}$ extracted from observations from 2013 to 2020 with example YORP + dissipation + gravity gradient averaged model runs. Circled stars indicate resonant tumbling.

The combined radar and optical data show clear evidence for GOES 8 being captured in a

$P_\psi/P_{\bar\phi} = 5{:}1$ tumbling resonance in February 2020 and likely in April 2018 as well. It is currently unclear whether these 5:1 resonances were LAM or SAM. In full dynamical simulations, the 5:1 SAM resonance was commonly observed when YORP and internal energy dissipation were considered. The inclusion of gravity gradients further increased the frequency of 5:1 SAM resonance capture (see Figure 3.7). For YORP-only simulations, the undamped tumbling cycles pushed the satellite through the narrow I_d region containing the 5:1 SAM resonance rapidly and at extreme β values where capture probability was found to be negligible for the resonance-averaged model (see Figure 5.26). This suggests that internal energy dissipation for GOES 8 is non-negligible. But with the December 2019 and February 2020 GOES 8 radar and optical observations showing a roughly 40% decrease in $P_{\bar\phi}$ and significant change in pole direction relative to the sun line (see Figure 7.23), the satellite does not appear to have reached a limit cycle. This in turn suggests that GOES 8's dissipation rate is not too large. As a result, GOES 8's dissipation appears large enough to prevent consistent tumbling cycles while still being low enough to allow significant tumbling spin state variation and possibly occasional forays into uniform rotation given its uniform spin state from 2013 through 2014. The GOES satellites were retired in their nominal sun-tracking mode with approximately zero spin rate. Full dynamics simulations started with zero spin rate showed tumbling spin up initially, so GOES 8 likely had to escape the tumbling regime at least once prior to its uniform rotation in 2013 and 2014.

One notable discrepancy between the observed and simulated GOES 8 5:1 resonances is the pole direction (i.e. β value) at capture. The February 18, 2020 radar observations suggest GOES 8's pole was within 30° of the sun or anti-sun direction (see Figure 7.8), with the tentative 3D RPD solution indicating the latter solution. The full and averaged model results in Figures 3.7 and 5.26 respectively show that 5:1 SAM resonance capture only occurs near $\beta = 90°$ with dissipation pushing capture to smaller β values. Analysis indicated 5:1 LAM resonance capture region was also limited to $\beta < 90°$. In either case, this is inconsistent with the 3D RPD pole solution which has β near 150°. On the other hand, these simulated resonance capture regions are more consistent with the February 18, 2020 pole solution near the sun line. Detailed fitting of the February 18, 2020

light curve observations is needed to validate this 3D RPD solution. If this pole solution is more consistent with the light curve than the alternative solution near the sun line, that would suggest a modeling discrepancy. One possible factor in this case would be thermal lag which is known to significantly change the pole evolution for asteroids. Thermal lag may shift the 5:1 resonance capture regions towards $\beta > 90°$.
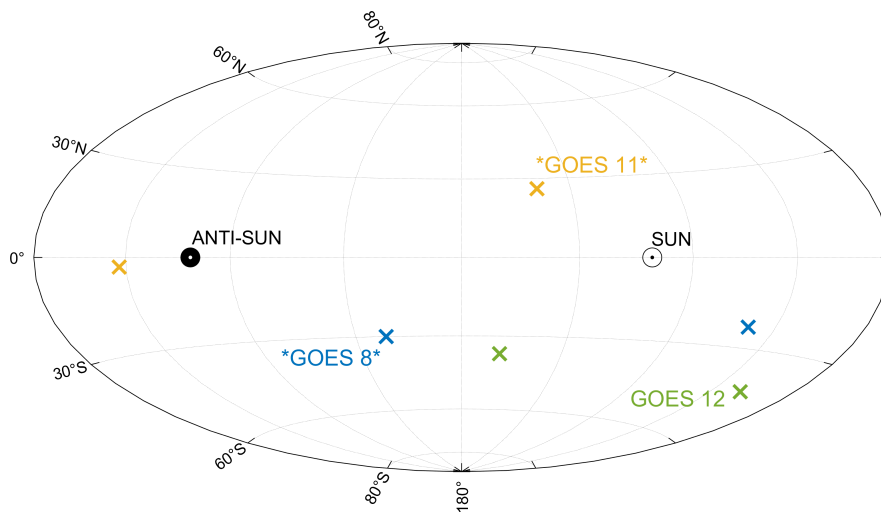
(a) Dec. 6, 2019
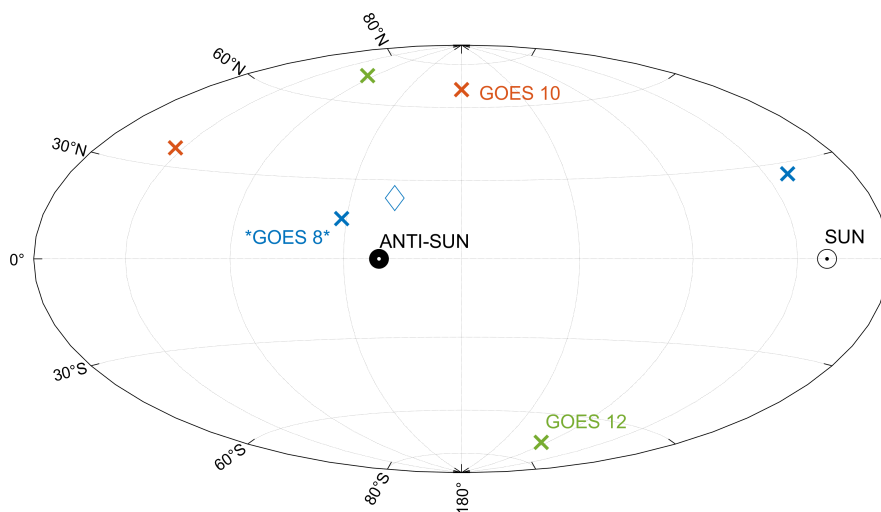
(b) Feb. 18, 2020

Figure 7.23: Radar-derived candidate poles for the GOES satellites in J2000 Ecliptic frame.

GOES 9 appears to have remained in slow tumbling from 2014 through at least 2018. The July 4, 2014 and July 3, 2016 light curves have very similar structure and frequency content, suggesting the satellite's pole direction and tumbling periods were nearly the same with a long axis precession period $P_{\bar{\phi}}$ of roughly 10 min. With the yearly spin state periodicity observed for the YORP + dissipation + gravity gradient tumbling limit cycles (see Figures 5.27 and 5.28), the tumbling periods and pole direction would be the same at given time each year. Furthermore, the period ratio corresponding to the likely July 3, 2016 tumbling periods ($\sim$4.7) places the satellite near the separatrix where the asymptotically stable YORP + dissipation + gravity gradient limit cycles were found in simulations (again see Figures 5.27 and 5.28). It is not clear whether GOES 9's July 2016 tumbling state is LAM or SAM since both are possible for the proposed period ratio. The former would have continuous rotation of the long axis (i.e. ψ) while to latter would instead have libration between two fixed values of ψ. The relatively low temporal resolution of the light curve may prevent disambiguation of these candidate states with high fidelity light curve fitting.

Modeling showed that GOES 9 should be subject to similar, if not larger, YORP-driven accelerations than GOES 8 (see Figure 5.1). In the full and averaged YORP + dissipation + gravity gradient simulations, larger spherical slug inertias resulted in faster capture into the tumbling limit cycles. So, one possible explanation for GOES 9's less variable spin rate compared to GOES 8 is that it has higher dissipation. When passivated at end of life, some fuel in valves and plumbing cannot be purged (Andrew Edwards, Optus, personal comm.). So it is possible that each of the GOES satellites has a different amount of residual fuel. Slight variations in material properties and construction of the satellites could account for some dissipation discrepancy as well. Alternatively, Figure 5.20a shows that the YORP + dissipation equilibria for some values of J are unstable. While the current fidelity model indicates GOES 8 should have at least one stable equilibrium (i.e. SAM+ and/or SAM-) for a wide range of J values, it is possible that neither equilibrium is stable for the true satellite. In this case, the satellite would never settle into a tumbling limit cycle. Even for the same dissipation, the stability of these equilibria also depends on the solar torque strength, which varies for each satellite given their different end of life configurations. Hopefully higher fidelity

modeling and additional observations can help determine the underlying reasons for the different evolutionary histories of these satellites.

GOES 11 also appears to have remained in the tumbling regime since at least 2014. The significant periods in Figure 7.16 show some evidence for yearly variation which could indicate capture into a tumbling limit cycle. Additional high quality light curves showing tumbling periods with yearly periodicity and radar-derived pole estimates remaining in a consistent orbit frame locations throughout the year would strongly support the hypothesis that GOES 9 and 11 have reached tumbling limit cycles. If they have, the extracted β values and periods would provide insight about their dissipation rates.

Of the five GOES 8-12 satellites, GOES 10 is distinct in that light curves and radar observations show it has remained in fast uniform rotation since at least 2014. Figure 5.1 showed that YORP-driven $\dot{\bar{\omega}}_e$ for GOES 10 was much smaller than for the other satellites. Similarly, Figure 5.2 showed much lower spin rate variation compared to GOES 8. This is directly attributable to GOES 10's end of life solar array angle which nearly minimizes solar torques over all possible β values. These modeling results are consistent with GOES 10's relatively constant uniform spin rate indicated by observations.

For GOES 12, the late 2019 and early 2020 observations indicate it was in uniform rotation and spinning up. This is notable given that the satellite was tumbling in 2014. While GOES 8's evolution provided evidence for YORP-driven transition from uniform rotation to tumbling, GOES 12's evolution confirmed that these satellites can also escape from the tumbling regime. Furthermore, GOES 12's escape suggests that, like GOES 8, its dissipation is not large enough to have yet forced capture into a tumbling limit cycle or that it does not have stable equilibria for its given dissipation.

One ubiquitous behavior from dynamical modeling was sun-tracking precession during YORP-driven tumbling cycles and steady state pole directions in the orbit frame for YORP + dissipation + gravity gradient limit cycles. Unfortunately, the ensemble of GOES pole estimates are currently too sparse to validate these simulated behaviors. While the radar-derived pole estimates for the

tumbling GOES 8 and 11 satellites in Figure 7.23 are near the sun/anti-sun directions in Feb. 2020 and Dec. 2019 respectively, this is by no means conclusive. Ultimately, more pole solutions are needed at higher cadences and at different times of year to determine whether the tumbling GOES satellite poles are systematically tracking the sun.

7.7   Implications

The observed and simulated spin state diversity of the GOES satellites has several notable implications for GEO debris mitigation. First of all, active debris removal (ADR) and satellite servicing/recycling efforts will often require detailed spin state knowledge of the target satellite, ideally well before rendezvous. The GOES spin state diversity illustrates that some satellites will be easier targets than others as slow uniform rotation greatly simplifies rendezvous and capture operations, particularly for large, non-cooperative objects. Capture of satellites with fast spin rates may simply not be feasible due to control limitations or risk of collisions. So ADR and satellite servicing operators will be forced to weigh a target's threat to active space assets or service value against its spin state. For targets like GOES 8 with highly variable spin states, long-term spin state prediction will be crucial to identify capture windows with favorable spin rates. For example, this would be when GOES 8 has decelerated to slow uniform rotation just before a transition to complex rotation or between tumbling cycles. It would advantageous to let YORP decelerate target satellites as much as possible, saving the ADR/servicing spacecraft fuel and time. With many potential targets, one might plan to deorbit the slowest spinning targets first, waiting for windows of predicted slow rotation to deorbit others.

The tumbling resonances observed for GOES 8 have implications for ADR and servicing. In these resonances, a satellite's attitude motion is nearly periodic. For general tumbling on the other hand, the attitude motion does not repeat. ADR/servicing spacecraft would likely have an easier time grappling a tumbling satellite with periodic motion compared to one without, especially if aiming for a particular feature on the satellite. For example, Northrop Grumman's Mission Extension Vehicle (MEV) docks with the apogee kick motor nozzle and concentric launch adapter ring

commonly found on GEO satellites [28]. Taken together, the GOES 8 observations and potential advantage of resonant tumbling over general tumbling for ADR/servicing motivate further dynamical and observational studies to investigate how common these resonances are among the tumbling defunct satellite population.

The strong dependence of GOES spin state evolution on end of life geometry and internal energy dissipation has another implication for GEO debris mitigation. Satellite designers and operators can potentially dictate post-disposal spin state evolution with factors other than the spin state at shutdown. In addition to deorbit and passivation, the solar arrays and other articulating appendages of satellites should be set in end of life configurations that minimize major axis solar torques. Also, building in dissipation with a small nutation damper or other device could yield asymptotically stable tumbling states/limit cycles with constant pole direction in the sun-satellite orbit frame (i.e. constant α and β). Ideally, these considerations would reduce maximum spin rates and spin state variability and make the pole direction more predictable. These behaviors would greatly facilitate any future capture for ADR and satellite servicing/recycling efforts. Slower spin rates would also reduce the potential for material shedding that could risk active GEO assets. Much of the high area-to-mass ratio debris at GEO is thought to be multi-layer insulation from defunct satellites and upper stages [67]. Finally, these stable tumbling states/limit cycles could potentially be leveraged for passive attitude control for on-orbit storage [47] or interplanetary cruise. A fixed β value would provide consistent (albeit not continuous) tumbling-averaged solar array illumination. Such a trade-off may be sufficient for low power hibernation.

Chapter 8

Application to Other Bodies

8.1   Box-Wing Satellite

Using the averaged models, the dynamics of a box-wing GEO satellite will be investigated. The 14 facet satellite shape model used in this investigation is provided in Figure 8.1. It is modeled off the Optus B family of satellites for which significant geometry information is available [62]. These satellites are built from the popular Boeing 601 satellite model [62]. Overall, the Optus B geometry is relatively generic and representative of most box-wing GEO satellites. The shape model consists of the main bus, two solar arrays, and a pair of antennas mounted on the east and west ($\pm\hat{\boldsymbol{b}}_1$) faces of the bus, tilted $\sim15°$ towards the $+\hat{\boldsymbol{b}}_2$ direction. The satellite's overall wingspan is 20.6 m. The optical properties for the bus and solar arrays are assumed to be the same as those for the GOES model in Table 2.2. The antenna reflections are assumed to be diffuse (i.e. $s_i = 0$). End of life properties for several retired Optus B satellites were generously provided by Andrew Edwards of Optus Australia (via personal communication). For this study, the mass properties for the Optus B3 satellite are used. The satellite had an end of life mass of 1320 kg and principal inertias of $I_l = 1704$ kg·m^2, $I_i = 5718$ kg·m^2, and $I_s = 6143$ kg·m^2. Rotation of the solar arrays around the $\hat{\boldsymbol{b}}_3$ over a range of reasonable solar array masses did not change the $\hat{\boldsymbol{b}}_1$ and $\hat{\boldsymbol{b}}_2$ directions by more than a few degrees. Also, Andrew Edwards stated that the off-axis inertias were negligible. So the principal axes are assumed to correspond to the $\hat{\boldsymbol{b}}_1$, $\hat{\boldsymbol{b}}_2$, and $\hat{\boldsymbol{b}}_3$ axes in Figure 8.1. The solar arrays will not generally be oriented with the sun/anti-sun side normal along $\hat{\boldsymbol{b}}_2$ as shown in Figure 8.1 since satellites are often shut down at times other than local midnight/noon. For

example, the end of life array angles θ_{sa} for Optus B1 and B3 provided by Andrew Edwards were 239° and 256° (with $\theta_{sa} = 0°$ at local midnight), corresponding to shutdown in the late afternoon.
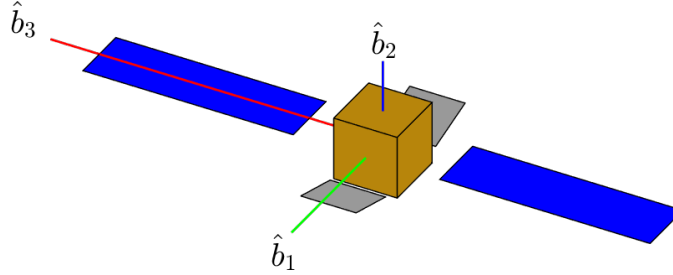
Figure 8.1: Box-wing satellite shape model with principal axes

Analytical tumbling-averaged quantities for the box-wing model are provided in Figure 8.2. Here, θ_{sa} is set to 45° (measured positive about $-\hat{\boldsymbol{b}}_3$). The center of mass is assumed to be 10 cm along $+\hat{\boldsymbol{b}}_3$ from the center of the bus (i.e. $\boldsymbol{r}_c = [0, 0, 10]^{\mathrm{T}}$ cm). For the $\dot{\overline{I_d}}$ contour in Figure 8.2d, $\overline{\omega}_e = 2\pi$ is arbitrarily assumed. A shaded plane intersects the contours at zero to better illustrate the sign changes. These contours have the same general structure as those for GOES 8 with $\theta_{sa} = 70°$ in Figure 5.9. $\overline{M_x}$ is positive for SAMs and negative for LAMs, $\overline{M_z}$ changes sign near the separatrix (dashed line) and $\beta \approx 90°$, and $\dot{\overline{I_d}}$ changes sign at $\beta \approx 90°$. So as in Figure 5.9, the satellite will tend to evolve clockwise in (β, I_d) space. Varying θ_{sa} and the $\hat{\boldsymbol{b}}_3$ center of mass offset changes the magnitudes of the quantities while preserving the structure. Similarly, for shifts along all principal directions (e.g. $\boldsymbol{r}_c = [5, 10, 10]^{\mathrm{T}}$), the general Figure 8.2 structure was retained. On the other hand, center of mass offsets in only the $\hat{\boldsymbol{b}}_1$ and/or $\hat{\boldsymbol{b}}_2$ directions result in $\overline{M_x} = \overline{M_z} = \dot{\overline{I_d}} = 0$ across all SAM states for all β values. For this box-wing satellite model, tumbling cycle behavior only requires an offset in the $\hat{\boldsymbol{b}}_3$ direction. This is due in part to the satellite having three distinct principal inertias which results in asymmetric sampling of the satellite geometry over the tumbling motion. Making the satellite prolate (i.e. $I_i = I_s$), resulted in $\overline{M_x} = \overline{M_z} = 0$ across all β given the symmetric sampling of the satellite geometry. For satellites with observed uniform spin rate variation, this variation could be achieved with just a $\hat{\boldsymbol{b}}_3$ offset. So there is a strong possibility that such satellites would exhibit tumbling cycle behavior if they spin down sufficiently.
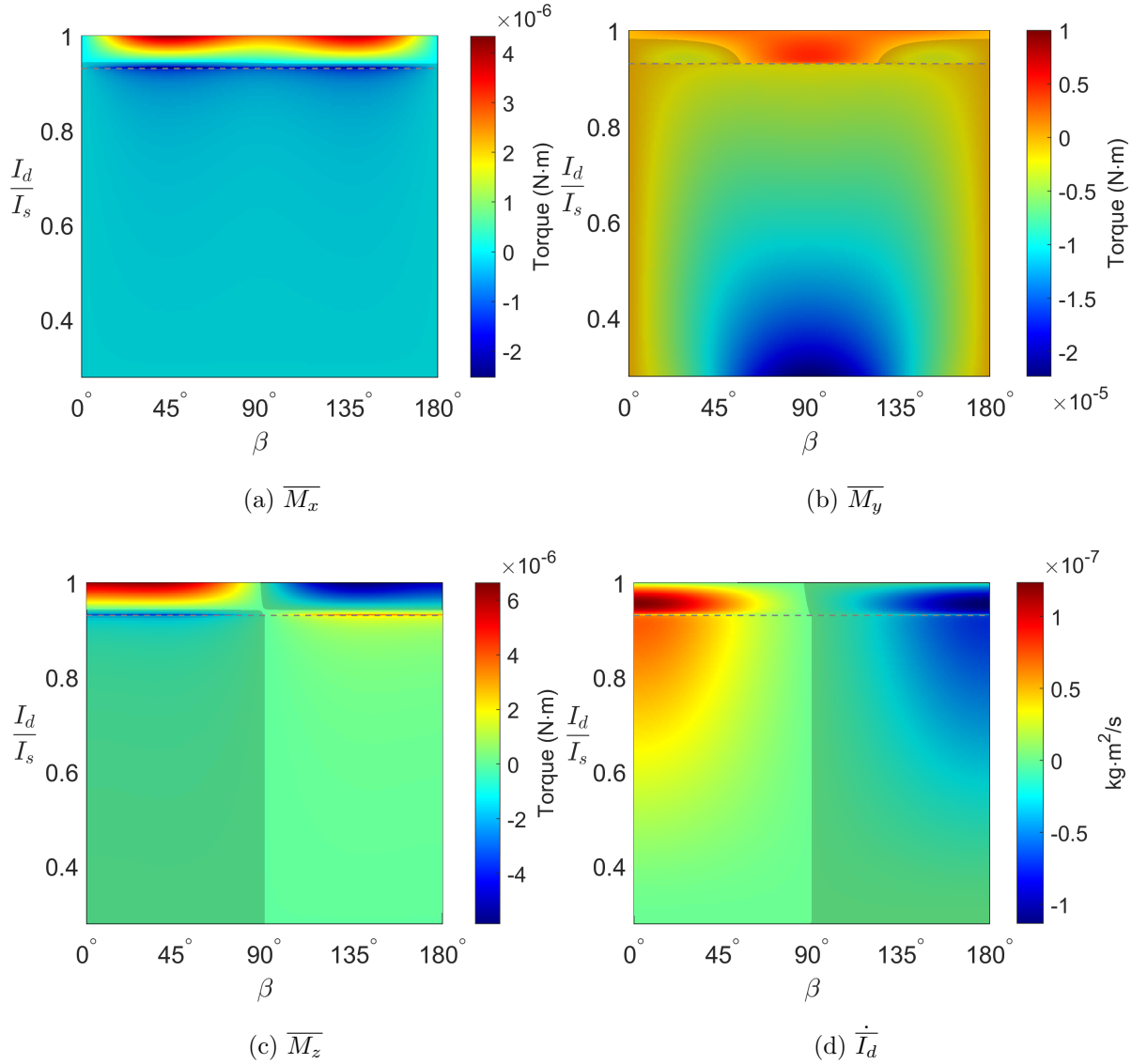
Figure 8.2: Box-wing satellite analytical tumbling-averaged YORP quantities ($\theta_{sa} = 45°$, center of mass shifted 10 cm along $+\hat{\boldsymbol{b}}_3$ axis from center of bus, SAM+/LAM+)

Example semi-analytical model evolution assuming only YORP is provided in Figure 8.3. The initial spin state is $\alpha = 0°$, $\beta = 165°$, $P_e = 2\pi/\omega_e = 5$ min, and $I_d/I_s = 1 - 10^{-6}$. Center of mass offsets of 5 and 10 cm along $+\hat{\boldsymbol{b}}_3$ from the center of the bus are considered. In both cases, the satellite undergoes a yearly uniform spin rate variation with a secular decrease. Once the satellite spin rate has decreased sufficiently, it enters a tumbling cycle with the pole precessing around the

sun-line (α circulation) and slowly moving from the anti-sun to sun direction (decreasing β). Given the larger associated torques, the satellite evolves more rapidly with the 10 cm offset. Nevertheless, $\overline{M_x}$, $\overline{M_y}$, and $\overline{M_z}$ in Figure 8.2 are roughly an order of magnitude smaller than the values for GOES 8 in Figure 4.5. Combined with its larger inertias, the box-wing satellite evolves more slowly than GOES 8. For example, comparing the 10 cm offset box-wing uniform spin down in Figure 8.3 to that for GOES 8 in Figure 5.3, GOES 8 decelerated in uniform rotation roughly 20 times faster than the box-wing.

(a) effective spin rate ω_e

(b) normalized dynamic moment of inertia I_d

(c) clocking angle α

(d) coning angle β
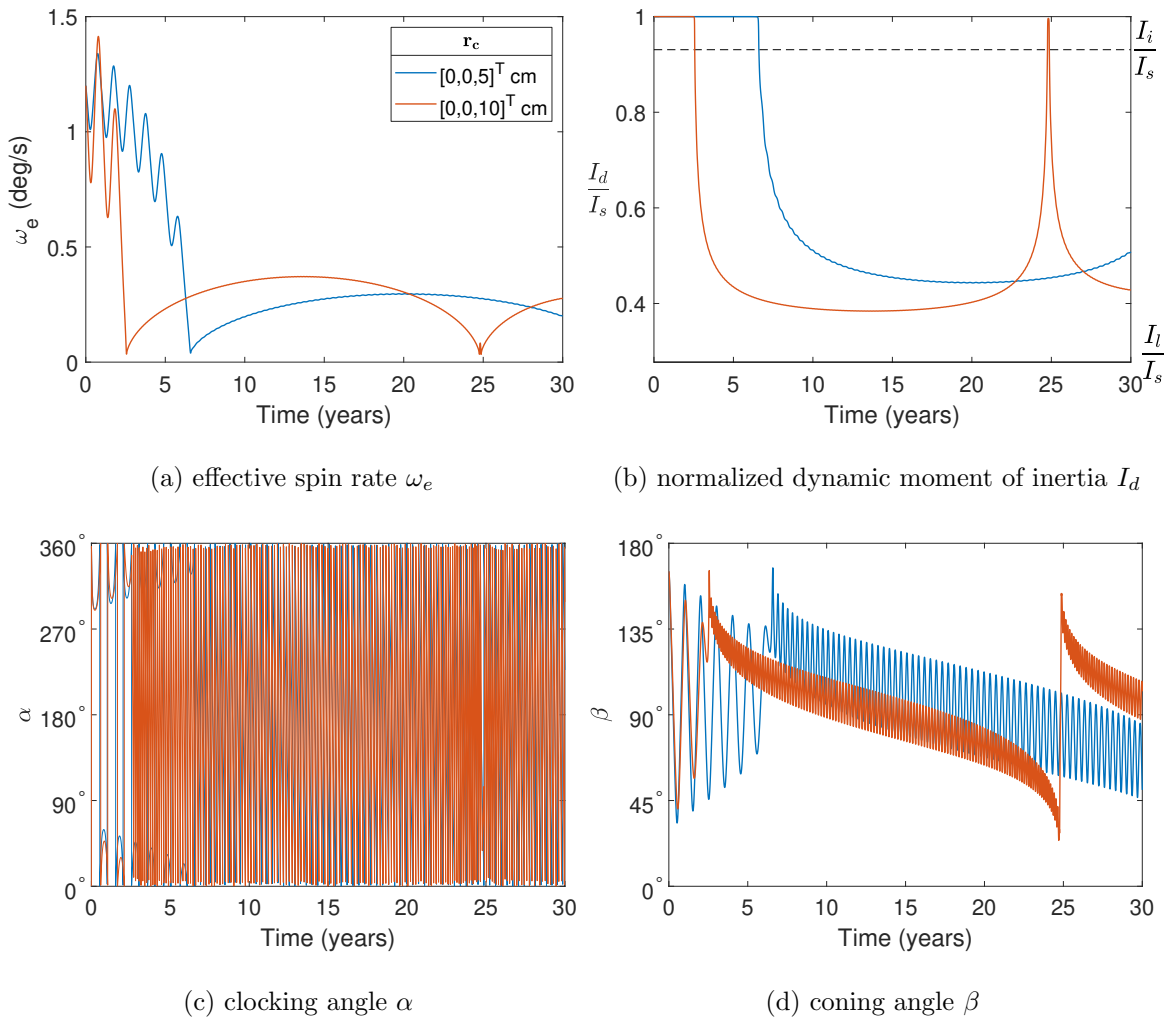
Figure 8.3: Box-wing satellite semi-analytical tumbling-averaged YORP evolution for different centers of mass (SAM+/LAM+)

Example averaged model evolution for the box-wing model considering YORP and internal energy dissipation is provided in Figure 8.4. The initial spin state is $\alpha = 0°$, $\beta = 165°$, $P_e = 2\pi/\omega_e = 20$ min, and $I_d/I_s = 0.98$ with $J = 2$ kg·m^2 and $\mu/J = 1$e-3 s^{-1}. Similar to the behavior observed for GOES for sufficiently large dissipation rates, the satellite asymptotically approaches a stable tumbling equilibrium on the SAM side of the separatrix with an effective spin period $P_e \approx 56$ min.

(a) effective spin rate ω_e

(b) normalized dynamic moment of inertia I_d

(c) clocking angle α

(d) coning angle β
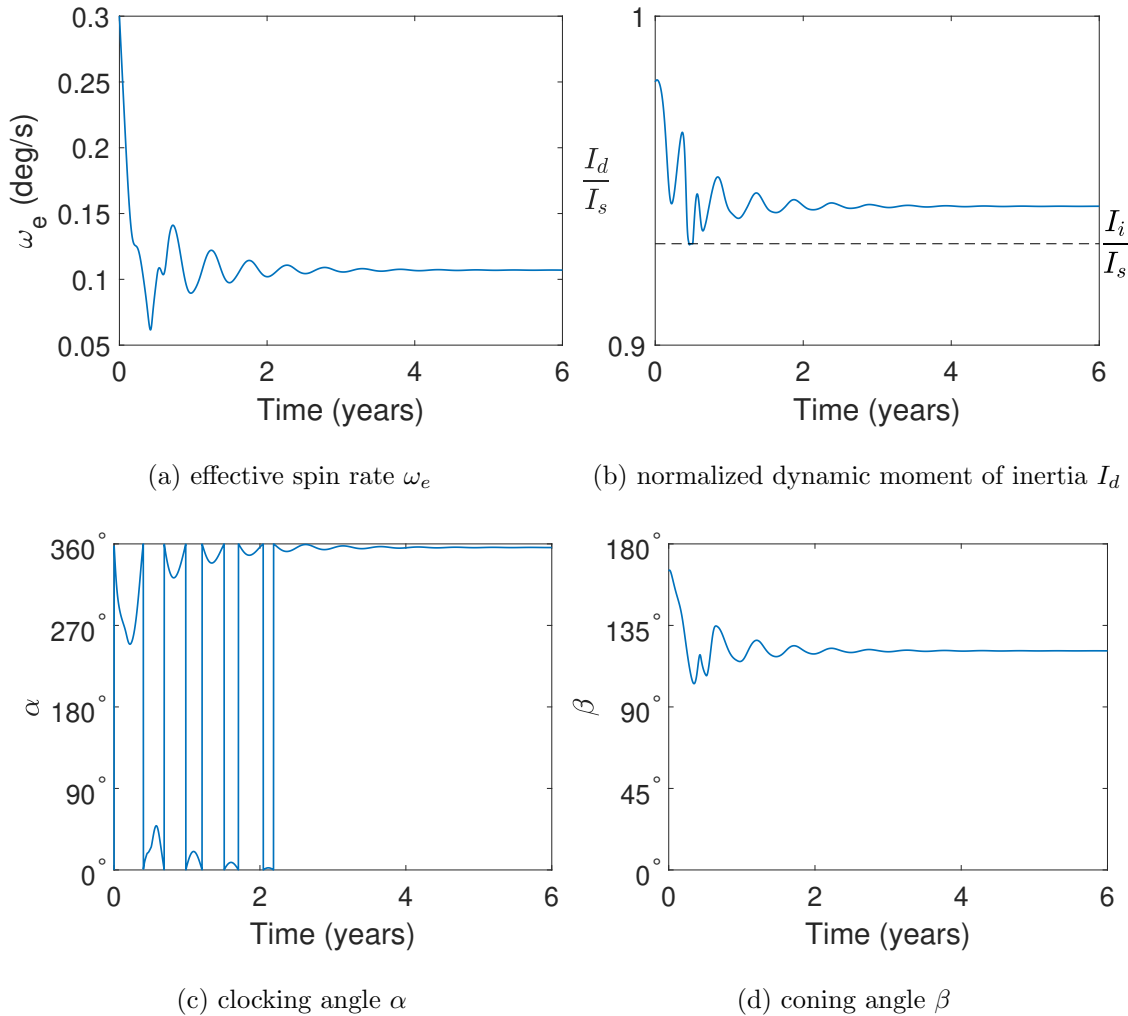
Figure 8.4: Box-wing satellite nuemrical tumbling-averaged YORP + dissipation evolution ($\boldsymbol{r}_c = [0, 0, 10]^T$ cm, $J = 2$ kg·m^2, $\mu/J = 1$e-3 s^{-1}, SAM+/LAM+)

8.2   Meter-Sized Asteroids

Meter-sized asteroids are generally monolithic rocks and are assumed to have negligible dissipation. Angular accelerations due to solar gravity gradient torques are independent of asteroid size D while YORP accelerations are proportional to $1/D^2$. So for meter-sized asteroids, gravity gradient accelerations will be many orders of magnitude smaller than YORP. Therefore, only YORP is considered in the current investigation. Here, we take models of observed asteroids and scale them down to smaller sizes. Reflections are assumed to be purely diffuse (i.e. $s_i = 0$). So given the assumption of instant thermal re-emission, the solar torques are independent of the asteroid reflectivity ρ_i. Circular heliocentric orbits are assumed with a semi-major axis of 1 AU.

8.2.1   Pseudo-Itokawa

The near-earth asteroid Itokawa has dimensions of $535 \times 294 \times 209$ m [42]. Figure 8.5 shows example averaged model spin state evolution for a 1/400 scale ($\sim$1.3 m) Itokawa model with the initial state $\alpha = 0°$, $\beta = 15°$, $P_e = 12$ hr, and $\overline{I}_d/I_s = 0.995$. Starting in slow tumbling near uniform rotation, the asteroid undergoes three tumbling cycles over roughly two years with rapid α circulation, β increasing over each tumbling cycle, and brief returns to near-uniform rotation. Figure 8.6 shows the signs of the analytically averaged parameter derivative contours with the Figure 8.5 evolution overlaid. The satellite evolves in the counter-clockwise direction in (β, I_d) space, alternately spinning up and down. The contours and pseduo-Itokawa's non-resonant tumbling-averaged YORP evolution largely echo that for GOES and the box-wing satellite.

(a) effective spin rate

(b) scaled dynamic moment of inertia

(c) clocking angle α

(d) coning angle β
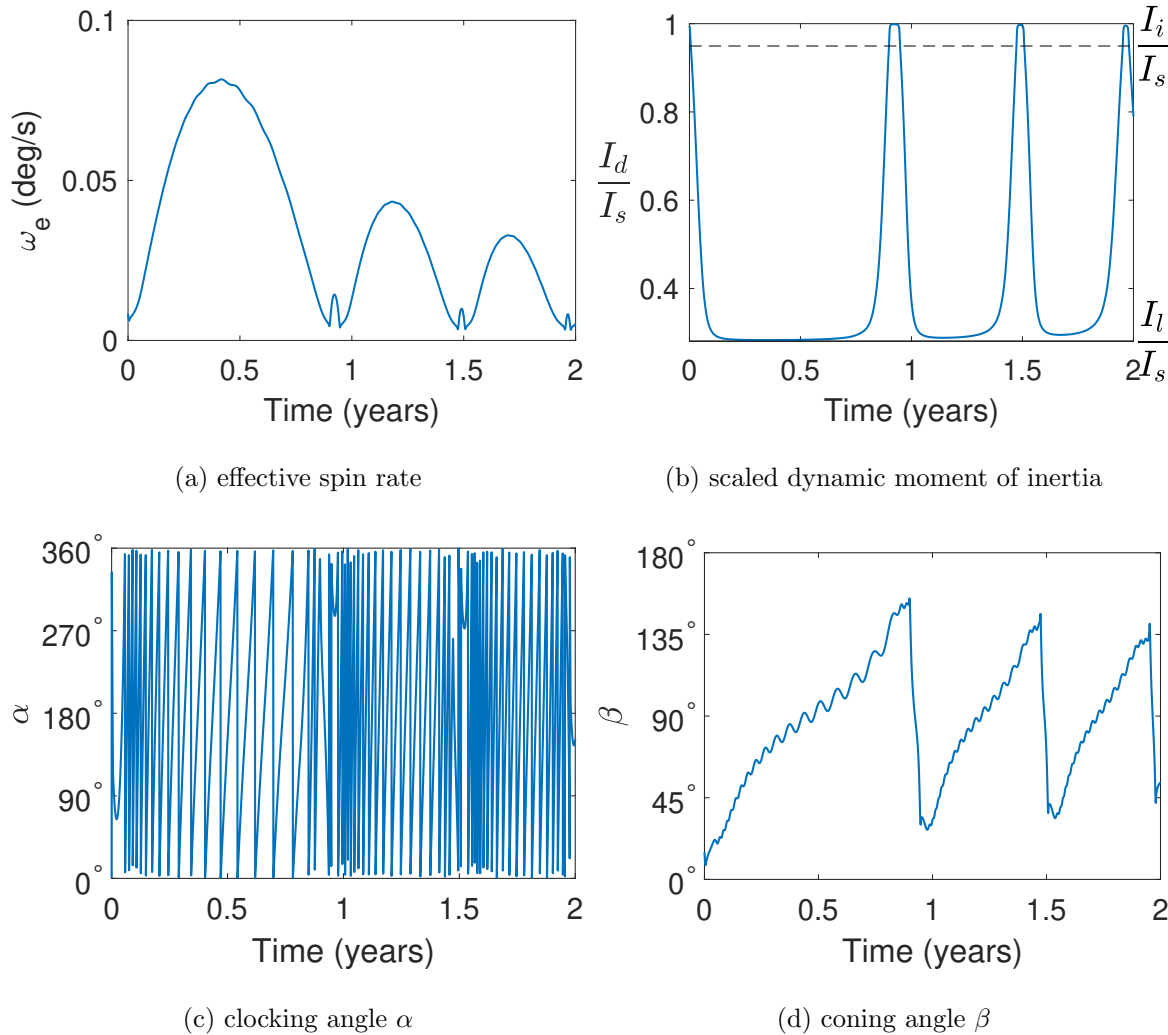
Figure 8.5: Analytically averaged evolution of 1.3 m pseudo-Itokawa.
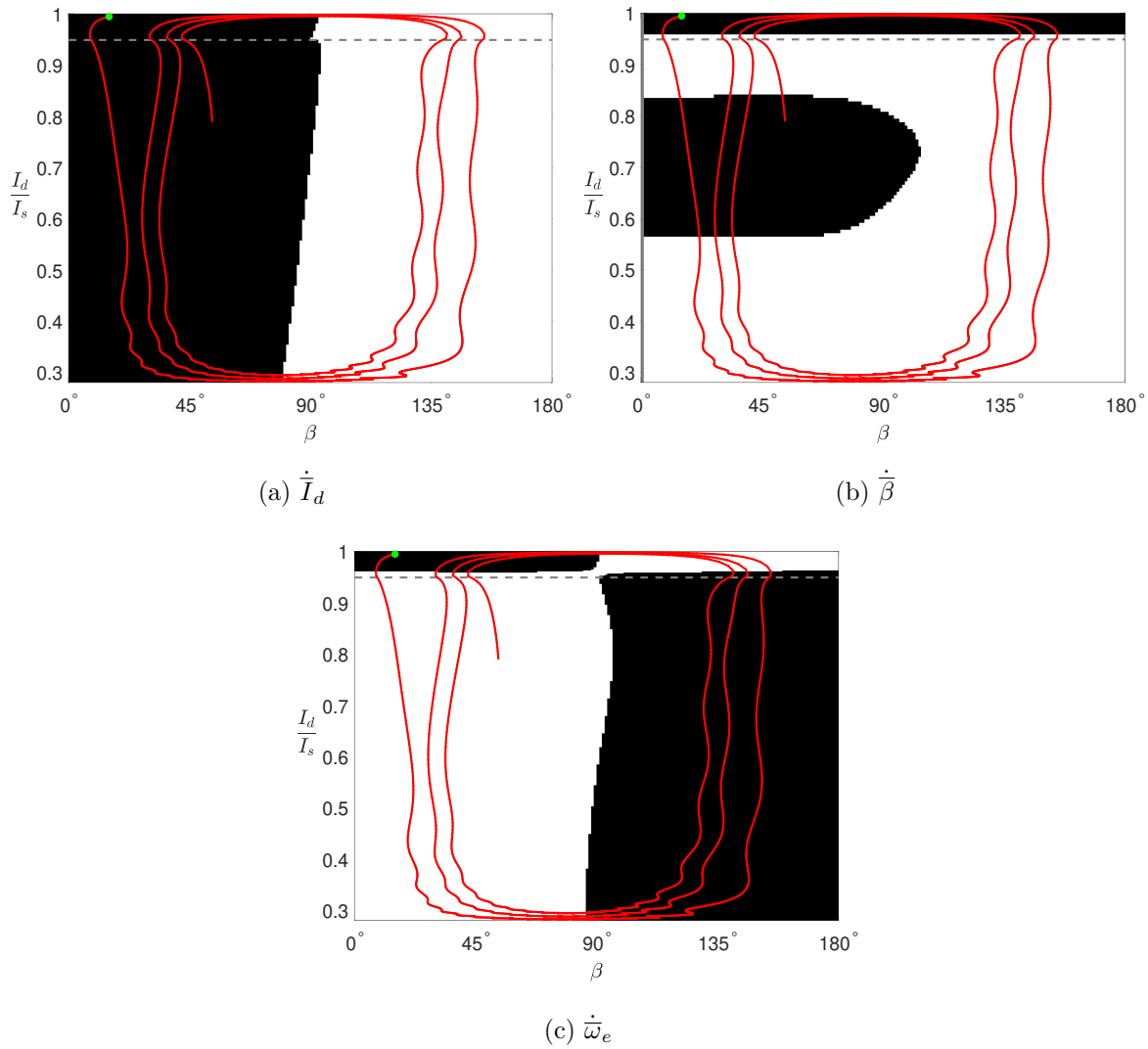
Figure 8.6: 1.4 m pseudo-Itokawa averaged parameter derivative signs (SAM+/LAM+) with Figure 8.5 evolution. Black and white denote negative and positive values respectively.

Figure 8.7a shows the corresponding Figure 8.5 evolution of $\boldsymbol{H}$ in the orbit frame over the first tumbling cycle ($\sim$1 year). Here, the asteroid exhibits sun-tracking precession. Plotting the asteroid obliquity (the angle between $\boldsymbol{H}$ and $\hat{\boldsymbol{X}}$) over this two year simulation, it averages to $\sim$90°.

(a) $\boldsymbol{H}$ over first tumbling cycle

(b) $\boldsymbol{H}$ obliquity
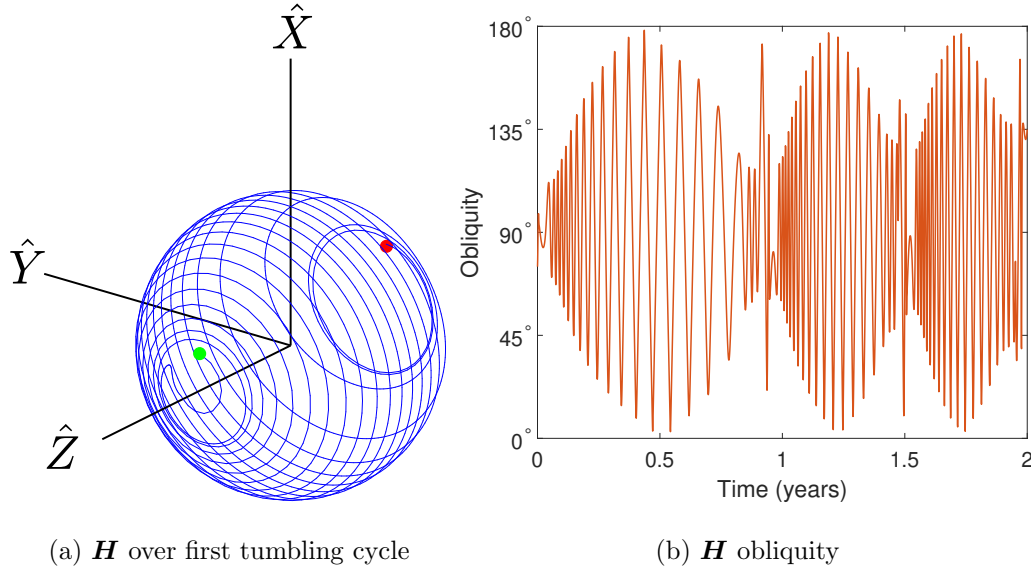
Figure 8.7: Evolution of 1.3 m pseudo-Itokawa pole direction for Figure 8.5 example.

8.2.2 Pseudo-Apophis

The full-scale Apophis shape model investigated here has dimensions of $410{\times}350{\times}320$ m. Figure 8.8 shows the averaged quantity contours and example evolution for a $1/400$ scale (~ 1 m) version with the initial state $\alpha = 0°$, $\beta = 165°$, $P_e = 12$ hr, and $\overline{I}_d/I_s = 0.8$. Starting in the tumbling regime with the pole near the anti-sun direction, the satellite initially proceeds clock-wise in (β, I_d) space. Given the patchwork structure of the contours, it then switches sense and evolves counter-clockwise, alternating between spin up and spin down. Over the three year evolution, the asteroid's obliquity averages approximately $90°$ as shown in Figure 8.8d due to extended phases of sun-tracking precession.

(a) $\dot{\overline{I}}_d$

(b) $\dot{\overline{\beta}}$

(c) $\dot{\overline{\omega}}_e$
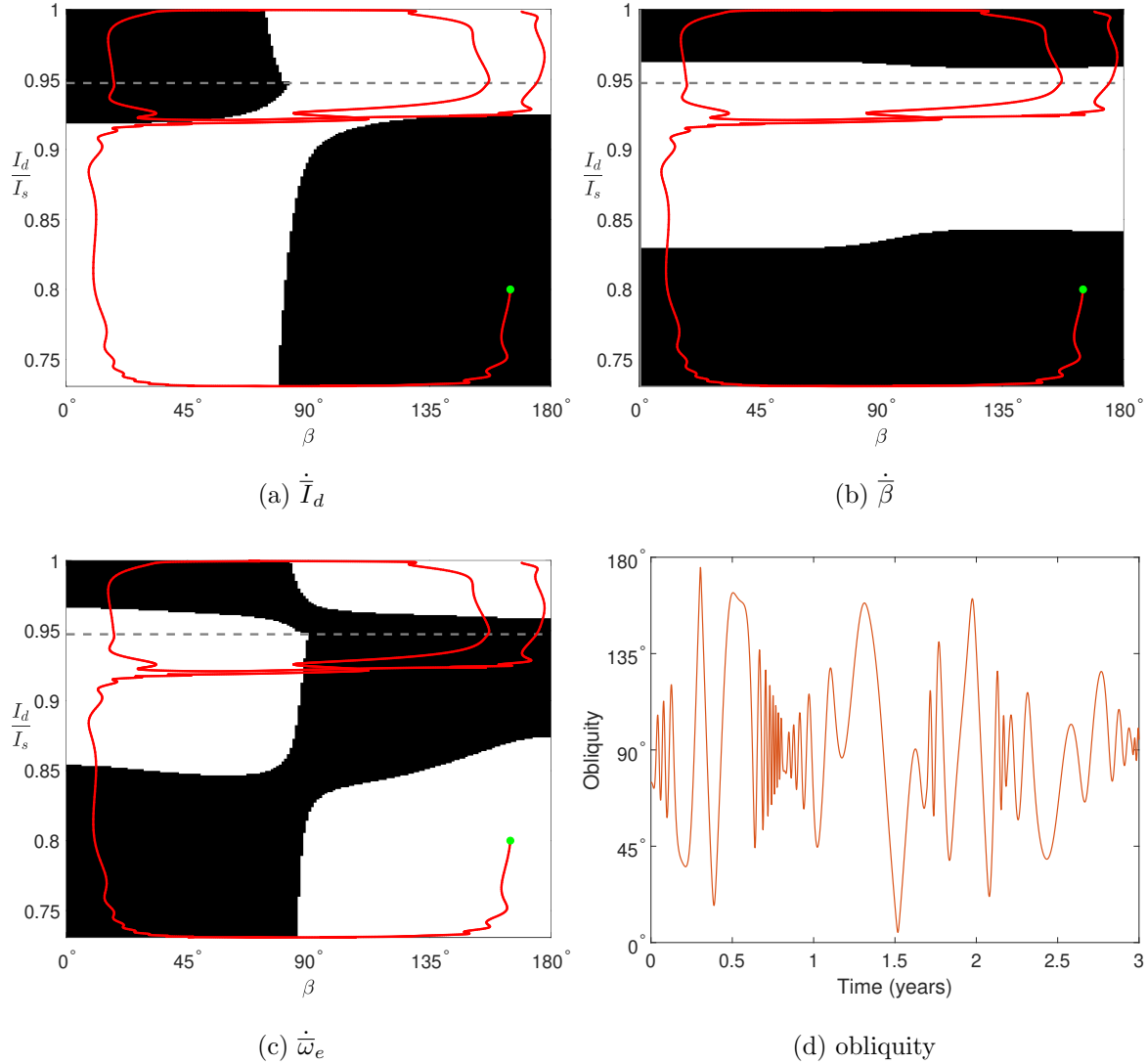
(d) obliquity

Figure 8.8: 1 m pseudo-Apophis averaged parameter derivative signs (SAM+/LAM+) with example evolution overlaid and corresponding obliquity.

8.2.3   Prevalence of Sun-Tracking Precession

Using the analytically averaged model, we will investigate the prevalence of sun-tracking precession for meter-sized asteroids. Figure 8.9 shows plots of $\overline{M}_y/|\boldsymbol{M}|$ vs. I_d and β for the asteroids Itokawa, Apophis, Toutatis, and 1998 ML14 along with their shape models. For Itokawa, Apophis, and Toutatis, $\overline{M}_y/|\boldsymbol{M}|$ is very close to ± 1 over the most of the $(\beta,\ I_d)$ space. This

indicates that the majority of the solar torque is along the $\pm\hat{\boldsymbol{y}}$ direction (i.e. perpendicular to both $\boldsymbol{H}$ and the sun line $\hat{\boldsymbol{Z}}$). So for meter-sized versions of these three asteroids undergoing slow rotation, pole motion will generally be dominated by precession about the sun/anti-sun line. Of the roughly 10 asteroids investigated, this $\overline{M}_y/|\boldsymbol{M}|$ structure was found for all asteroids with at least some elongation. So even in the absence of clean tumbling cycles, like those observed for pseudo-Itokawa above, pole motion for many meter-sized asteroids undergoing slow rotation should be dominated by sun-tracking precession. For the roughly spherical 1998 ML14, the relative strength of $\overline{M}_y$ is generally not as large, indicating somewhat weaker tendency for sun-tracking precession. Similar results were observed for the roughly spherical 1998 KY26.

(a) Itokawa

(b) Apophis

(c) Toutatis

(d) 1998 ML14
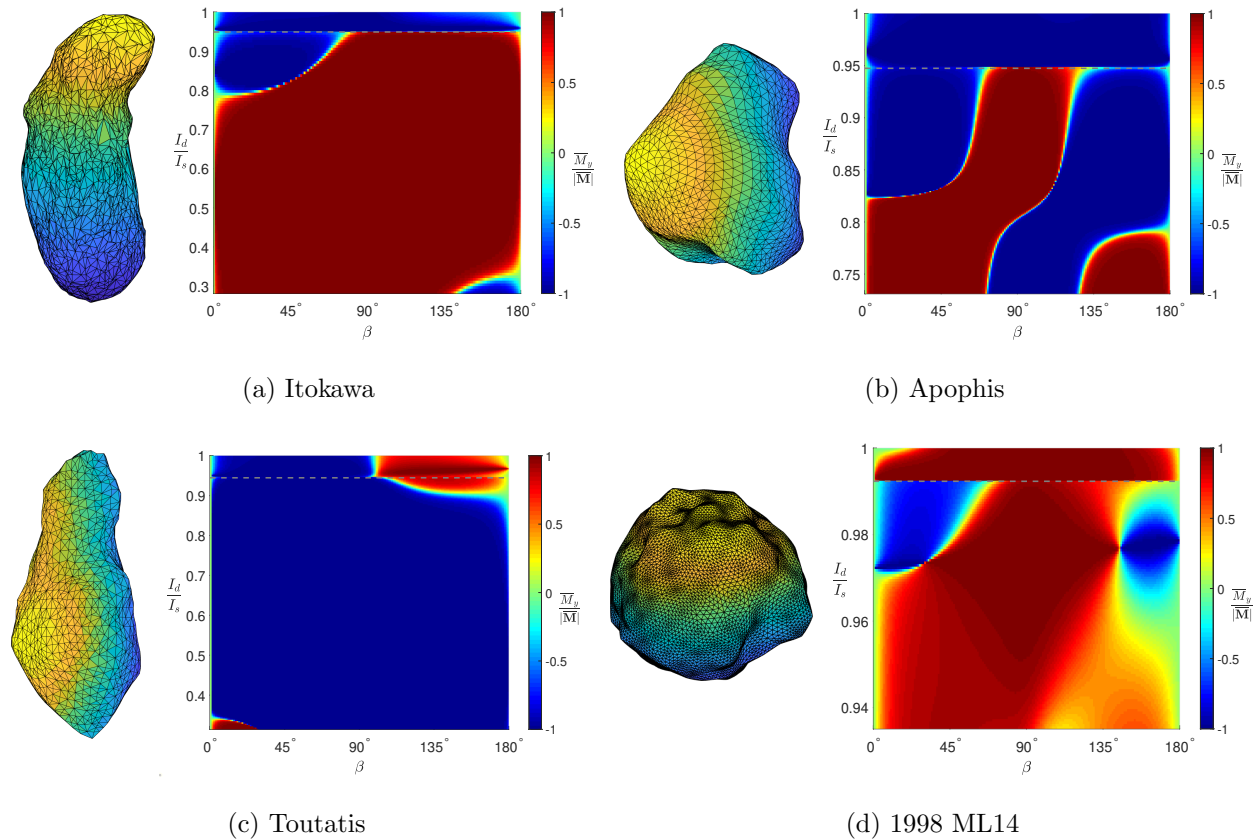
Figure 8.9: $\overline{M}_y/|\boldsymbol{M}|$ for several asteroids (SAM+/LAM+)

The dependence of the sun-tracking parameter δ/n on asteroid and orbital parameters will

now be investigated. As a reminder, for $\delta/n \gg 1$, pole motion will be dominated by sun-tracking precession. For $\delta/n \ll 1$, the pole will remain nearly inertially fixed (refer to Figure 5.6 and the associated discussion). Since $\delta = M/H$, it is proportional to $1/D^2$ and $1/\omega_e$. Figure 8.10a shows how δ/n for pseduo-Itokawa changes with asteroid diameter D (i.e. largest actual dimension) and effective spin period $P_e = 2\pi/\omega_e$ assuming a semi-major axis of 1 AU. Here δ was calculated assuming $I_d/I_s = 0.4$. For diameters of roughly one meter, one could expect significant spin-orbit coupling for $P_e < 20$ min. As the diameter shrinks, δ/n grows rapidly. Considering the asteroid orbit, solar radiation pressure and therefore δ are proportional to $1/a^2$, where a is the heliocentric semi-major axis. Furthermore, the mean motion n goes as $1/\sqrt{a^3}$, so δ/n is proportional to $1/\sqrt{a}$. Figure 8.10b illustrates this dependence. For the main belt, δ/n will be roughly 55-70% of the value at 1 AU.
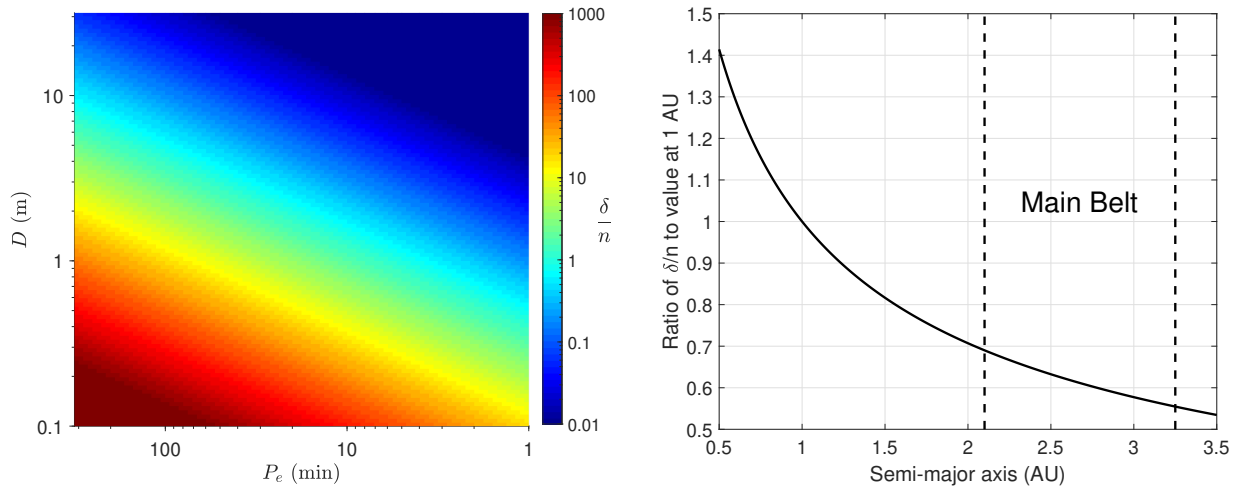
(a) δ/n for pseudo-Itokawa at 1 AU ($I_d/I_s = 0.4$)

(b) δ/n vs. semi-major axis

Figure 8.10: Dependence of sun-tracking parameter δ/n on size D, effective spin period P_e and semi-major axis

Overall, the prevalence of sun-tracking precession for slowly tumbling meter-sized asteroids observed with the analytically averaged YORP model has implications for the Yarkovsky effect. Semi-major axis drift due to the Yarkovsky effect is proportional to the cosine of the asteroid

obliquity [111]. So for obliquities of 90°, the diurnal Yarkovsky effect will be zero. The diurnal Yarkovsky effect generally dominates the seasonal component, and analysis indicates that the Yarkovsky effect still persists for tumbling asteroids [111]. Figure 8.7 shows that during tumbling cycles, pseudo-Itokawa's obliquity averages to roughly 90°. This suggests that sun-tracking precession may shut off the Yarkovsky effect. Such a tendency would reduce the semi-major axis drift of tumbling meter-sized asteroids and their corresponding escapes rates from the main asteroid belt through resonances. This would in turn affect the near-earth and main belt populations of these bodies. These population sizes have implications for crater formation rates on the Moon, larger asteroids, and other airless solar system bodies. Crater counts are used to estimate the geologic ages of surfaces [90]. On the other hand, any cases with fast rotation would cut off sun-tracking. It is also important to note that bare meter-sized rocks likely have non-negligible thermal conductivity [112], so YORP models incorporating thermal lag are needed to determine whether this sun-tracking behavior still persists. If it does, a focused study of the Yarkovsky effect for tumbling meter-sized asteroids would be valuable to further explore the impact of sun-tracking precession on drift rates. With YORP accelerations proportional to $1/D^2$, very small asteroids could rapidly reach fast spin rates and break apart. Rubincam [93] and Breiter et al. [20] hypothesized that these asteroid might be captured in tumbling states with alternating spin up and spin down which would prevent this disruption. The tumbling cycles observed here support this hypothesis.

Chapter 9

Conclusions and Future Work

Overall, this work developed dynamical models and observation analysis techniques that increased understanding of long-term general rotational dynamics of defunct satellites. The full and tumbling-averaged dynamical models uncovered rich dynamical structure for satellites subject to solar radiation torques, gravity gradients, and internal energy dissipation. Notable behaviors included repeated transitions between uniform and non-principal axis tumbling, spin-orbit coupling in the form of angular momentum sun-tracking precession, capture into fundamental tumbling period resonances, and stable tumbling states/limit cycles. Non-intuitively, these dynamical models showed that the tumbling cycles proposed by Albuja et al. [2] do not require internal energy dissipation as they hypothesized. Instead, these repeated transitions between uniform rotation and tumbling can be driven by YORP alone. The dynamical modeling also indicates that sufficiently high dissipation rates balance the YORP effect, preventing these tumbling cycles and resulting in stable tumbling states/limit cycles.

Methods were developed to extract fundamental tumbling periods and pole directions from optical light curves and Doppler radar observations. These two data types complement each other with light curves providing rich harmonic information and Doppler providing unambiguous precession periods and greatly narrowing possible poles directions. Spin state time histories of the GOES 8-12 satellites extracted from light curve and Doppler radar observations showed consistency with their simulated behavior, most notably spin state diversity, tumbling cycles, tumbling resonances, and stable tumbling states/limit cycles. These simulated and observed behaviors have significant

implications for active debris removal, satellite servicing, and satellite decommission procedures. Operators may be able to dictate the post-disposal spin state evolution of a satellite by properly setting its end of life configuration which would aid active debris removal and servicing efforts. The averaged solar torque, gravity gradient, and energy dissipation models allow for broad, rapid studies of long-term dynamics. Also, the averaging framework is readily extendable to higher fidelity ray-traced solar torque models and other perturbations (e.g. magnetic and eddy current torques). These averaged models could facilitate trade studies for the impact of end of life configurations and spin states on a satellite's long-term post-disposal spin state evolution.

Simulations showed that the behaviors observed for the GOES satellites apply to more general box-wing satellites. Similar behavior was also observed for meter-sized asteroids, with YORP-driven tumbling cycles and sun-tracking potentially shutting off Yarkovsky drift, reducing escape rates from the main asteroid belt, and preventing spin-driven disintegration.

Future Work

There are several notable areas for future work. These include:

- Broad dynamics model exploration for a wide array of bodies and end of life configurations.

- Higher fidelity solar torque modeling accounting for thermal lag.

- A higher order resonance-averaged model to investigate dynamics in the vicinity of tumbling equilibria and resonances.

- A complementary tumbling-averaged solar radiation pressure model for orbital dynamics.

- Extension of the averaged models to other orbital regimes (e.g. low earth orbit, lunar orbit) and perturbations (e.g. magnetic and eddy current torques, atmospheric drag).

- Continued satellite observation analysis to gain insight and validate modeling.

Areas for future work are discussed in more detail below.

While the modeling in this work uncovered rich dynamical structure that is largely consistent with observed evolution, detailed investigations were limited to a small number of bodies. As a result, further model exploration (both full and averaged) is needed to assess the prevalence of these behaviors in the general populations earth-orbiting satellites. This includes investigating a broad array of satellite shapes including rocket bodies as well as different configurations (dissipation rates, center of mass offsets, optical properties, array angles, and antenna configurations). It will be valuable to determine what behaviors persist and whether new ones emerge. For example, it is commonly assumed that internal energy dissipation will always result in defunct satellites and rocket bodies spinning about their maximum inertia axis. The asymptotically stable tumbling equilibria and limit cycles observed in this work due to the combined influence of YORP, dissipation, and gravity gradients would break this assumption. In brief, it is possible that tumbling satellites may not consistently return to uniform rotation. This would have significant implications for active debris removal and satellite servicing. Therefore the prevalence of stable tumbling states/limit cycles across a wide range of bodies and configurations should be studied.

The fidelity of the solar torque and dissipation models in this work was limited. So another area for future work is the development of higher fidelity models for these perturbations. For example, delayed thermal re-emission, which was neglected in this work, is known to significantly affect the long-term pole evolution of asteroids [23]. As a result, it would be valuable to determine how this thermal lag impacts the behaviors identified in this work. Unlike the current model which assumes the solar torques only depended on the instantaneous attitude, thermal lag would make the torques a function of the recent illumination history. This time dependence makes thermal lag challenging to incorporate in a tumbling-averaged sense given the presence of two fundamental periods. Higher fidelity modeling of reflections on the other hand can be readily incorporated in the current numerically averaged solar torque model. Detailed self-shadowing and multi-bounce effects incorporated through ray tracing may impact the simulated behaviors. Considerations for more realistic glossy reflections rather than just specular and diffuse could have an impact as well. In the averaged model, the averaged torques for a given body are only functions of two

parameters: the dynamic moment of inertia I_d and coning angle β in the non-resonant case, or γ and β in the resonant case. So a formulation could be developed where the averaged torques are expressed as an arbitrary order two-dimensional Fourier series. This way, the solar torque structure could be captured in a discrete set of Fourier coefficients rather than using the limited fidelity semi-analytical model or lookup tables. This could improve classification of different bodies in terms of their Fourier coefficients and allow for coefficient estimation. Finally, the spherical fuel slug dissipation model applied in this work may not accurately represent the dissipation behavior for many satellites, particularly those that have been completely passivated of fuel. So it would be valuable to explore alternative dissipation models that consider energy lost through flexure of satellite components. Angular momentum transferred to and from a satellite's reaction wheels may affect long-term dynamics.

It would also be valuable to further explore dynamics in the vicinity of tumbling YORP resonances and stable tumbling states. For GOES, the mutual proximity of higher order resonances and equilibria seemed to affect the probability of escape to uniform rotation, especially for low dissipation rates. As a result, interaction between tumbling resonances and equilibria could have a significant impact on long-term evolution. For the current averaged models, there is a discontinuous jump between non-resonant and resonant motion. So development of a higher order resonance-averaged model accounting for deviation from a resonance could be valuable to explore these dynamically complex, potentially chaotic regions.

A natural extension of the averaged models developed in this work is to attitude-dependent solar radiation pressure (SRP) modeling. Attitude-dependent SRP models employed for low area-to-mass ratio debris objects generally assume that an object is uniformly rotating or randomly tumbling. Complementary tumbling averaged SRP force models could be developed based off the approach in this work to explore coupled attitude and orbital dynamics for these objects.

Another area of future work is extending this averaging approach to different regimes such as low earth orbit (LEO) and low lunar orbit where the relative magnitudes of the attitude perturbations change significantly and different effects are introduced. It would be interesting to explore

whether representative averaged dynamics can accurately capture the full dynamics in these environments. In LEO and low lunar orbit, gravity gradient torque magnitudes increase significantly, eclipse durations are longer and more frequent, and re-radiation from the earth/moon surface may become non-negligible. In LEO, magnetic and eddy current torques also grow considerably and there is atmospheric drag at lower altitudes. With the debris and active satellite populations in LEO continuing to grow, accurate long-term attitude prediction for active debris removal (ADR) and conjunction-driven drag estimation will be very important.

Finally continued analysis of satellite observations, both past and future, is needed to gain insight about ongoing spin state evolution and to refine dynamical models. This applies to GOES 8-12 as well as other satellites to determine how prevalent tumbling cycles, sun-tracking, tumbling resonances, and stable tumbling are among the general defunct satellite population.

Bibliography

[1] A. A. Albuja, D. J. Scheeres, and J. W. McMahon. Evolution of angular velocity for defunct satellites as a result of YORP: An initial study. Advances in Space Research, 56(2):237–251, 2015.

[2] A.A. Albuja, D.J. Scheeres, R.L. Cognion, W.H. Ryan, and E.V. Ryan. The YORP effect on the GOES 8 and GOES 10 satellites: A case study. Advances in Space Research, 61(1):122–144, 2018.

[3] J. H. Alexander, P. J. Brown, C. L. Henderson, and A. P. Willmore. Ariel 1: The First International Satellite Experiment Results, chapter United Kingdom Experiments, pages 62–65. NASA, Washington, D.C., 1966.

[4] R. R. Allan and G. E. Cook. The long-period motion of the plane of a distinct circular orbit. Proceedings of the Royal Society, A 280:97–109, 1964.

[5] M. Ashikhmin and P. Shirley. An Anisotropic Phong BRDF Model, August 13, 2000.

[6] Astroscale. Elsa-d. `https://astroscale.com/elsa-d`, retrieved May. 7, 2021.

[7] R. R. Bate, D. D. Mueller, and J. E. White. Fundamentals of Astrodynamics. Dover Publications, New York, NY, 1971.

[8] G. Beekman. I.o. yarkovsky and the discovery of 'his' effect. Journal for the History of Astronomy, 37:71–86, 2006.

[9] T. Bennett and H. Schaub. Touchless Electrostatic Detumble Of A Representative Box-And-Panel Spacecraft Configuration. Proceedings of the 7th European Conference on Space Debris, Darmstadt. Germany, 2017.

[10] C. J. Benson, D. J. Scheeres, and N. A. Moskovitz. Spin state evolution of asteroid (367943) duende during its 2013 earth flyby. Icarus, 340, 2020.

[11] C. J. Benson, D. J. Scheeres, W. H. Ryan, and E. V. Ryan. Cyclic complex spin state evolution of defunct GEO satellites. Proceedings of the Advanced Maui Optical and Space Surveillance Technologies Conference, Maui, HI, 2018.

[12] C. J. Benson, D. J. Scheeres, W. H. Ryan, E. V. Ryan, and N. A. Moskovitz. GOES Spin State Diversity and the Implications for GEO Debris Mitigation. Acta Astronautica, 167:212–221, 2020.

[13] C. R. Binz, M. A. Davis, B. E. Kelm, and C. I. Moore. Optical Survey of the Tumble Rates of Retired GEO Satellites. Proceedings of the Advanced Maui Optical and Space Surveillance Technologies Conference, Maui, HI, 2014.

[14] R. P. Binzel. Collisional evolution in the eos and koronis asteroid families: Observational and numerical results. Icarus, 73:303–313, 1988.

[15] G. J. Black, P. D. Nicholson, W. F. Bottke, et al. On a possible rotation state of (433) eros. Icarus, 140:239–242, 1999.

[16] W. F. Bottke, A. Morbidelli, R. Jedicke, et al. Debiased orbital and absolute magnitude distribution of the near-earth objects. Icarus, 156(2):399–433, 2002.

[17] W. F. Bottke, D. Vokrouhlicky, D. P. Rubincam, and D. Nesvorny. The yarkovsky and yorp effects: Implications for asteroid dynamics. Annual Review of Earth and Planetary Sciences, 34:157–191, 2006.

[18] S. Breiter and M. Murawiecka. Tumbling asteroid rotation with the YORP torque and inelastic energy dissipation. Monthly Notices of the Royal Astronomical Society, 449:2489–2497, 2015.

[19] S. Breiter, A. Rozek, and D. Vokrouhlicky. Yarkovsky–O'Keefe–Radzievskii–Paddack effect on tumbling objects. Monthly Notices of the Royal Astronomical Society, 417(4):2478–2499, 2011.

[20] S. Breiter, D. Vokrouhlicky, and D. Nesvorny. Analytical yorp torques model with an improved temperature distribution function. Monthly Notices of the Royal Astronomical Society, 401:1933–1949, 2010.

[21] D. Brouwer. Solutions of the problem of artificial satellite theory without drag. Astronomical Journal, 64(1274), 1959.

[22] P. F. Byrd and M. D. Friedman. Handbook of Elliptic Integrals for Engineers and Scientists. Springer-Verlag, 2nd edition, 1970, pp. 18-20, 191-194, 282-287.

[23] D. Capek and D. Vokrouhlicky. The YORP effect with finite thermal conductivity. Icarus, 172:526–536, 2004.

[24] Nasa Goddard Space Flight Center. Osam-1: On-orbit servicing, assembly and manufacturing-1. https://nexis.gsfc.nasa.gov/osam-1.html, retrieved May. 7, 2021.

[25] S. R. Chesley, S. J. Ostro, D. Vokrouhlicky, et al. Direct detection of the yarkovsky effect via radar ranging to the near-earth asteroid 6489 golevka. Science, 302:1739–1742, 2003.

[26] S. Cicalo and D. J. Scheeres. Averaged rotational dynamics of an asteroid in tumbling rotation under the YORP torque. Celestial Mechanics and Dynamical Astronomy, 106(4):301–337, 2010.

[27] R. L. Cognion. Rotation rates of inactive satellites near geosynchronous earth orbit. Proceedings of the Advanced Maui Optical and Space Surveillance Technologies Conference, Maui, HI, 2014.

[28] Vicki Cox. Mission extension vehicle: Breathing life back into in-orbit satellites. `https://news.northropgrumman.com/news/features/mission-extension-vehicle-breathing-life-back-into-in-orbit-satellites`, retrieved Apr. 9, 2021.

[29] M. Cuk and J. A. Burns. Effects of thermal radiation on the dynamics of binary neas. Icarus, 176(2):418–431, 2005.

[30] D. R. Davis, S. J. Weidenschilling, P. Farinella, et al. Asteroids II, chapter Asteroidal collisional history: Effect on sizes and spins, pages 805–826. University of Arizona Press, Tucson, AZ, 1989.

[31] J. D. DeGumbia and Y. J. Tsui. Solar torque compensation determination system for the goes i-m series weather satellites. Proceedings of the AAS/GSFC International Symposium on Space Flight Dynamics, Greenbelt, MD, 1998.

[32] J. Durech, D. Vokrouhlicky, P. Pravec, et al. Yorp and yarkovsky effects in asteroids (1685) toro, (2100) ra-shalom, (3103) eger, and (161989) cacus. Astronomy and Astrophysics, 609, 2018.

[33] P. Dutre, K. Bala, and P. Bekaert. Advanced Global Illumination. AK Peters/CRC Press, 2nd edition, 2006.

[34] M. A. Earl and G. A. Wade. Observations of the Spin-Period Variation of Inactive Box-Wing Geosynchronous Satellites. Journal of Spacecraft and Rockets, 52(3):968–977, 2015.

[35] P. Farinella, D. R. Davis, P. Paolicchi, et al. Asteroid collisional evolutioni: An integrated model for the evolution of asteroid rotation rates. Astronomy and Astrophysics, 253:604–614, 1992.

[36] P. Farinella, R. Gonczi, Ch. Froeschle, and C. Froeschle. The injection of asteroid fragments into resonances. Icarus, 101:174–187, 1993.

[37] P. Farinella, D. Vokrouhlicky, and W. K. Hartmann. Meteorite delivery via yarkovsky orbital drift. Icarus, 132:378–387, 1998.

[38] D. Farnocchia, S. R. Chesley, D. Vokrouhlicky, et al. Near earth asteroids with measurable yarkovsky effect. Icarus, 224:1–13, 2013.

[39] J. V. Fedor. NASA Technical Note D-1855: The Effect of Solar Radiation Pressure on the Spin of Explorer XII. Goddard Space Flight Center, Greenbelt, MD, 1963.

[40] C. Frueh, D. Ferguson, C. Lin, and M. Jah. The effect of passive electrostatic charging on near-geosynchronous high area-to-mass ratio objects. Proceedings of the AAS Space Flight Mechanics Meeting, Sante Fe, NM, 2014.

[41] C. Frueh, T. M. Kelecy, and M. K. Jah. Coupled orbit-attitude dynamics of high area-to-mass ratio (HAMR) objects: influence of solar radiation pressure, Earth's shadow and the visibility in light curves. Celestial Mechanics and Dynamical Astronomy, 117:385–404, 2013.

[42] A. Fujiwara, J. Kawaguchi, D. K. Yoemans, et al. The rubble-pile asteroid itokawa as observed by hayabusa. Science, 312(5778):1330–1334, 2006.

[43] A. H. Greenberg, J. L. Margot, A. K. Verma, P. A. Taylor, and S. E. Hodge. Yarkovsky drift detections for 247 near-earth asteroids. The Astronomical Journal, 159(3), 2020.

[44] J. Hanus, M. Broz, B. D. Warner, et al. An anisotropic distribution of spin vectors in asteroid families. Astronomy and Astrophysics, 559:1725–1732, 2013.

[45] J. Hanus, M. Delbo, V. Ali-Lagoa, et al. Spin states of asteroids in the eos collisional family. Icarus, 299:84–96, 2018.

[46] A. W. Harris et al. Photoelectric Observations of Asteroids 3, 24, 60, 261, and 863. Icarus, 77(1):171–186, 1989.

[47] E. Harvie, A. Dress, and M. Phenneger. GOES On-Orbit Storage Mode Attitude Dynamics and Control. Advances in the Astronautical Sciences, 103(2):1095–1114, 1999.

[48] D. Helfrich. Landsat 7 Solar Array Testing Experiences. NASA 34th Aerospace Mechanics Symposium, Greenbelt, MD, 2000.

[49] C. W. Hergenrother, C. K. Maleszewski, M. C. Nolan, et al. The operational environment and rotational acceleration of asteroid (101955) bennu from osiris-rex observations. Nature Communications, 10(1291), 2019.

[50] K. Hirayama. Groups of asteroids probably of common origin. Astronomical Journal, 31:185–188, 1918.

[51] M. J. Holzinger, K. T. Alfriend, C. J. Wetterer, K. K. Luu, C. Sabol, and K. Hamada. Photometric Attitude Estimation for Agile Space Objects with Shape Uncertainty. Journal of Guidance, Control, and Dynamics, 37(3), 2014.

[52] J. Hughes and H. Schaub. Rapid Charged Geosynchronous Debris Perturbation Modeling of Electrodynamic Disturbances. Journal of the Astronautical Sciences, 65:135–156, 2018.

[53] J. Hughes and H. Schaub. Space Weather Influence on Electromagnetic Geosynchronous Debris Perturbations Using Statistical Fluxes. Space Weather, 16:391–405, 2018.

[54] P. C. Hughes. Spacecraft Attitude Dynamics. Dover Publications, New York, NY, 2004.

[55] S. A. Jacobson, D. J. Scheeres, and J. McMahon. Formation of the wide asynchronous binary asteroid population. The Astrophysical Journal, 760(1):60–81, 2014.

[56] M. Kaasalainen. Interpretation of lightcurves of precessing asteroids. Astronomy & Astrophysics, 376(1):302–309, 2001.

[57] Y. S. Karavaev, R. M. Kopyatkevich, M. N. Mishina, G. S. Mishin, P. G. Papushev, and P. N. Shaburov. The Dynamic Properties of Rotation and Optical Characteristics of Space Debris at Geostationary Orbit. Advances in the Astronautical Sciences, 119(2):1457–1466, 2004.

[58] W. A. Kaula. Theory of Satellite Geodesy. Blaisdell Publishing Co., Waltham, MA, 1966.

[59] D. G. King-Hele and D. M. C. Walker. Predicting the orbital lifetimes of earth satellites. Acta Astronautica, 18:123–131, 1988.

[60] D. Kirkwood. Meteoric Astronomy: a Treatise on Shooting-Stars, Fire-Balls, and Aerolites. J. B. Lippincott and Co., Philadelphia, PA, 1867.

[61] Y. Kozai. The motion of a close earth satellite. Astronomical Journal, 64(1274), 1959.

[62] Gunter Krebs. Optus b1, b2, b3. `https://space.skyrocket.de/doc_sdat/optus-b.html`, retrieved May. 13, 2021.

[63] D. Kucharski, G. Kirchner, F. Koidl, et al. Attitude and spin period of space debris envisat measured by satellite laser ranging. IEEE Transactions on Geoscience and Remote Sensing, 52(12), 2014.

[64] L. D. Landau and E. M. Lifshitz. Mechanics, volume 1. Pergamon Press, Oxford, England, 2nd edition, 1969, pp. 116-119.

[65] S. Lemmens. Classification of Geosynchronous Objects Issue 21. ESA Space Debris Office, 2019.

[66] R. Linares, J. L. Crassidis, and M. K. Jah. Particle Filtering Light Curve Based Attitude Estimation for Non-Resolved Space Objects (AAS 14-210). Proceedings of the 24th AAS/AIAA Space Flight Mechanics Meeting, Sante Fe, NM, 2014.

[67] J. C. Liou and J. K. Weaver. Orbital Dynamics of High Area-To Ratio Debris and Their Distribution in the Geosynchronous Region. Proceedings of the 4th European Conference on Space Debris, Darmstadt. Germany, 2005.

[68] S. Lowry et al. Direct detection of the asteroidal YORP effect. Science, 316:272–274, 2007.

[69] J. McMahon and D. J. Scheeres. Detailed prediction for the byorp effect on binary near-earth asteroid (66391) 1999 kw4 and implications for the binary population. Icarus, 209(2):494–509, 2010.

[70] H. R. Merson. The motion of a satellite in an ax-symmetric gravitation field. Geophysical Jorunal of the Royal Astronomical Society, 4(17), 1961.

[71] B. E. A. Mueller, N. H. Samarasinha, and M. J. S. Belton. The Diagnosis of Complex Rotation in the Lightcurve of 4179 Toutatis and Potential Applications to Other Asteroids and Bare Cometary Nuclei. Icarus, 158(2):305–311, 2002.

[72] D. Nesvorny, M. Broz, and V. Carruba. Asteroids IV, chapter Identification and Dynamical Properties of Asteroid Families, pages 297–321. University of Arizona Press, Tucson, AZ, 2015.

[73] G. W. Ojakangas and N. Hill. Toward realistic dynamics of rotating orbital debris and implications for light curve interpretation. Proceedings of the Advanced Maui Optical and Space Surveillance Technologies Conference, Maui, HI, 2011.

[74] J. A. O'Keefe. Tektites and Their Origin: Developments in Petrology. Elsevier, Amsterdam, 1976.

[75] E. J. Opik. Collision probabilities with the planets and the distribution of interplanetary matter. Proceedings of the Royal Irish Academy, 54:165–199, 1951.

[76] N. Ortiz Gomez and S. J. I. Walker. Eddy currents applied to de-tumbling of space debris: Analysis and validation of approximate proposed methods. Acta Astronautica, 114:34–53, 2015.

[77] S. J. Ostro. Planetary radar astronomy. Review of Modern Physics, 65(4), 1993.

[78] S. J. Paddack. Rotational bursting of small celestial bodies: Effects of radiation pressure. Journal of Geophysical Research, 74(17):4379–4381, 1969.

[79] K. C. Pande. Attitude control of spinning spacecraft by radiation pressure. Journal of Spacecraft, 13(12):765–768, 1976.

[80] P. Papushev, Y. Karavaev, and M. Mishina. Investigations of the evolution of optical characteristics and dynamics of proper rotation of uncontrolled geostationary artificial satellites. Advances in Space Research, 43(9):1416–1422, 2009.

[81] W. B. Patterson and K. E. Kissell. Comparison of the Theoretical Solar Radiation Effects and the Observed Accelerations of the PAGEOS Satellite. Journal of Spacecraft, 12(9):539–543, 1975.

[82] F. Piergentili, F. Santoni, and P. Seitzer. Attitude Determination of Orbiting Objects from Lightcurve Measurements. IEEE Transactions on Aerospace and Electronic Systems, 53(1), 2017.

[83] P. Pravec et al. Tumbling Asteroids. Icarus, 173(1):108–131, 2005.

[84] P. Pravec, D. Vokrouhlicky, D. Polishook, et al. Formation of asteroid pairs by rotational fission. Nature Letters, 466:1085–1088, 2010.

[85] W. H. Press, S. A. Teukolsky, W. T. Vetterling, and B. P. Flannery. Numerical Recipes. Cambridge University Press, Cambridge, UK, 3rd edition, 2007, pp. 309-318.

[86] A. Rachman, T. Schildknecht, and A. Vananti. Analysis of temporal evolution of debris objects' rotation rates inside aiub light curve database (iac-18-a6.3). Proceedings of the 69th International Astronautical Congress, Bremen, Germany, 2018.

[87] V.V. Radzievskii. mechanism for the disintegration of asteroids and meteorites. Doklady Akademii Nauk, 97:49–52, 1954.

[88] C. D. Rahn and P. M. Barba. Reorientation Maneuver for Spinning Spacecraft. Journal of Guidance, Control, and Dynamics, 14(4):724–728, 1991.

[89] D. C. Richardson, W. F. Bottke, and S. G. Love. Tidal distortion and disruption of earth-crossing asteroids. Icarus, 134:47–76, 1998.

[90] S. J. Robbins. New crater calibrations for the lunar crater-age chronology. Earth and Planetary Science Letters, 403:188–198, 2014.

[91] A. J. Rosengren, D. K. Skoulidou, K. Tsiganis, and G. Voyatzis. Dynamical Cartography of Earth satellite orbits. Advances in Space Research, 63(1):443–460, 2019.

[92] D. P. Rubincam. Yarkovsky thermal drag on small asteroids and mars- earth delivery. Journal of Geophysical Research, 103(E1):1725–1732, 1998.

[93] D. P. Rubincam. Radiative Spin-up and Spin-down of Small Asteroids. Icarus, 148(1):2–11, 2000.

[94] W. H. Ryan and E. V. Ryan. Photometric Studies of Rapidly Spinning Decommissioned GEO Satellites. Proceedings of the Advanced Maui Optical and Space Surveillance Technologies Conference, Maui, HI, 2015.

[95] N. H. Samarasinha and M. F. A'Hearn. Observational and Dynamical Constraints on the Rotation of Comet P/Halley. Icarus, 93(2):194–225, 1991.

[96] N. H. Samarasinha and B. E. A. Mueller. Component periods of non-principal-axis rotation and their manifestations in the lightcurves of asteroids and bare cometary nuclei. Icarus, 248:347–356, 2015.

[97] H. Schaub and D. F. Moorer Jr. Geosynchronous large debris reorbiter: Challenges and prospects. The Journal of the Astronautical Sciences, 59(1):165–180, 2012.

[98] H. Schaub and J. L. Junkins. Analytical Mechanics of Space Systems. American Insitute of Aeronautics and Astronautics, 3rd edition, 2014, pp. 11, 86-89, 110.

[99] D. J. Scheeres. Rotational fission of contact binary asteroids. Icarus, 189:370–385, 2007.

[100] D. J. Scheeres. The dynamical evolution of uniformly rotating asteroids subject to YORP. Icarus, 188(2):430–450, 2007.

[101] D. J. Scheeres. Orbital Motion in Strongly Perturbed Environments. Springer, 1st edition, 2012, pp. 73-86.

[102] D. J. Scheeres. Disaggregation of small, cohesive rubble pile asteroids due to yorp. Icarus, 304:183–191, 2018.

[103] D. J. Scheeres, S. J. Ostro, R. A. Werner, et al. Effects of gravitational interactions on asteroid spin states. Icarus, 147:106–118, 2000.

[104] T. Schildknecht. Optical surveys for space debris. The Astronomy and Astrophysics Review, 14(1):41–111, 2007.

[105] J. Silha, J. N. Pittet, M. Hamara, and T. Schildknecht. Apparent rotation properties of space debris extracted from photometric measurements. Advances in Space Research, 61:844–861, 2018.

[106] D. E. Smith and K. E. Kissell. Anomalous Accelerations of the PAGEOS Spacecraft. Proceedings of COSPAR, Seattle, WA, 1971.

[107] Space Systems/Loral. GOES I-M Databook (Rev. 1). NASA, 1996. https://goes.gsfc.nasa.gov/text/goes.databook.html, retrieved Sept. 9, 2017.

[108] Y. Tsuda, T. Saiki, R. Funase, and Y. Mimasu. Generalized Attitude Model for Spinning Solar Sail Spacecraft. Journal of Guidance, Control, and Dynamics, 34(4):967–974, 2013.

[109] D. A. Vallado and W. D. McClain. Fundamentals of Astrodynamics and Applications. Microcosm Press, Hawthorne, CA, 4th edition, 2013, Chs. 2, 9.

[110] J. C. van der Ha and V. J. Lappas. Long-term attitude drift of spinning spacecraft under solar radiation torques. Journal of Guidance, Control, and Dynamics, 30(5):1470–1479, 2007.

[111] D. Vokrouhlicky, W. F. Bottke, S. R. Chesley, D. J. Scheeres, and T. S. Statler. Asteroids IV, chapter The Yarkovsky and YORP Effects, pages 509–532. University of Arizona Press, Tucson, AZ, 2015.

[112] D. Vokrouhlicky, S. Breiter, D. Nesvorny, and W. F. Bottke. Generalized YORP evolution: Onset of tumbling and new asymptotic states. Icarus, 191(2):636–650, 2007.

[113] D. Vokrouhlicky and D. Capek. YORP-Induced Long-Term Evolution of the Spin State of Small Asteroids and Meteoroids: Rubincam's Approximation. Icarus, 159:449–467, 2002.

[114] D. Vokrouhlicky and P. Farinella. Efficient delivery of meteorites to the earth from a wide range of asteroid parent bodies. Nature, 407:606–608, 2000.

[115] G. W. Wetherill and C. R. Chapman. Meteorites and the Early Solar System, chapter Asteroids and meteorites, pages 35–67. University of Arizona Press, Tucson, AZ, 1988.

[116] C. J. Wetterer and M. Jah. Attitude Estimation from Light Curves. Journal of Guidance, Control, and Dynamics, 32(5), 2009.

[117] J. Wisdom. Meteorites may follow a chaotic route to earth. Nature, 315:731–733, 1985.

[118] V. Zappala, A. Cellino, A. Dell'Oro, F. Migliorini, and P. Paolicchi. Reconstructing the original ejection velocity fields of asteroid families. Icarus, 124:156–180, 1996.

Appendix A

Averaged Quantities

From Ref. [22], we can obtain the following elliptic function averages,

$$\frac{1}{4K} \int_0^{4K} \operatorname{sn} \tau d\tau = 0 \tag{A.1}$$

$$\frac{1}{4K} \int_0^{4K} \operatorname{cn} \tau d\tau = 0 \tag{A.2}$$

$$\frac{1}{4K} \int_0^{4K} \operatorname{dn} \tau d\tau = \frac{\pi}{2K} \tag{A.3}$$

$$\frac{1}{4K} \int_0^{4K} \operatorname{sn}^2 \tau d\tau = \frac{K - E}{k^2 K} \tag{A.4}$$

$$\frac{1}{4K} \int_0^{4K} \operatorname{cn}^2 \tau d\tau = \frac{E - k'^2 K}{k^2 K} \tag{A.5}$$

$$\frac{1}{4K} \int_0^{4K} \operatorname{dn}^2 \tau d\tau = \frac{E}{K} \tag{A.6}$$

$$\frac{1}{4K} \int_0^{4K} \operatorname{sn}^2 \tau \operatorname{dn} \tau d\tau = \frac{\pi}{4K} \tag{A.7}$$

$$\frac{1}{4K} \int_0^{4K} \operatorname{cn}^2 \tau \operatorname{dn} \tau d\tau = \frac{\pi}{4K} \tag{A.8}$$

$$\frac{1}{4K} \int_0^{4K} \mathrm{dn}^3 \tau d\tau = \frac{(k'^2 + 1)\pi}{4K} \tag{A.9}$$

$$\frac{1}{4K} \int_0^{4K} \mathrm{sn}^4 \tau d\tau = \frac{(k^2 + 2)K - 2(k^2 + 1)E}{3k^4 K} \tag{A.10}$$

$$\frac{1}{4K} \int_0^{4K} \mathrm{cn}^4 \tau d\tau = \frac{(4k^2 - 2)E - k'^2(3k^2 - 2)K}{3k^4 K} \tag{A.11}$$

$$\frac{1}{4K} \int_0^{4K} \mathrm{dn}^4 \tau d\tau = \frac{2(k'^2 + 1)E - k'^2 K}{3K} \tag{A.12}$$

$$\frac{1}{4K} \int_0^{4K} \mathrm{sn}^2 \tau \, \mathrm{cn}^2 \tau d\tau = \frac{(1 + k'^2)E - 2k'^2 K}{3k^4 K} \tag{A.13}$$

$$\frac{1}{4K} \int_0^{4K} \mathrm{sn}^2 \tau \, \mathrm{dn}^2 \tau d\tau = \frac{(2k^2 - 1)E + k'^2 K}{3k^2 K} \tag{A.14}$$

$$\frac{1}{4K} \int_0^{4K} \mathrm{cn}^2 \tau \, \mathrm{dn}^2 \tau d\tau = \frac{(1 + k^2)E - k'^2 K}{3k^2 K} \tag{A.15}$$

where E is the complete elliptic integral of the second kind [85] and $k'^2 = 1 - k^2$.

A.1   Long Axis Modes

After averaging over ϕ, we follow Ref. [26] and write all averaged expressions in terms of $\overline{a_{z1}}$, $\overline{a_{z2}}$, and $\overline{a_{z3}}$ because they are independent of ϕ. Following the notation of Eq. 4.8, for LAMs we have the following expressions with (1, 2, 3) subscripts denoting the $\mathcal{B}$ frame vector components and using f as a placeholder for d and r.

$$\overline{f_z} = f_3 \overline{a_{z3}} \tag{A.16}$$

$$\overline{f_x n_x} = \frac{1}{2}\left(f_3 n_3 - f_1 n_1\right)\overline{a_{z1}^2} + \frac{1}{2}\left(f_3 n_3 - f_2 n_2\right)\overline{a_{z2}^2} + \frac{1}{2}\left(f_1 n_1 + f_2 n_2\right) \tag{A.17}$$

$$\overline{f_y n_x} = \frac{1}{2}\left(f_2 n_1 - f_1 n_2\right)\overline{a_{z3}} \tag{A.18}$$

$$\overline{f_z n_z} = f_1 n_1 \overline{a_{z1}^2} + f_2 n_2 \overline{a_{z2}^2} + f_3 n_3 \overline{a_{z3}^2} \tag{A.19}$$

$$\overline{f_x n_x n_z} = \frac{1}{2}\left(f_1 n_1 n_3 + f_2 n_2 n_3\right)\overline{a_{z3}} - \frac{1}{2}\left(f_3 n_1^2 + 2f_1 n_1 n_3 - f_3 n_3^2\right)\overline{a_{z1}^2 a_{z3}} - \frac{1}{2}\left(f_3 n_2^2 + 2f_2 n_2 n_3 - f_3 n_3^2\right)\overline{a_{z2}^2 a_{z3}} \tag{A.20}$$

$$\overline{f_y n_x n_z} = \frac{1}{2}\left(f_3 n_1 n_2 - f_2 n_1 n_3\right)\overline{a_{z1}^2} + \frac{1}{2}\left(f_1 n_2 n_3 - f_3 n_1 n_2\right)\overline{a_{z2}^2} + \frac{1}{2}\left(f_2 n_1 n_3 - f_1 n_2 n_3\right)\overline{a_{z3}^2} \tag{A.21}$$

$$\overline{f_z n_x^2} = \frac{1}{2}\left(f_3 n_1^2 + f_3 n_2^2\right)\overline{a_{z3}} - \frac{1}{2}\left(f_3 n_1^2 + 2f_1 n_1 n_3 - f_3 n_3^2\right)\overline{a_{z1}^2 a_{z3}} - \frac{1}{2}\left(f_3 n_2^2 + 2f_2 n_2 n_3 - f_3 n_3^2\right)\overline{a_{z2}^2 a_{z3}} \tag{A.22}$$

$$\overline{f_z n_z^2} = \left(f_3 n_1^2 + 2f_1 n_1 n_3\right)\overline{a_{z1}^2 a_{z3}} + \left(f_3 n_2^2 + 2f_2 n_2 n_3\right)\overline{a_{z2}^2 a_{z3}} + f_3 n_3^2 \overline{a_{z3}^3} \tag{A.23}$$

$$\begin{aligned}
\overline{f_x n_x^3} = &+ \frac{3}{8}\left(3f_3 n_1^2 n_3 - 2f_1 n_1^3 - 3f_2 n_1^2 n_2 - f_1 n_1 n_2^2 + 3f_1 n_1 n_3^2 + f_3 n_2^2 n_3 + f_2 n_2 n_3^2\right)\overline{a_{z1}^2} \\
&+ \frac{3}{8}\left(f_2 n_1^2 n_2 + f_3 n_1^2 n_3 - f_1 n_1 n_2^2 + f_1 n_1 n_3^2 - 2f_2 n_2^3 + 3f_3 n_2^2 n_3 + 3f_2 n_2 n_3^2\right)\overline{a_{z2}^2} \\
&+ \frac{3}{8}\left(f_1 n_1^3 - 3f_3 n_1^2 n_3 - 3f_1 n_1 n_3^2 + f_3 n_3^3\right)\overline{a_{z1}^4} + \frac{3}{8}\left(f_2 n_2^3 - 3f_3 n_2^2 n_3 - 3f_2 n_2 n_3^2 + f_3 n_3^3\right)\overline{a_{z2}^4} \\
&+ \frac{3}{8}\left(3f_2 n_1^2 n_2 - 3f_3 n_1^2 n_3 + 3f_1 n_1 n_2^2 - 3f_1 n_1 n_3^2 - 3f_3 n_2^2 n_3 - 3f_2 n_2 n_3^2 + 2f_3 n_3^3\right)\overline{a_{z1}^2 a_{z2}^2} \\
&+ \frac{3}{8}\left(f_1 n_1^3 + f_2 n_1^2 n_2 + f_1 n_1 n_2^2 + f_2 n_2^3\right)
\end{aligned} \tag{A.24}$$

$$\begin{aligned}
\overline{f_x n_x n_z^2} = &+ \frac{1}{2}\left(f_1 n_1^3 - 2f_3 n_1^2 n_3 + f_2 n_2 n_1^2 - 4f_1 n_1 n_3^2 + f_3 n_3^3 - f_2 n_2 n_3^2\right)\overline{a_{z1}^2} \\
&+ \frac{1}{2}\left(f_2 n_2^3 - 2f_3 n_2^2 n_3 + f_1 n_1 n_2^2 - 4f_2 n_2 n_3^2 + f_3 n_3^3 - f_1 n_1 n_3^2\right)\overline{a_{z2}^2} \\
&+ \frac{1}{2}\left(- f_1 n_1^3 + 3f_3 n_1^2 n_3 + 3f_1 n_1 n_3^2 - f_3 n_3^3\right)\overline{a_{z1}^4} \\
&+ \frac{3}{2}\left(f_2 n_1^2 n_2 + f_3 n_1^2 n_3 - f_1 n_1 n_2^2 + f_1 n_1 n_3^2 + f_3 n_2^2 n_3 + f_2 n_2 n_3^2 - \frac{2}{3}f_3 n_3^3\right)\overline{a_{z1}^2 a_{z2}^2} \\
&+ \frac{1}{2}\left(- f_2 n_2^3 + 3f_3 n_2^2 n_3 + 3f_2 n_2 n_3^2 - f_3 n_3^3\right)\overline{a_{z2}^4} + \frac{1}{2}\left(f_1 n_1 n_3^2 + f_2 n_2 n_3^2\right)
\end{aligned} \tag{A.25}$$

$$\overline{f_y n_x^3} = -\frac{3}{8}\Big((f_2 n_1^3 - f_1 n_2 n_1^2 - 3f_2 n_1 n_3^2 + 2f_3 n_2 n_1 n_3 + f_1 n_2 n_3^2)\overline{a_{z1}^2 a_{z3}}$$
$$+\frac{3}{8}\Big(f_1 n_2^3 - f_2 n_1 n_2^2 - 3f_1 n_2 n_3^2 + 2f_3 n_1 n_2 n_3 + f_2 n_1 n_3^2\Big)\overline{a_{z2}^2 a_{z3}} \tag{A.26}$$
$$-\frac{3}{8}\Big((-f_2 n_1^3 + f_1 n_1^2 n_2 - f_2 n_1 n_2^2 + f_1 n_2^3)\overline{a_{z3}}$$

$$\overline{f_y n_x n_z^2} = +\frac{1}{2}\Big(f_2 n_1^3 - f_1 n_2 n_1^2 - 3f_2 n_1 n_3^2 + 2f_3 n_2 n_1 n_3 + f_1 n_2 n_3^2\Big)\overline{a_{z1}^2 a_{z3}}$$
$$-\frac{1}{2}\Big(f_1 n_2^3 - f_2 n_1 n_2^2 - 3f_1 n_2 n_3^2 + 2f_3 n_1 n_2 n_3 + f_2 n_1 n_3^2\Big)\overline{a_{z2}^2 a_{z3}} \tag{A.27}$$
$$-\frac{1}{2}\Big(f_1 n_2 - f_2 n_1)n_3^2 \overline{a_{z3}}$$

$$\overline{f_z n_x^2 n_z} = +\frac{1}{2}\Big(f_1 n_1^3 - 4f_3 n_1^2 n_3 + f_1 n_1 n_2^2 - 2f_1 n_1 n_3^2 - f_3 n_2^2 n_3 + f_3 n_3^3\Big)\overline{a_{z1}^2}$$
$$+\frac{1}{2}\Big(f_2 n_1^2 n_2 - f_3 n_1^2 n_3 + f_2 n_2^3 - 4f_3 n_2^2 n_3 - 2f_2 n_2 n_3^2 + f_3 n_3^3\Big)\overline{a_{z2}^2} + \frac{1}{2}\Big(f_3 n_3 n_1^2 + f_3 n_3 n_2^2\Big)$$
$$+\frac{1}{2}\Big(-f_1 n_1^3 + 3f_3 n_1^2 n_3 + 3f_1 n_1 n_3^2 - f_3 n_3^3\Big)\overline{a_{z1}^4} + \frac{1}{2}\Big(-f_2 n_2^3 + 3f_3 n_2^2 n_3 + 3f_2 n_2 n_3^2 - f_3 n_3^3\Big)\overline{a_{z2}^4}$$
$$+\frac{3}{2}\Big(-f_2 n_1^2 n_2 + f_3 n_1^2 n_3 - f_1 n_1 n_2^2 + f_1 n_1 n_3^2 + f_3 n_2^2 n_3 + f_2 n_2 n_3^2 - \frac{2}{3}f_3 n_3^3\Big)\overline{a_{z1}^2 a_{z2}^2}$$
$$\tag{A.28}$$

$$\overline{f_z n_z^3} = +\Big(3f_3 n_1^2 n_3 + 3f_1 n_1 n_3^2 - 2f_3 n_3^3\Big)\overline{a_{z1}^2} + \Big(3f_3 n_2^2 n_3 + 3f_2 n_2 n_3^2 - 2f_3 n_3^3\Big)\overline{a_{z2}^2}$$
$$+\Big(f_1 n_1^3 - 3f_3 n_1^2 n_3 - 3f_1 n_1 n_3^2 + f_3 n_3^3\Big)\overline{a_{z1}^4} + \Big(f_2 n_2^3 - 3f_3 n_2^2 n_3 - 3f_2 n_2 n_3^2 + f_3 n_3^3\Big)\overline{a_{z2}^4} \tag{A.29}$$
$$+3\Big(f_2 n_1^2 n_2 - f_3 n_1^2 n_3 + f_1 n_1 n_2^2 - f_1 n_1 n_3^2 - f_3 n_2^2 n_3 - f_2 n_2 n_3^2 + \frac{2}{3}f_3 n_3^3\Big)\overline{a_{z1}^2 a_{z2}^2} + f_3 n_3^3$$

$$\overline{g a_{z1}\delta_1} = +\frac{2}{3\pi}\Big(6n_1 n_3 r_2 u_x^2 u_z - 4n_1 n_3 r_2 u_z^3\Big)\overline{a_{z1}^4} + \frac{1}{4}\Big(2n_1 r_2 u_z^2 - n_1 r_2 u_x^2\Big)\overline{a_{z1}^2 a_{z3}}$$
$$+\frac{2}{3\pi}\Big(6n_1 n_2 r_3 u_x^2 u_z - 4n_1 n_3 r_2 u_z^3 - 4n_1 n_2 r_3 u_z^3 + 6n_1 n_3 r_2 u_x^2 u_z\Big)\overline{a_{z1}^2 a_{z2}^2} \tag{A.30}$$
$$+\frac{4}{3\pi}\Big(2n_1 n_3 r_2 u_z^3 - n_1 n_2 r_3 u_x^2 u_z - 2n_1 n_3 r_2 u_x^2 u_z\Big)\overline{a_{z1}^2}$$

$$\overline{g a_{z2}\delta_2} = +\frac{2}{3\pi}\Big(4n_1 n_2 r_3 u_z^3 + 4n_2 n_3 r_1 u_z^3 - 6n_1 n_2 r_3 u_x^2 u_z - 6n_2 n_3 r_1 u_x^2 u_z\Big)\overline{a_{z1}^2 a_{z2}^2}$$
$$+\frac{2}{3\pi}\Big(4n_2 n_3 r_1 u_z^3 - 6n_2 n_3 r_1 u_x^2 u_z\Big)\overline{a_{z2}^4} + \frac{1}{4}\Big(n_2 r_1 u_x^2 - 2n_2 r_1 u_z^2\Big)\overline{a_{z2}^2 a_{z3}} \tag{A.31}$$
$$+\frac{4}{3\pi}\Big(n_1 n_2 r_3 u_x^2 u_z - 2n_2 n_3 r_1 u_z^3 + 2n_2 n_3 r_1 u_x^2 u_z\Big)\overline{a_{z2}^2}$$

$$\overline{ga_{z3}\delta_3} = + \frac{2}{3\pi}\left(6n_1n_3r_2u_x^2u_z - 4n_1n_3r_2u_z^3\right)\overline{a_{z1}^2a_{z3}^2} + \frac{1}{4}\left(n_1r_2u_x^2 - 2n_1r_2u_z^2\right)\overline{a_{z1}^2a_{z3}}$$
$$+ \frac{2}{3\pi}\left(4n_2n_3r_1u_z^3 - 6n_2n_3r_1u_x^2u_z\right)\overline{a_{z2}^2a_{z3}^2} - \frac{1}{4}\left(n_2r_1u_x^2 - 2n_2r_1u_z^2\right)\overline{a_{z2}^2a_{z3}} \tag{A.32}$$
$$+ \frac{4}{3\pi}\left(n_2n_3r_1u_x^2u_z - n_1n_3r_2u_x^2u_z\right)\overline{a_{z3}^2} - \frac{1}{4\pi}\left(n_1r_2u_x^2 - n_2r_1u_x^2\right)\overline{a_{z3}}$$

A.2 Short Axis Modes

The following averaged expressions hold for SAMs,

$$\overline{f_z} = f_2\overline{a_{z2}} \tag{A.33}$$

$$\overline{f_xn_x} = \frac{1}{2}\left(f_3n_3 - f_1n_1\right)\overline{a_{z1}^2} + \frac{1}{2}\left(f_3n_3 - f_2n_2\right)\overline{a_{z2}^2} + \frac{1}{2}\left(f_1n_1 + f_2n_2\right) \tag{A.34}$$

$$\overline{f_yn_x} = \frac{1}{2}(f_1n_3 - f_3n_1)\overline{a_{z2}} \tag{A.35}$$

$$\overline{f_zn_z} = f_1n_1\overline{a_{z1}^2} + f_2n_2\overline{a_{z2}^2} + f_3n_3\overline{a_{z3}^2} \tag{A.36}$$

$$\overline{f_xn_xn_z} = + \frac{1}{2}\left(f_2n_3^2 - f_2n_1^2 - 2f_1n_2n_1 + 2f_3n_2n_3\right)\overline{a_{z1}^2a_{z2}}$$
$$+ \frac{1}{2}\left(f_2n_3^2 - f_2n_2^2 + 2f_3n_2n_3\right)\overline{a_{z2}^3} + \frac{1}{2}\left(f_2n_2^2 - f_3n_2n_3 + f_1n_1n_2 - f_2n_3^2\right)\overline{a_{z2}} \tag{A.37}$$

$$\overline{f_yn_xn_z} = + \frac{1}{2}\left(f_1n_2n_3 - 2f_2n_1n_3 + f_3n_1n_2\right)\overline{a_{z1}^2} + \frac{1}{2}\left(2f_1n_2n_3 - f_2n_1n_3 - f_3n_1n_2\right)\overline{a_{z2}^2}$$
$$+ \frac{1}{2}\left(f_2n_1n_3 - f_1n_2n_3\right) \tag{A.38}$$

$$\overline{f_zn_x^2} = + \frac{1}{2}\left(f_2n_3^2 - f_2n_1^2 - 2f_1n_2n_1 + 2f_3n_2n_3\right)\overline{a_{z1}^2a_{z2}} + \frac{1}{2}\left(f_2n_3^2 - f_2n_2^2 + 2f_3n_2n_3\right)\overline{a_{z2}^3}$$
$$+ \frac{1}{2}\left(f_2n_1^2 + f_2n_2^2 - 2f_3n_3n_2\right)\overline{a_{z2}} \tag{A.39}$$

$$\overline{f_zn_z^2} = \left(f_2n_1^2 + 2f_1n_2n_1 - f_2n_3^2 - 2f_3n_2n_3\right)\overline{a_{z1}^2a_{z2}} + \left(f_2n_2^2 - 2f_3n_2n_3 - f_2n_3^2\right)\overline{a_{z2}^3} + \left(f_2n_3^2 + 2f_3n_2n_3\right)\overline{a_{z2}} \tag{A.40}$$

$$\overline{f_x n_x^3} = +\frac{1}{8}\left(3f_1 n_1^3 - 9f_3 n_1^2 n_3 - 9f_1 n_1 n_3^2 + 3f_3 n_3^3\right)\overline{a_{z1}^4} + \frac{3}{8}\left(3f_2 n_2^3 - 3f_3 n_2^2 n_3 - 3f_2 n_2 n_3^2 + f_3 n_3^3\right)\overline{a_{z2}^4}$$

$$+\frac{9}{8}\left(9f_2 n_1^2 n_2 - f_3 n_1^2 n_3 + f_1 n_1 n_2^2 - 9f_1 n_1 n_3^2 - 9f_3 n_2^2 n_3 - 9f_2 n_2 n_3^2 + \frac{2}{3}f_3 n_3^3\right)\overline{a_{z1}^2 a_{z2}^2}$$

$$+\frac{3}{8}\left(-2f_1 n_1^3 - f_2 n_1^2 n_2 + 3f_3 n_1^2 n_3 - f_1 n_1 n_2^2 + 3f_1 n_1 n_3^2 + f_3 n_2^2 n_3 + f_2 n_2 n_3^2\right)\overline{a_{z1}^2}$$

$$+\frac{3}{8}\left(-f_2 n_1^2 n_2 + f_3 n_1^2 n_3 - f_1 n_1 n_2^2 + f_1 n_1 n_3^2 - 2f_2 n_2^3 + 3f_3 n_2^2 n_3 + 3f_2 n_2 n_3^2\right)\overline{a_{z2}^2}$$

$$+\frac{3}{8}\left(3f_1 n_1^3 + 3f_2 n_1^2 n_2 + 3f_1 n_1 n_2^2 + 3f_2 n_2^3\right) \tag{A.41}$$

$$\overline{f_x n_x n_z^2} = +\frac{1}{2}\left(-f_1 n_1^3 + 3f_3 n_1^2 n_3 + 3f_1 n_1 n_3^2 - f_3 n_3^3\right)\overline{a_{z1}^4} + \frac{1}{2}\left(-f_2 n_2^3 + 3f_3 n_2^2 n_3 + 3f_2 n_2 n_3^2 - f_3 n_3^3\right)\overline{a_{z2}^4}$$

$$+\frac{3}{2}\left(-f_2 n_1^2 n_2 + f_3 n_1^2 n_3 - f_1 n_1 n_2^2 + f_1 n_1 n_3^2 + f_3 n_2^2 n_3 + f_2 n_2 n_3^2 - \frac{2}{3}f_3 n_3^3\right)\overline{a_{z1}^2 a_{z2}^2}$$

$$+\frac{1}{2}\left(f_1 n_1^3 - 2f_3 n_1^2 n_3 + f_2 n_2 n_1^2 - 4f_1 n_1 n_3^2 + f_3 n_3^3 - f_2 n_2 n_3^2\right)\overline{a_{z1}^2}$$

$$+\frac{1}{2}\left(f_2 n_2^3 - 2f_3 n_2^2 n_3 + f_1 n_1 n_2^2 - 4f_2 n_2 n_3^2 + f_3 n_3^3 - f_1 n_1 n_3^2\right)\overline{a_{z2}^2} + \frac{1}{2}\left(f_1 n_1 n_3^2 + f_2 n_2 n_3^2\right) \tag{A.42}$$

$$\overline{f_y n_x^3} = +\frac{3}{8}\left(f_3 n_1^3 - f_1 n_1^2 n_3 - 2f_3 n_1 n_2^2 + 4f_2 n_1 n_2 n_3 - f_3 n_1 n_3^2 - 2f_1 n_2^2 n_3 + f_1 n_3^3\right)\overline{a_{z1}^2 a_{z2}}$$

$$+\frac{3}{8}\left(-3f_1 n_2^2 n_3 + f_3 n_1 n_2^2 + 2f_2 n_1 n_2 n_3 + f_1 n_3^3 - f_3 n_1 n_3^2\right)\overline{a_{z2}^3}$$

$$+\frac{3}{8}\left(-f_3 n_1^3 + f_1 n_3 n_1^2 - f_3 n_1 n_2^2 - 2f_2 n_3 n_1 n_2 + 3f_1 n_3 n_2^2\right)\overline{a_{z2}} \tag{A.43}$$

$$\overline{f_y n_x n_z^2} = +\frac{1}{2}\left(-f_3 n_1^3 + f_1 n_1^2 n_3 + 2f_3 n_1 n_2^2 - 4f_2 n_1 n_2 n_3 + f_3 n_1 n_3^2 + 2f_1 n_2^2 n_3 - f_1 n_3^3\right)\overline{a_{z1}^2 a_{z2}}$$

$$+\frac{1}{2}\left(3f_1 n_2^2 n_3 - f_3 n_1 n_2^2 - 2f_2 n_1 n_2 n_3 - f_1 n_3^3 + f_3 n_1 n_3^2\right)\overline{a_{z2}^3}$$

$$+\frac{1}{2}\left(-2f_1 n_2^2 n_3 + 2f_2 n_1 n_2 n_3 + f_1 n_3^3 - f_3 n_1 n_3^2\right)\overline{a_{z2}} \tag{A.44}$$

$$\overline{f_z n_x^2 n_z} = +\frac{1}{2}\left(-f_1 n_1^3 + 3f_3 n_1^2 n_3 + 3f_1 n_1 n_3^2 - f_3 n_3^3\right)\overline{a_{z1}^4} + \frac{1}{2}\left(-f_2 n_2^3 + 3f_3 n_2^2 n_3 + 3f_2 n_2 n_3^2 - f_3 n_3^3\right)\overline{a_{z2}^4}$$

$$+\frac{3}{2}\left(-f_2 n_1^2 n_2 + f_3 n_1^2 n_3 - f_1 n_1 n_2^2 + f_1 n_1 n_3^2 + f_3 n_2^2 n_3 + f_2 n_2 n_3^2 - \frac{2}{3}f_3 n_3^3\right)\overline{a_{z1}^2 a_{z2}^2}$$

$$+\frac{1}{2}\left(f_1 n_1^3 - 4f_3 n_1^2 n_3 + f_1 n_1 n_2^2 - 2f_1 n_1 n_3^2 - f_3 n_2^2 n_3 + f_3 n_3^3\right)\overline{a_{z1}^2}$$

$$+\frac{1}{2}\left(f_2 n_1^2 n_2 - f_3 n_1^2 n_3 + f_2 n_2^3 - 4f_3 n_2^2 n_3 - 2f_2 n_2 n_3^2 + f_3 n_3^3\right)\overline{a_{z2}^2} + \frac{1}{2}\left(f_3 n_3 n_1^2 + f_3 n_3 n_2^2\right) \tag{A.45}$$

$$\overline{f_z n_z^3} = + \left(f_1 n_1^3 - 3f_3 n_1^2 n_3 - 3f_1 n_1 n_3^2 + f_3 n_3^3\right)\overline{a_{z1}^4} + 3\left(f_3 n_1^2 n_3 + f_1 n_1 n_3^2 - \frac{2}{3}f_3 n_3^3\right)\overline{a_{z1}^2}$$

$$+ 3\left(f_2 n_1^2 n_2 - f_3 n_1^2 n_3 + f_1 n_1 n_2^2 - f_1 n_1 n_3^2 - f_3 n_2^2 n_3 - f_2 n_2 n_3^2 + \frac{2}{3}f_3 n_3^3\right)\overline{a_{z1}^2 a_{z2}^2} \tag{A.46}$$

$$+ \left(f_2 n_2^3 - 3f_3 n_2^2 n_3 - 3f_2 n_2 n_3^2 + f_3 n_3^3\right)\overline{a_{z2}^4} + 3\left(f_3 n_2^2 n_3 + f_2 n_2 n_3^2 - \frac{2}{3}f_3 n_3^3\right)\overline{a_{z2}^2} + f_3 n_3^3$$

$$\overline{ga_{z1}\delta_1} = \frac{2}{3\pi}\left(6n_1 n_3 r_2 u_x^2 u_z - 4n_1 n_3 r_2 u_z^3\right)\overline{a_{z1}^4} + \frac{1}{4}\left(n_1 r_3 u_x^2 - 2n_1 r_3 u_z^2\right)\overline{a_{z1}^2 a_{z2}}$$

$$+ \frac{2}{3\pi}\left(6n_1 n_2 r_3 u_x^2 u_z - 4n_1 n_3 r_2 u_z^3 - 4n_1 n_2 r_3 u_z^3 + 6n_1 n_3 r_2 u_x^2 u_z\right)\overline{a_{z1}^2 a_{z2}^2} \tag{A.47}$$

$$+ \frac{4}{3\pi}\left(2n_1 n_3 r_2 u_z^3 - n_1 n_2 r_3 u_x^2 u_z - 2n_1 n_3 r_2 u_x^2 u_z\right)\overline{a_{z1}^2}$$

$$\overline{ga_{z2}\delta_2} = \frac{2}{3\pi}\left(4n_1 n_2 r_3 u_z^3 + 4n_2 n_3 r_1 u_z^3 - 6n_1 n_2 r_3 u_x^2 u_z - 6n_2 n_3 r_1 u_x^2 u_z\right)\overline{a_{z1}^2 a_{z2}^2}$$

$$- \frac{3}{12}\left(n_1 r_3 u_x^2 + n_3 r_1 u_x^2 - 2n_1 r_3 u_z^2 - 2n_3 r_1 u_z^2\right)\overline{a_{z1}^2 a_{z2}}$$

$$+ \frac{2}{3\pi}\left(4n_2 n_3 r_1 u_z^3 - 6n_2 n_3 r_1 u_x^2 u_z\right)\overline{a_{z2}^4} - \frac{1}{4}\left(n_3 r_1 u_x^2 - 2n_3 r_1 u_z^2\right)\overline{a_{z2}^3} \tag{A.48}$$

$$+ \frac{4}{3\pi}\left(n_1 n_2 r_3 u_x^2 u_z - 2n_2 n_3 r_1 u_z^3 + 2n_2 n_3 r_1 u_x^2 u_z\right)\overline{a_{z2}^2} + \frac{1}{4}\left(n_1 r_3 u_x^2 - 2n_3 r_1 u_z^2\right)\overline{a_{z2}}$$

$$\overline{ga_{z3}\delta_3} = \frac{2}{3\pi}\left(6n_1 n_3 r_2 u_x^2 u_z - 4n_1 n_3 r_2 u_z^3\right)\overline{a_{z1}^2 a_{z3}^2} + \frac{2}{3\pi}\left(4n_2 n_3 r_1 u_z^3 - 6n_2 n_3 r_1 u_x^2 u_z\right)\overline{a_{z2}^2 a_{z3}^2}$$

$$- \frac{1}{4}\left(n_3 r_1 u_x^2 - 2n_3 r_1 u_z^2\right)\overline{a_{z2} a_{z3}^2} + \frac{4}{3\pi}\left(n_2 n_3 r_1 u_x^2 u_z - n_1 n_3 r_2 u_x^2 u_z\right)\overline{a_{z3}^2} \tag{A.49}$$

Appendix B

Expressions for $\ddot{\varphi}$ and $\ddot{\tau}_r$

From Eq. 2.31, for both LAMs and SAMs,

$$\dot{\varphi} = \frac{2\pi}{P_{\bar{\phi}}} = \frac{H}{I_l} \left[1 - \frac{(I_s - I_l)}{I_s} \frac{\Pi(K(k), n)}{K(k)} \right] \tag{B.1}$$

Taking the time derivative of Eq. B.1, we have,

$$\ddot{\varphi} = \frac{\dot{H}}{I_l} \left[1 - \frac{(I_s - I_l)}{I_s} \frac{\Pi}{K} \right] - \frac{H(I_s - I_l)}{I_l I_s} \frac{d}{dt}\left(\frac{\Pi}{K} \right) \tag{B.2}$$

Evaluating the cascading terms using the solutions provided in Ref. [22], we find,

$$\frac{d}{dt}\left(\frac{\Pi}{K} \right) = \frac{K\dot{\Pi} - \Pi\dot{K}}{K^2} \tag{B.3}$$

$$\dot{\Pi} = \left(\frac{\partial \Pi}{\partial k} \frac{\partial k}{\partial I_d} + \frac{\partial \Pi}{\partial n} \frac{\partial n}{\partial I_d} \right) \dot{I}_d \tag{B.4}$$

$$\frac{\partial \Pi}{\partial k} = \frac{k(E - k'^2 \Pi)}{k'^2 (k^2 + n)} \tag{B.5}$$

$$\frac{\partial \Pi}{\partial n} = \frac{-(k^2 + n)K + nE + (k^2 - n^2)\Pi}{2n(n+1)(n+k^2)} \tag{B.6}$$

$$\dot{K} = \frac{\partial K}{\partial k} \frac{\partial k}{\partial I_d} \dot{I}_d \tag{B.7}$$

$$\frac{\partial K}{\partial k} = \frac{E - k'^2 K}{k k'^2} \tag{B.8}$$

where $E = E(k)$ is the complete elliptic integral of the second kind and $k'^2 = 1 - k^2$ [22, 85].

Then for LAM rotation states we have,

$$\frac{\partial k}{\partial I_d} = \frac{1}{2} \frac{(I_s - I_l)}{(I_s - I_d)} \sqrt{\frac{I_s - I_i}{(I_i - I_l)(I_d - I_l)(I_s - I_d)}} \tag{B.9}$$

$$\frac{\partial n}{\partial I_d} = 0 \tag{B.10}$$

$$\dot{\tau}_r = \frac{2\pi}{P_\psi} = \frac{\pi \omega_e}{2K} \sqrt{\frac{I_d(I_i - I_l)(I_s - I_d)}{I_l I_i I_s}} = \frac{\pi H}{2K} c \tag{B.11}$$

$$c = \sqrt{\frac{(I_i - I_l)(I_s - I_d)}{I_d I_l I_i I_s}} \tag{B.12}$$

$$\ddot{\tau}_r = \frac{\pi}{2K} \left[\dot{H} c + H \left(\dot{c} - c \frac{\dot{K}}{K} \right) \right] \tag{B.13}$$

$$\dot{c} = -\frac{1}{2c} \frac{(I_i - I_l)}{I_d{}^2 I_l I_i} \dot{I}_d \tag{B.14}$$

Similarly for SAMs,

$$\frac{\partial k}{\partial I_d} = -\frac{1}{2} \frac{(I_s - I_l)}{(I_d - I_l)} \sqrt{\frac{I_i - I_l}{(I_s - I_i)(I_d - I_l)(I_s - I_d)}} \tag{B.15}$$

$$\frac{\partial n}{\partial I_d} = -\frac{I_l}{I_s} \frac{(I_s - I_l)}{(I_d - I_l)^2} \tag{B.16}$$

$$\dot{\tau}_r = \frac{2\pi}{P_\psi} = \frac{\pi \omega_e}{2K} \sqrt{\frac{I_d(I_s - I_i)(I_d - I_l)}{I_l I_i I_s}} = \frac{\pi H}{2K} c \tag{B.17}$$

$$c = \sqrt{\frac{(I_s - I_i)(I_d - I_l)}{I_d I_l I_i I_s}} \tag{B.18}$$

$$\ddot{\tau}_r = \frac{\pi}{2K}\left[\dot{H}c + H\left(\dot{c} - c\frac{\dot{K}}{K}\right)\right] \tag{B.19}$$

$$\dot{c} = \frac{1}{2c}\frac{(I_s - I_i)}{I_d{}^2 I_i I_s}\dot{I}_d \tag{B.20}$$

Appendix C

Expressions for Averaged Steady State Dissipation Coefficients

$$t_{11} = 2\left\{\overline{\omega_1^2\omega_2^2} + \overline{\omega_1^2\omega_3^2} + \overline{\omega_2^2\omega_3^2}\left(I_l^2 + I_s^2 - I_lI_s\right)/I_i^2 + \overline{\omega_1^2}\mu^2/J^2\right\} \tag{C.1}$$

$$t_{12} = 2\left\{\overline{\omega_2^2\omega_3^2}\left(I_l - I_s\right)/I_i - \overline{\omega_1^2\omega_2^2} - \overline{\omega_1^2\omega_3^2}\left(I_i - I_l\right)/I_s\right\} \tag{C.2}$$

$$t_{13} = 2\left\{-\overline{\omega_1^2\omega_3^2} - \overline{\omega_2^2\omega_3^2}\left(I_l - I_s\right)/I_i - \overline{\omega_1^2\omega_2^2}\left(I_i - I_s\right)/I_l\right\} \tag{C.3}$$

$$t_{14} = 2\left\{\overline{\omega_2^2\omega_3^2}\left(I_l^2 + I_s^2 - 2I_lI_s\right)/I_i^2 - \overline{\omega_1^2\omega_2^2}\left(I_i - I_s\right)/I_l - \overline{\omega_1^2\omega_3^2}\left(I_i - I_l\right)/I_s\right\} \tag{C.4}$$

$$t_{21} = 2\left\{\overline{\omega_2^2\omega_3^2}\left(I_l - I_s\right)/I_i - \overline{\omega_1^2\omega_2^2} - \overline{\omega_1^2\omega_3^2}\left(I_i - I_l\right)/I_s\right\} \tag{C.5}$$

$$t_{22} = 2\left\{\overline{\omega_1^2\omega_2^2} + \overline{\omega_2^2\omega_3^2} + \overline{\omega_1^2\omega_3^2}\left(I_i^2 + I_l^2 - I_iI_l\right)/I_s^2 + \overline{\omega_2^2}\mu^2/J^2\right\} \tag{C.6}$$

$$t_{23} = 2\left\{\overline{\omega_1^2\omega_2^2}\left(I_i - I_s\right)/I_l - \overline{\omega_2^2\omega_3^2} + \overline{\omega_1^2\omega_3^2}\left(I_i - I_l\right)/I_s\right\} \tag{C.7}$$

$$t_{24} = 2\left\{\overline{\omega_1^2\omega_3^2}\left(I_i^2 + I_l^2 - 2I_iI_l\right)/I_s^2 + \overline{\omega_2^2\omega_3^2}\left(I_l - I_s\right)/I_i + \overline{\omega_1^2\omega_2^2}\left(I_i - I_s\right)/I_l\right\} \tag{C.8}$$

$$t_{31} = 2\left\{-\overline{\omega_1^2\omega_3^2} - \overline{\omega_2^2\omega_3^2}\left(I_l - I_s\right)/I_i - \overline{\omega_1^2\omega_2^2}\left(I_i - I_s\right)/I_l\right\} \tag{C.9}$$

$$t_{32} = 2\left\{\overline{\omega_1^2\omega_2^2}\left(I_i - I_s\right)/I_l - \overline{\omega_2^2\omega_3^2} + \overline{\omega_1^2\omega_3^2}\left(I_i - I_l\right)/I_s\right\} \tag{C.10}$$

$$t_{33} = 2\left\{\overline{\omega_1^2\omega_3^2} + \overline{\omega_2^2\omega_3^2} + \overline{\omega_1^2\omega_2^2}\left(I_i^2 + I_s^2 - I_iI_s\right)/I_l^2 + \overline{\omega_3^2}\mu^2/J^2\right\} \tag{C.11}$$

$$t_{34} = 2\left\{\overline{\omega_1^2\omega_2^2}\left(I_i^2 + I_s^2 - 2I_iI_s\right)/I_l^2 - \overline{\omega_2^2\omega_3^2}\left(I_l - I_s\right)/I_i + \overline{\omega_1^2\omega_3^2}\left(I_i - I_l\right)/I_s\right\} \tag{C.12}$$